NASA-CR-194340

Guide to Magellan Image Interpretation

John P. Ford
Jeffrey J. Plaut
Catherine M. Weitz
Tom G. Farr
David A. Senske
Ellen R. Stofan
Gregory Michaels
Timothy J. Parker

November 1, 1993

NASA

National Aeronautics and
Space Administration

Jet Propulsion Laboratory
California Institute of Technology
Pasadena, California

Guide to Magellan Image Interpretation

John P. Ford
Jeffrey J. Plaut
Catherine M. Weitz
Tom G. Farr
David A. Senske
Ellen R. Stofan
Gregory Michaels
Timothy J. Parker

November 1, 1993

Foreword

This book will occupy a prominent place on the shelves of many students and geologists who will analyze the Venus radar data acquired by the Magellan spacecraft. Because the Magellan images are so well documented here and in other Magellan Project documentation cited herein, it is likely that Magellan data will serve as training material for Earth studies. It is an enormous data set; the Magellan Mission had the daunting task of mapping all of Venus, which is nearly Earth size but with no obscuring ocean basins. In the early phases of mission planning over a decade ago, radar interpretation as applied to the understanding of geologic features was an infant science. Most planetary scientists were accustomed to interpreting conventional optical images, and few were familiar with the peculiarities of radar images. Today there are many more scientists who are expert in using radar data, but there will long remain a strong need for the information in this book, even for those of us who feel that we know all the foibles of the Magellan data sets.

R. Stephen Saunders
Magellan Project Scientist

Acknowledgments

Abstract

An overview of Magellan Mission requirements, radar system characteristics, and methods of data collection is followed by a description of the image data, mosaic formats, areal coverage, resolution, and pixel DN-to-dB conversion. The availability and sources of image data are outlined. Applications of the altimeter data to estimate relief, Fresnel reflectivity, and surface slope, and the radiometer data to derive microwave emissivity are summarized and illustrated in conjunction with corresponding SAR image data. Same-side and opposite-side stereo images provide examples of parallax differences from which to measure relief with a lateral resolution many times greater than that of the altimeter. Basic radar interactions with geologic surfaces are discussed with respect to radar-imaging geometry, surface roughness, backscatter modeling, and dielectric constant.

Techniques are described for interpreting the geomorphology and surface properties of surficial features, impact craters, tectonically deformed terrain, and volcanic landforms. The morphologic characteristics that distinguish impact craters from volcanic craters are defined. Criteria for discriminating extensional and compressional origins of tectonic features are discussed. Volcanic edifices, constructs, and lava channels are readily identified from their radar outlines in images. Geologic map units are identified on the basis of surface texture, image brightness, pattern, and morphology. Superposition, cross-cutting relations, and areal distribution of the units serve to elucidate the geologic history.

Contents

Chapter 1. Magellan: The Mission and the System

John P. Ford

Introduction

The Magellan mission to Venus was launched from Cape Canaveral, Florida, aboard Space Shuttle Atlantis on May 4, 1989. After an interplanetary cruise of 15 months, the space-craft arrived at Venus on August 10, 1990, and was inserted into a near-polar elliptical orbit. Following 4 weeks of in-orbit checkout, mapping operations commenced on September 15, 1990. The primary requirements of this mission were to map at least 70% of the surface at a resolution better than 300 m [Saunders et al., 1992] and to determine the global relief at a horizontal resolution of about 10 km and a vertical accuracy of 80 m or better [Ford and Pettengill, 1992]. Data at these resolutions facilitate the detailed analysis of tectonic, volcanic, eolian, and impact features. A timeline of 243 days was necessary to achieve these "prime-mission" requirements. This timeline, termed Cycle 1, is the interval in which the planet made one full rotation under the surveillance of the Magellan orbiting radar sensor.

The scientific objectives of the Magellan mission were

(1) To provide a global characterization of landforms and tectonic features.
(2) To distinguish and understand impact processes.
(3) To define and explain erosion, deposition, and chemical processes.
(4) To model the interior density distribution.

At the start of Magellan mapping, the spacecraft orbit was adjusted to a period of 3.259 hours. Continued repetition of the basic mapping-orbit profile during Cycle 1 produced image data of about 83.7% of the planet. The extended mission added two cycles of mapping (see Chapter 2), a cycle devoted to gravity measurement, and a period of aerobraking maneuvers designed to circularize the orbit.

Pre-Magellan Observations

Radar observations of the Venusian surface were first obtained in the 1960s by Earth-based radio telescopes at Goldstone, California; Haystack, Massachusetts; and Arecibo, Puerto Rico. The data provided low-resolution images (1 to 20 km) and information about the scattering properties of the surface. From 1978 to 1981, the U.S. Pioneer–Venus orbiter obtained images from about 40°N to 10°S with a resolution of about 30 km and altimeter data from about 78°N to 63°S with a footprint size of about 100 km and an altitude accuracy of about 100 m [Pettengill et al., 1980]. These data revealed that Venus consists of about 65% rolling plains, 27% lowlands, and 8% highlands [Masursky et al., 1980]. The understanding of topography, surface properties, and the tectonic evolution of Venus that was gained from these studies, and was supplemented by surface sample data from the Soviet Veneras 8 to 10 and 13 to 14, is summarized by McGill et al. [1983].

In 1983 and 1984, the Soviet Veneras 15 and 16 acquired the first orbital synthetic-aperture radar (SAR) images of the northern hemisphere. About 25% of the surface was covered at a resolution of 1 to 2 km. Corresponding altimeter coverage was obtained with a footprint of 40 to 50 km and an altitude accuracy of 50 m. These data showed the presence of tectonic features such as domical uplifts, low ridge belts, heavily deformed terrain (tesserae), pronounced circular features (coronae), and a variety of plains and impact craters [Barsukov et al., 1986].

The results of these Earth-based-imaging, orbital-mapping, and radar-altimeter experiments revealed the need for global radar data coverage of the Venusian surface at orders-of-magnitude higher resolution. They provided incentives for determining the objectives of the Magellan mission, designing

the Magellan sensor system, and planning the mission operations.

The Magellan Radar Sensor

The Magellan sensor is a single instrument capable of acquiring radar data in three different modes. In the SAR imaging and the radiometer modes, the system is connected to a 3.7-m-diameter parabolic high-gain antenna (HGA) fixed at 25 deg off nadir in a direction normal to the spacecraft trajectory. The SAR operates at a wavelength of 12.6 cm (S-band, 2.385 GHz) with horizontal parallel transmit/receive polarization (HH). This enables the pulsed microwave energy to penetrate the thick cloud cover (mostly carbon dioxide) that envelops the planet and to discriminate small-scale surface roughness. In the altimeter mode, the system is connected to a smaller, nadir-directed altimeter horn antenna (ALTA). The geometry of data acquisition is shown in Figure 1-1.

Because of the elliptical orbit, it was necessary to vary the SAR imaging geometry (look angle/incidence angle) and

viewing direction so as to obtain maximum surface coverage. The antennas, however, were fixed, and this operation was accomplished by means of spacecraft attitude adjustments. Three reaction wheels mounted in the forward module of the spacecraft (one for each possible axis of rotation) provided the momentum required to achieve such adjustments. The beam-width of the altimeter antenna was wide enough to maintain nadir-directed transmit/receive capability within the limits of these adjustments. Details of the system design are given in Saunders et al. [1990] and Johnson [1991]. Characteristics of the sensor and the orbit are listed in Table 1-1.

Burst Mode of Data Collection

Magellan radar data were obtained by a process known as the burst mode of operation, in which the sensor acquired SAR, altimeter, and radiometer data sequentially in batches several times per second. Each batch or burst period included time-domain multiplexing of transmitted SAR and altimeter pulses, received SAR and altimeter echoes, and received
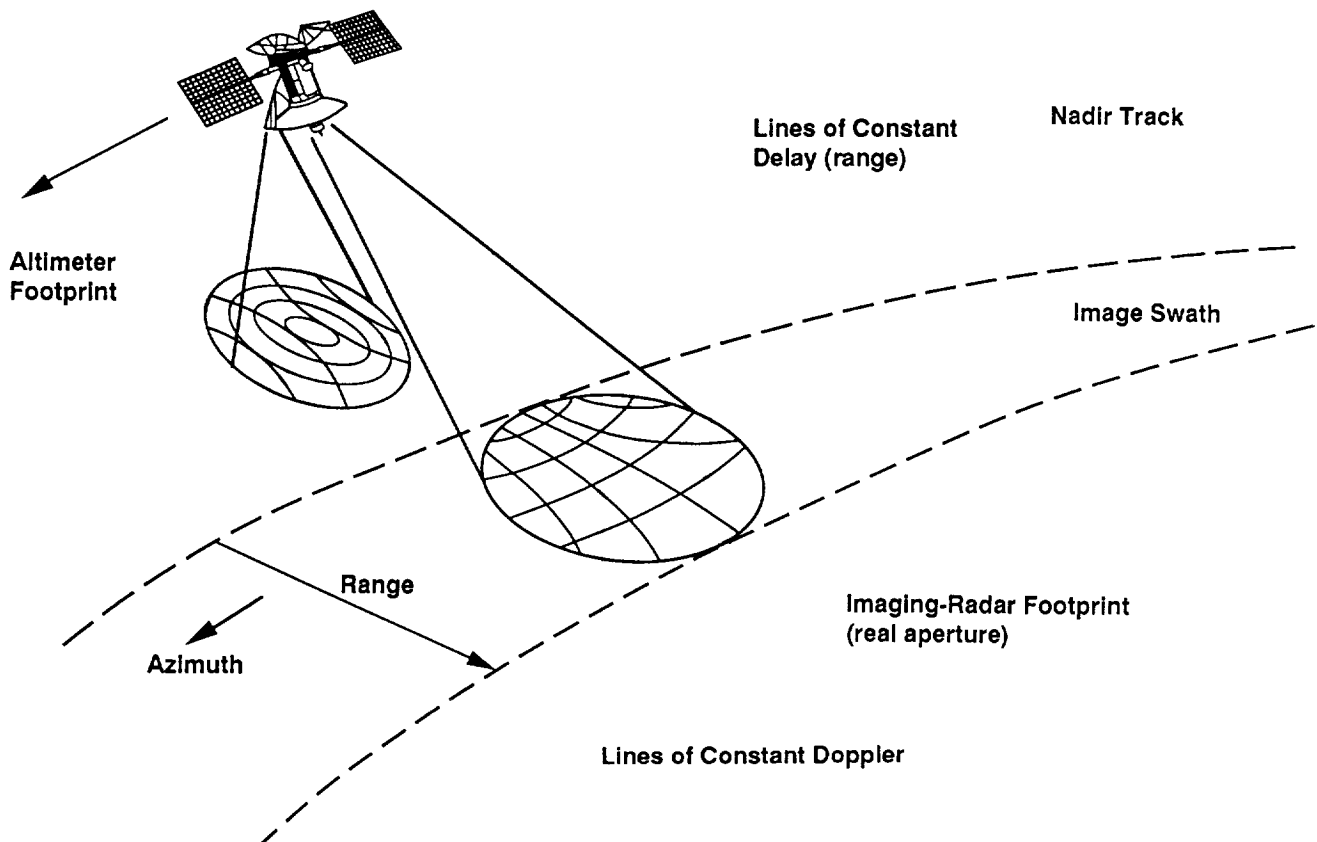

Figure 1-1. Magellan observing geometry in the SAR imaging, altimeter, and radiometer modes of operation. Cross-track resolution is obtained from the time-delay (range) coordinate. Along-track resolution comes from Doppler-frequency analysis. Resolution in the radiometer mode is determined from the high-gain antenna pattern.

2

Table 1-1. Magellan radar system and orbit characteristics

Parameter	Value
Radar system characteristics	
Wavelength, cm	12.6
Operating frequency, GHz	2.385
Modulation bandwidth, MHz	2.26
Transmitted pulse length, μs	26.5
SAR antenna	
Gain, dB	36.0
Angular beamwidth, deg	2.1 × 2.5
Altimeter antenna	
Gain, dB	19.0
Angular beamwidth, deg	10 × 30
Polarization	HH
Effective slant-range resolution, m	88
Along-track resolution, m	120
Orbit characteristics	
Periapsis altitude, km	289
Periapsis latitude, °N	9.5
Altitude at pole, km	2000
Inclination, deg	85.5
Period, hr	3.259
Repeat cycle, days	243

passive microwave energy. Using the HGA, the SAR first transmitted a burst of 150 to 800 pulses, each with a length of 26.5 μs, for a period from 25 to 250 ms. Because of the long duration of this mode, the received SAR echoes were interleaved with the transmitted pulses (Figure 1-2). After the last SAR echo had been received, the sensor switched to the altimeter mode and, using the horn antenna, transmitted a burst of 17 nadir-directed pulses. All the altimeter pulses were transmitted before the first altimeter echo was received. Switching to the radiometer mode, the sensor used the HGA to receive naturally emitted energy from the planet surface for a period of 50 ms.

Mapping-Orbit Profile

Mapping started when Magellan was located above the north pole and the HGA was pointed toward the Venusian surface. Because this occurred in the descending node of the orbit, the mapping-orbit profile proceeded clockwise in a west-to-east direction (Figure 1-3). In the left-viewing geometry of Cycle 1, the HGA was pointed east of the spacecraft nadir track. Mapping continued for 37.2 min with onboard tape recording of the radar data. During this interval, a systematic sequence of preprogrammed commands controlled the spacecraft attitude, the radar pulse repetition frequency (PRF), and timing of the echo sampling. In Cycle 1, the nominal incidence angle was varied by rotating the spacecraft attitude to obtain the best resolution at a fixed signal-to-noise ratio (see Chapter 2). In all mapping cycles, the PRF and timing of the echo sampling were adjusted continuously to compensate for the changing altitude of the spacecraft, from over 2000 km in polar latitudes to about 290 km at periapsis.

Radar mapping was followed in each orbit profile by rotation of the spacecraft and alignment of the HGA to play back the recorded radar data to a Deep Space Network (DSN) station. Deep Space Communications Complexes are situated about 120 deg apart in longitude, in California (at Goldstone, 190 km northeast of Los Angeles), Australia (40 km southwest of Canberra), and Spain (60 km west of Madrid). The playback period is divided into 56.6 min before and 57.2 min after apoapsis (8458 km), with an intervening interval of 14 min for star scan and for reaction-wheel desaturation. Desaturation reduces the velocity of the reaction wheels to zero in each orbit, and thus maintains their readiness to control the rotation of the spacecraft in each succeeding orbit.

After completion of playback, the spacecraft was rotated to orient the HGA toward Venus for a renewed mapping orbit. Thus the mapping mission consisted of programmed intervals of data collection, data playback to Earth, and spacecraft housekeeping.

Because the area of new terrain observed by the sensor in equatorial latitudes is much greater than at the poles, it is possible to map high latitudes on alternating orbits with an acceptable margin of overlap. In Cycle 1, this technique was used to reduce redundancy and maximize areal coverage. Mapping started at the north pole in each alternate orbit and continued to about 57°S latitude. These swaths are termed "immediate." In the intervening orbits, mapping started at about 70°N and extended to 74°S latitude. These swaths are "delayed." An idle time of about 7 min occurred at the end of each immediate swath and the beginning of each delayed swath (Figure 1-3). The spacecraft attitude controls and the radar command sequences described above were preprogrammed and relayed at intervals to the Magellan spacecraft to satisfy mission requirements throughout the three mapping cycles.
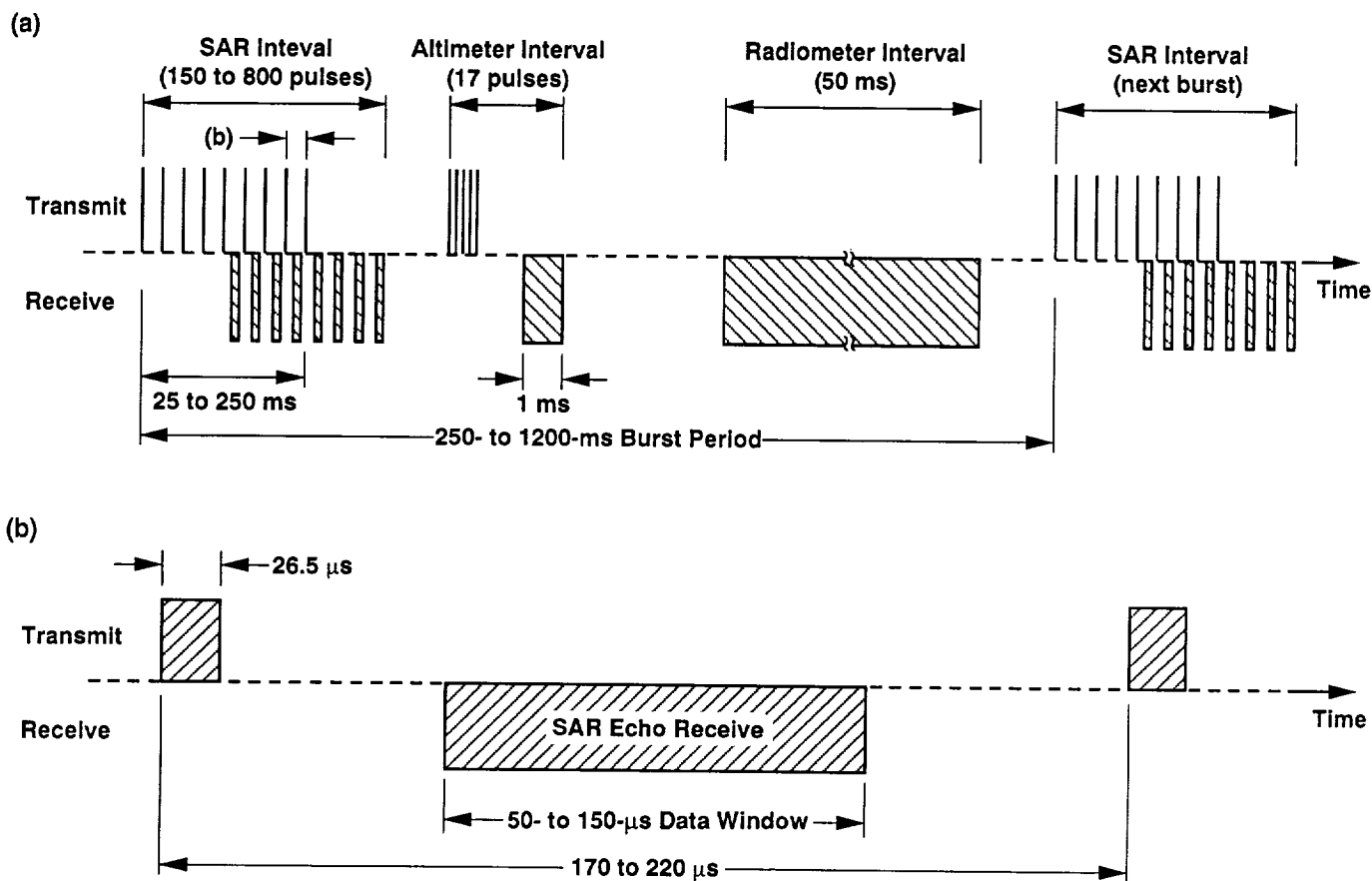
(a)

(b)

Figure 1-2. Burst-mode method of data collection [adapted from Pettengill et al., 1991]: (a) time-domain multiplexing of SAR, altimeter, and radiometer intervals; (b) detail of the receive interval between transmitted SAR pulses.
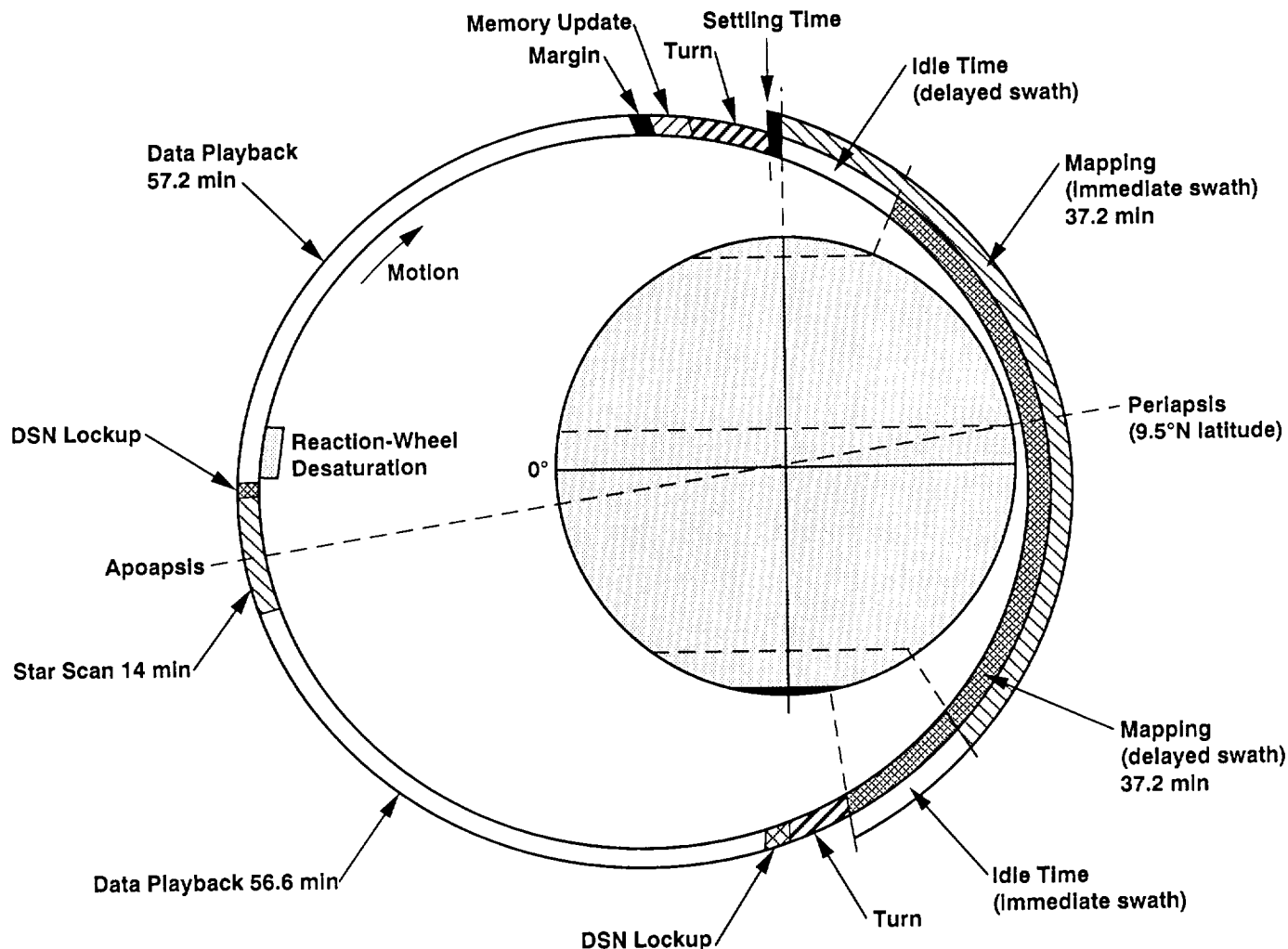
Figure 1-3. Magellan mapping orbit profile [adapted from C. Young, 1990].

References

Barsukov, V. L., et al., 1986, "The geology and geomorphology of the Venus surface as revealed by the radar images obtained by Veneras 15 and 16," *Proc. Lunar Planet. Sci. Conf. 16th, Part 2, J. Geophys. Res.*, v. 91, suppl., p. D378–D398.

Ford, P. G., and G. H. Pettengill, 1992, "Venus topography and kilometer-scale slopes," *J. Geophys. Res.*, v. 97, no. E8, p. 13,103–13,114.

Johnson, W. T. K., 1991, "Magellan imaging radar mission to Venus," *IEEE Proc.*, v. 79, p. 777–790.

Masursky, H., W. M. Kaula, G. E. McGill, G. H. Pettengill, G. G. Schaber, and G. Schubert, 1980, "Pioneer Venus radar results: Geology from images and altimetry," *J. Geophys. Res.*, v. 85, p. 8232–8260.

McGill, G. E., et al., 1983, "Topography, surface properties, and tectonic evolution," in *Venus*, edited by D. M.

Hunten, L. Colin, T. M. Donahue, and V. I. Moroz, The University of Arizona Press, Tucson, Arizona, p. 69–130.

Pettengill, G. H., D. B. Campbell, and H. Masursky, 1980, "The surface of Venus," *Sci. Am.*, v. 243, no. 2, p. 54–65.

Pettengill, G. H., P. G. Ford, W. T. K. Johnson, R. K. Raney, and L. A. Soderblom, 1991, "Magellan: Radar performance and data products," *Science*, v. 252, p. 260–265.

Saunders, R. S., G. H. Pettengill, R. E. Arvidson, W. L. Sjogren, W. T. K. Johnson, and L. Pieri, 1990, "The Magellan Venus radar mapping mission," *J. Geophys. Res.*, v. 95, p. 8339–8355.

Saunders, R. S., et al., 1992, "Magellan Mission Summary," *J. Geophys. Res.*, v. 97, no. E8, p. 13,067–13,090.

Young, C., editor, 1990, *The Magellan Venus Explorer's Guide*, Publication 90-24, Jet Propulsion Laboratory, Pasadena, California, 197 p.

Chapter 2. Magellan Image Data

John P. Ford and Jeffrey J. Plaut

Introduction

The Magellan radar mapping mission produced the first global, high-resolution (~100-m) image data set of Venus [Saunders et al., 1992]. Images were obtained from September 1990 to September 1992 during three mapping cycles (Figure 2-1). A total of 4225 usable SAR imaging orbits was obtained. The area covered by each orbit is typically 20 km wide and 17,000 km long. Ninety-eight percent of the surface was imaged and many areas were viewed more than once with different imaging geometries and/or directions of illumination. Magellan image data products consist of mosaics in a variety of formats and scales. Figure 2-2 is a global radar mosaic. Details concerning the characteristics of the mosaics and the images, the imaging cycles, and information about the availability of data and data products are presented in this chapter.

Image Data Records

Raw SAR data received from the Magellan spacecraft are processed into basic image data records (BIDRs). Each BIDR strip is accompanied by a corresponding altimeter/radiometer composite data record (ARCDR) for each orbit. In the altimeter mode, nadir-directed radar pulses measured the distance between the spacecraft and the Venusian surface. In the radiometric mode, the radar system monitored the microwave thermal emission of the surface. The primary image data product is the full-resolution BIDR (F-BIDR). Because the long, narrow format of the F-BIDR image is not useful for geologic mapping, adjacent image strips are assembled into mosaicked image data records (MIDRs).

Details of SAR image acquisition can be found in the Experimenter's Notebook. This computer file provides an investigator with the orbital elements, uplink commands,
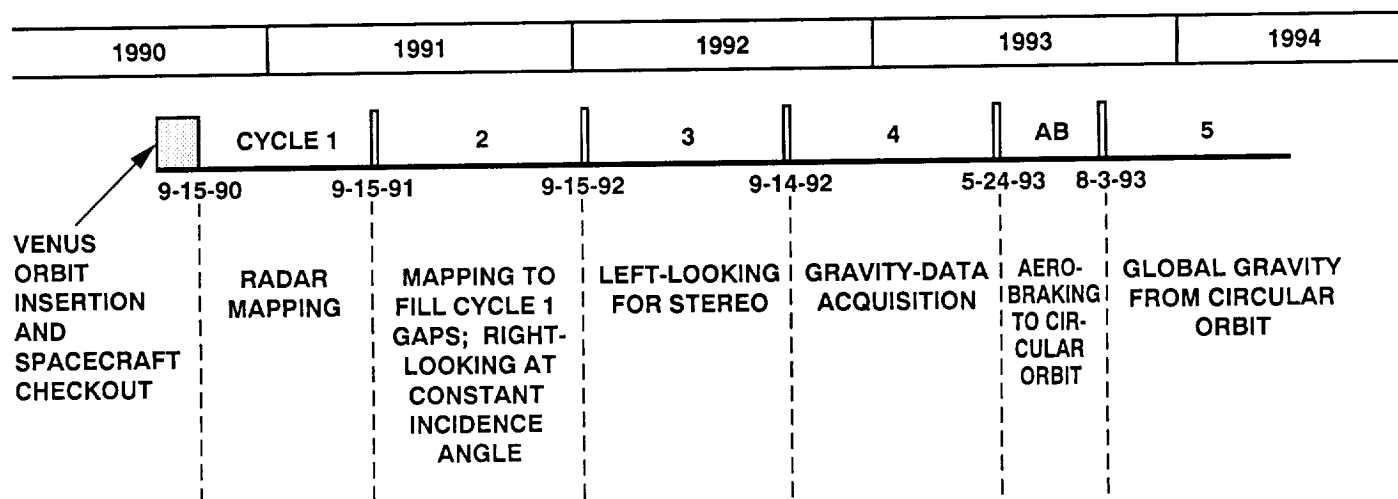

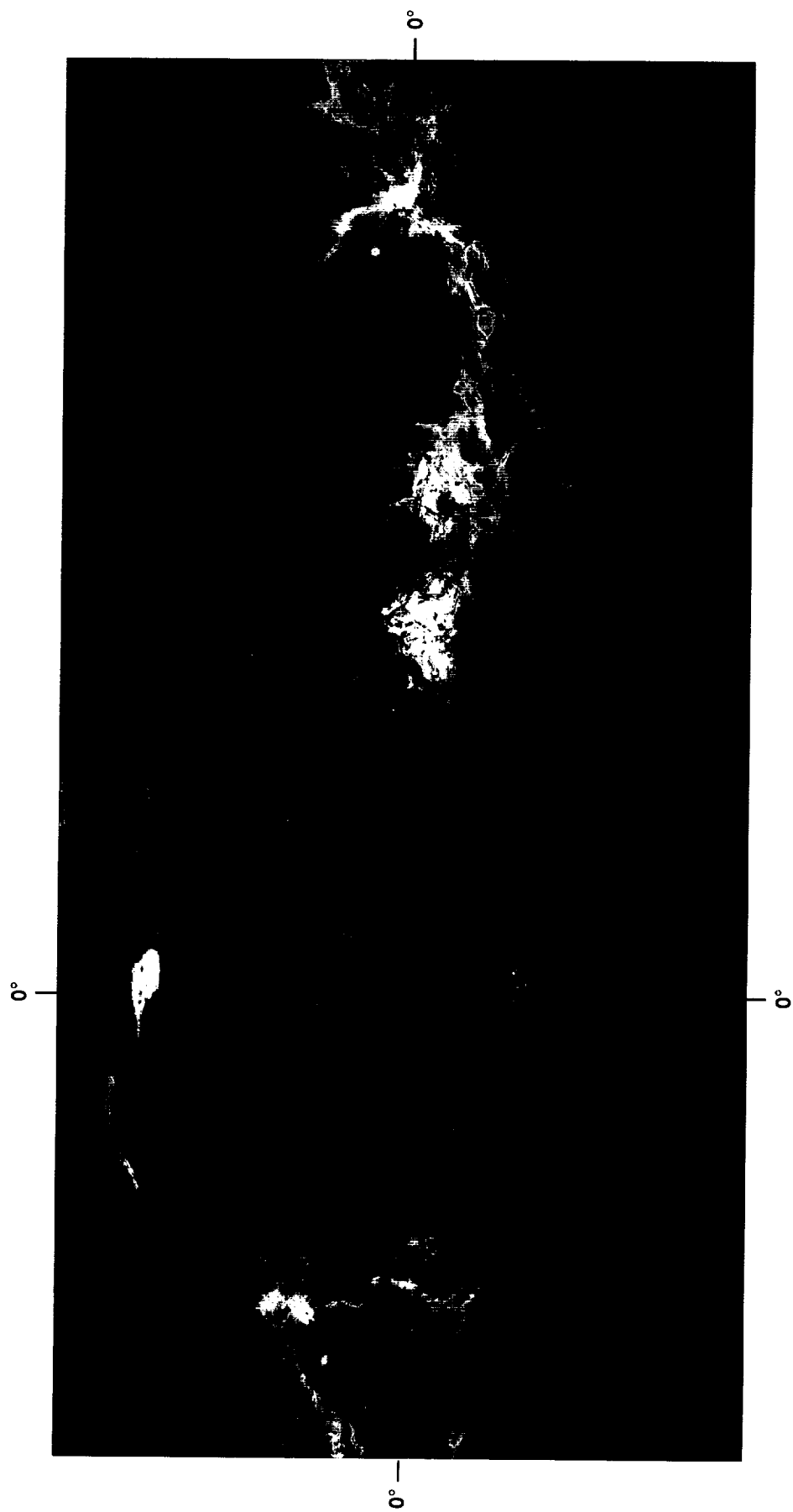Figure 2-1. Mission mapping baseline and gravity-data acquisition plan.

Figure 2-2. Global radar mosaic of Venus.

downlink text observations, and radar imaging geometry (including incidence angles and image coordinates) that were effective during the course of the mission. The image data obtained between 89°N and 89°S latitude have been processed to a sinusoidal equal-area map projection. Within 10 deg of the poles, the data were also processed to an oblique sinusoidal projection.

Mosaicking

Orbit determinations based on short data arcs from a single day's tracking provide the basis for SAR processing, locating individual pixels, and mosaicking the image strips. The final ephemeris data are sufficiently accurate to allow mosaicking of image data strips by a process of dead reckoning without the use of tie points.

Mosaicking algorithms have been developed to produce smooth boundaries between adjacent orbits. In some mosaicked images, however, a dark or bright banding runs parallel to the orbit boundaries. This banding is the result of small differences in antenna pointing, spacecraft navigation, and topographic modeling that resulted in the application of slightly inaccurate radiometric factors in the processor.

Image mosaics consisting of 7168 lines × 8192 samples provide the base for standard Magellan photographic image products (MIDRs) (Figure 2-3). Full-resolution mosaicked image data records (F-MIDRs) use the full resolution (75 m) of the input F-BIDRs, and cover an area approximately 5 deg on a side. Each F-MIDR has a photomosaic identifier in the general form of F-MIDRP.xxHyyy;C, where P stands for photomosaic, H represents the hemisphere (N for north; S for south), xx is approximate latitude (deg) and yyy is approximate longitude (deg) at the center of the mosaic, and C denotes the cycle (1, 2, or 3) in which the data were acquired. In Cycle 1, C is a single digit corresponding to the version number. In Cycles 2 and 3, three-digit numbers are used: The first digit indicates the cycle and the last is the version number. For example, F-MIDRP.60N026;301 is an F-MIDR photomosaic centered near 60°N latitude and 26°E longitude from Cycle 3 and is version 1.

Mosaics of larger areas are obtained by compressing the resolution of the BIDRs. Three levels of compressed MIDRs have been produced (C1-MIDR, 15 deg on a side and 225-m resolution; C2-MIDR, 45 deg on a side and 675-m resolution; C3-MIDR, 120 × 80 deg and 2025-m resolution; see Figure 2-3). Each stage of compression involves the spatial averaging of 3 × 3 arrays of pixels from the next higher resolution image data record. Thus, C1-MIDRs are produced from C1-BIDRs. C2-MIDRs and C3-MIDRs are compressed from C1-MIDRs. Each of the C1-, C2-, and C3-MIDR photomosaic identifiers denotes the coordinates of the mosaic

center and the acquisition cycle as described above for the F-MIDRs.

After mosaicking, the images are contrast enhanced, annotated, and masked to produce photographic output data for scientific analysis. Unenhanced digital data are stored on computer-compatible tapes (CCTs), write-once-read-many (WORM) optical disks, and compact disks read-only memory (CD-ROMs); in addition, these data have been written to film. The CD-ROMs also contain numerous documentation files.

Resolution

In the F-BIDRs, the image pixel size is sampled to 75 m in both cross-track and along-track directions. The spatial resolution of the images in the cross-track direction and the number of looks used to process the data vary with latitude. The number of looks corresponds with the number of independent observations made for each resolution element. Increasing the number of looks reduces the speckle noise that occurs in coherent radar imaging, but it also reduces the spatial resolution of the images. The number of looks and the pixel resolution as functions of latitude for the first mission cycle are listed in Table 2-1.

Table 2-1. Number of looks and pixel resolution for Cycle 1 image data[a]

Latitude, deg	Number of looks	Cross-track resolution, m	Along-track resolution, m
90	14	250	110
82	15	211	110
60	9	155	110
45	8	125	110
30	6	108	110
10	5	101	110
−10	5	108	110
−25	5	125	110
−40	11	155	110
−62	15	211	110
−70	14	250	110

[a]From Saunders et al., 1992.

Pixel values in the F-BIDRs represent the observed radar backscatter coefficient relative to an empirically derived formula [Muhleman, 1964] that describes the average backscatter $\sigma^0(\theta)$ of the Venusian surface as a function of incidence angle θ. This formula states

$$\sigma^0(\theta) = \frac{K_1 \cos\theta}{(\sin\theta + K_2 \cos\theta)^3}$$

where the constants $K_1 = 0.0188$ and $K_2 = 0.111$.

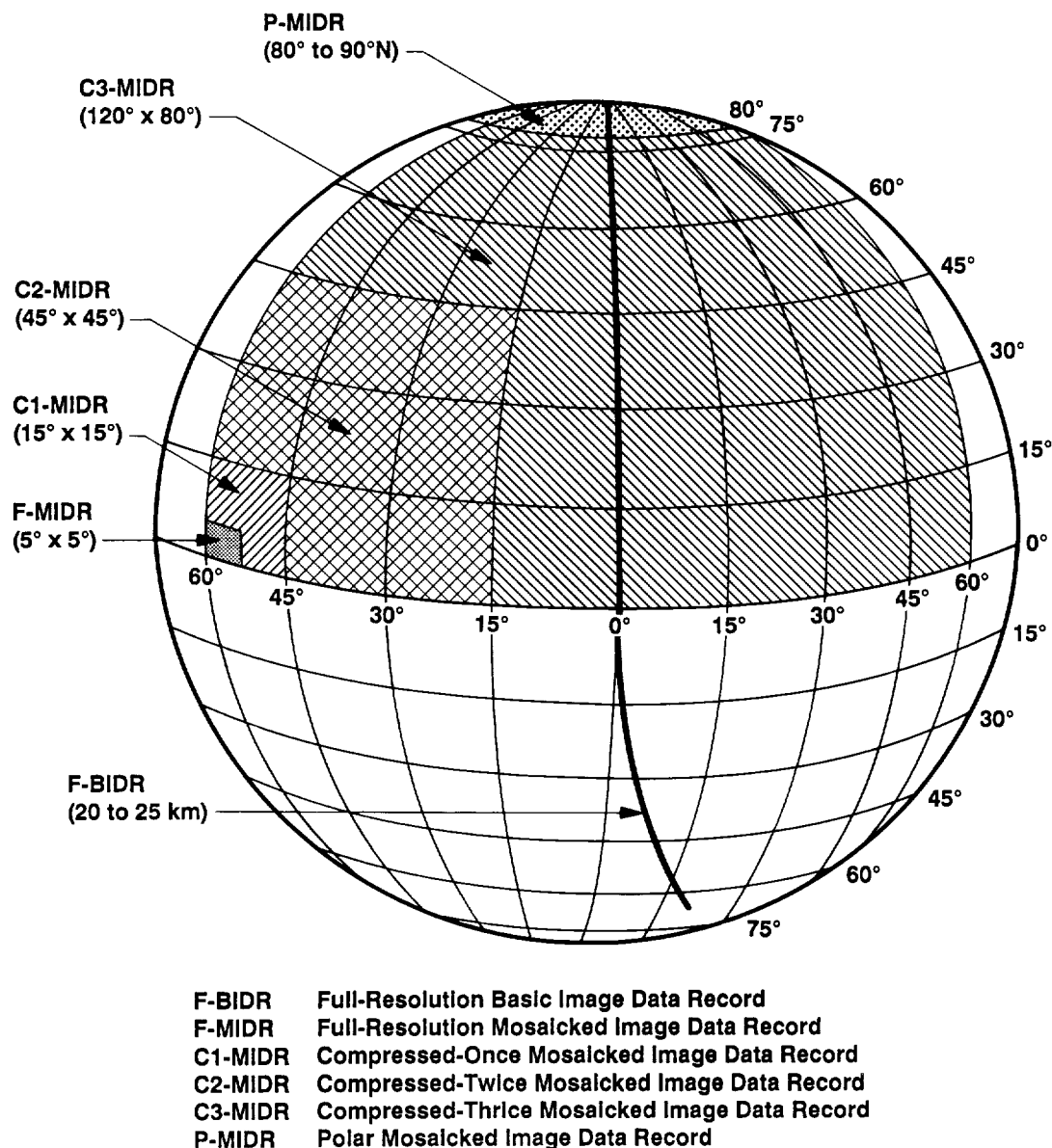| F-BIDR | Full-Resolution Basic Image Data Record |
F-MIDR	Full-Resolution Mosaicked Image Data Record
C1-MIDR	Compressed-Once Mosaicked Image Data Record
C2-MIDR	Compressed-Twice Mosaicked Image Data Record
C3-MIDR	Compressed-Thrice Mosaicked Image Data Record
P-MIDR	Polar Mosaicked Image Data Record

Figure 2-3. Image data products.

In lieu of these intended values, the SAR processor was implemented with erroneous values of $K_1 = 0.0118$ and $\theta = \theta + 0.5$ deg. Thus, pixel values in the F-BIDRs are based on an approximation of the intended backscatter function $\sigma^0(a)$ where:

$$\sigma^0(a) = \frac{0.0118\cos(\theta + 0.5\deg)}{\left[\sin(\theta + 0.5\deg) + 0.111\cos(\theta + 0.5\deg)\right]^3}$$

The pixel DN values range from 1 to 251. A DN value of 101 corresponds to a measured backscatter function equal to that of the approximation model (a DN of 111 represents

the expected value according to the correct Muhleman model). The relative backscatter coefficient σ^0 of other pixel DN values is given by

$$\sigma^0 = 0.2 \left(\text{pixel DN} - 101\right) \text{ dB}$$

Non-SAR Data

Venusian topography, roughness, and compositional characteristics of the surface cannot be determined from image data alone; altimetry and radiometry measurements have provided important additional information necessary for

10

the interpretation of these parameters. Details of these non-SAR experiments are outlined in Chapter 3.

Image Brightness

Brightness variations in Magellan images result primarily from three different surface variables: (1) topographic effects, (2) roughness, and (3) electrical properties, each of which is influenced to some extent by variations in the radar incidence angle and/or the direction of illumination. A guide to the interpretation of these effects in the images is provided in Chapters 5 through 9.

At the scale of the radar resolution, topography may have a pronounced effect on image brightness; terrain that slopes toward the imaging sensor appears bright and spatially compressed relative to terrain that slopes away, which appears dark and spatially expanded. Where the incidence angle θ < 20 deg, small changes in slope give large changes in backscatter. In cases where broad regional slopes are too small to provide brightness contrast, altimetry data are needed to distinguish large-scale positive and negative relief.

In the absence of topographic effects, surface roughness at the scale of the radar wavelength may dominate the backscatter where the incidence angle θ > 20 deg and < 60 deg. Rough surfaces have a notably higher backscatter than smooth surfaces. Though the Magellan data have been normalized to a model that describes the average backscatter of Venus (see above), surface roughness can strongly influence image brightness.

In addition to topographic or surface-roughness effects, the intrinsic reflectivity properties of the surface can have a major influence on image brightness; high dielectric constants (controlled by composition and/or bulk density) enhance radar backscatter.

Cycles of Coverage

Each of the three mapping cycles was limited in the amount of image coverage that could be obtained. After the first mapping cycle, image acquisition was directed toward filling gaps and obtaining data from different viewing angles and directions. As the spacecraft orbited from north to south, the SAR when pointed east was "left-looking"; when pointed west it was "right-looking." Variations of incidence angle with latitude in each of the three cycles are listed in Table 4-1 and shown in Figure 4-3.

Cycle 1

The purpose of Cycle 1—from mid-September 1990 to mid-May 1991—was to acquire radar mapping data of 70% of the surface at a resolution better than 300 m (Figure 2-1). Because of the elliptical orbit, the spacecraft altitude varied from about 2000 km near the north pole to 290 km at 9.5°N latitude (periapsis). To maintain an acceptably high signal-to-noise ratio throughout each mapping orbit and compensate for the increasing signal loss as the distance to the surface increased, it was necessary to decrease the incidence angle progressively with increasing latitude on either side of periapsis.

Left-looking images were obtained at incidence angles that varied from about 45 deg at periapsis to about 16 deg at high latitudes (Figure 4-3). About 83.7% of the surface was covered (Figure 2-4). Superior conjunction (when Venus passed behind the Sun) precluded the acquisition of data from 110 of the 1790 orbits needed to obtain a full 360 deg of longitudinal coverage. Other gaps resulted from geometric limitations (1.5%) that precluded viewing the south polar region and data losses (8.6%) caused by overheating of the electronics system, failure of one of the onboard tape recorders, attitude-control anomalies, and erroneous attitude updates.

Cycle 2

Cycle 2—from mid-May 1991 to mid-January 1992—was dedicated to filling gaps caused by superior conjunction in Cycle 1 and obtaining coverage of the south polar area. The latter requirement necessitated reorientation of the spacecraft in a right-looking geometry. The images were obtained with a mostly constant incidence angle of about 25 deg in the latitudes from 65°N to 45°S and with smaller angles toward the south pole (Figure 4-3).

During the data playbacks in Cycle 2, the spacecraft electronic bays were overheated by solar illumination. To compensate for this, the spacecraft was cooled by pointing the high-gain antenna toward the Sun. Since tape playback could not be relayed to Earth during these Sun-pointing periods, the amount of mapping data obtained was significantly less than in Cycle 1. The surface coverage in Cycle 2 amounts to 54.5% (Figure 2-5); cumulative coverage of the surface rose to 96%.

An eight-orbit stereo test in mid-Cycle 2 showed that Magellan could revisit areas mapped in Cycle 1 with a different left-looking incidence angle and successfully produce same-side stereo image pairs. This stereo data test pointed the way for acquiring stereo coverage in mission Cycle 3.

An error in the implementation of the SAR processing algorithm caused a slight degradation in the quality of the images during Cycles 2 and 3. The error is manifested as a
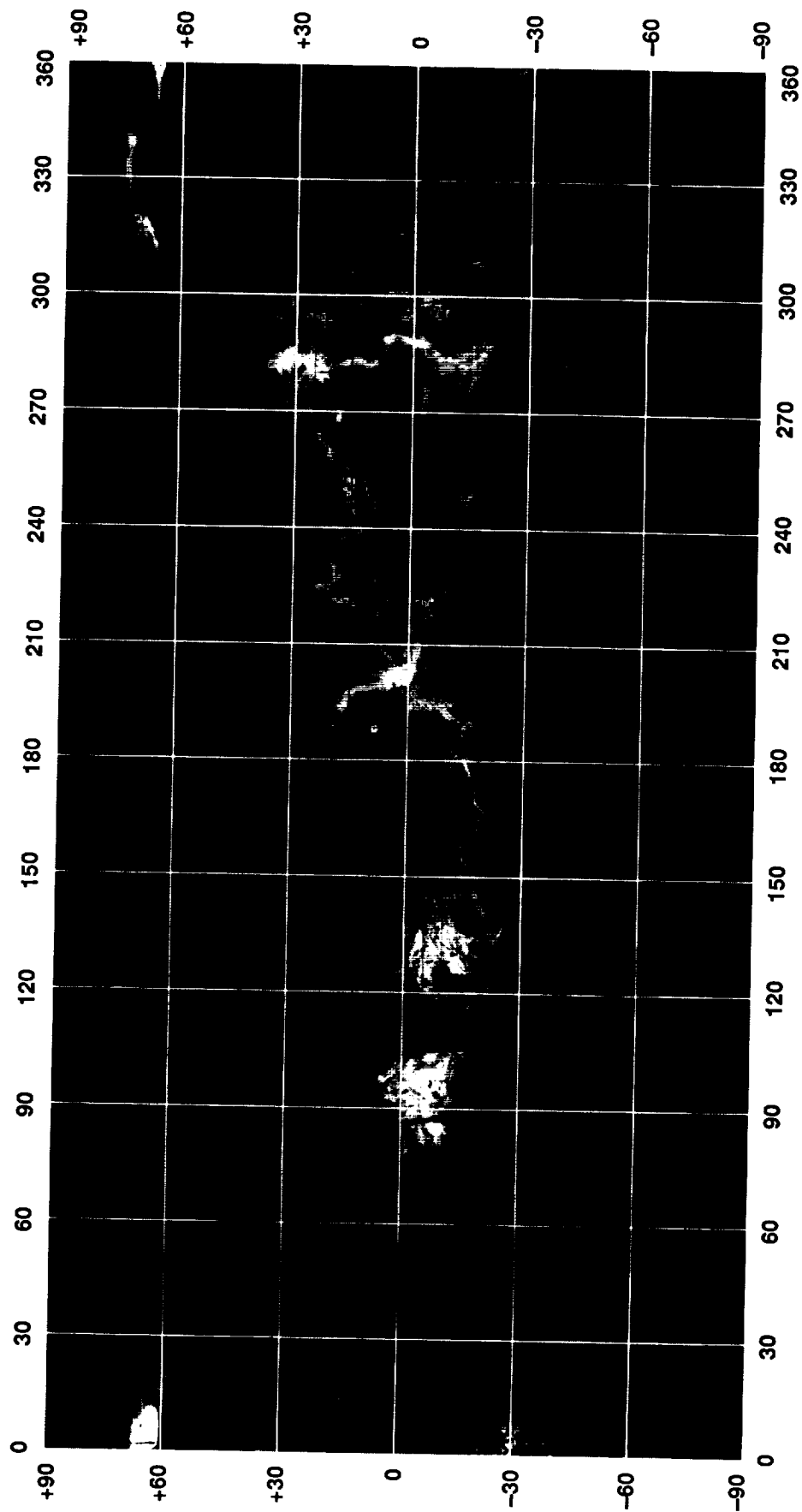
Figure 2-4. Mosaic of Cycle-1 coverage (left-looking).

12

reduction in the dynamic range (gray levels) of the images. The lower end of the brightness scale was "clipped," such that all pixels intended to have DN values between 1 and about 75 were reassigned to a narrow range near 75. This resulted in a loss of detail in the dark regions of the images. The data were eventually reprocessed to restore the full dynamic range, but most image mosaics (F-MIDRs and C-MIDRs) from Cycles 2 and 3 were constructed from the reduced dynamic range data. The orbits affected by this problem range from 2773 to 4515.

Cycle 2 orbits 2689 through 2901 were originally processed with a topographic model different than that used for the remainder of the Magellan SAR data. The model was intended to improve the location of features, but unfortunately it produced greater distortion. The orbits were eventually reprocessed, but artifacts from the original processing appear in most of the mosaics that include images from these orbits. One area of study that can be affected by these distortions is height determination based on opposite-side stereo pairs (see Chapter 4).
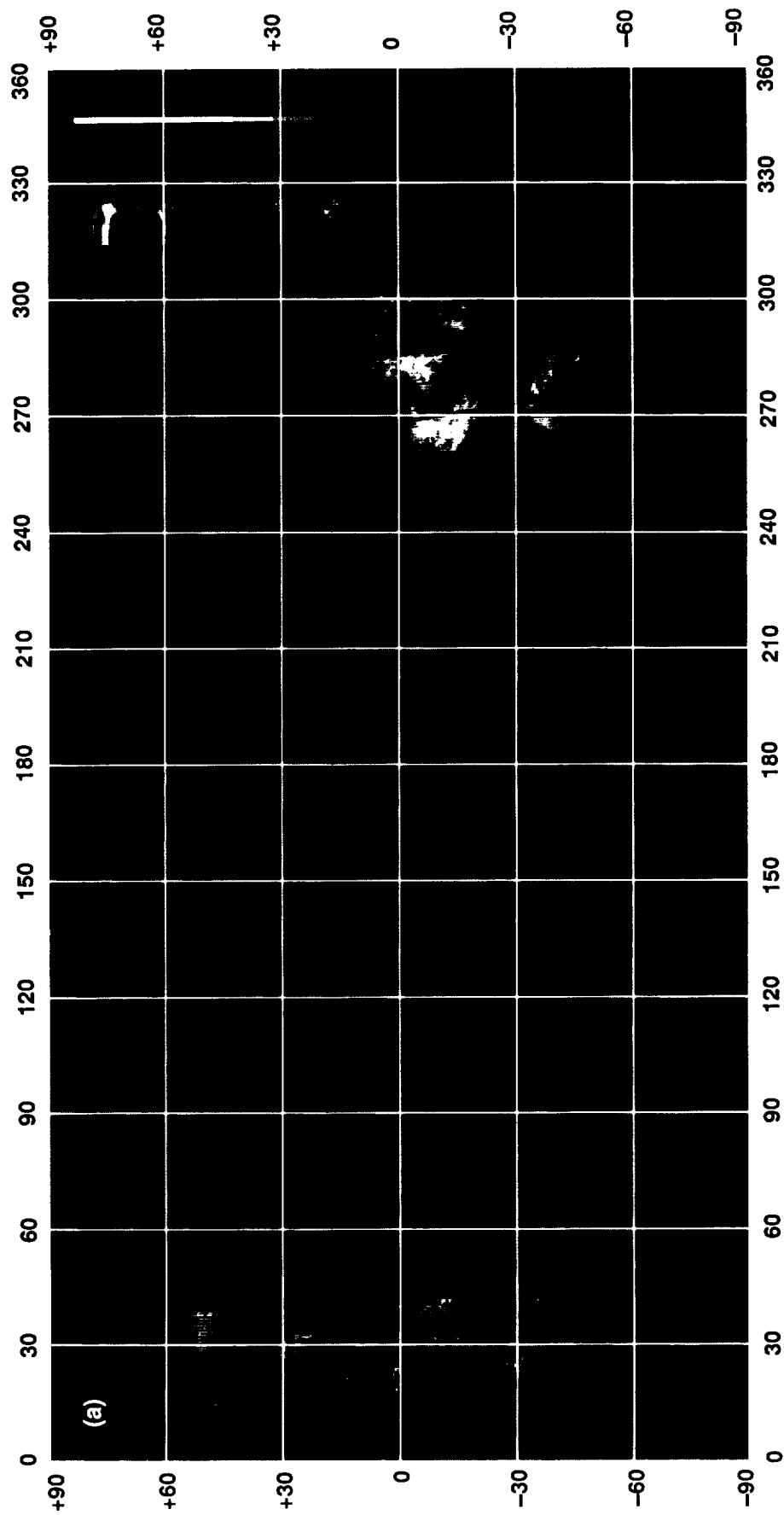
Cycle 3

Cycle 3—from mid-January to mid-September 1992—emphasized the acquisition of stereo image coverage. The ability to obtain data during this period was marked by both success and failure. About 21.3% of the surface was covered by left-looking images at incidence angles mostly smaller than those used in Cycles 1 and 2 (Figures 2-6 and 4-3). Additional coverage of Maxwell Montes was obtained at incidence angles larger than those in Cycle 1. Failure of the primary downlink transmitter and deterioration of the secondary transmitter reduced the signal-to-noise ratio in the data and created numerous gaps in coverage. Loss of data also occurred during solar occultations. However, an additional 2% of the planet was covered at the nominal Cycle 1 incidence angle profile in the final two weeks of this cycle. The cumulative coverage of the surface rose to 98%.

Cycle 4

At the termination of radar mapping in Cycle 3, the mission was dedicated to gravity observations in Cycle 4. Gravity data can be collected only when periapsis is unocculted from Earth. This condition existed for the full duration of Cycle 4. Gravity data were acquired by pointing Magellan's high-gain antenna toward Earth and recording changes in the radio signal's Doppler shift. In this mode, it is not possible to acquire image or altimetry data. The gravity data were reduced to measure spacecraft velocity changes as small as 0.1 mm sec^{-1}. Gravity maps will indicate density variations in the planet's interior. Because of the elliptical orbit, the gravity resolution varies as a function of altitude. It is highest at periapsis and lowest at the polar regions. Thus, high-resolution gravity data can be obtained only at low latitudes. An aerobraking maneuver to circularize the orbit will equalize the gravity resolution around the planet (Figure 2-1). This will enable the acquisition of uniformly high-resolution gravity data at all latitudes.

Availability of Data

To ensure that a complete and well documented data set is available to the scientific community and to the general public, Magellan CCTs and CD-ROMs have been distributed to the National Space Science Data Center (NSSDC). The NSSDC is the principal repository and distributor of Magellan CD-ROMs. Some SAR mosaics have been combined with digital elevation data to produce perspective views. Programs on video cassettes have been created that use thousands of perspective scenes incrementally to simulate flights over the surface of Venus. Information on the availability of these and other Magellan products is given in the appendix.

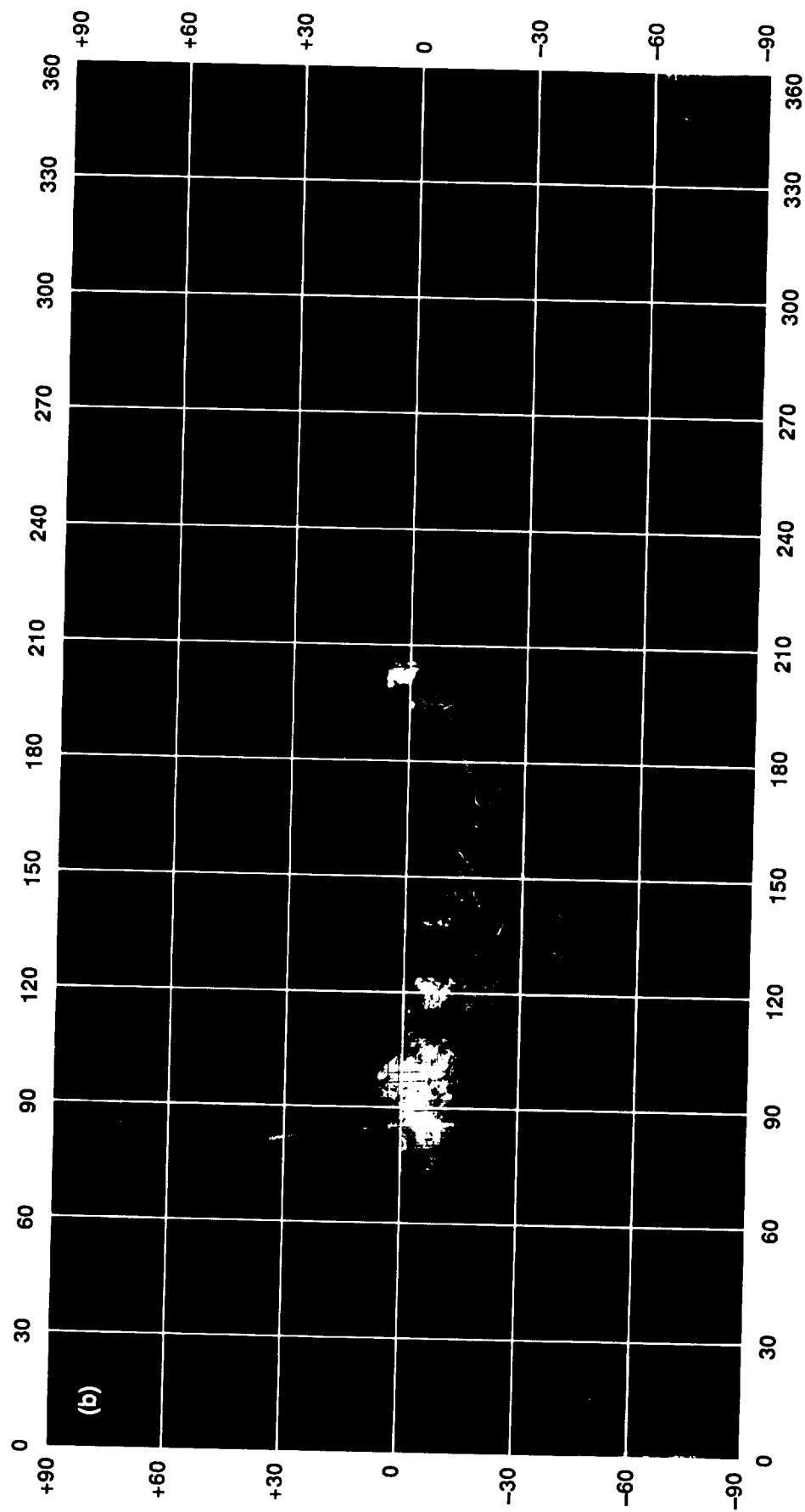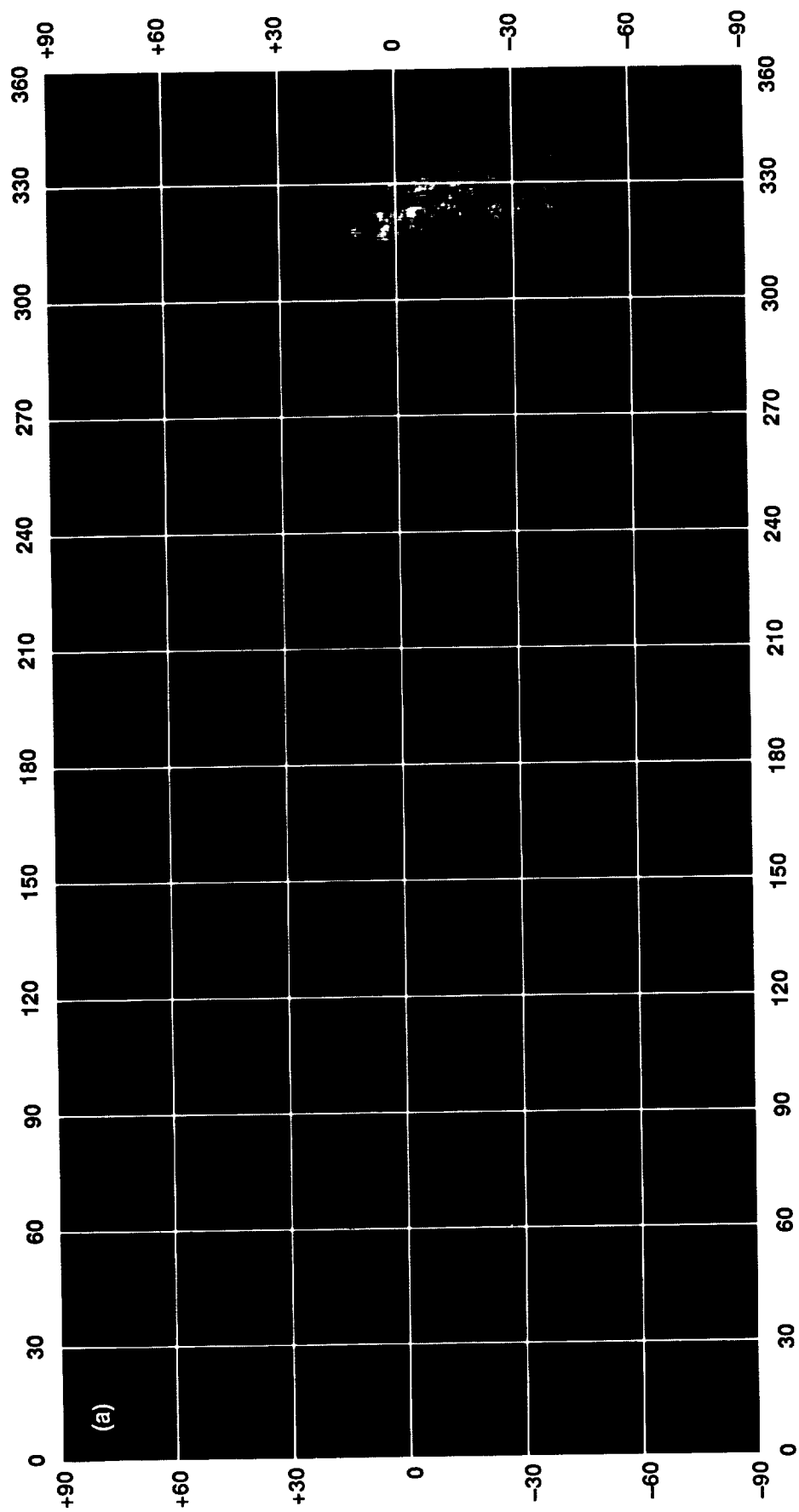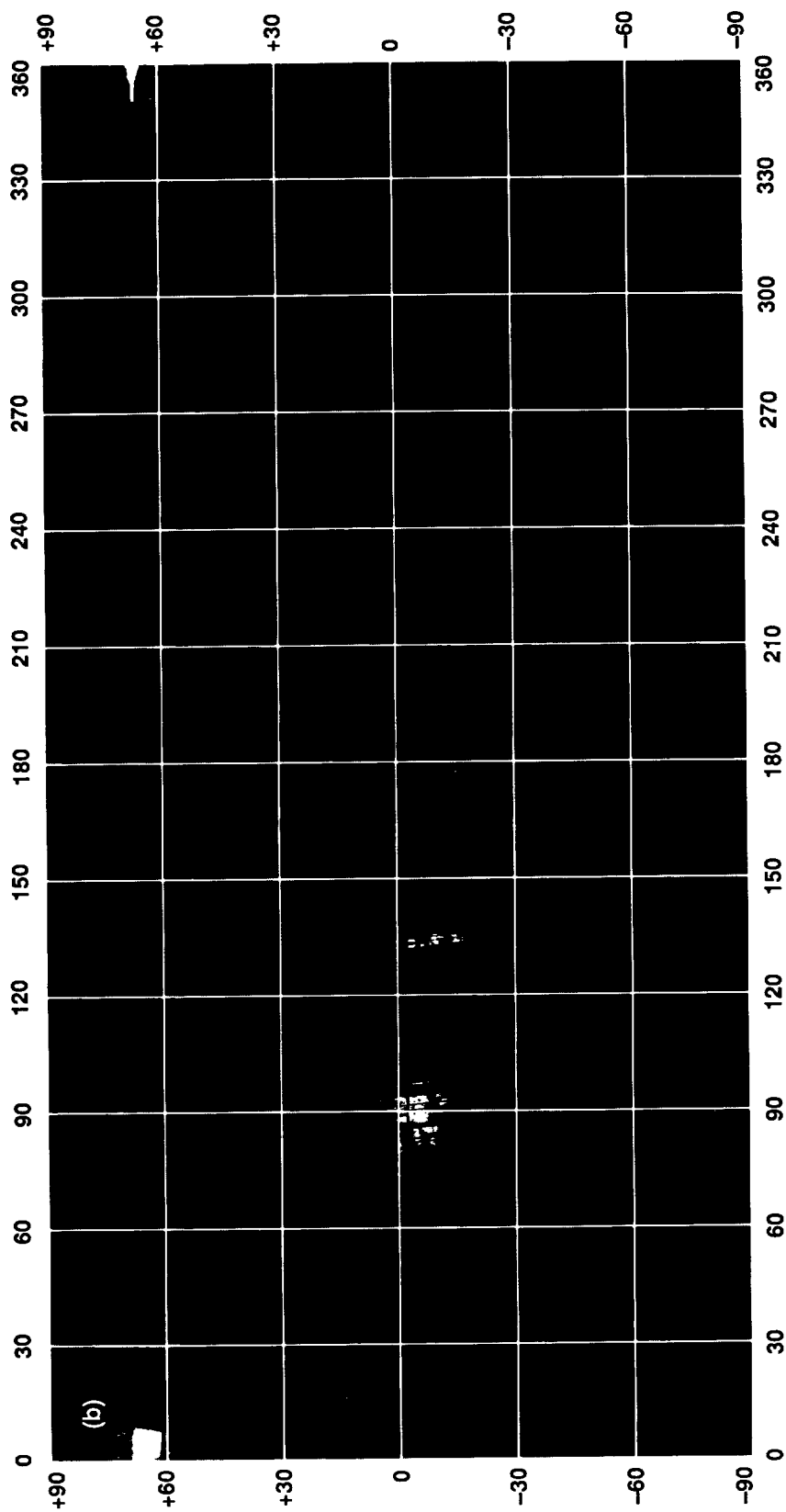Figure 2-5. Mosaics of Cycle-2 coverage: (a) left-looking; (b) right-looking.

(a)

16

Figure 2-6. Mosaics of Cycle-3 coverage: (a) left-looking; (b) stereo left-looking.

17

References

Muhleman, D. O., 1964, "Radar scattering from Venus and the Moon," *Astron. J.*, v. 69, p. 34–41.

Saunders, R. S., et al., 1992, "Magellan mission summary," *J. Geophys. Res.*, v. 97, no. E8, p. 13,067–13,090.

Chapter 3. The Non-SAR Experiments

Jeffrey J. Plaut

Introduction

The Magellan radar system operated simultaneously in three modes: synthetic-aperture radar (SAR), altimetry, and radiometry. Data obtained from the altimeter and radiometer modes are extremely important components of many studies of the surface of Venus. This chapter describes the altimetry and radiometry systems and the resulting data sets. Applications that integrate the various data sets, including SAR image data, are presented at the end of the chapter.

Altimetry and Derived Data

The Altimetry System

The altimeter, with a nadir-looking geometry, is designed to precisely determine the distance between the spacecraft and a patch of surface approximately 10 to 30 km in diameter (the size of the altimeter "footprint"). Knowledge of the spacecraft's orbital position relative to the center of Venus is combined with the spacecraft-to-surface distance determined by the round-trip travel time of the altimeter signals to produce a topographic map of the surface. The time delays and Doppler-frequency shifts of the echoes are used to isolate portions of the echoes and associate them uniquely with areas of the surface. In addition, the altimeter echoes are analyzed for their intensity and time dispersion to estimate the reflectivity and rms slope for each altimeter footprint.

Altimetry Data

A typical Magellan altimetry orbit consists of about 1000 footprints. The resolution varies with spacecraft altitude, and hence with surface latitude, as shown in Table 3-1. The altimetry experiment was designed to produce a net of mea-

Table 3-1. Altimeter footprint dimensions

Latitude	Cross-track dimension (E–W), km	Along-track dimension (N–S), km
80°, –60°	27	15
70°, –50°	24	11
60°, –40°	21	8
50°, –30°	19	11
40°, –20°	16	8
30°, –10°	14	9
20°, 0°	13	9
10°	12	8

surements with spacing between the footprints approximately equal to the size of the footprints themselves.

Processing of Magellan altimetry data involved generation of an echo "profile" for each footprint [Pettengill et al., 1991; Ford and Pettengill, 1992]. This profile represents the strength of the received echo as a function of time delay (Figure 3-1). For relatively flat, uniform areas of Venus, most of the echo power is expected to come in a short period of time. The profile for these areas therefore displays a strong peak and a rapidly diminishing "tail" (Figure 3-1(a)). The specular (mirror-like) reflection from the nadir dominates the echo profile, while reflections from points off nadir (at larger incidence angles) make only small contributions to the tail of the echo.

If the surface within the footprint contains topographic undulations (slopes of a few degrees or more) at scales larger than the 12-cm wavelength, echoes from favorably oriented slopes off nadir may contribute strong specular reflections. In this situation, the peak of the echo profile is weaker because some surfaces at the nadir are tilted away from the spacecraft,
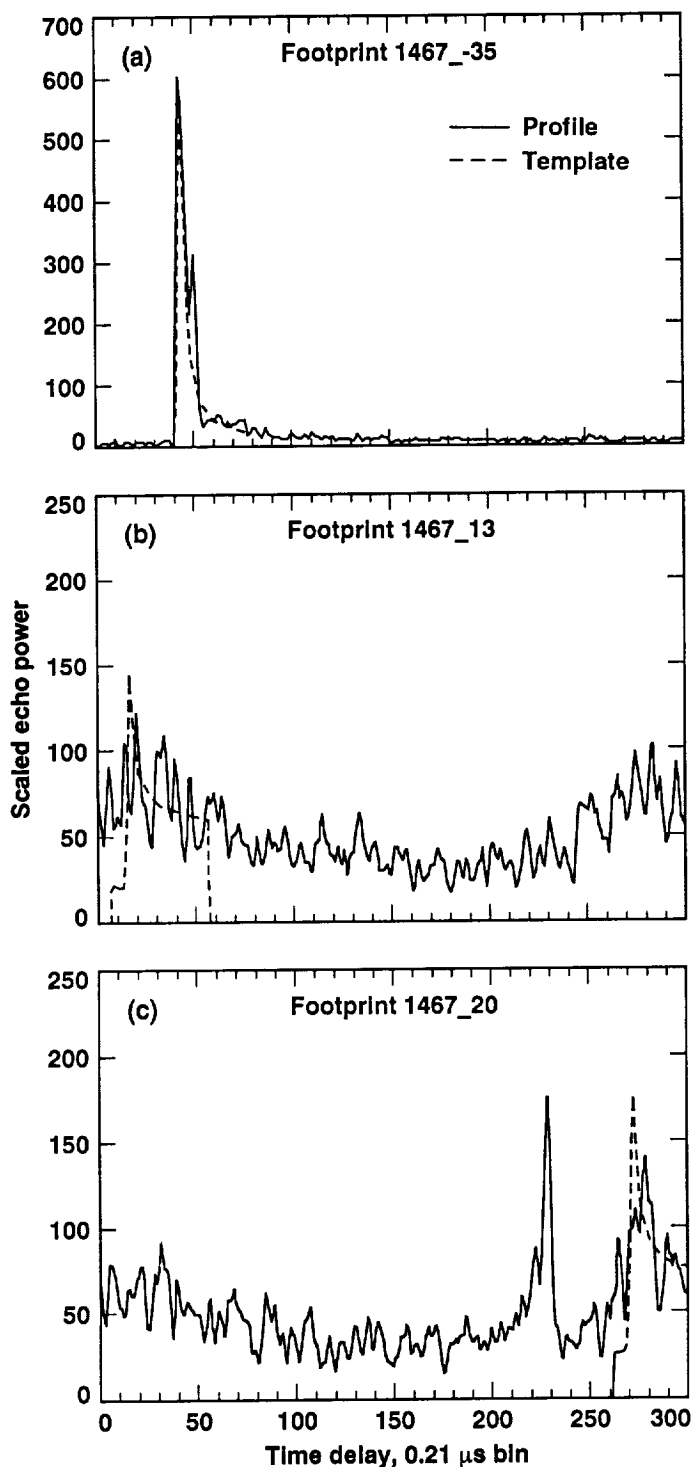
Figure 3-1. Altimeter echo profiles showing echo power vs. time for (a) a flat surface (12.40°N, 187.76°E; rms slope = 1.8 deg), (b) an undulating surface (8.87°N, 188.06°E; rms slope = 6.7 deg), and (c) an area with multiple "peak" contributions (8.35°N, 188.10°E; Sapas Mons summit).

and the tail is stronger than that from a flat surface (Figure 3-1(b)). The echo profile is even more complex when the topography within or near the footprint varies rapidly at large (km) scales. When steep cliffs, valleys, or mountains are illuminated by the altimeter, several strong echoes may return to the spacecraft at different times, creating an ambiguity in the height determination for that footprint (Figure 3-1(c)) [Plaut, 1992].

Before Magellan arrived at Venus, a library of simulated altimeter echo profiles or "templates" was developed [Ford and Pettengill, 1992]. Each template provides the predicted response of a surface, based on three parameters: the distance from the spacecraft, the root-mean-square (rms) slope of surface undulations at scales greater than the wavelength, and the intrinsic Fresnel reflectivity of the surface. In data processing, the three parameters are found by matching the best template to the observed echo profile. In simple terms, the distance is determined by the position of the strongest peak in the profile, the rms slope is determined by the dispersion of the echo in time (the shape of the tail), and the reflectivity is determined by the overall strength of the echo.

Processed Magellan altimetry data are available in two forms: the Altimetry–Radiometry Composite Data Record (ARCDR), and the Global Data Record (GxDR). The ARCDR is an orbit-by-orbit data set that contains all of the derived parameters (e.g., radius, rms slope, reflectivity, and emissivity) for each altimeter and radiometer footprint. The latitude and longitude of each footprint are provided in the ARCDR, so specific features seen in the image data can be identified in the ARCDR by their map coordinates. While the ARCDR is a huge table of data, the GxDR takes the more familiar form of an image map. All measurements of planetary radius reported in the ARCDR are compiled in image form, using filtering and interpolation techniques, to form the GTDR, a global topographic map of the planet (Figure 3-2). Reflectivity, rms slope, and emissivity data are shown on the GREDR, GSDR, and GEDR, respectively (Figures 3-3 to 3-5). The GxDR maps are presented on CD-ROM in several map projections: a full global sinusoidal equal-area projection; a Mercator projection showing latitudes between 65° north and south; and polar stereographic projections centered on the north and south poles, extending to 47° north and south latitude, respectively. The GTDR data sets can be used to study regional topographic patterns and are particularly useful when combined with SAR image data to show the relationships between topography and morphologic features in the images.

Reflectivity and RMS Slope Data

As described in the previous section, processing of the altimetry data involved the simultaneous estimation of planetary radius, Fresnel reflectivity, and surface rms slope.
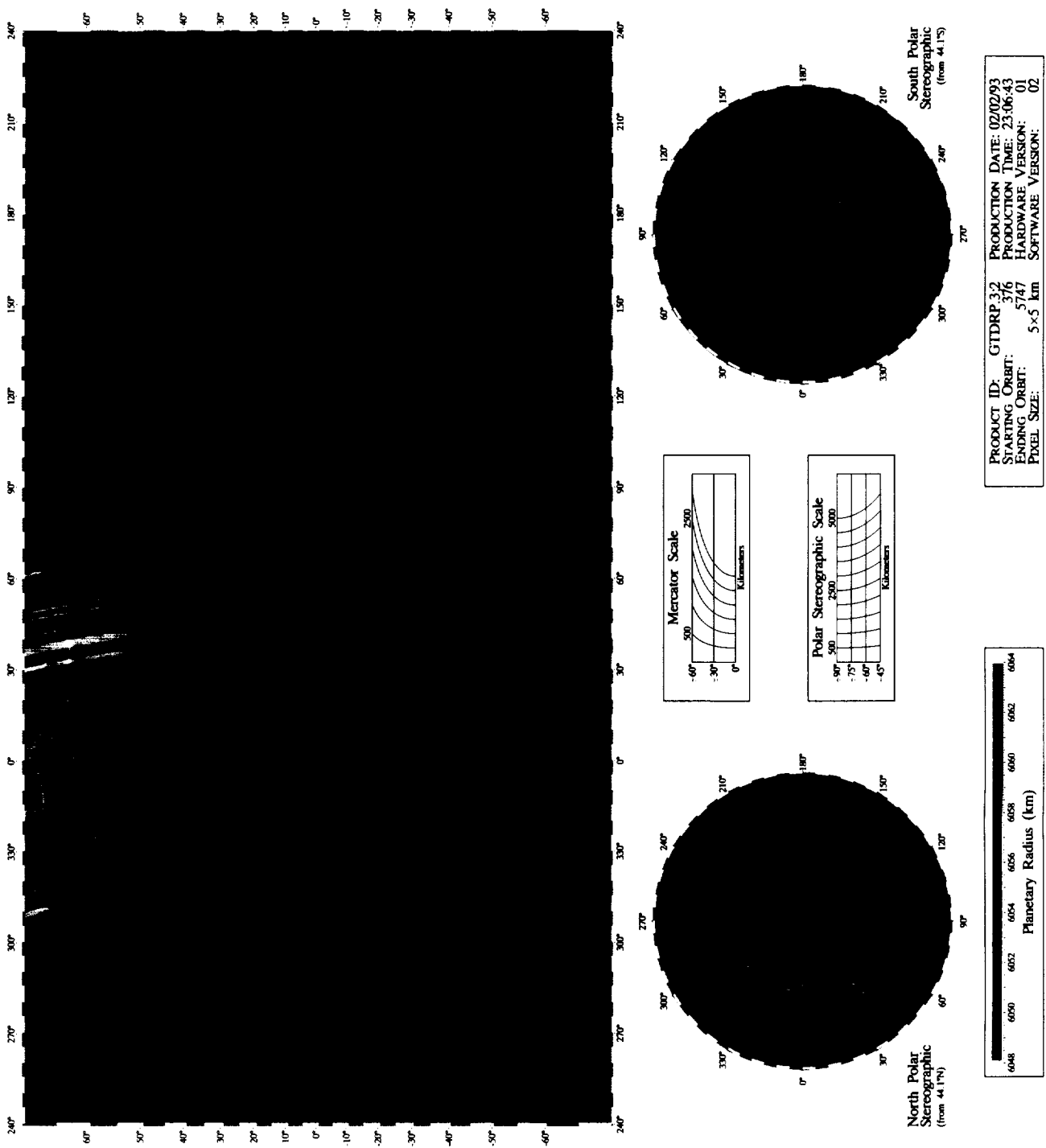
Figure 3-2. Global topography from Magellan altimetry (GTDR).

North Polar
Stereographic
(from 44.1°N)

South Polar
Stereographic
(from 44.1°S)

Mercator Scale

Polar Stereographic Scale

PRODUCT ID:	GTDRP.3.2	PRODUCTION DATE:	02/02/93
STARTING ORBIT:	376	PRODUCTION TIME:	23:06:43
ENDING ORBIT:	5747	HARDWARE VERSION:	01
PIXEL SIZE:	5×5 km	SOFTWARE VERSION:	02

Planetary Radius (km)

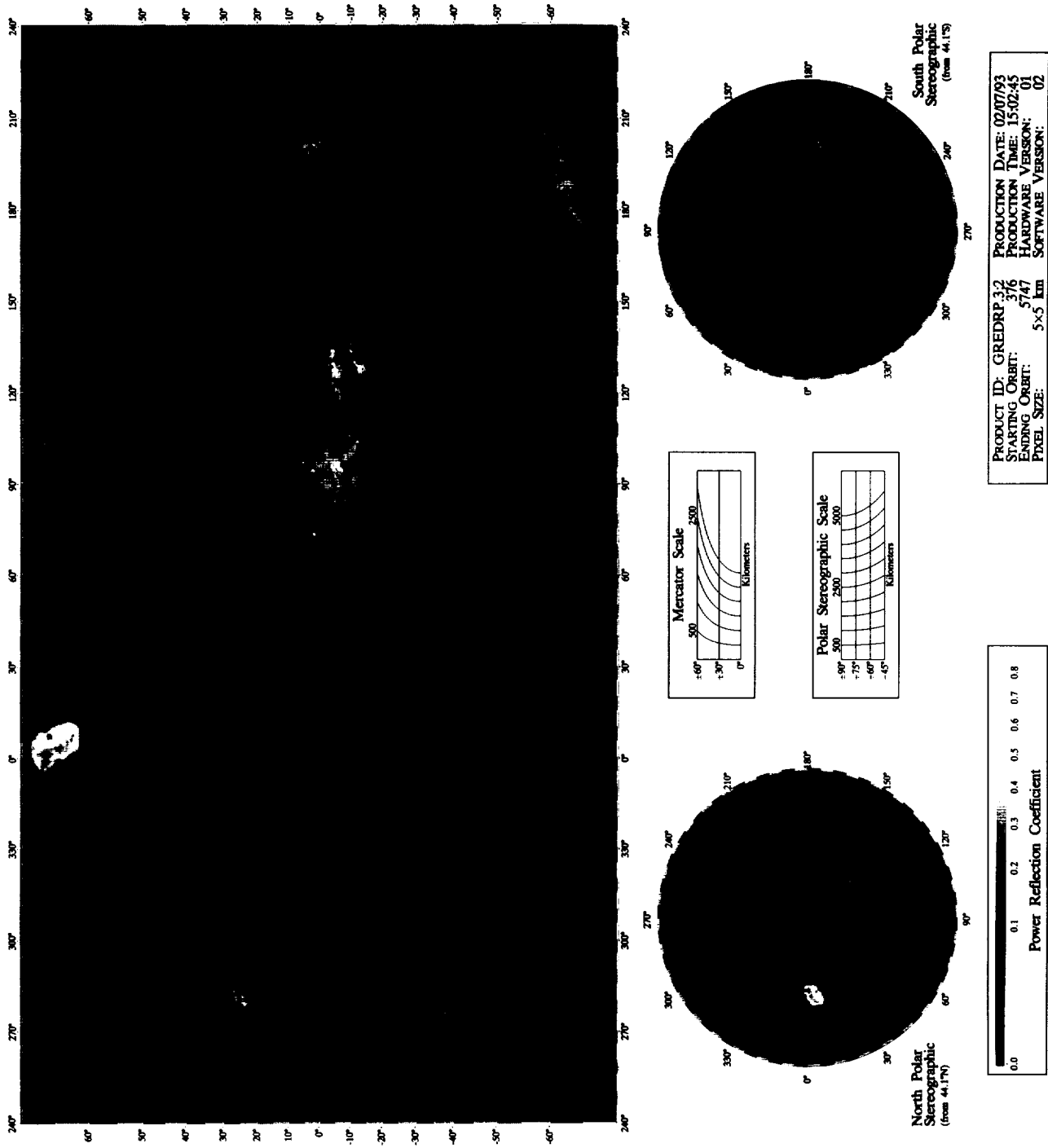6048 6050 6052 6054 6056 6058 6060 6062 6064

Figure 3-3. Global reflectivity from Magellan altimetry (GREDR).

Figure 3-4. Global rms slope from Magellan altimetry (GSDR).
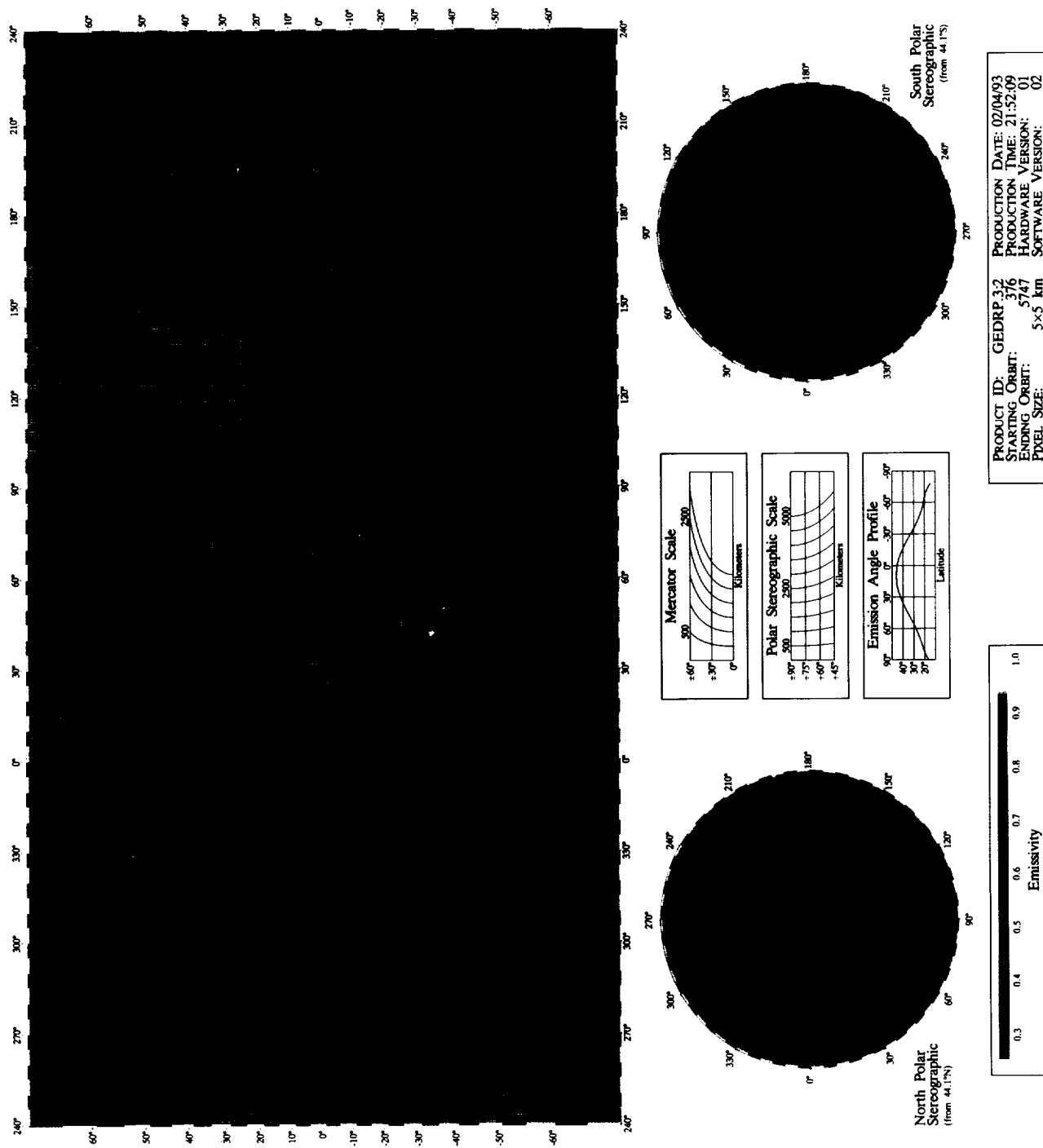
Figure 3-5. Global emissivity from Magellan radiometry (GEDR).

24

Through the template matching procedure, values of reflectivity and rms slope are obtained for each altimeter footprint.

Hagfors [1970] derived an expression that accurately predicts the intensity of radar backscatter from many planetary surfaces, as a function of incidence angle, Fresnel reflectivity, and a large-scale roughness parameter C:

$$\sigma^0(\theta) = (\rho C/2)\left(\cos^4\theta + C\sin^2\theta\right)^{-3/2}$$

where

σ^0 = specific radar backscatter cross section

θ = incidence angle, deg

ρ = Fresnel reflection coefficient (reflectivity)

C = roughness parameter, equivalent to

$1/(\text{rms slope in rad})^2$

This scattering function has proven to be appropriate for much of the surface of Venus, at incidence angles less than about 15 deg. Although recent studies [e.g., Tyler et al., 1992] have shown that other functional forms may better describe the scattering behavior of much of Venus, the Hagfors equation applied to Magellan altimetry data can be used to quantify the reflectivity and slope properties of the surface. All altimeter echo profiles have been matched to templates that were derived from the Hagfors scattering function.

Fresnel reflectivity is a measure of the efficiency of a surface in reflecting electromagnetic radiation. A reflectivity of 1.0 represents perfect, total reflection. The typical plains surface of Venus has a reflectivity of about 0.1. Reflectivity (ρ) can be related to the dielectric constant (e) of the surface:

$$\rho = \left|\frac{1-\sqrt{e}}{1+\sqrt{e}}\right|^2$$

A refinement to the determination of reflectivity can be made when a nadir-looking altimeter measurement is accompanied by a side-looking SAR backscatter measurement. Since both of these Magellan datasets are nearly global in coverage, this refinement or "correction" to the reflectivity is possible for almost every altimeter footprint. As described by Pettengill et al. [1988], subwavelength roughness, which dominates the scattering at large (SAR) incidence angles, tends to randomly scatter a nadir-pointing signal, diminishing the power of the echo detected by the altimeter. If this scattering effect is not taken into account, a rough surface will appear to have a reflectivity lower than that of a smooth surface composed of the same material. By estimating the areal coverage of random scatterers from the SAR backscatter cross

sections, the reflectivity derived from the template matching procedure can be "corrected" (increased) to a value that is more likely to represent the material properties of the surface, independent of roughness. In the ARCDR files, the uncorrected reflectivity value is reported, along with the correction factor to be applied.

The rms slope parameter is used to quantify the topographic undulation of the terrain, at scales ranging from tens of centimeters to a few kilometers. Magellan altimeter-derived rms slopes for a typical plains surface are in the range of 1 to 3 deg. Tectonic terrains that are severely fractured show values as high as 10 deg. Measurements of terrain slope characteristics of terrestrial test sites have shown that while the rms slope values derived from radar data can serve as a good relative measure of slopes, the absolute magnitude of the values may not accurately describe the actual slopes of the surface. The model from which the rms slopes are derived assumes that the slopes are random in orientation. The template matching algorithm may break down in cases where an organized pattern of slopes affects the scattering. Such a breakdown was observed in Magellan data on surfaces within certain impact parabolic features that showed a strongly asymmetric backscatter behavior between the right- and left-looking SAR data [Plaut et al., 1992].

Radiometry and Derived Emissivity

The radiometry experiment employed the high gain antenna in a passive mode to detect thermal radiation emitted by the surface of Venus at radio wavelengths [Pettengill et al., 1992]. Surface emissivity, an electrical property essentially independent of temperature, can be derived from the radiometry measurements to aid in the interpretation of the relative influence of dielectric constant and roughness on observations acquired by Magellan's SAR, altimeter, and the radiometer itself.

All objects emit radiation across the broad range of the electromagnetic spectrum, including the radio frequencies. The amount of energy emitted, or radiance, depends on the object's temperature and emissivity, as expressed in Stefan's law:

$$R = \sigma e T^4$$

where

R = total radiance, Wm^{-2}

$\sigma = 5.67 \times 10^{-8}\,\text{Wm}^{-2}\text{K}^{-4}$ (Stefan–Boltzmann constant)

e = emissivity

T = temperature, K

Emissivity, which ranges from 0 to 1, is a measure of how well an object approximates a perfect blackbody radiator. A good emitter is required by thermal balance to be a good absorber, and hence a poor reflector. Ideally, then, the sum of the emissivity and the Fresnel reflectivity should equal one. This applies when measurements are integrated over the full upper hemisphere, which is not the case for Magellan emission and reflection measurements. In practice, the Magellan emissivity and reflectivity estimates track one another in the expected fashion, although their sum typically ranges between 0.90 and 0.95.

To solve the Stefan equation for emissivity, the radiance and temperature must be known. Magellan's antenna acquired the radiance measurements, while the temperature for any given area of the surface was assumed to be a well-behaved function of surface elevation. Observations from Earth and by previous spacecraft indicated that temperatures at the surface of Venus are essentially constant at a given elevation, regardless of time of the Venusian day, or other atmospheric factors. Surface elevations derived from Magellan altimetry data are thus converted to physical temperature estimates, and used in the above equation to solve for emissivity. The actual procedure is slightly more complex, incorporating factors such as the absorption and emission by the atmosphere, reflection of ambient "warm sky" radiation from the surface, and the detailed response of the high gain antenna [Pettengill et al., 1992].

Because the radiometry measurements were interleaved with the SAR observations, the two data sets have the same geometry; incidence angles of the SAR data are equivalent to the emission angles of the radiometry data (see Table 4-1). The radiometry footprint size varies with spacecraft altitude, and hence with latitude (Table 3-2). Parameters associated with each radiometry footprint are reported in the ARCDR files on CD-ROM. The full global ensemble of emissivity determinations is compiled on the GEDR (Figure 3-5), which may be found in digital form on the GxDR CD-ROM.

The emissivity of natural surfaces is controlled primarily by the dielectric constant. Material of high dielectric constant is generally a good reflector and hence a poor emitter. Emission from a surface that is smooth at the wavelength scale is easily modeled, given a value of dielectric constant. Conversely, a measurement of emissivity can be converted to a value of dielectric constant, if the surface is assumed to be smooth. The mean value of surface emissivity observed by Magellan is 0.845, which corresponds to a smooth-surface dielectric constant of about 4.0 [Pettengill et al., 1992]. A rougher surface tends to have a higher emissivity when observed at the horizontal polarization used by Magellan.

Table 3-2. Radiometer footprint dimensions (Cycle 1)

Latitude	Cross-track dimension (E–W), km	Along-track dimension (N–S), km
10°	23	15
23°, –3°	29	19
46°, –26°	36	27
62°, –42°	51	41
83°, –63°	77	64
90°, –67°	91	77

Many surfaces known to be rough from SAR observations— such as tesserae, rough lava flows, and crater ejecta blankets— have emissivities 0.05 to 0.10 higher than surrounding plains. Magellan emissivity also shows the expected behavior as a function of emission angle: emissivities at large emission angles (low latitudes) average about 0.05 less than those at small emission angles (high latitudes).

The most noteworthy features in the emissivity data occur in two settings: near the top of the planet's highest mountains and in association with certain impact craters. Most of the blue and violet areas in Figure 3-5 (emissivities less than 0.7) correspond to areas above approximately the 6053.5-km radius contour. Emissivity values in these areas drop as low as 0.3, implying dielectric constants as high as 80, which far exceed values measured for terrestrial rocks [Ulaby et al., 1990]. A class of materials that have the electrical properties necessary to enhance the dielectric constant to the observed levels are iron sulfides, including pyrrhotite and pyrite [Pettengill et al., 1988; Klose et al., 1992]. It is proposed that the unique atmospheric conditions at high elevations (lower temperature and pressure) promote chemical weathering of the soils or rock coatings to produce the high dielectric minerals.

An exciting discovery from early Magellan emissivity data was the parabolic-shaped, low-emissivity features associated with some impact craters [Arvidson et al., 1991; Campbell et al., 1992]. These features correspond with many of the green areas in Figure 3-5. They often appear dark in SAR image data, but the correlation between low emissivity and low SAR backscatter is often not strong, implying that dielectric differences are the primary cause of the lowered emissivity [Plaut and Arvidson, 1992]. The favored model for the formation of these features involves interactions between the cloud of impact debris lofted into the atmosphere and the strong east-to-west winds known to exist at about 60 km altitude [Campbell et al., 1992]. Why the dielectric constants would be enhanced on the resulting fallout deposits has yet to be explained.

26

Incorporating the Data Sets Into Image Analysis

Analysis of Magellan data is significantly enhanced when relationships can be discerned between features seen in the SAR data and in the non-SAR data sets. Examples in this section show the various methods for combining the data to increase interpretability.

SAR image brightness is dominated by small-scale roughness effects for most of the planet's surface. Topography can influence brightness where slopes are steep enough to significantly alter the local incidence angle. In many cases, however, the SAR data do not indicate the large-scale trends in topography. In these instances, it is useful to compare or combine the SAR data and the topographic information from the altimetry experiment. Figure 3-6 shows the Artemis region in SAR image data and gray-scale altimetry. The altimetry image is extracted from the GTDR file, with a displayed range of planetary radius values from 6047 km to 6058 km. In this representation, black areas represent the lowest elevations and white areas represent the highest elevations. The altimetry data convey much topographic information that cannot be gleaned from the SAR image, such as the complex form of the corona trough, the gentle topographic swell outboard of the trough, and the dramatic asymmetric scarp-and-valley features

in the central, northern and northwestern portions of the corona.

Image processing techniques can be used to explore the relationships between morphologic features observed in the SAR images and topography. A common method for combining data sets is the color overlay, in which color-coded elevation data are "painted" over the SAR image. This can be accomplished by separating a color elevation image into its hue, saturation, and intensity components, substituting the SAR image for the intensity component, and recombining the components into a color representation. Topographic contours may be added to further emphasize differences in elevation. Figure 3-7 is a combined elevation-and-SAR image of a region east of Devana Chasma. The color coding and topographic contours show large variations in the elevation of parts of the tessera outliers, as well as the prominent highs associated with two radially fractured features.

Visualization of topography and SAR image morphology is also possible using three-dimensional perspective rendering. The elevation data are used to simulate a view from an oblique direction, with the SAR image superimposed on the topographic shapes. This technique is used to generate the dramatic animated video "flyover" segments. The vertical scale is commonly exaggerated to emphasize subtle topo-

Figure 3-6. SAR image (left) and topography (right) of Artemis Corona. Planetary radius values between 6047 km (black) and 6058 km (white) are displayed in the topography image.
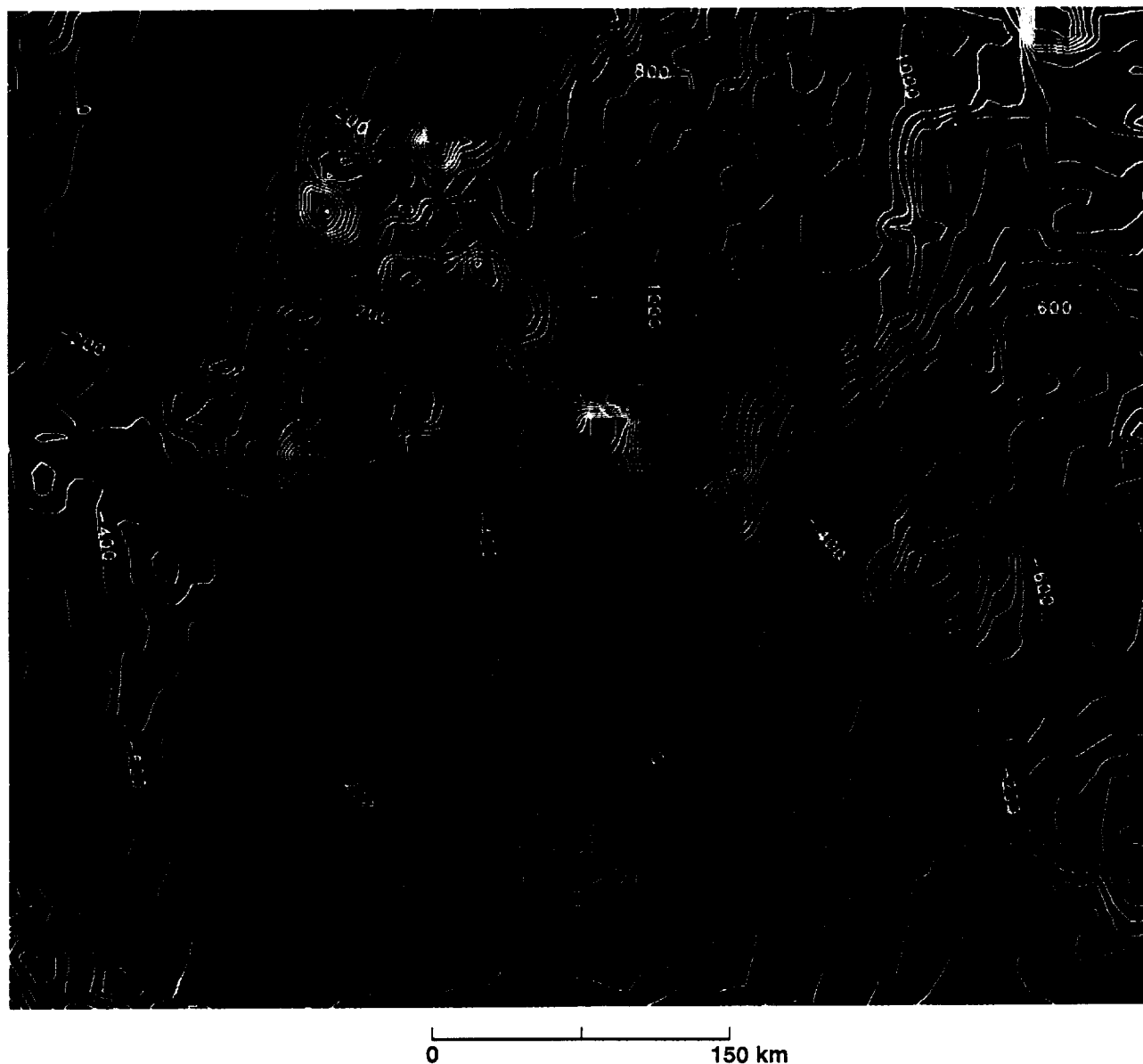
```
0                           150 km
```

Figure 3-7. Combined SAR image and topography data for a region east of Devana Chasma. Center coordinates are 15°N, 292°E. Contour interval is 200 m.

graphic features, particularly when the lateral dimension of the area is large. Magellan three-dimensional perspective views are typically generated with vertical exaggeration factors of 10 to 20. Figure 3-8 is a three-dimensional perspective view of Western Eistla Regio, showing the Guor Linea rift structure associated with the large volcanic edifices Sif Mons and Gula Mons, which loom on the horizon.

Because emissivity is governed mostly by the dielectric properties of the surface, it is often useful to combine emissivity and SAR data to explore the relative influences of

roughness and dielectric effects on SAR backscatter cross sections. Many high-backscatter regions, particularly at high elevations, appear bright in the SAR data because of their high dielectric constants (i.e., low emissivities) and not because of increased roughness. Figure 3-9 shows the emissivity of the Atla Regio highlands overlain on SAR image data. The strongest emissivity anomaly (values as low as 0.34) occurs on Ozza Mons, in the upper right of the image. The highest elevations, however, show a return to higher emissivities as well as lower surface roughness, leading to very low SAR

Figure 3-8. Simulated three-dimensional perspective view of Guor Linea (foreground) and Sif Mons and Gula Mons (left and right on the skyline, respectively). Vertical exaggeration of relief is 22.5 times.

backscatter cross sections [the "dark summits" of Pettengill et al., 1992]. Interestingly, Maat Mons (left center) shows low emissivity values only on its southwest flanks. Klose et al. [1992] suggest that the irregular pattern of emissivity on Maat Mons could imply that recent volcanic resurfacing has not allowed sufficient time for the weathering of surface rocks to produce the high dielectric materials seen on other mountaintops.
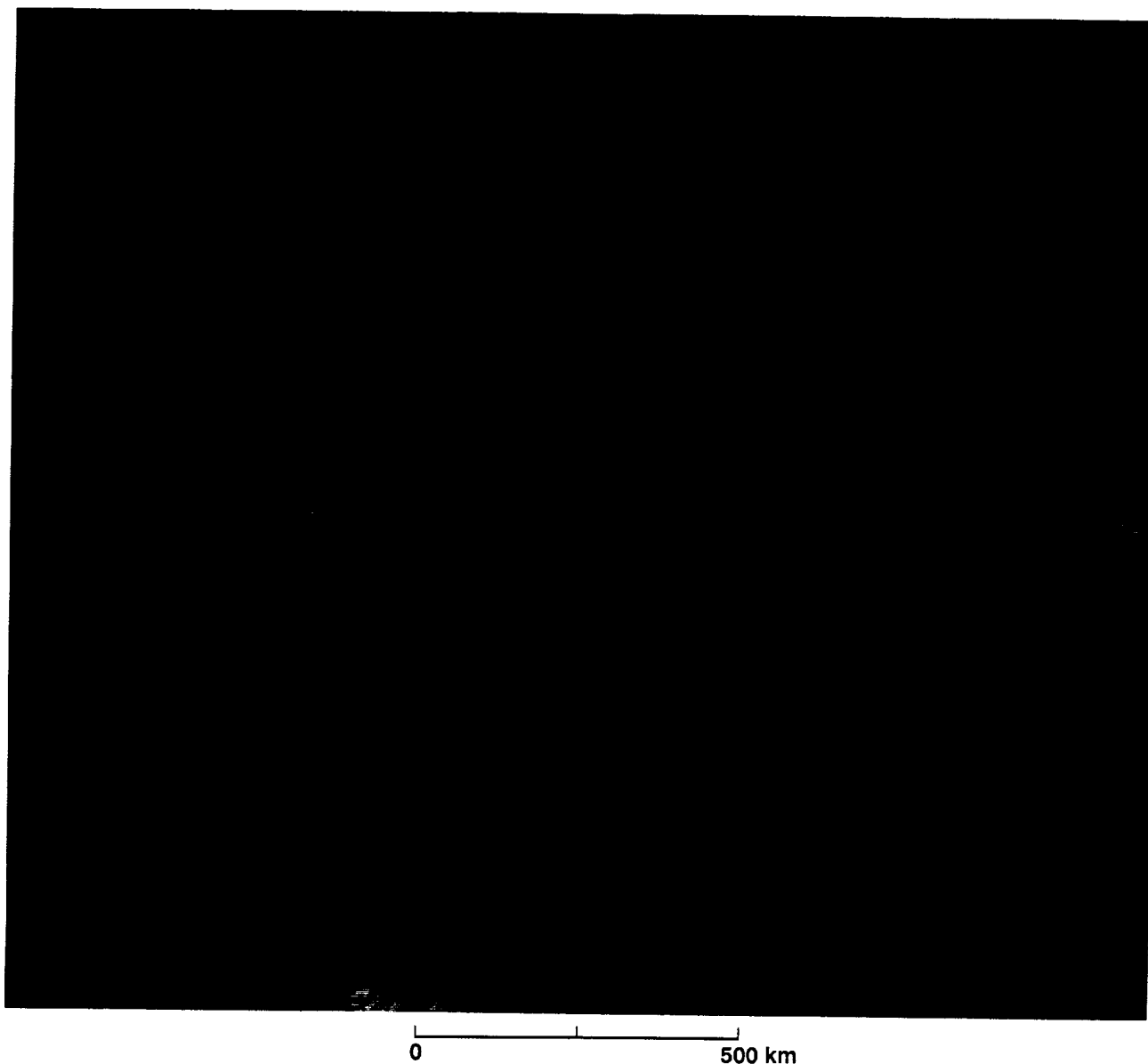
0   500 km

Figure 3-9. Emissivity of Atla Regio overlain in color on SAR image data. Emissivity values range from 0.35 (violet) to 0.95 (red). Note the relatively high emissivity values at the "dark summit" of Ozza Mons (upper right center) and on all but the southwest flank of Maat Mons (left center).

References

Arvidson, R. E., V. R. Baker, C. Elachi, R. S. Saunders, and J. A. Wood, 1991, "Magellan: Initial analysis of Venus surface modification," *Science*, v. 252, p. 270–275.

Campbell, D. B., N. J. S. Stacy, W. I. Newman, R. E. Arvidson, E. M. Jones, G. S. Musser, A. Y. Roper, and C. Schaller, 1992, "Magellan observations of extended impact related features on the surface of Venus," *J. Geophys. Res.*, v. 97, p. 16,249–16,277.

Ford, P. G., and G. H. Pettengill, 1992, "Venus topography and kilometer-scale slopes," *J. Geophys. Res.*, v. 97, p. 13,103–13,114.

Hagfors, T., 1970, "Remote probing of the moon by infrared and microwave emissions and by radar," Radio Sci., v. 2, p. 445–465.

Klose, K. B., J. A. Wood, and A. Hashimoto, 1992, "Mineral equilibria and the high radar reflectivity of Venus mountaintops," *J. Geophys. Res.*, v. 97, p. 16,353–16,369.

Pettengill, G. H., P. G. Ford, and B. D. Chapman, 1988, "Venus: Surface electromagnetic properties," *J. Geophys. Res.*, v. 93, p. 14,881–14,892.

Pettengill, G. H., P. G. Ford, W. T. K. Johnson, R. K. Raney, and L. A. Soderblom, 1991, "Magellan: Radar performance and data products," *Science*, v. 252, p. 260–265.

Pettengill, G. H., P. G. Ford, and R. J. Wilt, 1992, "Venus surface radiothermal emission as observed by Magellan," *J. Geophys. Res.*, v. 97, p. 13,091–13,102.

Plaut, J. J., 1992, "'Problem' footprints in Magellan altimetry data" (abstract), papers presented to the International Colloquium on Venus, LPI Contract No. 789, p. 90–92.

Plaut, J. J., and R. E. Arvidson, 1992, "Comparison of Goldstone and Magellan radar data in the equatorial plains of Venus," *J. Geophys. Res.*, v. 97, p. 16,279–16,291.

Plaut, J. J., R. S. Saunders, E. R. Stofan, R. L. Kirk, G. G. Schaber, L. A. Soderblom, P. G. Ford, G. H. Pettengill, D. B. Campbell, J. J. S. Stacy, R. E. Arvidson, and R. Greeley, 1992, "Anomalous scattering behavior of selected impact 'parabola' features: Magellan cycle-to-cycle comparisons" (abstract), papers presented to the International Colloquium on Venus, LPI Contract No. 789, p. 92–93.

Tyler, G. L., R. A. Simpson, M. J. Maurer, and E. Holmann, 1992, "Scattering properties of the Venusian surface: Preliminary results from Magellan," *J. Geophys. Res.*, v. 97, p. 13,115–13,139.

Ulaby, F. T., T. H. Bengal, M. C. Dobson, J. R. East, J. B. Garvin, and D. L. Evans, 1990, "Microwave dielectric properties of dry rocks," *IEEE Trans. Geosci. Rem. Sens.*, v. 28, p. 325–336.

Chapter 4. Stereo Imaging

Jeffrey J. Plaut

Introduction

Topographic features in radar images are always distorted to some degree. The amount of distortion depends on the topographic relief and on the incidence angle of the observation. Magellan's extended mission (Cycles 2 and 3)—with a viewing geometry different than that used in Cycle 1—provided the opportunity to derive heights and depths of features at a lateral resolution comparable to that of the SAR images themselves. In this chapter, the mechanics of radar stereoscopic (stereo) imaging are presented, along with a description of the Magellan stereo image data set and examples that apply the techniques to Magellan images.

Radar Image Distortion—Why Stereo Works

The location of a resolution cell in a radar image is determined across track by the range (distance) between the antenna and the feature (measured as a time delay of the echo), and along track by the Doppler shift expected for a given piece of terrain. The range–Doppler coordinates of a resolution cell can be easily transformed into planetary coordinates (i.e., latitude and longitude) under an assumption of the large-scale shape of the surface. In the case of Magellan data, the large-scale shape of the surface (at scales of hundreds of km) is modeled as gently sloping (the "topo model") or as a portion of a perfect planetary sphere.

Use of the range coordinate to locate a resolution cell leads to a distortion of topographic features known as relief displacement. For example, high areas return an echo sooner than the surroundings, and thus are displaced toward the spacecraft in the image plane; the opposite is true for low areas. These effects are known as "foreshortening" and "elongation," respectively. In the extreme case of foreshortening, an echo is received from the top of a mountain before an echo from the near-range base of the mountain, leading to "layover," where, on the image, the top is superimposed on the base. Foreshortening and elongation can often complicate analyses of radar images, but they also allow the use of stereometric techniques to determine feature heights.

The amount of relief displacement is a simple function of the height of the feature and the incidence angle of the observation (Figure 4-1). Smaller incidence angles produce greater distortion for a given amount of topographic relief. Thus, by comparing the distortions measured on two images taken at different incidence angles, the heights of features can be determined. Terrain relief can also be perceived visually, using same-side (illuminated from the same direction) stereo image pairs and a stereoscope.

Estimating Heights From Stereo Data

Feature heights may be obtained from same-side stereo image pairs (Figure 4-1), such as those from Cycles 1 and 3, and from opposite-side stereo image pairs (Figure 4-2), such as those from Cycles 1 and 2, or 2 and 3. In either case, an accurate measurement can be made only if the two points between which a height difference is to be found can be identified as unambiguously identical in both images. Errors in identification of the points will propagate as errors in the height determination of the feature. The appearance of features is often more similar in same-side image pairs than in opposite-side image pairs, making the selection of points
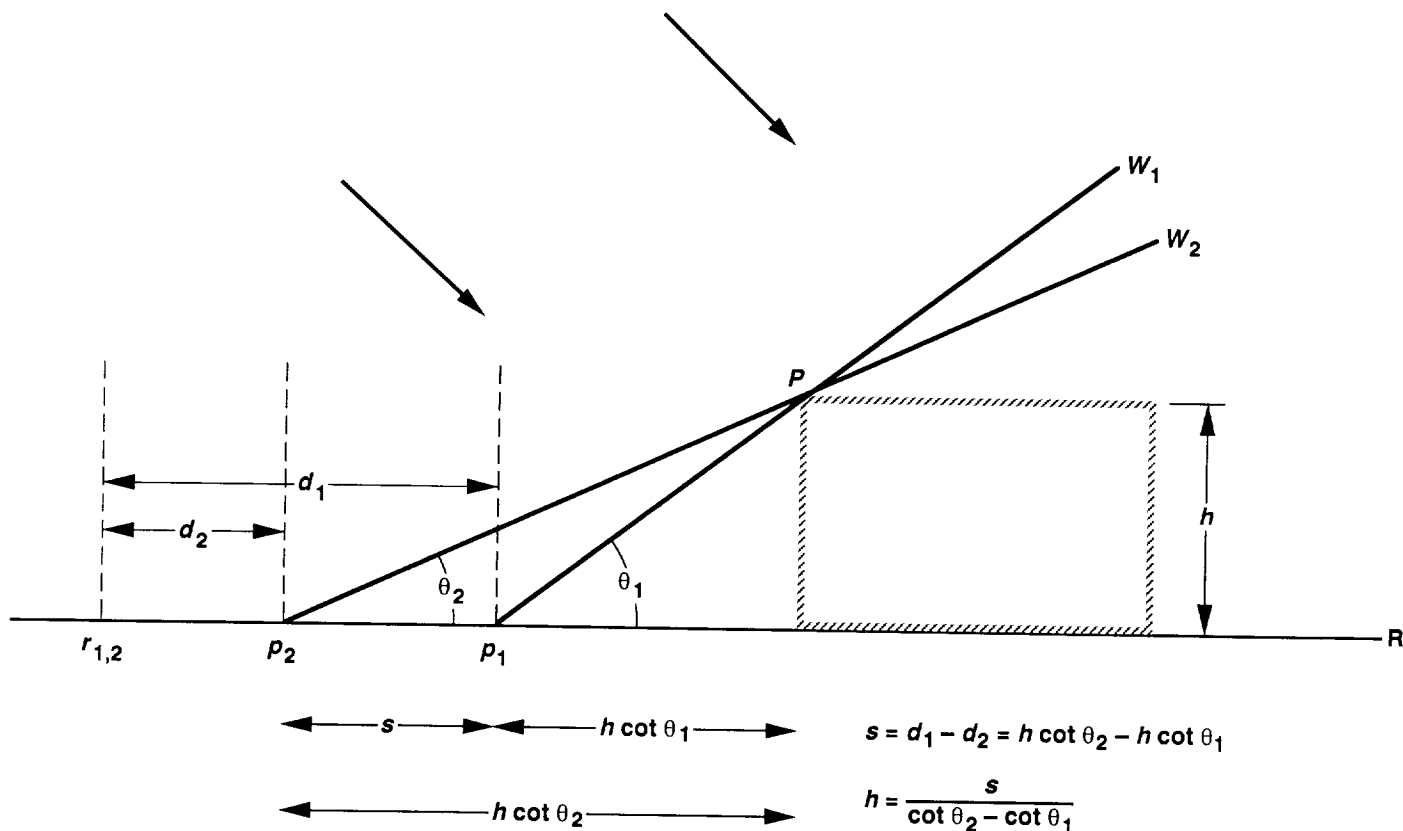
$$s = d_1 - d_2 = h \cot \theta_2 - h \cot \theta_1$$

$$h = \frac{s}{\cot \theta_2 - \cot \theta_1}$$

Figure 4-1. Solving for heights using same-side stereo images. Measurements are taken from the separate images of a same-side stereo image pair to determine the height of point P above the reference plane, R. As wavefront W_1 intercepts point P, the projection in range space (i.e., time delay) places the echo from P at point p_1 on plane R. Similarly in the second image, the echo from point P is placed at point p_2. Identify a point $r_{1,2}$ in a low-relief area on the plane R, and measure the distance from $r_{1,2}$ to p_1 on image 1, and from $r_{1,2}$ to p_2 on image 2. The difference between these distances $(d_1 - d_2)$ is s, the parallax of point P. Using the incidence angles of the two observations (θ_1 and θ_2), the height h of the feature is obtained by dividing s by the parallax-to-height ratio ($\cot \theta_2 - \cot \theta_1$).

easier and more accurate on the two same-side images. On the other hand, because the displacements on the opposite-side image pairs are opposite in direction, a larger parallax than that from a same-side pair is obtained, making height determinations more accurate, provided identical points are identified on both images.

Stereo measurements are best made from high-resolution digital data (e.g., Magellan F-MIDRs), in which the precise pixel location of features can be made on a video monitor. Hard-copy prints may also be used, but the image pair must be enlarged to a single scale. Once the separation of the two features has been measured on the images and converted to a ground distance, the height difference is easily calculated, using the parallax-to-height ratio of Figure 4-1 or 4-2. The incidence angles of the two observations can be obtained from Table 4-1 (represented graphically in Figure 4-3), or from the ancillary files on Magellan CD-ROMS. Note that

the parallax-to-height ratio is obtained with slightly different formulas for same- and opposite-side stereo pairs (Figures 4-1 and 4-2).

Magellan Stereo Data

Magellan Cycle 1 data were obtained in a left-looking, variable incidence angle mode. To maximize image quality, incidence angles were varied as a function of spacecraft altitude. In the Cycle 2 right-looking mode, the incidence angle was constant at about 25 deg for most of each orbit. Incidence angles in Cycle 3 were selected to provide images suitable to produce a stereo pair with corresponding Cycle 1 images. Figures 2-4 through 2-6 show the coverage for each of the three imaging cycles, and Table 4-1 lists the associated incidence angles.
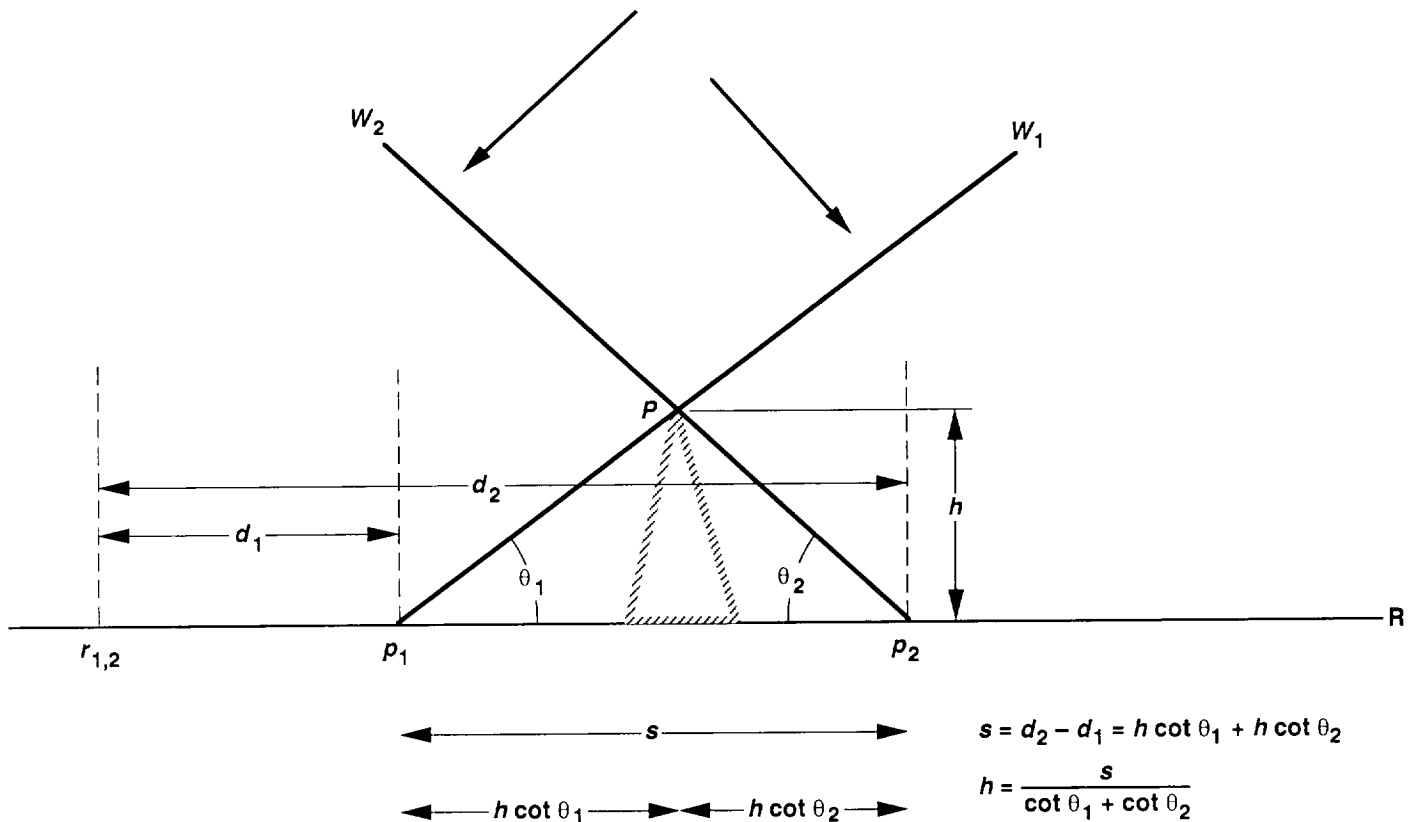
Figure 4-2. Solving for heights using opposite-side stereo images. The procedure is similar to that used for same-side images. Here the parallax, s, is equal to $d_2 - d_1$. Using the incidence angles of the two observations (θ_1 and θ_2), height h of the feature is obtained by dividing s by the parallax-to-height ratio ($\cot \theta_1 + \cot \theta_2$).

Several complications arise in using Magellan stereo data for height determinations. First, in most regions, the SAR imaging data are projected onto a low-resolution topographic model, derived from pre-Magellan observations. This was necessary to minimize errors in locating features in regions where the elevation differed greatly from the Venus average. At a local scale, the topographic model does not affect stereometric measurements, but at a regional scale, particularly in areas of large relief, height differences in the topographic model must be added to any stereo-derived height differences. A second complication is related to the geometry of the SAR observations, and to the fact that all relief displacements occur in the *cross-track* direction. The cross-track direction is generally to the east in Cycles 1 and 3 and to the west in Cycle 2, but it is not precisely east or west, particularly at high latitudes. The most accurate measurements of relief displacement are made in the cross-track direction, which can usually be determined by plotting a line perpendicular to the edge of an orbital swath. In most Magellan MIDRs, swath edges are visible either along data

gaps or as "shading" artifacts. A third complication occurs when stereo measurements are to be made between orbital swaths that were processed using different spacecraft orbital navigation solutions. These "navigation boundaries" can be identified by viewing stereo image pairs with a stereoscope. The boundary will appear as a linear discontinuity in relief, parallel to the orbital tracks. Height determinations obtained across such boundaries are likely to be unreliable.

Applications of Stereo Analysis

The simplest use of Magellan stereo image pairs is visual examination with a stereoscope. A stereoscope directs one image of the stereo pair to one eye and the other image to the other eye. For most Magellan same-side stereo data, the Cycle 1 image (large incidence angle) goes to the left eye, and the Cycle 3 image (small incidence angle) goes to the right eye (for the Maxwell Montes area, the image positions should be reversed; see Table 4-1). Opposite-side stereo image pairs

Table 4-1. Magellan SAR incidence angle profiles

Latitude, deg	Incidence angle,[a] deg			
	Cycle 1	Cycle 2	Cycle 3, Maxwell Montes	Cycle 3, stereo
90	16.5			
85	18.5			
80	20.2			
75	22.0	24.4	27.1	13.4
70	23.9	24.9	30.8	13.5
65	26.0	25.1	33.4	14.1
60	28.3	25.1	35.1	15.2
55	30.8	25.1	35.9	16.6
50	33.3	25.1	36.1	18.2
45	35.8	25.1	35.8	19.8
40	38.1	25.1	35.1	21.4
35	40.3	25.0	34.2	22.7
30	42.1	25.0	33.1	23.9
25	43.6	25.0	31.9	24.8
20	44.8	24.9	30.6	25.3
15	45.5	24.9		25.6
10	45.7	24.9		25.5
5	45.6	24.9		25.2
0	44.9	24.9		24.5
-5	43.8	24.9		23.6
-10	42.3	24.9		22.6
-15	40.4	25.0		21.4
-20	38.1	25.1		20.1
-25	35.5	25.1		18.7
-30	32.8	25.2		17.4
-35	30.1	25.3		16.2
-40	27.5	25.3		15.2
-45	25.1	25.3		14.3
-50	23.1	25.1		
-55	21.6	24.7		
-60	20.5	24.1		
-65	19.7	23.1		
-70	18.5	21.6		
-75	16.3	19.7		
-80		17.4		
-85		14.8		
-90		12.7		

[a]Incidence angle values are representative for each cycle, within ±0.5 deg. More precise values for a given orbit range and MIDR product may be found in the GEOM.TAB files that accompany the SAR image data on Magellan MIDR CD-ROMs.

are often difficult to fuse with a stereoscope. When the images are perceived to merge, variations in relief become apparent as a three-dimensional image. Figures 4-4 and 4-5 are Magellan stereo image pairs that can be viewed with a stereoscope. The perceived relief relative to the horizontal scale is usually about five to ten times the actual relief, depending on the incidence angles used [Leberl et al., 1992]. For precise determinations of relief, measurements of parallax should be made on a computer monitor or on photographic enlargements (see below).

Stereo pairs can also be viewed with color anaglyphs and 3-D color filter glasses. Figure 4-6 is a Magellan stereo anaglyph in which the Cycle 1 image is tinted red and the Cycle 2 image (from the left-looking stereo test) is tinted blue. Standard 3-D glasses, with the red filter on the left eye and the blue filter on the right eye, accomplish the same effect as a stereoscope by providing each image of the pair exclusively to the appropriate eye. Anaglyphs can be generated on color video monitors with Magellan digital image data. Cycle 1 data should be sent to the red channel, and Cycle 3 data should be sent to both the blue and green channels. The amount of lateral offset between the left and right images is not important, as long as the eye is able to fuse the images without too much strain.

Examples of parallax differences used to measure relief are shown in Figures 4-7 and 4-8. Figure 4-7 is an opposite-side full-resolution stereo pair (Cycles 1 and 2) of a scalloped dome. The left image, from Cycle 1, was acquired in the left-looking mode at an incidence angle of 40 deg. The right image, from Cycle 2, was acquired in the right-looking mode at an incidence angle of 25 deg. The parallax difference between the left edge of the westernmost pit and the scarp of the dome is 243 − 118 = 125 pixels. Using the formula in Figure 4-2, the parallax-to-height ratio for these images is 3.34. The relief can then be calculated:

$$125 \text{ pixels} \times 75 \text{ m/pixel} / 3.34 = 2807 \text{ m}$$

This measurement is consistent with the altimeter data, which indicate that the dome summit lies 2.2 to 3.0 km above the surroundings.

Figure 4-8 is a same-side stereo pair (Cycles 1 and 3) of a caldera (volcanic depression). The incidence angles used were 42.5 deg (Cycle 1, left image) and 22.7 deg (Cycle 3, right image). The parallax difference between features on the rim and floor of the caldera is 23 pixels. Using the formula in Figure 4-1 and a parallax-to-height ratio of 1.30, the relief is

$$23 \text{ pixels} \times 75 \text{ m/pixel} / 1.30 = 1327 \text{ m}$$

This is again consistent with altimeter measurements of the feature. Further examples of stereometric techniques applied to Magellan data may be found in Leberl et al., 1991 and 1992, and Moore et al., 1992.

Digital Elevation Models

Stereo images are also used to derive topographic relief through the automated generation of digital elevation models (DEMs). In this technique, computer algorithms match features between the images of a stereo pair, calculate the
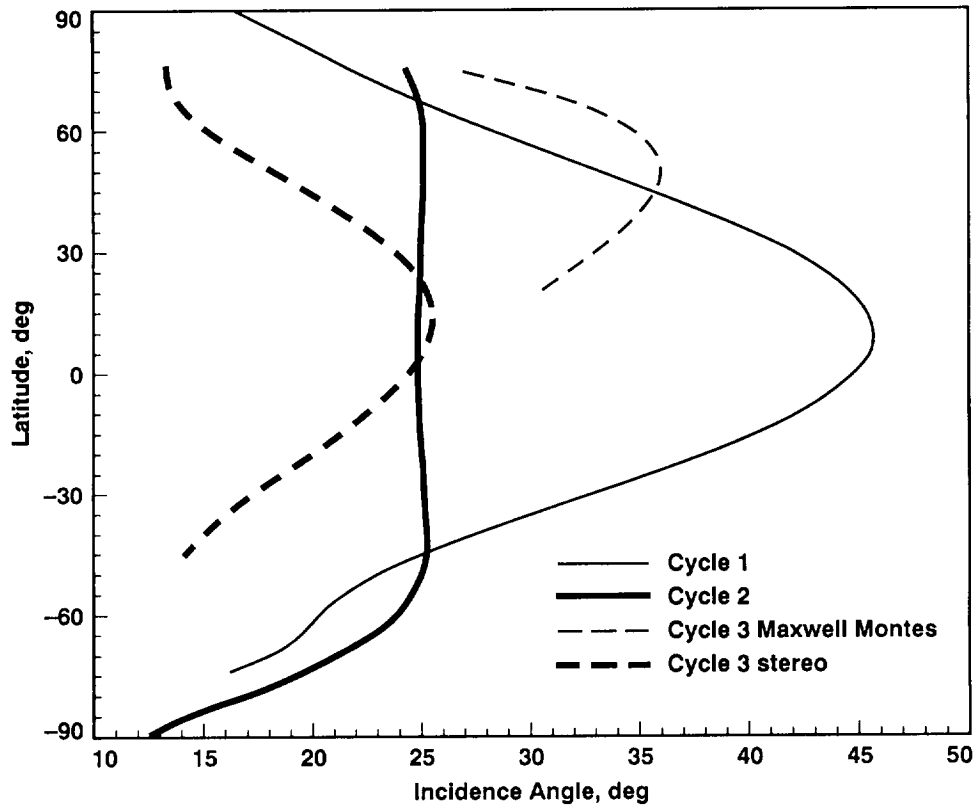
Figure 4-3. Magellan SAR incidence angles as a function of latitude for the three imaging cycles. The Maxwell Montes data consist of orbits 4031 through 4131. Gap-filling portions of Cycles 2 and 3 used the standard Cycle 1 incidence angles.

parallax of every pixel, and generate a topographic map for the entire scene. The calculation is identical to that for the manual derivations of heights and depths of features, but the automated DEM procedure has the advantage of producing an elevation measurement for every pixel. Topographic maps produced in this way have a lateral resolution close to the

image resolution (~100 m), which is 100 times better than the typical resolution of the altimeter. Geologists studying the morphology (shapes) of Venusian surface features will find the DEMs extremely valuable in their analyses. Where DEMs are not available, geologists can estimate the relief of features using the manual techniques outlined in this chapter.
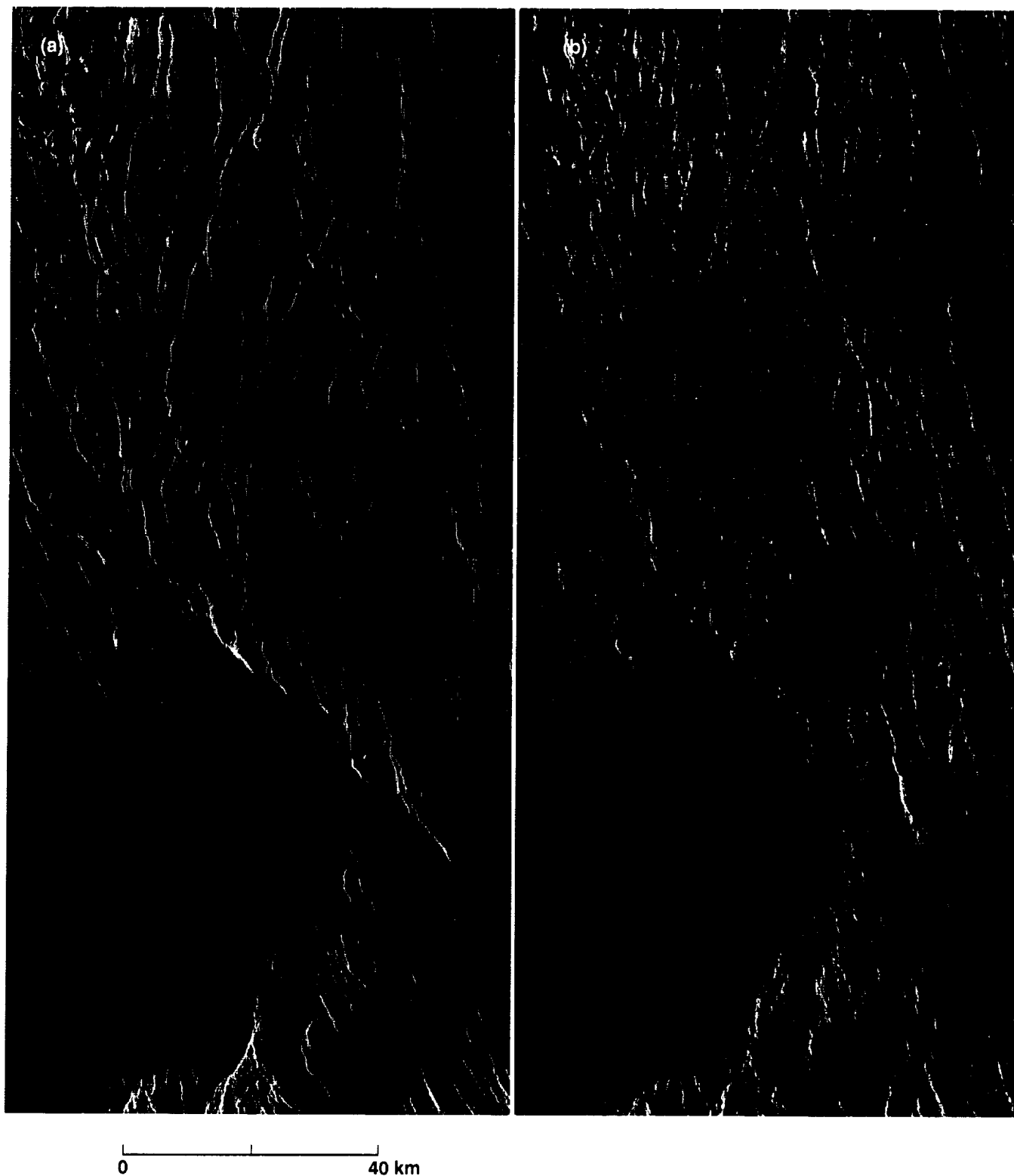
Figure 4-4. Stereo image pair showing complex ridge terrain and a smooth-floored depression in the Ovda region of Aphrodite Terra: (a) Cycle 1 image with illumination from the left at an incidence angle of 43 deg; (b) Cycle 2 image with illumination from the left at an incidence angle of 23 deg. Cycle 2 data were acquired during the stereo test orbits 2674 through 2681. The total relief in this scene is about 2.6 km; the center coordinates are 8°S, 74°E. Perception of relief may be obtained with stereo glasses or a stereoscope. Some individuals may be able to fuse the images without the aid of these devices.

38

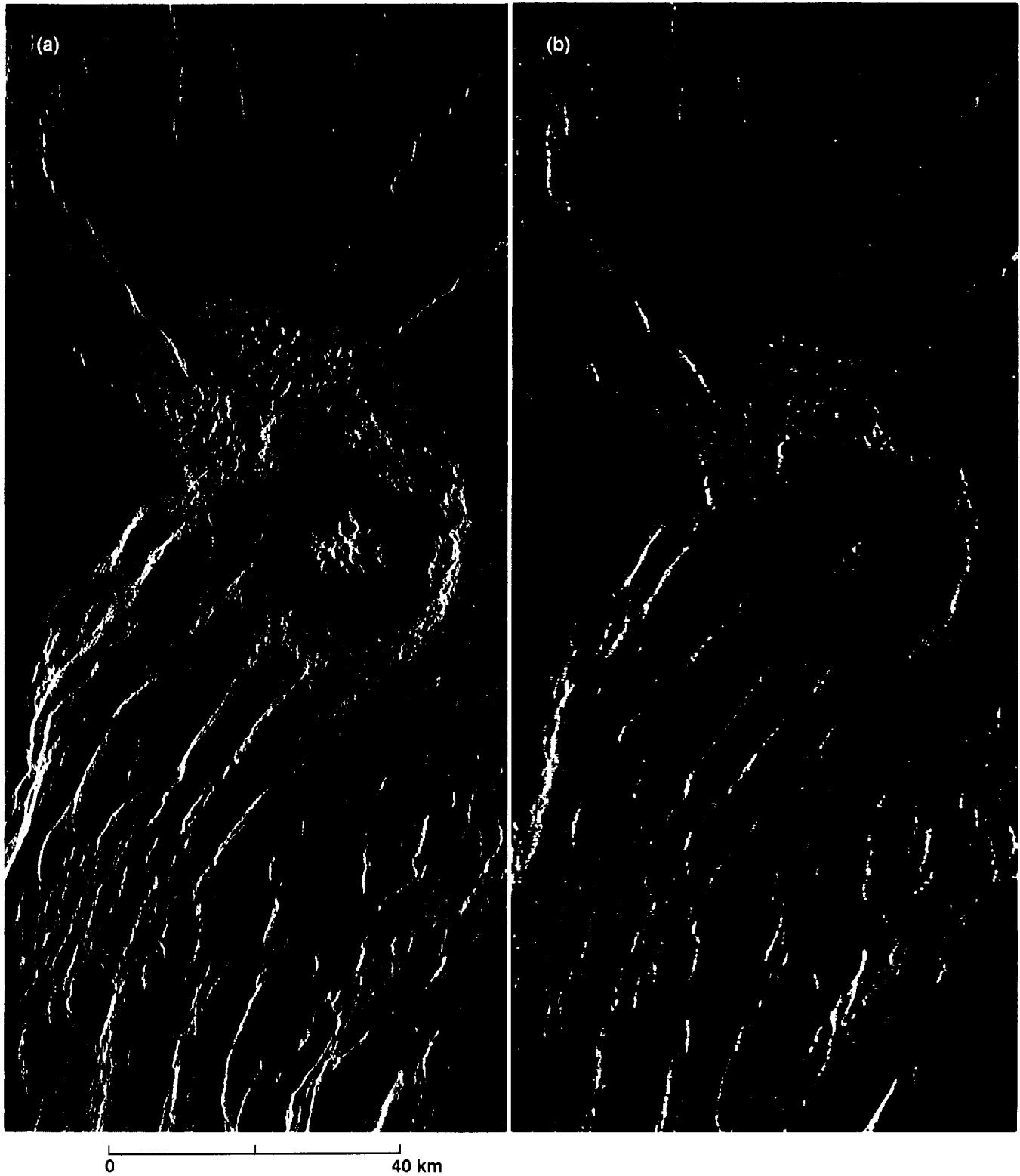0   40 km

Figure 4-5. Stereo image pair of crater Geopert-Meyer: (a) Cycle 1 image with illumination from the left at an incidence angle of 28 deg; (b) Cycle 3 image with illumination from the left at an incidence angle of 15 deg. The center coordinates are 60°N, 26.5°E. The crater lies above an escarpment at the edge of a ridge belt in southern Ishtar Terra. West of the crater the scarp has more than 1 km of relief.
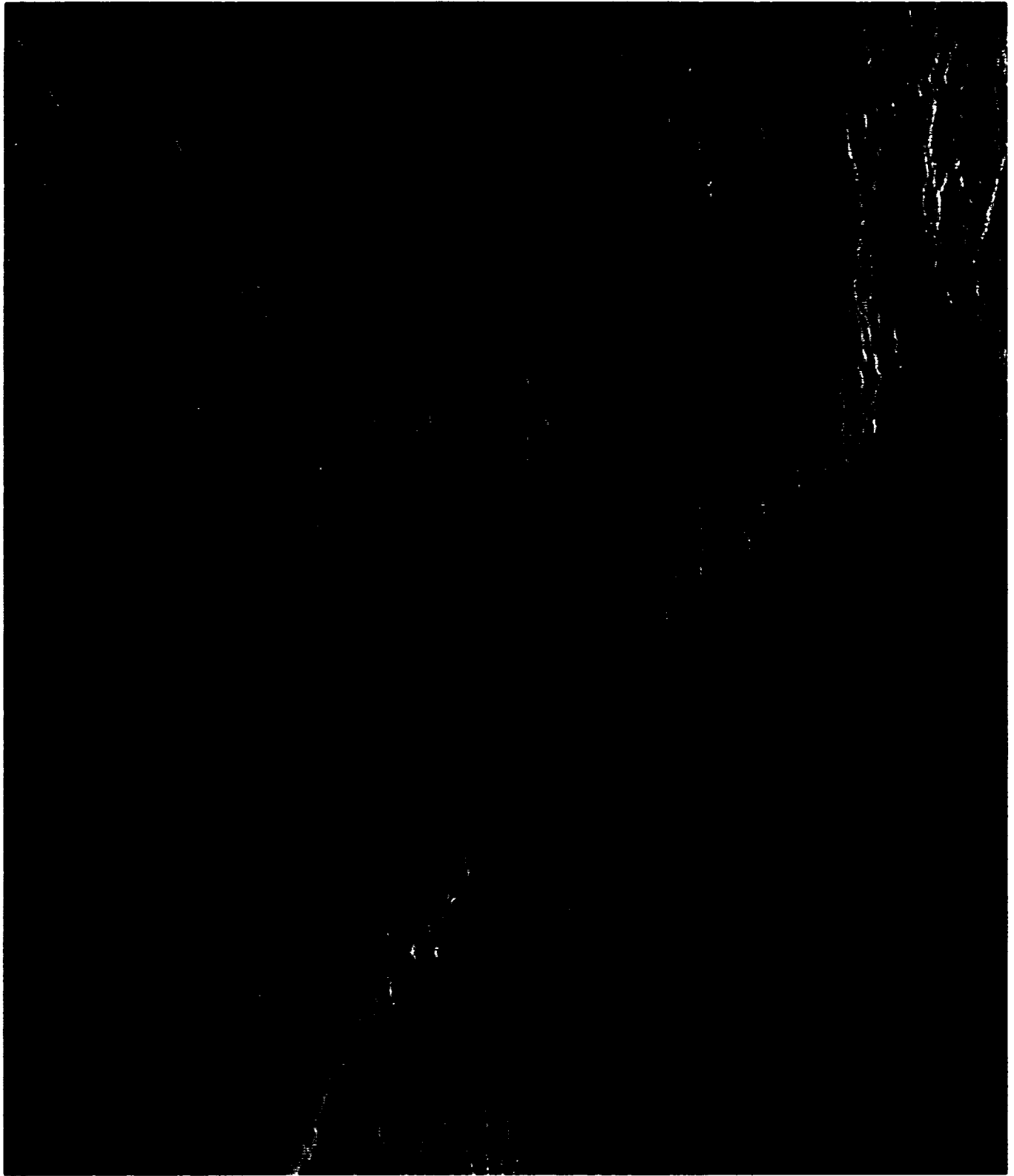
39

Figure 4-6. Stereo anaglyph of Magellan SAR images, suitable for viewing with standard 3-D glasses (red filter on left eye, blue filter on right). The image shows a complex pattern of troughs, ridges and depressions in the Ovda region of Aphrodite Terra. The center coordinates are 13°N, 73.8°E.
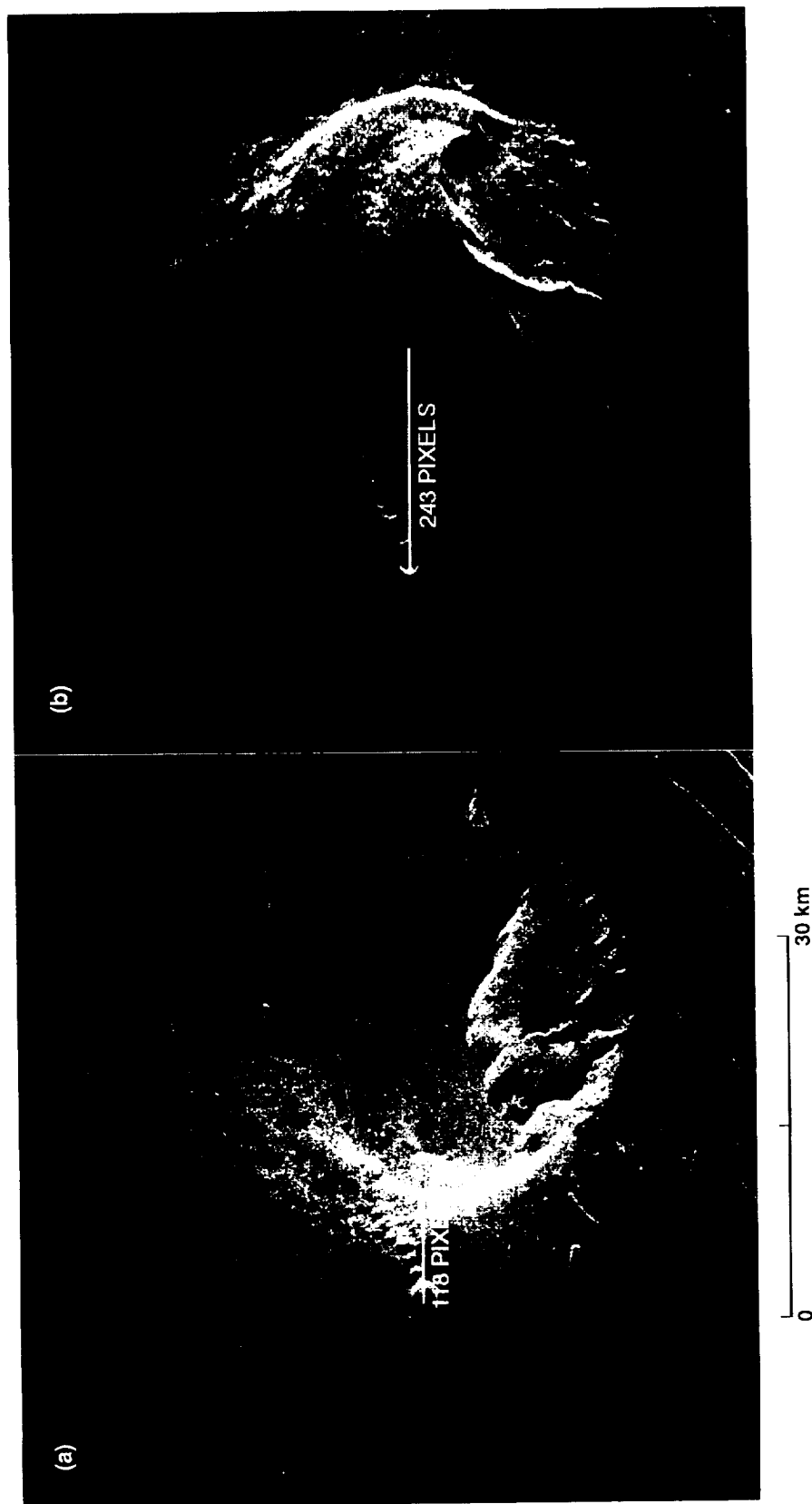
40

Figure 4-7. Volcanic dome with collapsed margins: (a) Cycle 1 image with illumination from the left at an incidence angle of 40 deg; (b) Cycle 2 image with illumination from the right at an incidence angle of 25 deg. The center coordinates are 16°S, 211.5°E. From a measurement of the parallax difference between the westernmost pit edge and the dome margin in the two images, a height difference of 2.8 km is found.
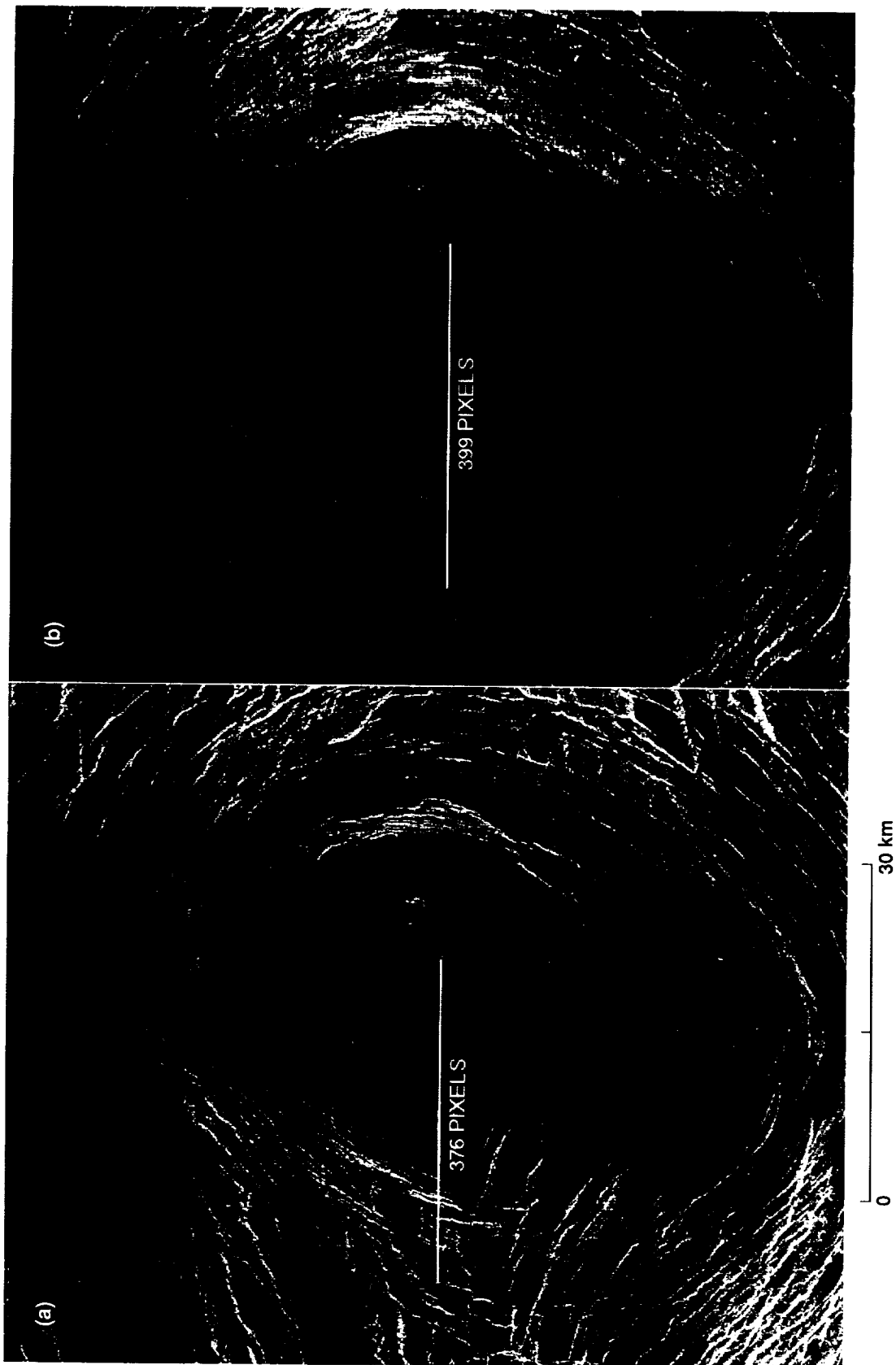
399 PIXELS

(b)

376 PIXELS

(a)

0   30 km

Figure 4-8. Caldera (volcanic pit): (a) Cycle 1 image with illumination from the left at an incidence angle of 22.7 deg; (b) Cycle 3 image with illumination from the left at an incidence angle of 42.5 deg. The center coordinates are 9.5°S, 69°E. The parallax difference between features on the rim and floor gives a depth of 1.3 km for the caldera.

42

References

Leberl, F. W., K. Maurice, J. Thomas, and W. Kober, 1991, "Radargrammetric measurements from the initial Magellan coverage of planet Venus," *Photogramm. Eng. Rem. Sens.*, v. 57, p. 1561–1570.

Leberl, F. W., J. K. Thomas, and K. E. Maurice, 1992, "Initial results from the Magellan stereo experiment," *J. Geophys. Res.*, v. 97, p. 13,675–13,689.

Moore, H. J., J. J. Plaut, P. M. Schenk, and J. W. Head, 1992, "An unusual volcano on Venus," *J. Geophys. Res.*, v. 97, p. 13,479–13,493.

Chapter 5. Radar Interactions With Geologic Surfaces

Tom G. Farr

Introduction

The correct geologic interpretation of radar images depends critically on a knowledge of how radar waves interact with natural surfaces. There are significant differences between the microwave and more familiar optical wavelengths in the mechanics of imaging and in the measured characteristics of the target. Because of the side-looking illumination geometry, all radar images are distorted to some extent. In addition, the longer wavelength of radar waves makes them most sensitive to surface roughness at scales near the radar wavelength. Of secondary importance are variations in the dielectric constant of the target; this parameter is similar for dry geologic materials except metallic compounds, which may be present at high elevations on Venus. The geometric and electromagnetic interactions of radar waves with natural surfaces, then, must be considered for accurate interpretation of Magellan SAR images.

The Geometry of Radar Imaging

Since radars depend on the measurement of range to create an image in the cross-track direction, they are forced to look to the side to allow the sensor to differentiate between objects to the left and right of the ground track; in the along-track direction, platform motion and Doppler frequency shift create the image. Synthetic aperture and matched-filter techniques, described by Elachi [1988], are used to obtain high resolution in these directions.

This side-looking geometry has a number of descriptive terms and peculiarities that must be understood when interpreting radar images (Figure 5-1). The angle at which the radar images the target as measured from the horizontal at the antenna is called the depression angle. The look angle, θ_l, is the complement of the depression angle. At the target, local undulations combined with the look angle create a local incidence angle, θ_i (Figure 5-1). Note that even for horizontal terrain, the look angle does not equal the local incidence angle because of planetary curvature. This effect is small for aircraft sensors but significant for spacecraft:

$$\theta_i = \arcsin\left(\frac{r+H}{r}\sin\theta_l\right)$$

where r is the radius of Venus and H is the altitude of the spacecraft.

The fact that imaging radars divide the range into small intervals to create range pixels yields a projected geometry when the slant-range pixels are written to film (Figure 5-2). A slant-range image appears compressed in the near range because of this projection. Assuming a horizontal surface, the simple transformation

$$G = H\sqrt{\frac{1}{\cos^2\theta_i}-1}$$

produces a ground-range image, where G is the ground-range distance. Note, however, that topographic variations are not accounted for in this transformation.

Topographic variations are distorted in the same way as the overall image: Their near-range points are compressed relative to their far-range points (Figure 5-3). The general
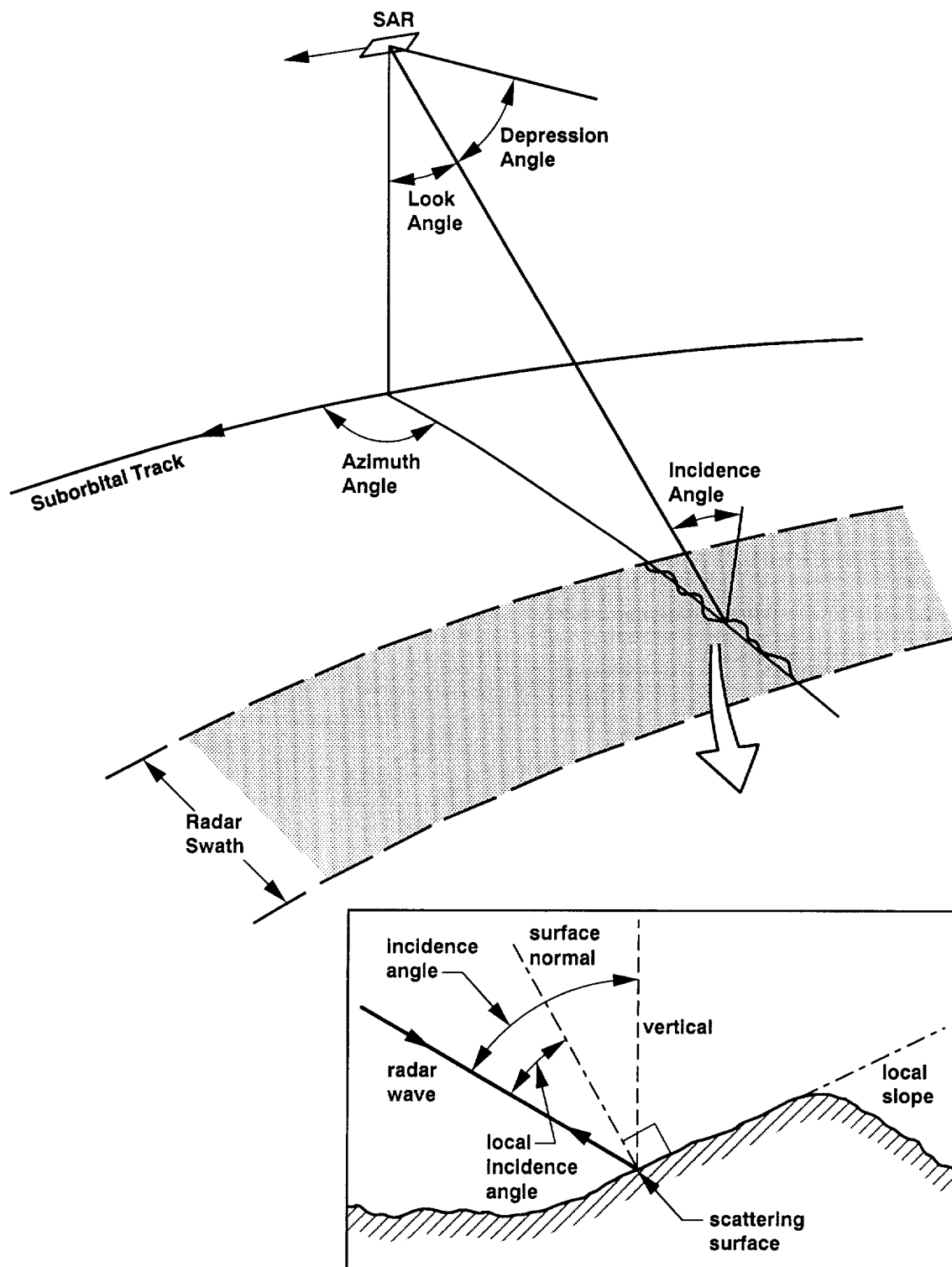
Figure 5-1. Geometry of radar image acquisition. The depression angle is complementary to the look angle; the incidence angle may be affected by planetary curvature. Local incidence angle may be affected by local topography.
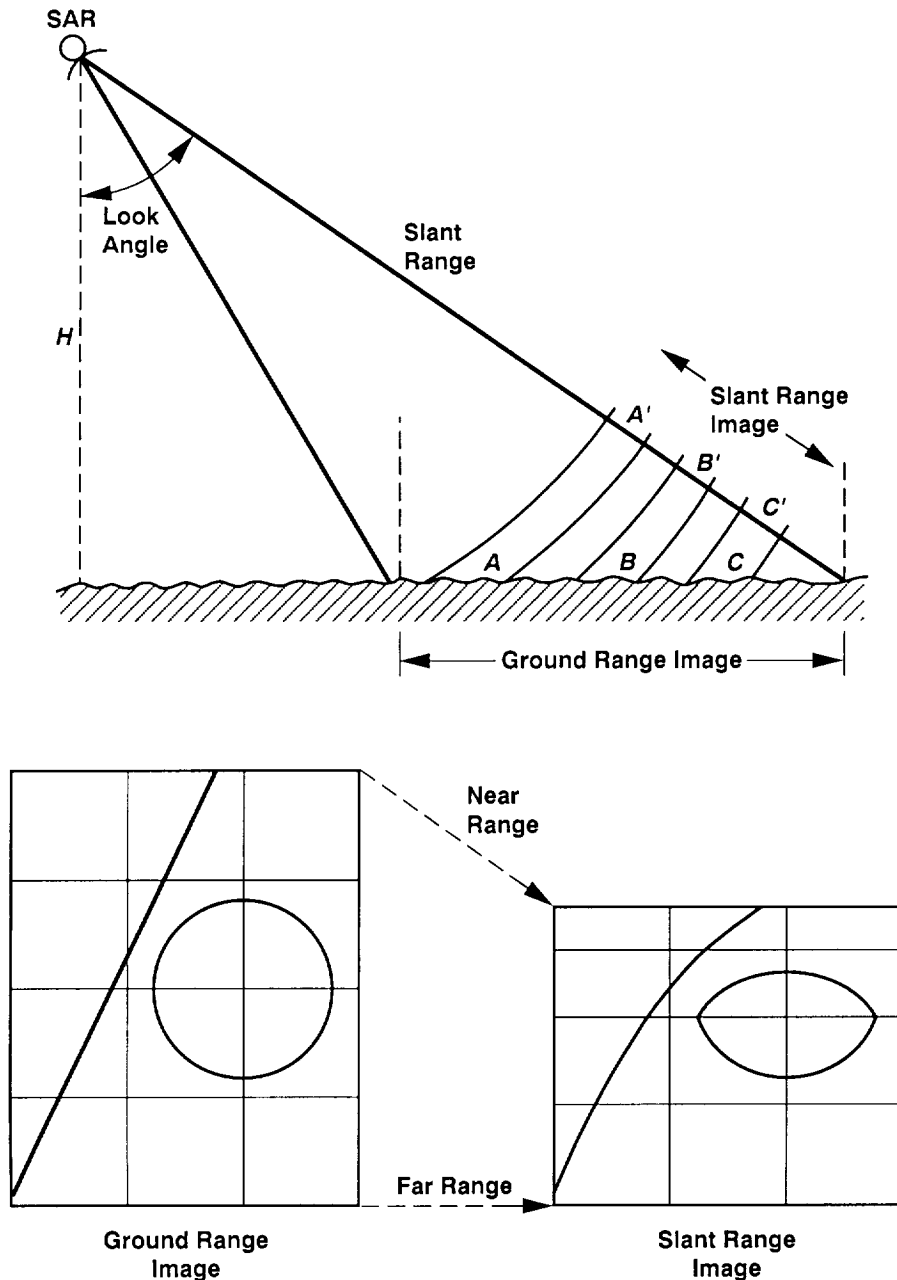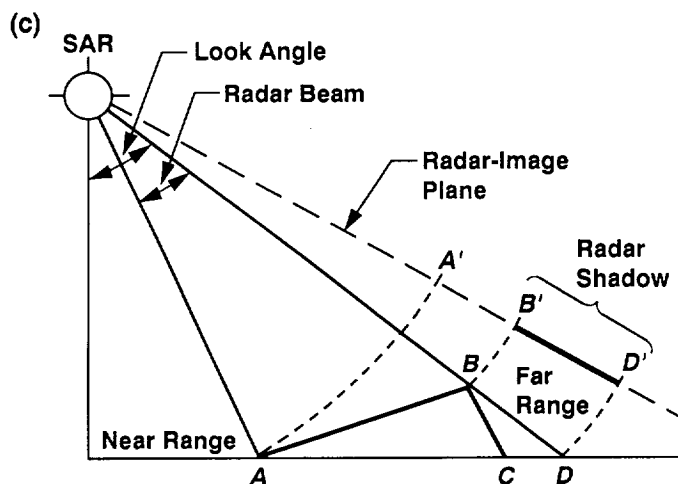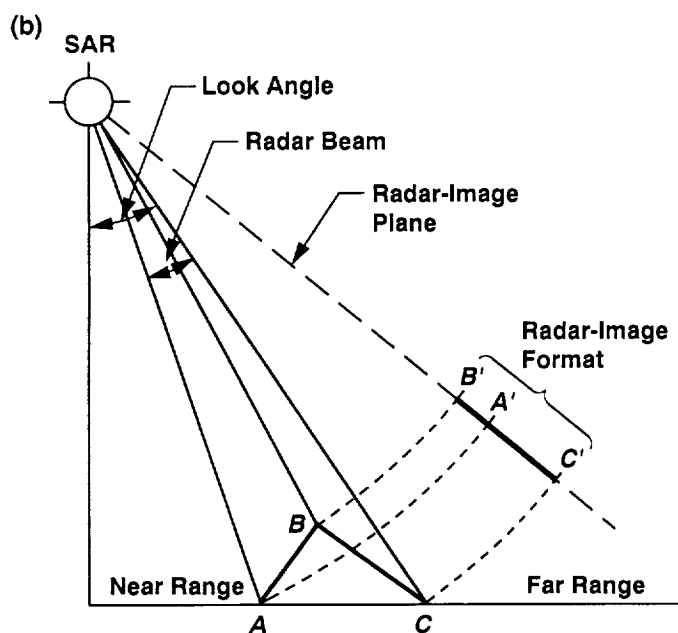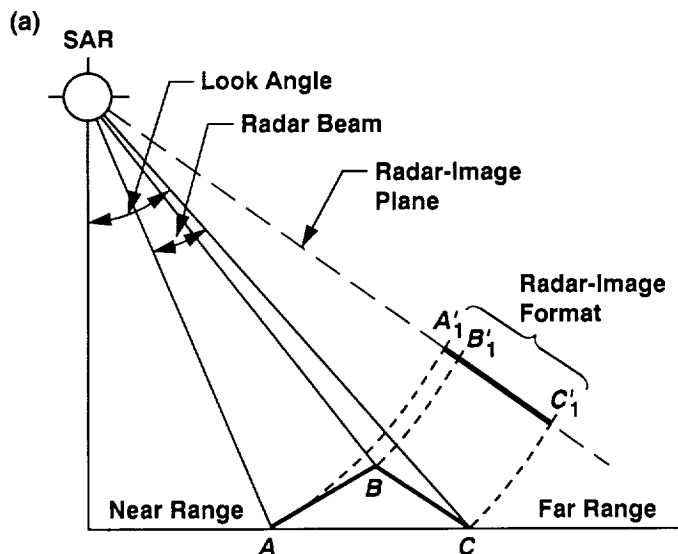
Figure 5-2. Slant-range and ground-angle geometries. Knowledge of the spacecraft height, H, and incidence angle allows correction of slant-range geometry, where targets in near range appear compressed with respect to those in far range.

case of radar foreshortening compresses the image of a mountain's near-range slope and extends the image of its back slope (Figure 5-3(a)). The effect is obviously exacerbated by small look angles and steep slopes to the extreme case of layover, in which the top of the mountain is imaged before the bottom of the near-range slope (Figure 5-3(b)). Image data in the laid-over area are lost. Image data can also be lost on the

backslope if the slope is steep enough and the look angle large enough to put the slope in radar shadow (Figure 5-3(c)). Layover and shadow can be seen in a Seasat SAR image of the Alaska Range (Figure 5-4), where the top of a mountain is superimposed on the glacier at its foot, while the backslopes of the mountains are in shadow. Seasat SAR had a look angle of about 20 deg.

(a) SAR

Look Angle
Radar Beam
Radar-Image Plane
Radar-Image Format

A'_1 B'_1
C'_1
B
Near Range | Far Range
A | C

(b) SAR

Look Angle
Radar Beam
Radar-Image Plane
Radar-Image Format

B' A'
C'
B
Near Range | Far Range
A | C

(c) SAR

Look Angle
Radar Beam
Radar-Image Plane

A'
B'
B' | D'
B Far Range
Radar Shadow
Near Range
A | C D

As a generalization, since most slope angles on Earth are less than about 35 deg, imaging radars with small look angles, such as Seasat, enhance the topography at the expense of surface roughness information (discussed later). Conversely, larger look angles, such as SIR-A's 47 deg, reduce the effect of topography and enhance the sensitivity to surface roughness (Figure 5-5).

These aspects of imaging radar geometry are especially important in interpreting Magellan SAR images, as the look angle varies systematically with latitude (Figure 4-3). The wide range of look angles extends beyond the range of the Seasat SAR and SIR-A angles and encompasses shallow slope angles typical of eroded terrain, through angles equal to the angle of repose of loose granular material (i.e., sand and talus), to over-steepened angles typical of tectonically active mountains. Thus, different types of relief will be accentuated depending on latitude.

The orientation of linear features relative to the radar look direction or azimuth also controls the visibility of the features (Figure 5-6). Where the illumination is *parallel* to the structure, there is little effect on the local incidence angle and therefore no enhancement of the structure. Conversely, topographic variations stand out where illumination is *normal* to the structure. Obviously, this effect is accentuated by a small look angle.

A dramatic example of another look–azimuth effect is shown in Figure 5-7, which is a pair of Magellan SAR images obtained from nearly opposite look directions at nearly the same look angle. Bright areas in the upper image, which is illuminated from the west (left), are not present in the lower image, which is illuminated from the east. A possible explanation is that asymmetric ripples or dunes are oriented approximately north–south, with local slope angles equal to the look angle on the west and much different angles on the east. Another possibility is that the surface changed, perhaps in response to wind action, in the 8-month interval between the two passes.

Roughness

Radar waves impinging on a surface scatter from the surface and near-surface volume. Very smooth surfaces at the

Figure 5-3. Geometric distortions in radar images: (a) radar image foreshortening, where the slope facing the radar is compressed to segment $A' - B'$ while the backslope is extended to segment $B' - C'$; (b) radar layover, an extreme case of foreshortening, where the top of the mountain, B', is imaged before the bottom, A'; (c) radar shadowing, where the backslope of the mountain, $B' - D'$, is not illuminated by the radar, and no data are acquired.
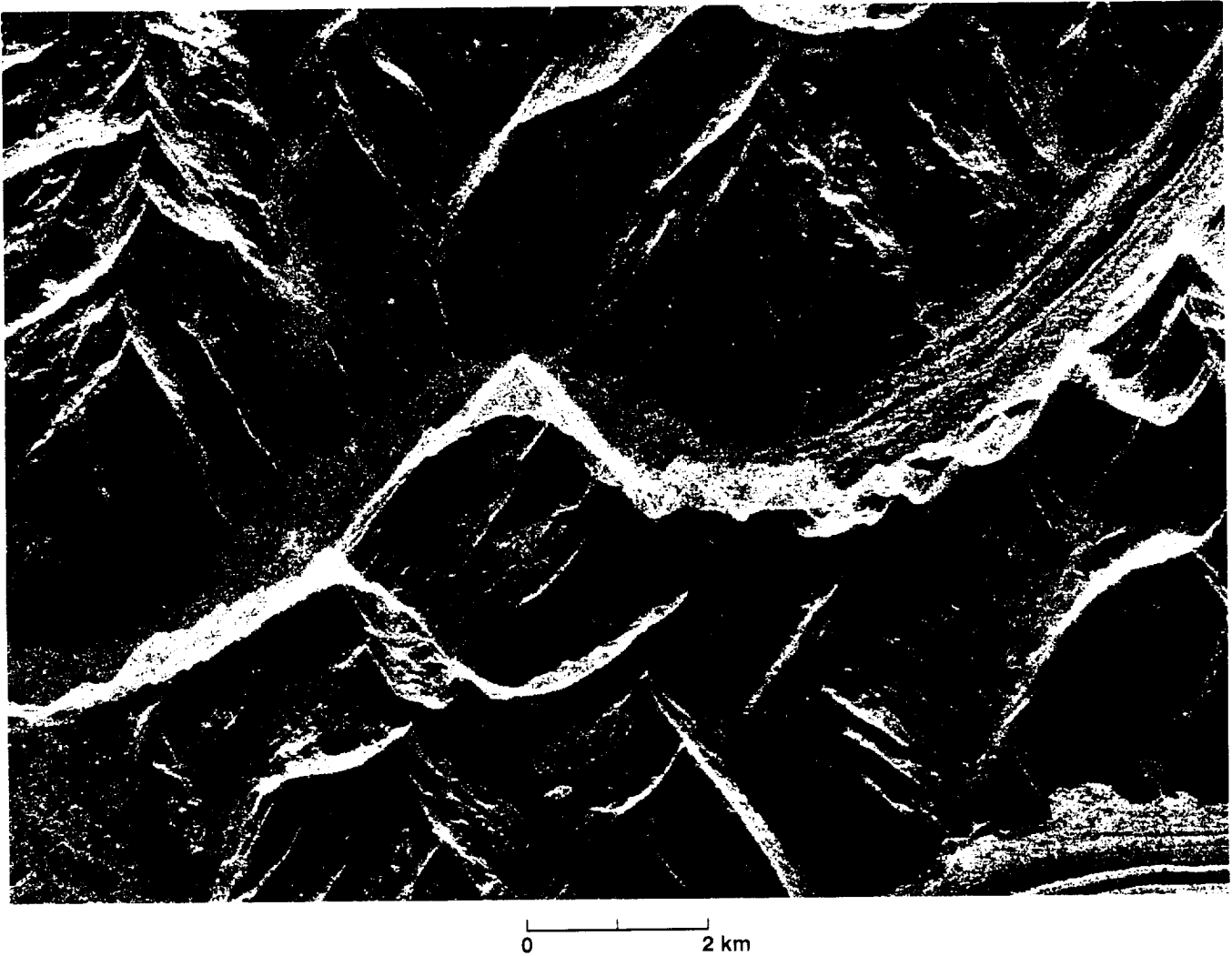
48

0   2 km

Figure 5-4. Example of radar image layover. Seasat image of the Alaska Range showing the top of a mountain imaged onto the glacier at its foot (center). Shadows are also present on many of the backslopes of these steep mountains. Illumination is from the top [from Ford et al., 1989].

scale of the radar wavelength (λ) scatter the incident radiation in the specular direction (Figure 5-8); this scattering is a mirrorlike reflection often called "specular reflection." Rougher surfaces cause more of the radar energy to be scattered randomly until it reaches a diffuse, Lambertian distribution. The Magellan SAR, like most imaging radars, is monostatic, i.e., the same antenna is used for transmission and reception. Comparison of the cases in Figure 5-8 shows that the smooth surface has no component of its return in the direction of the transmission arrow, so the resulting image tone would be black. With increasing roughness, more energy is scattered back to the antenna, resulting in lighter image tones for rougher surfaces.

Changes in the local incidence angle for the surfaces shown in Figure 5-8 produce characteristic curves of image brightness, quantified as radar backscatter vs. incidence angle (Figure 5-9). Clearly, a smooth surface produces a sharp peak when the radar illumination is perpendicular to it (incidence angle = 0 deg), while a very rough surface scatters the signal equally in all directions with little dependence on incidence angle. The curves in Figure 5-9 show that smooth surfaces can be brighter than rough surfaces at small incidence angles (typically less than 20 to 25 deg); these small angles are typical for the Magellan SAR data in the high latitudes of Venus. An erroneous interpretation of roughness can result if look angle is not taken into account.

49

N
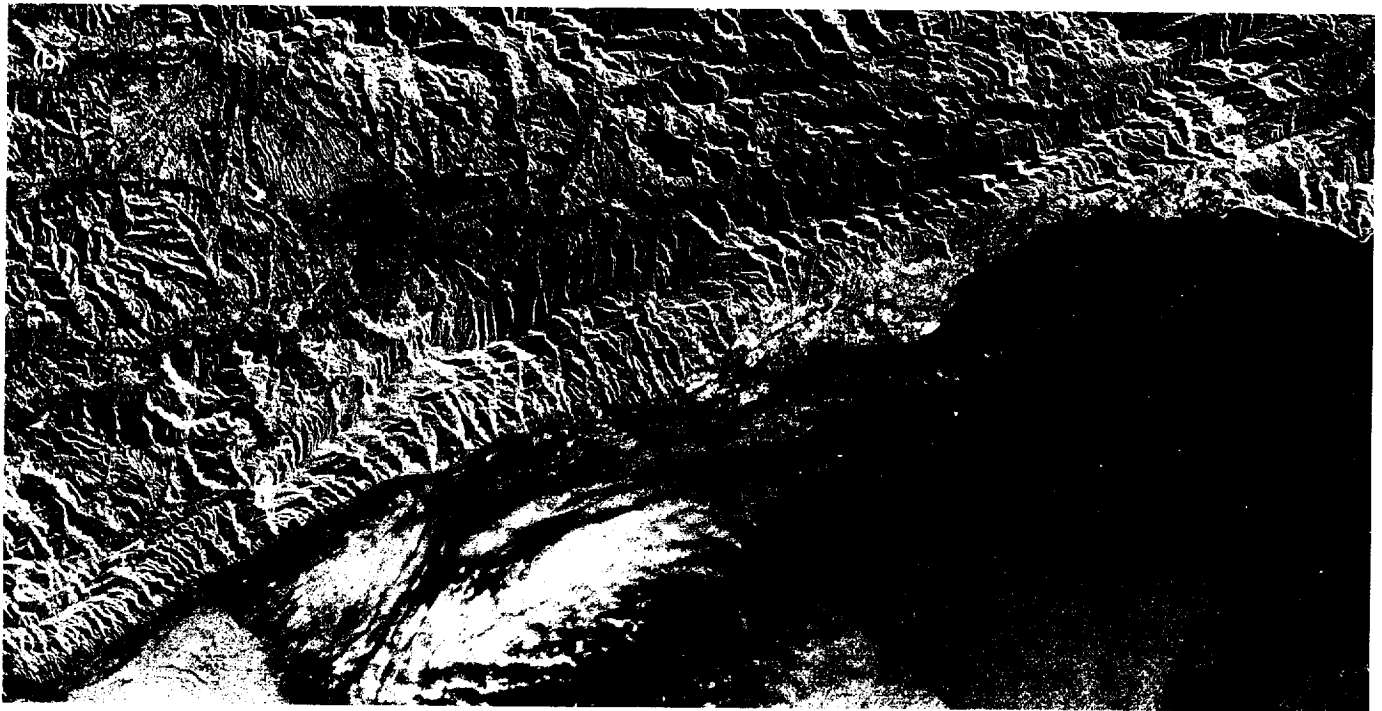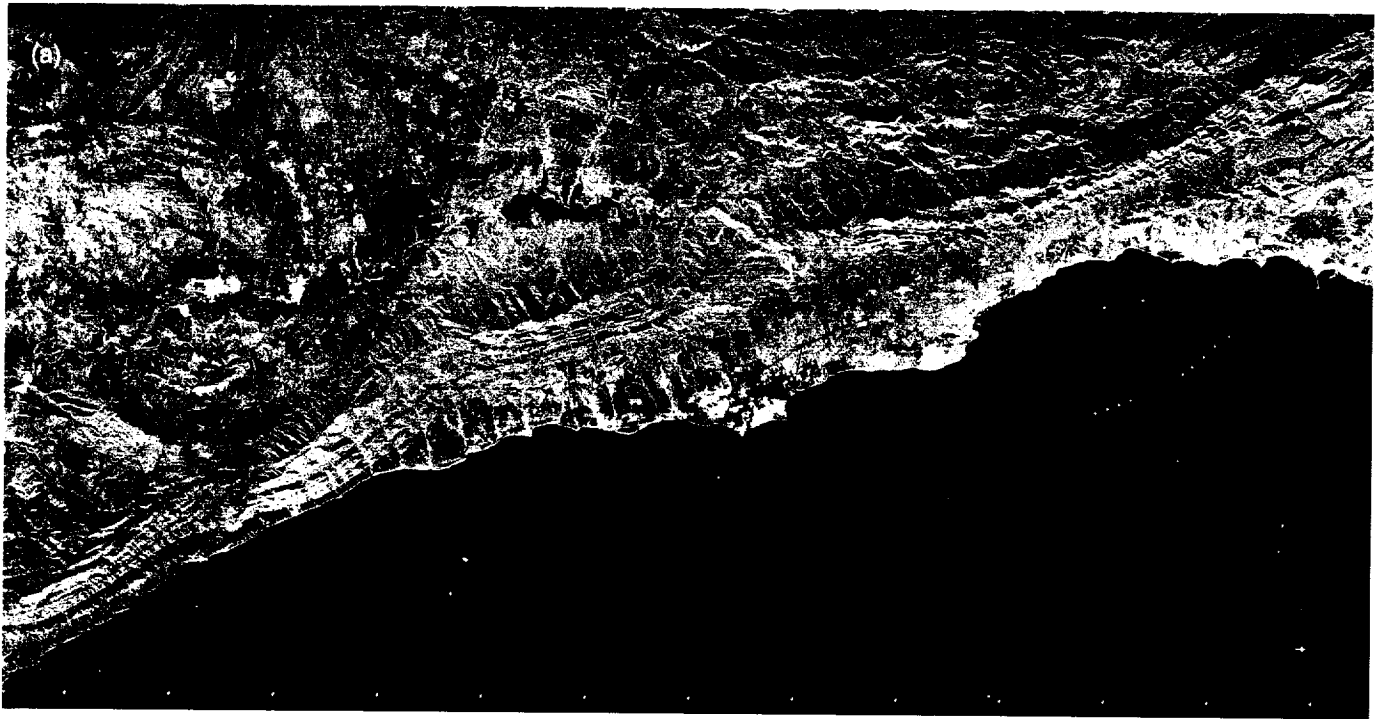
0   20 km

Figure 5-5. Enhancement of roughness and topography: (a) SIR-A image of the Santa Ynez Mountains in California obtained at about a 50-deg incidence angle—at this angle, surface roughness effects dominate the image; (b) Seasat image of the scene in (a) obtained at about a 20-deg incidence angle—at this small angle, topography is enhanced because the slopes are closer to this small value. Illumination is from the bottom in (a) and from the lower left corner in (b).
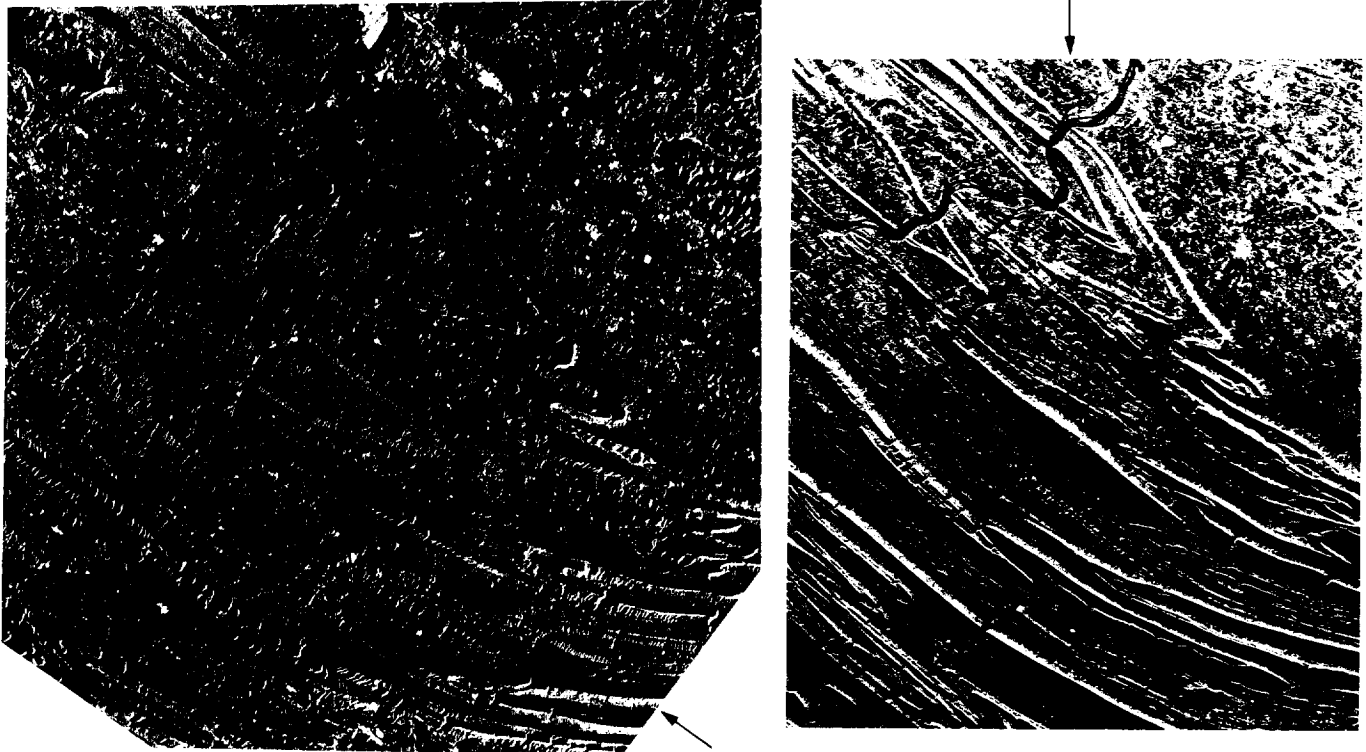
Figure 5-6. Azimuth viewing effects in radar images. Seasat observed the folded Appalachians in Pennsylvania from two directions, shown by the arrows. The structures are highlighted where illumination is nearly perpendicular to the ridges, while the contrasts in topography almost disappear where the illumination is parallel to the ridges.

The scattering behavior of radar waves from rough surfaces can be quantified through the use of scattering models that relate surface roughness to the radar backscatter [e.g., Ulaby et al., 1982; Fung and Pan, 1987; Kim et al., 1992; Rodríguez et al., 1992; Rodríguez and Kim, 1992]. However, before discussing the scattering models themselves, the quantitative description of surface roughness deserves some review.

A breakpoint between smooth and rough surfaces (and the corresponding dominant radar scattering mechanisms) is loosely implied by the Rayleigh criterion. According to this criterion, a surface is considered smooth if the root-mean-square (rms) height of the microrelief is less than one-eighth of the radar wavelength divided by the cosine of the incidence angle:

$$h < \lambda/8 \cos \theta$$

where h is the rms height, λ is the wavelength, and θ is the incidence angle. Because this criterion does not consider an intermediate category of surfaces between definitely smooth and definitely rough, it was modified by Peake and Oliver

[1971] to include factors that define the upper and lower values of rms surface smoothness or roughness. The modified Rayleigh criterion considers a surface smooth where

$$h < \lambda/25 \cos \theta$$

and rough where

$$h > \lambda/4.4 \cos \theta$$

Field measurements of different types of surfaces have led researchers to experiment with a variety of different descriptors [e.g., Schaber et al., 1976 (geologic surfaces); Ulaby et al., 1982 (agricultural surfaces)]. This illustrates one of the difficulties associated with modeling the radar behavior of natural surfaces. Regardless of the description that is used, it follows from the equations that at any incidence angle a given surface appears rougher as the wavelength decreases and, independent of wavelength, a given surface appears smoother as the incidence angle increases.

Describing the roughness of a surface by its rms height excludes any description of the scales of roughness. The scales of roughness can be described by calculating the
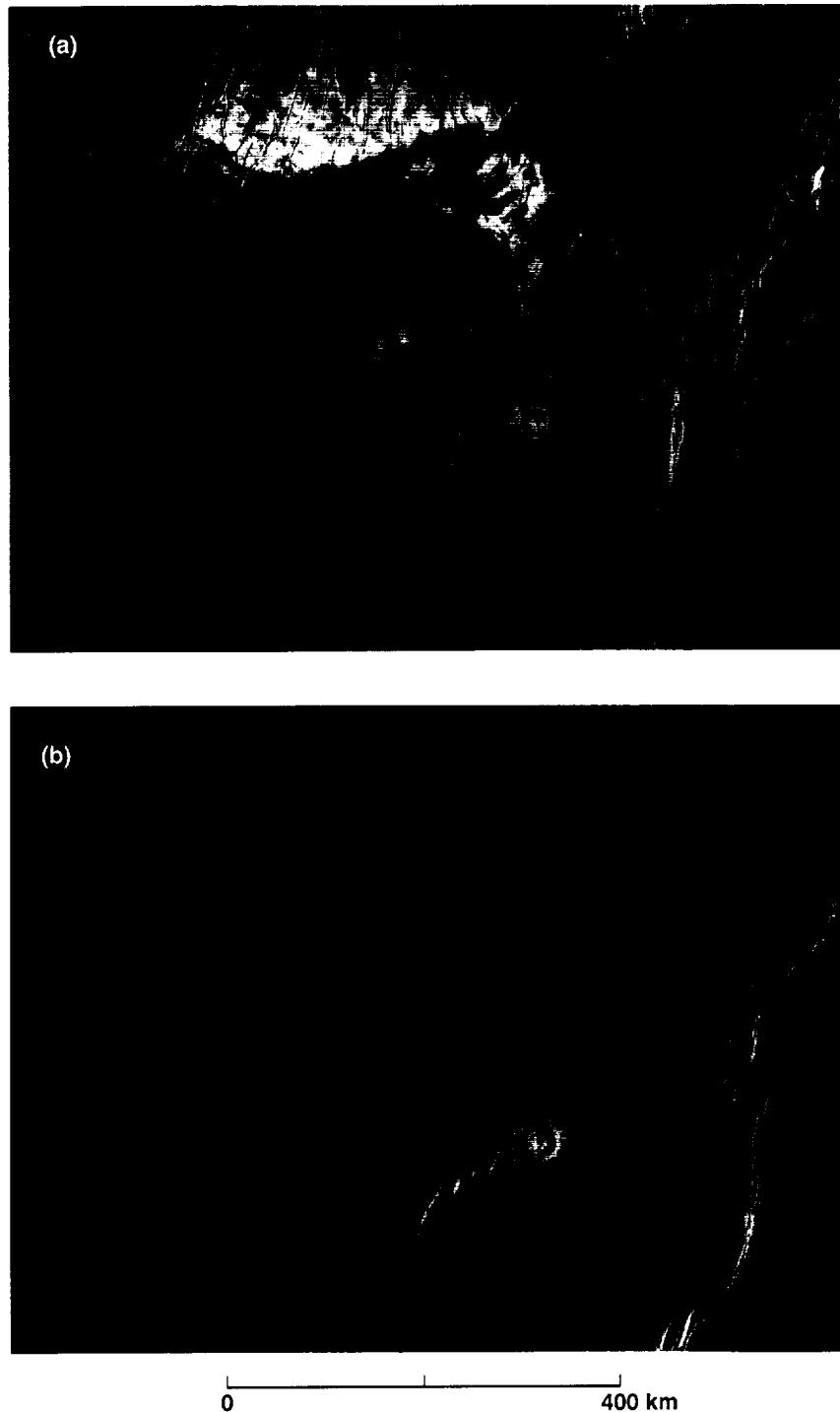
51

0   400 km

Figure 5-7. Azimuth viewing effects in Magellan SAR images of an area centered at about 58°S, 200°E in Imdr Regio: (a) obtained in February 1991 with illumination from the west (left) at an incidence angle of about 21 deg; (b) obtained in October 1991 with illumination from the east (right) at an incidence angle of about 24 deg. Many bright areas in (a) are not present in (b), which indicates (1) the surface has asymmetric roughness with slopes of about 21 deg facing west (to give the bright return) and much different slopes facing east, or (2) the surface was altered by surficial processes in the 8 months between the two images.

Smooth: no return

Slightly Rough: slightly diffuse

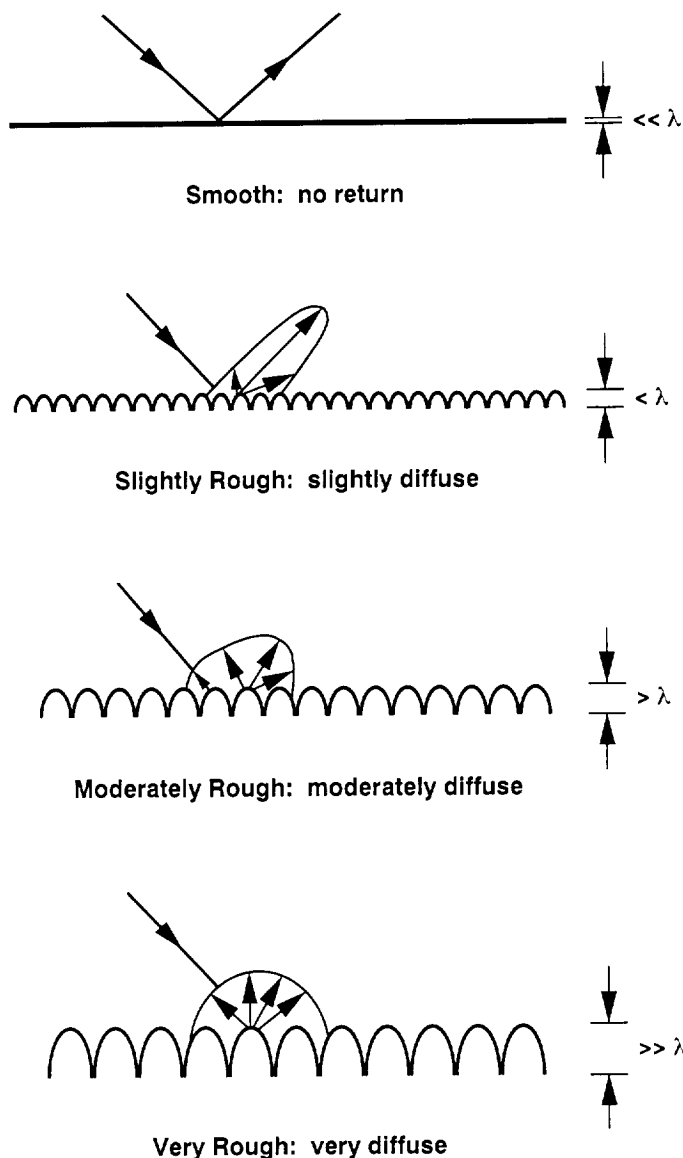**Moderately Rough: moderately diffuse**

Very Rough: very diffuse

Figure 5-8. Surface roughness effects on radar backscatter. Surfaces whose roughness is much less than the radar wavelength scatter in the specular direction. Rougher surfaces scatter more energy in all directions, including the direction back to the receiving antenna.

correlation length of profiles: Correlation length is a measure of how quickly heights change along a profile. The autocorrelation function for a surface profile is calculated by sequentially stepping the profile across a stationary copy, multiplying, and normalizing. This function is unity for 0 steps, or lags, and drops as the number of lags increases. The rate of the drop-off, measured by the lag at which the autocorrelation value equals 1/e, is called the correlation length, l. Smoother surfaces have larger correlation lengths [e.g., Ulaby et al., 1982, p. 822].
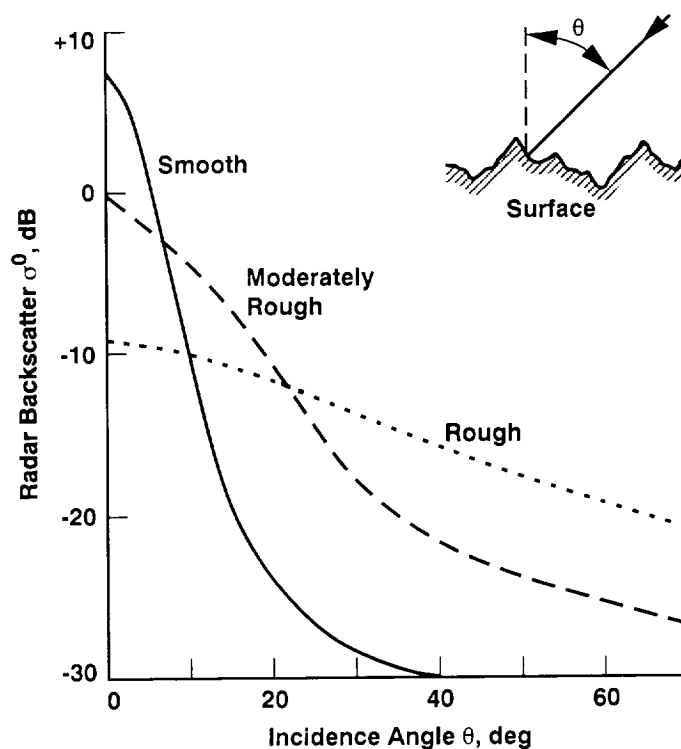

Figure 5-9. Radar backscatter as a function of incidence angle for representative surfaces. For angles less than about 25 deg, smoother surfaces have greater backscatter than rougher surfaces.

Another way to describe quantitatively both the amplitude and scale of surface roughness is through the power spectrum, or power spectral density, usually of profiles. Without going into the mathematical details that are better covered in several texts [e.g., Bendat and Piersol, 1986] and recent papers [e.g., Brown and Scholz, 1985], the power spectrum is basically the Fourier transform of the profile (or two-dimensional topography). This produces a plot showing power, or variance, as a function of spatial frequency, or scale. These functions are usually plotted as power in m^2/cycle/m, or m^3, vs. spatial wave number (= $\Lambda/2\pi$, where Λ is spatial wavelength). When plotted in log–log coordinates, the functions are approximately linear [e.g., Berry and Hannay, 1978; Farr, 1992], indicating a power-law relationship between roughness and scale. This relationship simplifies the quantitative description of the power spectrum of a profile to two parameters: the slope and offset (y-intercept). Power spectrum slope is a measure of self-similarity related to the fractal dimension, D, by [Brown, 1985]

$$D = \frac{5 + slope}{2}$$

53

Power spectrum offset is a measure of overall roughness, sometimes called "roughness amplitude" [Huang and Turcotte, 1989]. For centimeter–meter scales, power spectrum offset has been empirically related to h by [Evans et al., 1992]:

$$h = 40e^{(\textit{offset})}$$

Scattering Models

There are two main types of scattering models: facet and Bragg. Facet-type models assume that the roughness is smaller and curvatures larger than λ, so specular scattering dominates from the smooth, tilted facets. The various names for facet-type models include Physical Optics, Geometric Optics, Kirchoff Approximation, Stationary-Phase Approximation, Scalar-Wave Approximation, and the Hagfors Model. In general, these models are most useful at small incidence angles and for smooth surfaces; no cross-polarization terms are predicted.

As an example, the Stationary-Phase Approximation (SPA) is given as [e.g., Kim et al., 1992; Rodríguez et al., 1992]:

$$\sigma_{pp}^0 = \frac{\rho^2 l^2 e^{-(l \tan \theta / 2h)^2}}{4h^2 \cos^4 \theta}$$

where

ρ = Fresnel reflectivity at $\theta = 0$

$$= \left| \frac{1 - \sqrt{\varepsilon}}{1 + \sqrt{\varepsilon}} \right|^2$$

Note that the SPA gives the same value of σ^0 for both HH and VV polarizations. This is typical of facet-type models since they assume normal reflections from the facets.

The Hagfors Model is better known for its planetary radar applications [e.g., Tyler et al., 1992]:

$$\sigma^0 = \frac{C\rho}{2} \left(\cos^4 \theta + C \sin^2 \theta \right)^{-3/2}$$

where

$C^{-1/2}$ = rms slopes (in radians)

Bragg models are based on Bragg resonance (e.g., X-ray crystallography). These models assume that h and l are smaller than λ, yielding diffuse scattering. Better known Bragg-type models include the Small Perturbation Model and the Muhleman Model. In general, these models are most

useful for large θ and rougher surfaces, including ocean and geologic surfaces; no cross-polarization is predicted for first-order Bragg models. As an example of a Small Perturbation Model (SPM),

$$\sigma_{pp}^0 = 8k^4 h^2 \cos^4 \theta \left| \alpha_{pp} \right|^2 W(2k \sin \theta)$$

where

pp = hh or vv polarization

$k = \lambda / 2\pi$

$$\alpha_{hh} = \frac{\varepsilon - 1}{\left(\cos \theta + \sqrt{\varepsilon - \sin^2 \theta} \right)^2}$$

$$\alpha_{vv} = \frac{(\varepsilon - 1)(\varepsilon + \varepsilon \sin^2 \theta - \sin^2 \theta)}{\left(\varepsilon \cos \theta + \sqrt{\varepsilon - \sin^2 \theta} \right)^2}$$

and W is the power spectrum evaluated at $2k \sin \theta$ *only* (i.e., the SPM selects only a single scale of roughness, dependent on λ and θ). Note that the ratio of σ_{vv}^0 and σ_{hh}^0 has no roughness dependence and is dependent only on ε and θ. Note also that for realistic values of ε and θ, σ_{vv}^0 is always larger than σ_{hh}^0.

Assuming a Gaussian form for the autocorrelation function of the surface, we can reduce W to a function of l [Ulaby et al., 1982]:

$$W(2k \sin \theta) = \left(l^2 / 2 \right) e^{-(kl \sin \theta)}$$

The Muhleman Model is an empirical model based on the Bragg model, used in planetary radar studies [e.g., Tyler et al., 1992]:

$$\sigma^0 = \frac{\beta \cos \theta}{(\sin \theta + \alpha \cos \theta)^3}$$

α and β are empirical constants, set to 0.111 and 0.0118, respectively, for Magellan SAR data processing (see Chapter 2).

A third type of model seeks to combine the facet and Bragg models; this is the two-scale model, which assumes that a surface can be decomposed into smooth, large-scale facets with small-scale roughness superimposed.

With the development of calibrated radar sensors [van Zyl, 1990] and accurate measurements of centimeter-scale surface roughness [Wall et al., 1991], inversions of some of the models given above have been attempted and validated. Van Zyl et al. [1991] inverted the SPM with three-wavelength (68-, 24-, and 5.5-cm) AIRSAR data to obtain power spectra of lava flow surfaces in the Mojave Desert. They found that varying both λ and θ determined points along the W vs.

54

2k sin θ power spectrum. Varying λ from 68 to 5.5 cm at constant θ (the AIRSAR case) spans a much larger range of 2k sin θ than does varying θ from typical values of 15 to 50 deg with constant λ (the Magellan SAR case). However, since most natural surfaces seem to have similar power spectrum slopes [Farr, 1992], the single-λ case may still provide significant information on the power spectrum offset (Table 5-1) [Farr, 1992]. It is evident that more work needs to be done on the variability and significance of power spectrum slope.

Table 5-1. Measures of roughness and σ⁰ for natural surfaces at Pisgah Lava Field[a]

Parameter	Surface		
	Aa	Pahoehoe	Playa
Above (+) or below (−) Rayleigh criterion at			
θ = 25 deg[b]	+	+	−
θ = 45 deg[b]	+	+	−
RMS height at 1-cm spacing, cm	39.8	2.97	0.83
Correlation length, cm	110	102	35.6
Power spectrum			
Slope	−1.95	−2.57	−2.34
Offset	−0.55	−2.06	−2.71
σ⁰ (25 deg, 5.4 cm, HH), dB	−5.8	−8.5	−11.5
σ⁰ (45 deg, 5.4 cm, HH), dB	−6.9	−12.5	−16.5
σ⁰ (25 deg, 25 cm, HH), dB	−5.9	−14.0	−20.0
σ⁰ (45 deg, 25 cm, HH), dB	−7.9	−18.0	−23.0

[a]From Arvidson et al., 1993.
[b]Rayleigh criterion for λ = 12 cm, θ = 25 deg: 1.6 cm;
Rayleigh criterion for λ = 12 cm, θ = 45 deg: 2.1 cm.

Dielectric Constant (ε)

Dielectric constant is a measure of how well electromagnetic waves couple with a material. The relative dielectric constant, ε, has a real part, ε', which is the permittivity of the material, and an imaginary part, ε", called the loss factor. Metals have a very high dielectric constant, approaching infinity for conducting materials. A vacuum has a dielectric constant of 1.0. Most other natural materials have real dielectric constants between 2 and 10 and very small imaginary dielectric constants, between 0.01 and 0.1 [Carmichael, 1982; Ulaby et al., 1982, p. 2081; Ulaby et al., 1990]. Water with dissolved ions, because of its

polarizability, has a dielectric constant much higher, around 80, producing significant effects in radar images of wet areas.

Except for the effect of moisture, the effect of dielectric constant variations on radar images is of secondary importance to surface roughness variations. This is because most natural rocks and soils have dielectric constants that occupy a narrow range of values.

Dielectric constant determines the strength of the Fresnel reflection coefficient in the various scattering models discussed above, and therefore must be understood if quantitative models of radar backscatter are to be constructed. Factors important in the Venusian environment that will affect the dielectric constant are the density of a material and the presence of metals. An empirical relationship has been developed between density, r, and dielectric constant. Ulaby et al. [1990] found that ε ≅ 1.96^r for a variety of terrestrial rocks.

It has been well established that the highlands of Venus exhibit strong backscatter in radar images and low emissivity in passive radiometer data—characteristics of high dielectric constant material [Pettengill et al., 1988]. Most models at this time favor the presence, either as inclusions or weathering products, of free metals or metallic compounds [Klose et al., 1992]. Since liquid water is not stable on Venus' surface, metals are the only known material that could produce the inferred high dielectric constants.

The loss factor, ε", determines the strength of absorption of radar waves by the material. For most materials, this factor decreases with wavelength. Dry, well-sorted granular materials are those most easily penetrated by radar waves—to a depth of several wavelengths [Elachi et al., 1984; Farr et al., 1986; Schaber et al., 1986]. On Venus, such granular materials may make up the extended impact-crater-related parabolas [Campbell et al., 1992], wind streaks, and dunes [Greeley et al., 1992].

References

Arvidson, R. E., M. K. Shepard, E. A. Guinness, S. B. Petroy, J. J. Plaut, D. L. Evans, T. G. Farr, R. Greeley, N. Lancaster, and L. R. Gaddis, 1993, "Characterization of lava-flow degradation in the Pisgah and Cima volcanic fields, California, using Landsat Thematic Mapper and AIRSAR data," Geol. Soc. Amer. Bull., v. 105, p. 175–188.

Bendat, J. S., and A. G. Piersol, 1986, Random Data, Analysis and Measurement Procedures, 2nd ed., New York: John Wiley and Sons, 566 pp.

Berry, M. V., and J. H. Hannay, 1978, "Topography of random surfaces, comment and reply," Nature, v. 273, p. 573.

Brown, S. R., 1985, "A note on the description of surface roughness using fractal dimension," *Geophys. Res. Lett.*, v. 14, p. 1095–1098.

Brown, S. R., and C. H. Scholz, 1985, "Broad bandwidth study of the topography of natural rock surfaces," *J. Geophys. Res.*, v. 90, p. 12575–12582.

Campbell, D. B., N. J. S. Stacy, W. I. Newman, R. E. Arvidson, E. M. Jones, G. S. Musser, A. Y. Roper, and C. Schaller, 1992, "Magellan observations of extended impact crater related features on the surface of Venus," *J. Geophys. Res.*, v. 97, p. 16,249–16,277.

Carmichael, R. S., 1982, *Handbook of Physical Properties of Rocks, Volume 1*, Florida: CRC Press, 404 pp.

Elachi, C., L. E. Roth, and G. G. Schaber, 1984, "Spaceborne radar subsurface imaging in hyperarid regions," *IEEE Trans. Geosci. Rem. Sens.*, v. GE-22, p. 383–388.

Elachi, C., 1988, *Spaceborne Radar Remote Sensing: Applications and Techniques*, New York: IEEE Press, 254 pp.

Evans, D. L., T. G. Farr, and J. J. van Zyl, 1992, "Estimates of surface roughness derived from synthetic aperture radar (SAR) data," *IEEE Trans. Geosci. Rem. Sens.*, v. 30, p. 382–389.

Farr, T. G., C. Elachi, Ph. Hartl, and K. Chowdhury, 1986, "Microwave penetration and attenuation in desert soil: A field experiment with the Shuttle Imaging Radar," *IEEE Trans. Geosci. Rem. Sens.*, v. GE-24, p. 590–594.

Farr, T. G., 1992, "Microtopographic evolution of lava flows at Cima volcanic field, Mojave Desert, California," *J. Geophys. Res.*, v. 97, p. 15171–15179.

Ford, J. P., et al., 1989, *Spaceborne Radar Observations: A Guide for Magellan Radar-Image Analysis*, Publication 89-41, Jet Propulsion Laboratory, Pasadena, California, 126 p.

Fung, A. K., and G. W. Pan, 1987, "A scattering model for perfectly conducting random surfaces: I. Model development," *Int. J. Remote Sens.*, v. 8, p. 1579–1593.

Greeley, R., R. E. Arvidson, C. Elachi, M. A. Geringer, J. J. Plaut, R. S. Saunders, G. Schubert, E. R. Stofan, E. J. P. Thouvenot, S. D. Wall, and C. M. Weitz, 1992, "Aeolian features on Venus: Preliminary Magellan results," *J. Geophys. Res.*, v. 97, p. 13,319–13,345.

Huang, J., and D. L. Turcotte, 1989, "Fractal mapping of digitized images: Application to the topography of Arizona and comparisons with synthetic images," *J. Geophys. Res.*, v. 94, p. 7491–7495.

Kim, Y., E. Rodríguez, and S. L. Durden, 1992, "A numerical assessment of rough surface scattering theories: Vertical polarization," *Radio Sci.*, v. 27, p. 515–527.

Klose, K. B., J. A. Wood, and A. Hashimoto, 1992, "Mineral equilibria and the high radar reflectivity of Venus mountaintops," *J. Geophys. Res.*, v. 97, p. 16,353–16,369.

Peake, W. H., and T. L. Oliver, 1971, *The Response of Terrestrial Surfaces at Microwave Frequencies*, Columbus, Ohio: Ohio State University, Electroscience Laboratory, 2440-7, Technical Report AFAL-TR-70-301.

Pettengill, G. H., P. G. Ford, and G. D. Chapman, 1988, "Venus: Surface electromagnetic properties," *J. Geophys. Res.*, v. 93, p. 14,881–14,892.

Rodríguez, E., and Y. Kim, 1992, "A unified perturbation expansion for surface scattering," *Radio Sci.*, v. 27, p. 79–93.

Rodríguez, E., Y. Kim, and S. L. Durden, 1992, "A numerical assessment of rough surface scattering theories: Horizontal polarization," *Radio Sci.*, v. 27, p. 497–513.

Schaber, G. G., G. L. Berlin, and W. E. Brown, 1976, "Variations in surface roughness within Death Valley, California: geologic evaluation of 25-cm-wavelength radar images," *Geol. Soc. Am. Bull.*, v. 87, p. 29–41.

Schaber, G. G., J. F. McCauley, C. S. Breed, and G. R. Olhoeft, 1986, "Shuttle imaging radar: Physical controls on signal penetration and subsurface scattering in the eastern Sahara," *IEEE Trans. Geosci. Rem. Sens.*, v. GE-24, p. 603–623.

Tyler, G. L., R. A. Simpson, M. J. Maurer, and E. Holmann, 1992, "Scattering properties of the Venusian surface: Preliminary results from Magellan," *J. Geophys. Res.*, v. 97, p. 13,115–13,139.

Ulaby, F. T., R. K. Moore, and A. K. Fung, 1982, *Microwave Remote Sensing, Volumes 1, 2*, and *3*, Massachusetts: Addison-Wesley, 2162 pp.

Ulaby, F. T., T. H. Bengal, M. C. Dobson, J. R. East, J. B. Garvin, D. L. Evans, 1990, "Microwave dielectric properties of dry rocks," *IEEE Trans. Geosci. Rem. Sens.*, v. 28, p. 325–336.

van Zyl, J. J., 1990, "A technique to calibrate polarimetric radar images using only image parameters and trihedral corner reflectors," *IEEE Trans. Geosci. Rem. Sens.*, v. GE-28, p. 337–348.

van Zyl, J. J., C. F. Burnette, and T. G. Farr, 1991, "Inference of surface power spectra from inversion of multifrequency polarimetric radar data," *Geophys. Res. Lett.*, v. 18, p. 1787–1790.

Wall, S. D., T. G. Farr, J.-P. Muller, P. Lewis, and F. W. Leberl, 1991, "Measurement of surface microtopography," *Photogramm. Eng. Rem. Sens.*, v. 57, p. 1075–1078.

Chapter 6. Surface Modification Processes

Catherine M. Weitz

Introduction

Wind-related features provide direct evidence for the interaction of an atmosphere with a surface, and the dominant process currently affecting the surface of Venus appears to be wind. At least four kinds of eolian features have been identified on Venus: wind streaks, dunes, yardangs, and extended crater deposits [Greeley et al., 1992; Arvidson et al., 1991]. The orientation of these features provides clues to the wind direction at the time of their formation. In addition to eolian activity, there is evidence for degradation of lava flows on the plains. Arvidson et al. [1992] found that young volcanic flows in Sedna Planitia have higher backscatter cross-sections than older flows. Volcanoes and tessera units at high elevations generally have high backscatter cross sections, high reflectivity, and low emissivity values. There is a strong possibility that at these high elevations a chemical reaction causes the minerals in the rocks and soils to weather to materials with higher dielectric constants [Pettengill et al., 1988; Klose et al., 1992]. Finally, mass movements, including rock slumps, rock and/or block slides, rock avalanches, debris avalanches, and possibly debris flows have been identified on Venus [Malin et al., 1992].

Eolian Features

Large areas on Earth and Mars are covered by eolian features [Cutts and Smith, 1973; Breed et al., 1979]; these features were predicted for Venus [Greeley et al., 1984; Saunders et al., 1990]. Images of the surface and measurements of near-surface winds made by the Russian Venera landers suggest local modification of the surface by wind.

The Venera 9 and 10 landers measured wind velocities between 0.5 and 1.0 m/s at 1 m above the Venusian surface [Florensky et al., 1977]; these speeds are believed to be capable of transporting particles on the surface.

Wind Streaks

Most wind streaks on Earth and Mars are associated with topographic obstacles, and the streaks form in response to turbulence around the obstacles. Wind streaks on Earth are visible in radar images typically when roughness differences (such as those between bedrock and sediment) result in contrasts in the backscatter cross sections [Greeley et al., 1989; Saunders et al., 1990]. Wind streaks occur in several forms and in a variety of settings on Earth. Field observations of a wind streak at the Amboy lava flow in California indicate that the streak is dark at visible wavelengths because the basalt surfaces are swept free of sand. In radar images, the streak appears bright because the basalt surface has no mantling of sand to smooth the surface [Greeley et al., 1989; Saunders et al., 1990]. In Seasat and Shuttle radar images, streaks are usually visible where deposits of windblown sand appear radar dark against the surrounding radar-bright exposures of rougher alluvium or bedrock [Greeley et al., 1983 and 1989; Saunders et al., 1990]. Similarly, most wind streaks seen in Magellan images are visible because of differences in roughness between the streak and the surrounding terrain [Greeley et al., 1992]. The majority of streaks on Venus appear to be associated with impact craters, suggesting that the streaks represent debris produced during the impact and later modified by surface winds.

Wind streaks on Venus can be classified by their radar appearance and plan-view shape; five different shapes are

identified: fan, linear, transverse-ragged, transverse-smooth, and wispy [Greeley et al., 1992]. The *fan* streaks shown in Figure 6-1 are radar bright, but several have radar-dark halos. These halos could represent accumulation of debris around the edge of the erosional core. The orientation of the fan streaks indicates a wind from the north. The rougher, heavily fractured underlying terrain appears bright on the image compared to the adjacent smooth terrain. Because the underlying fractured terrain is visible only in the streaks, the streaks are probably areas of nondeposition or scouring.

Linear streaks are typically more than 20 times longer than their widths and generally occur in sets. Dozens of radar-dark and radar-bright streaks are visible in Figure 6-2. In this image, it is difficult to determine whether these are dark streaks on a bright background or bright streaks on a dark background, which also makes determination of wind direction difficult. However, several radar-bright fan streaks associated with small volcanic domes to the south of the linear streaks indicate a wind flow from the northwest. The linear streaks are located near Mead, the largest impact crater on Venus (see Chapter 7).

Transverse streaks form downwind of topographic barriers; these barriers, such as fractures, ridges, and hills, are perpendicular to the wind direction. Examples of *transverse-ragged* streaks are illustrated in Figure 6-3. These radar-dark streaks occur on radar-dark lava flows and indicate a wind flow from the southeast. "Ragged" refers to the serrated margin on the downwind side of the streak sets. The streaks are depositional in character because they obscure the underlying terrain, and their low backscatter indicates a composition of fine material that has smoothed the underlying terrain. Figure 6-4 shows transverse-ragged radar-dark streaks associated with tessera terrain in northwestern Aphrodite Terra. The region slopes to the west, yet the wind streaks indicate a wind from the west; thus, the streaks indicate a wind flowing upslope. The source of the debris composing the streaks may be the tessera terrain, which appears heavily fractured in this region.

A *transverse-smooth* streak is shown in Figure 6-5. The radar-bright streak has formed on the downwind (south) side of a hill. "Smooth" refers to the downwind margin of the streak. The streak obscures the underlying terrain and is brighter than the surrounding terrain, which suggest that the streak covers the surrounding terrain with rougher material.

Wispy streaks are probably composed of fine debris because they are always radar dark. They consist of wavy, meandering patterns usually associated with ridges and impact craters. It is often difficult to determine the source of the streak and the wind direction because of this meandering

character. In Figure 6-6, however, the wispy streaks clearly originate from a dark splotch (Chapter 7) that is probably debris from an object that was pulverized as it traveled through the dense Venusian atmosphere [Schaber et al., 1992; Schultz, 1992]. Because the origin of the streaks is clear, a wind from the northeast can be inferred.

Dunes

Dunes on Earth result from the accumulation of saltated particles. Radar echoes from sand dunes are highly directional and sensitive to the imaging geometry of the radar system. Studies of look-angle effects of terrestrial dunes in airborne, Seasat, and shuttle radar images indicate that dunes are bright in small-look-angle radar images because of quasi-specular reflections from smooth dune faces that are near normal to the radar beam (i.e., the local incidence angle at the dune face is zero) [Blom and Elachi, 1981 and 1987]. Strong radar backscatter from dune slip faces is possible only at look angles less than the angle of repose for windblown sand, which is 33 deg on Earth. At look angles > 33 deg, radar scattering from terrestrial dune faces is not returned to the antenna, and a black image tone appears in the radar images [Blom and Elachi, 1981 and 1987].

Two possible dune fields have been identified on Venus [Weitz et al., 1992; Greeley et al., 1992]. The first, centered at 25°S, 340°E, is located in an outflow deposit about 100 km north of the 65-km-diameter impact crater Aglaonice (Figure 6-7). It appears that the wind has reworked the outflow deposits to form wind streaks and dunes. The dunes range in length from 0.5 to 5 km and the nearby wind streaks indicate a westward wind flow, with the dunes oriented transverse to the wind. The radar look angle at this latitude is approximately 35 deg, so assuming a similar slope geometry for Venusian dunes, the dune slip faces may be oriented nearly perpendicular to the radar illumination, producing quasi-specular reflections as on Earth.

The Fortuna-Meshkenet dune field (Figure 6-8) is in a valley between Ishtar Terra and Meshkenet Tessera. Approximately 40 radar-bright fan streaks occur within the field. The wind streaks indicate that the dunes are oriented transverse to a prevailing wind from the east-southeast. The streaks appear to originate from small, radar-bright cones (Figure 6-9) and probably consist of the same high radar reflectivity material as the cones. The Cycle 1 image (Figure 6-8) and the Cycle 2 image (Figure 6-10) were both obtained at a 25-deg look angle, but from opposite sides. There appears to be no movement of the dunes or streaks between the Cycle 1 and 2 images. Because the illumination directions are opposite and because there are dune faces in the southern
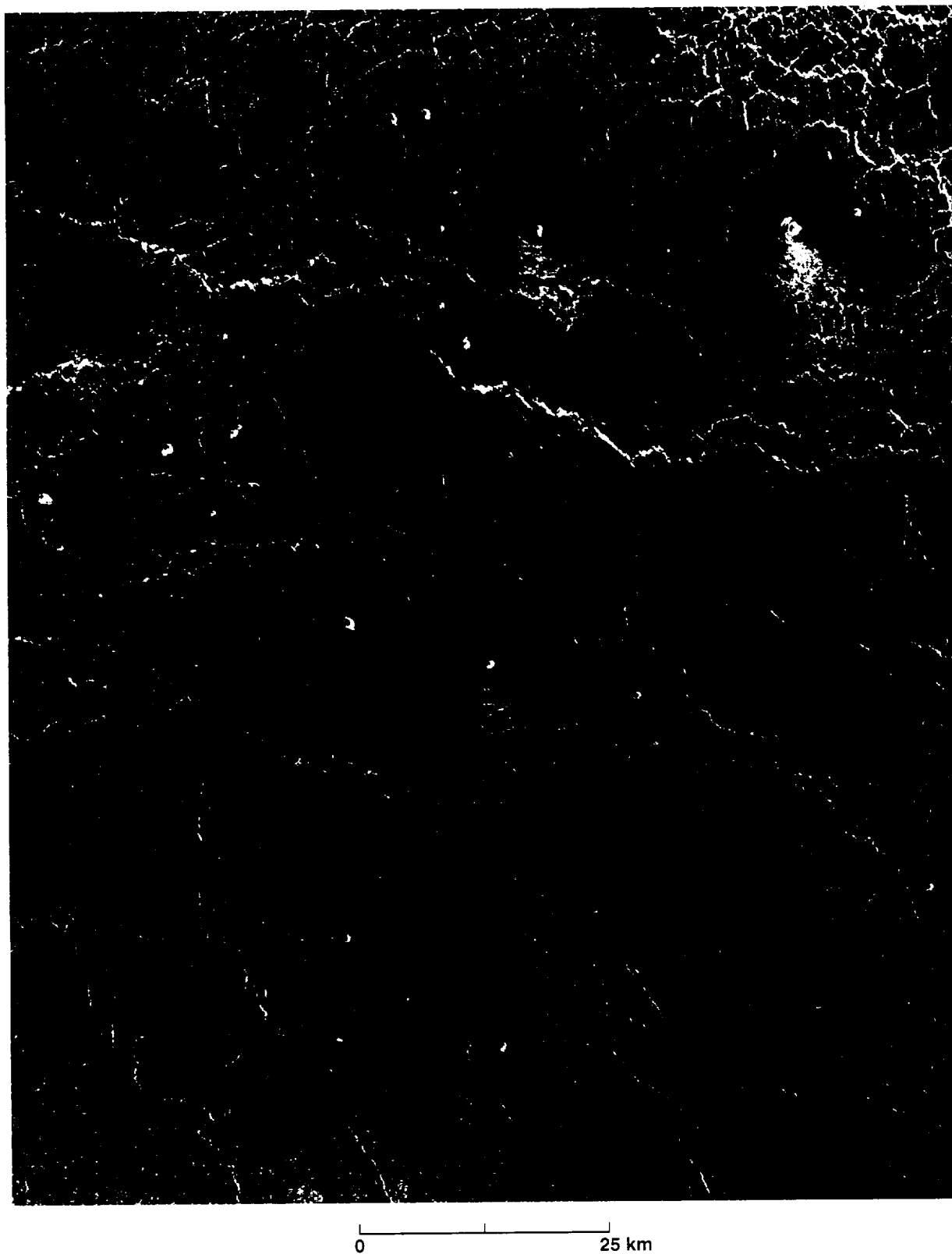
0   25 km

Figure 6-1. Radar-bright fan streaks, some of which have a radar-dark halo. The streaks probably represent zones of scouring or nondeposition. The wind streaks indicate a southward wind flow. Radar illumination is from the left at an incidence angle of 44 deg.
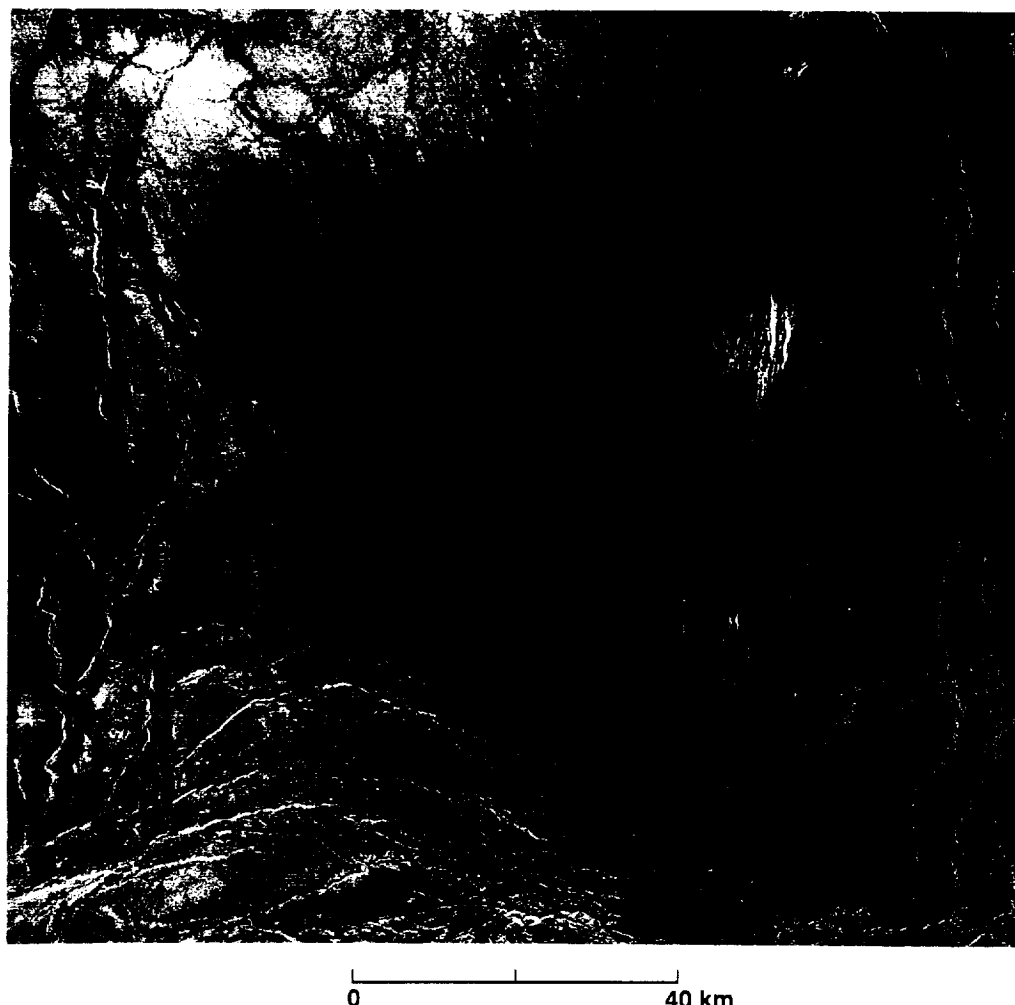
Figure 6-2. Linear radar-bright and -dark wind streaks centered at 15°N, 60.43°E. It is difficult to determine if the streaks represent radar-bright streaks on a dark background or radar-dark streaks on a bright background. Some radar-bright fan streaks near the bottom of the image indicate a wind direction from the northwest. Radar illumination is from the left at an incidence angle of 46 deg.

part of the dune field that are parallel to the radar illumination, there must be other scattering effects, such as a change in roughness or dielectric constant, to account for the high back-scatter for these features in both images.

Yardangs

Yardangs are streamlined hills oriented parallel to the prevailing winds and produced by wind erosion of rock or soft sediments. They are visible in radar images because of their linear shape, sharp boundaries, and topographic relief. Some possible yardangs have been identified in one location on Venus, centered at 9°N, 60.5°E [Greeley et al., 1992]. The yardangs shown in Figure 6-11 are sets of slightly sinuous, parallel ridges and grooves. The features are believed to be yardangs rather than wind streaks because they have well-defined boundaries and they do not originate from topographic features. The yardangs occur in two sets with both sets indicating a wind from the northeast. Because the yardangs are about 300 km southeast of the crater Mead, they are interpreted as deposits from the formation of Mead that have been eroded by later winds.

Crater Extended Deposits

Large radar-dark parabolic deposits associated with impact craters seem unique to Venus. These features are also related to eolian activity [Arvidson et al., 1991; Campbell et al., 1992] (Figure 6-12). The majority of the 57 parabolic-shaped features identified by Campbell et al. [1992] on data
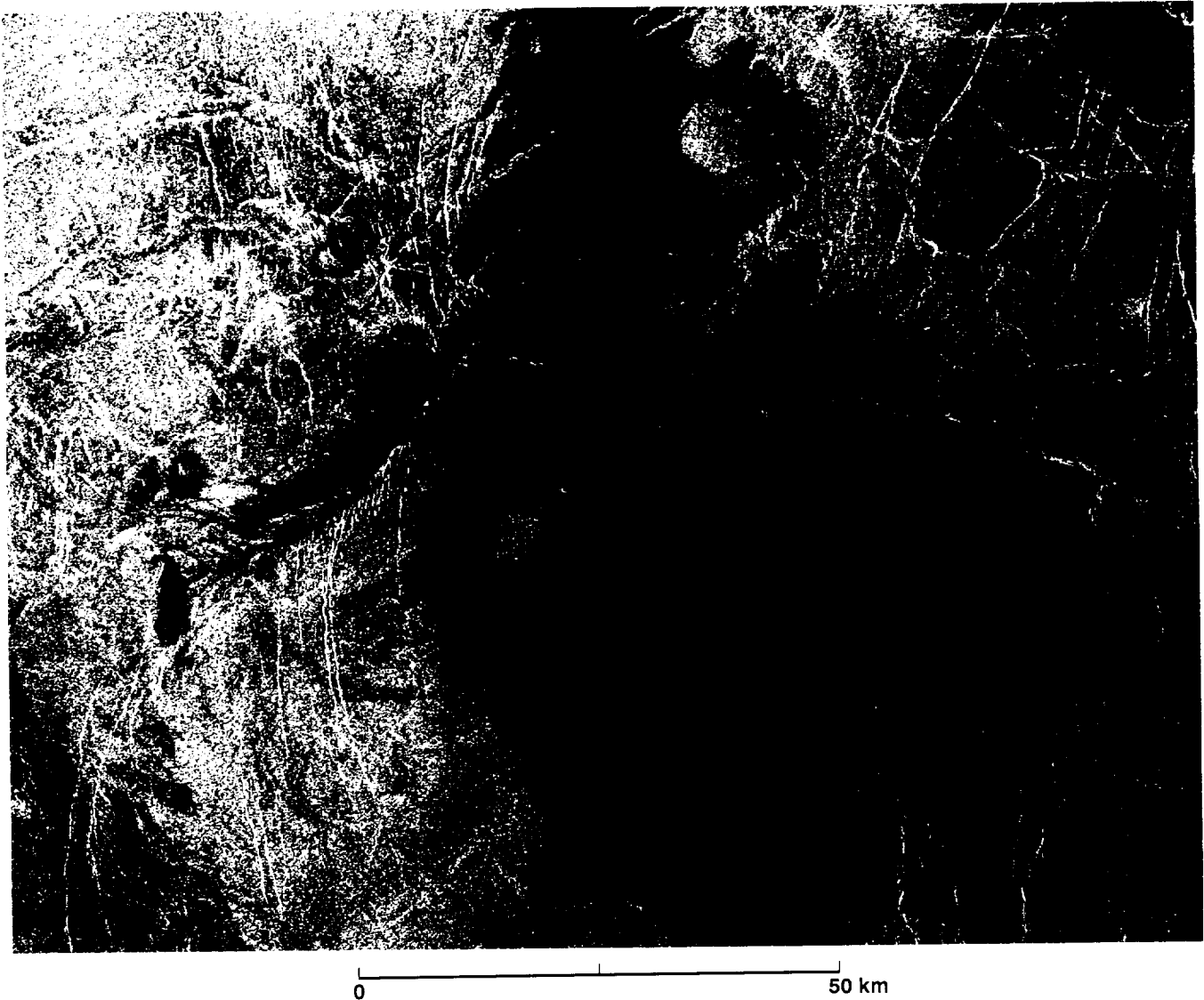
Figure 6-3. Radar-dark transverse-ragged streaks on radar-dark lava flows. The streaks are composed of fine debris and indicate a wind direction from the southeast. Radar illumination is from the left at an incidence angle of 45 deg.

covering 92% of the surface are oriented east–west with the apex at the east end and the impact crater located west of the apex. Nine extended circular features associated with impact craters were also identified. Many parabolic features also have signatures in the emissivity and reflectivity data; lower emissivities and higher reflectivities imply higher dielectric constants [Plaut and Arvidson, 1992]. The parabolic deposits are believed to represent some of the youngest stratigraphic features on Venus. These deposits are apparently fine ejecta lofted to high altitudes where strong prevailing zonal east-to-west winds carry the particles many hundreds of kilometers

before deposition [Campbell et al., 1992]. Because the material is fine, it has lower backscatter than the rougher surrounding terrain it mantles. Wind streaks are often associated with the parabolic features [Schultz, 1992].

Surficial Modification of Lava Flows

Backscatter signatures of the lava flows of different ages in Sedna Planitia were studied by Arvidson et al. [1992] to determine the degradation of lava flows with time. Young flows were found to have backscatter values similar to those
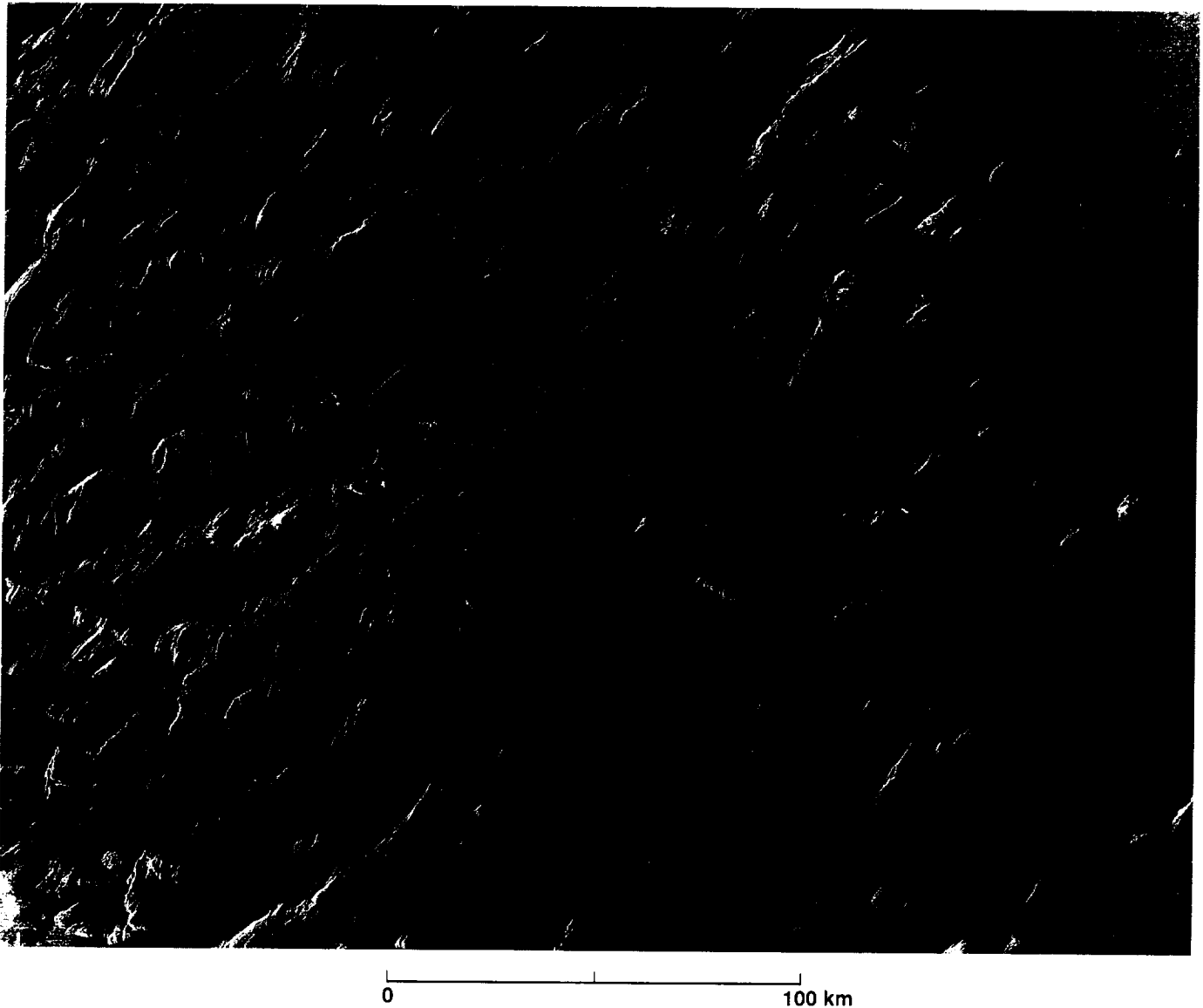
Figure 6-4. Radar-dark transverse-ragged streaks in Ovda Regio indicate that the wind is flowing upslope from the west to the east. The streaks may represent debris eroded from the tesserae. Radar illumination is from the left at an incidence angle of 46 deg.

of fresh terrestrial basalt flows. Older flows have backscatter signatures similar to those of degraded terrestrial basalt flows. Arvidson et al. concluded that in situ mechanical and chemical weathering were the dominant mechanisms that degraded the Venusian plains. Mechanical weathering would tend to fill any depressions in the lava flows with debris and rubble. Once the depressions were filled, the smoother surface would yield decreased backscatter cross-sections for these older flows. Chemical weathering would cause volume changes that would also smooth the surface and decrease backscatter.

Surficial Modification at High Elevations

Analyses of Pioneer Venus radar images revealed that the highest mountain peaks have very high backscatter cross sections and reflectivities [Pettengill et al., 1988; Garvin et al., 1985]. Magellan data also show strong correlations between high elevation, high backscatter cross section, high reflectivity, and low emissivity. Figure 6-13 shows central and northern parts of Ovda Regio. The complex structures indicate several tectonic events over a long history. The youngest event is the flooding of low-lying basins by smooth

Figure 6-5. Transverse-smooth streak located at 26.2°N, 331.4°E. The radar-bright streak, which may represent a deposit of rough material, indicates a wind from the northeast. Radar illumination is from the left at an incidence angle of 43 deg.

(radar-dark) lava flows; the ridges and fractures are rougher and consequently appear brighter. The brightest terrain in the image is at the highest elevations.

The most likely explanation for the very high backscatter cross sections at high elevations is chemical alteration [Pettengill et al., 1988; Klose et al., 1992]. Klose et al. [1992] studied the relationship between altitude and emissivity for different highland regions and noted that above a critical altitude emissivity undergoes an abrupt and steep decrease that must denote a difference in surface mineralogy between the elevations. This suggests that the material at the higher elevations has been weathered to material with bulk dielectric constants higher than those of the surface material at the lower elevations, because the higher bulk dielectric constant causes a stronger radar return. The mineral most

likely responsible for the low emissivities on mountaintops appears to be the electrical semiconductor pyrite (FeS_2) [Pettengill et al., 1988; Klose et al., 1992].

One exception to this behavior is Maat Mons, a volcano high enough to produce a low emissivity zone near its summit. The lack of a low emissivity zone may mean that volcanic activity at Maat Mons is relatively recent, and the volcanic rocks at the highest altitudes have not had time to weather significantly [Klose et al., 1992].

Mass Movements

Mass movements, including rock slides, rock and debris avalanches, and possible debris flows, have been identified in areas of high relief and steep slopes in the Magellan images [Malin, 1992]. Figure 6-14 shows at least three landslides along a 5.5-km-high scarp north of Dali Chasma. The landslides extend as much as 30 km from the base of the scarp. The hummocky surfaces of the landslides cause them to appear brighter than the adjacent smoother material.

Many steep-sided volcanic domes have rock slides associated with them [Guest et al., 1992; Malin, 1992]. Figure 6-15 shows a rock-slide avalanche on the eastern flank of a volcanic dome. The dome is very bright and foreshortened on the flank facing the radar, indicating that the dome is steep sided; the steep, unstable margins of the dome are the most likely cause for the collapse that formed the rock slide. The very rough, hummocky surface of the landslide is radar bright compared with the smoother, radar-dark plains surrounding it.
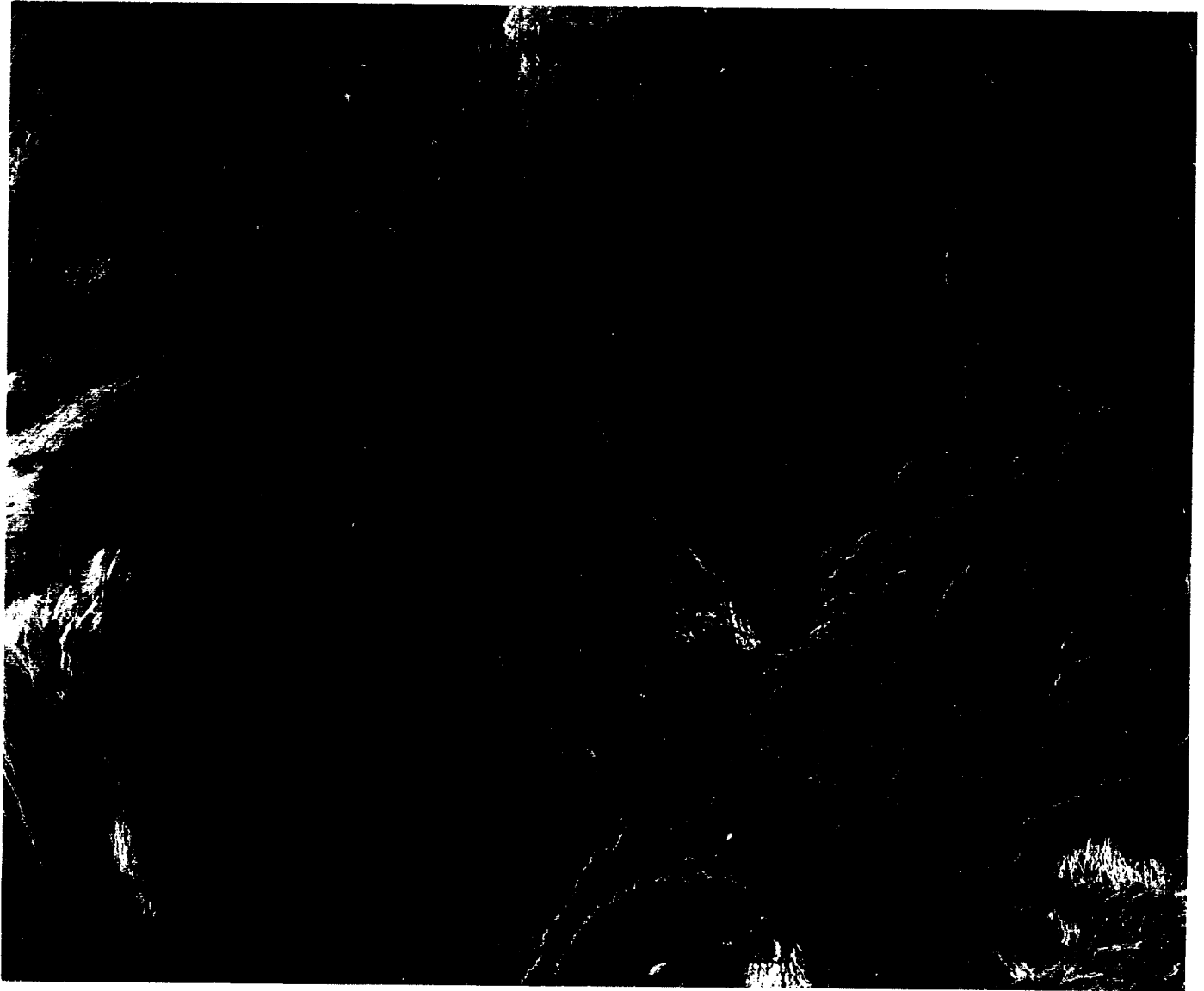
0   50 km

Figure 6-6. Wispy streaks originating from a radar-dark splotch. The streaks and the splotch represent fine debris that has mantled the underlying, rougher surface. Radar illumination is from the left at an incidence angle of 40 deg.
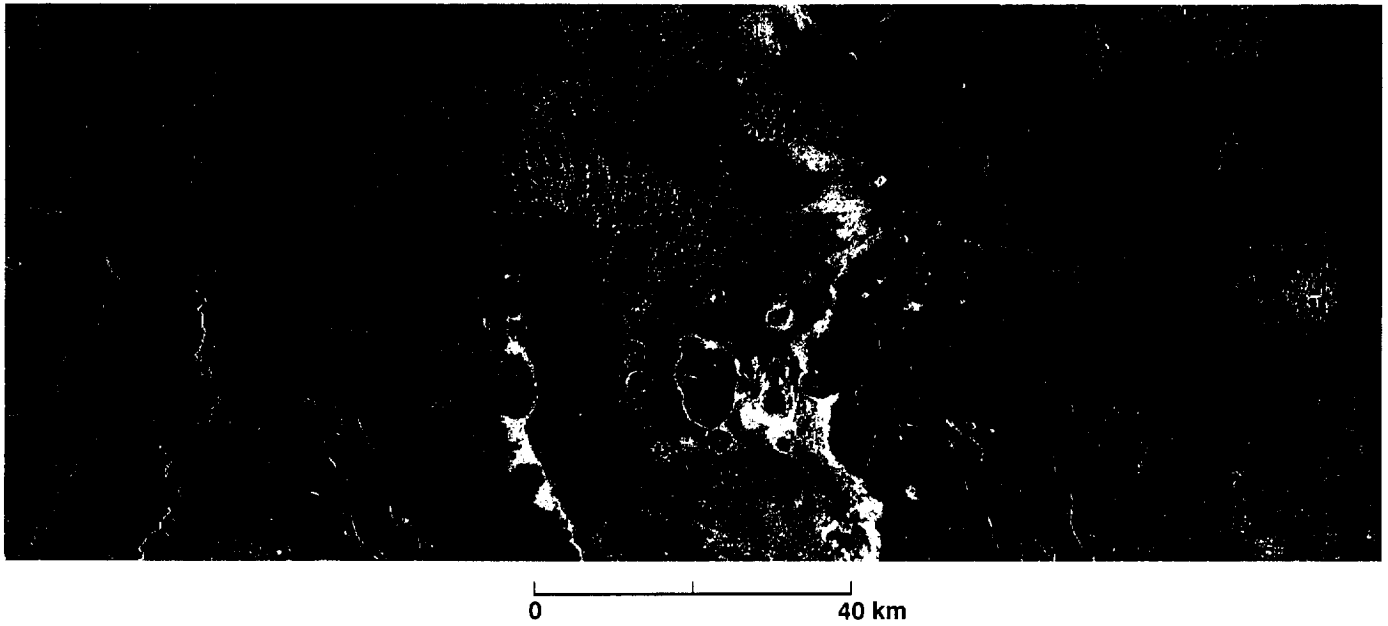
0   40 km

Figure 6-7. Radar-bright outflow deposits from the crater Aglaonice have been reworked by the wind to produce wind streaks and dunes (25°S, 339°E). The wind, which is flowing from the east to the west, has produced linear radar-bright and -dark streaks and dunes that are transverse to the streaks. The bright appearance of the dunes results from quasi-specular returns from dune faces oriented normal to the radar illumination. Radar illumination is from the left at an incidence angle of 35 deg.
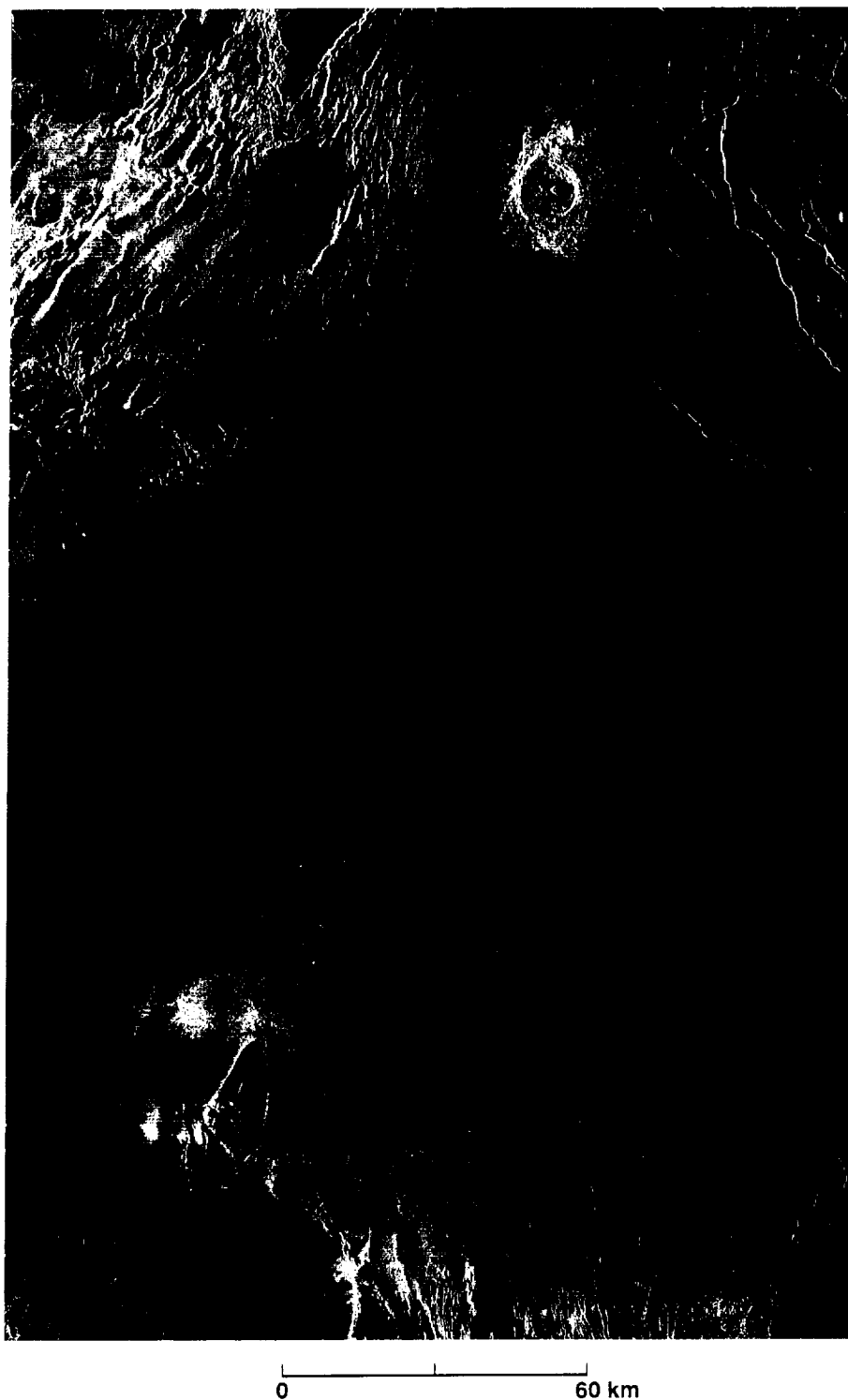
Figure 6-8. Approximately 40 radar-bright streaks are located within a dune field centered at 67.7°N, 90.5°E. The wind streaks indicate that the dunes are oriented transverse to the prevailing winds. Radar illumination is from the left at an incidence angle of 25 deg.
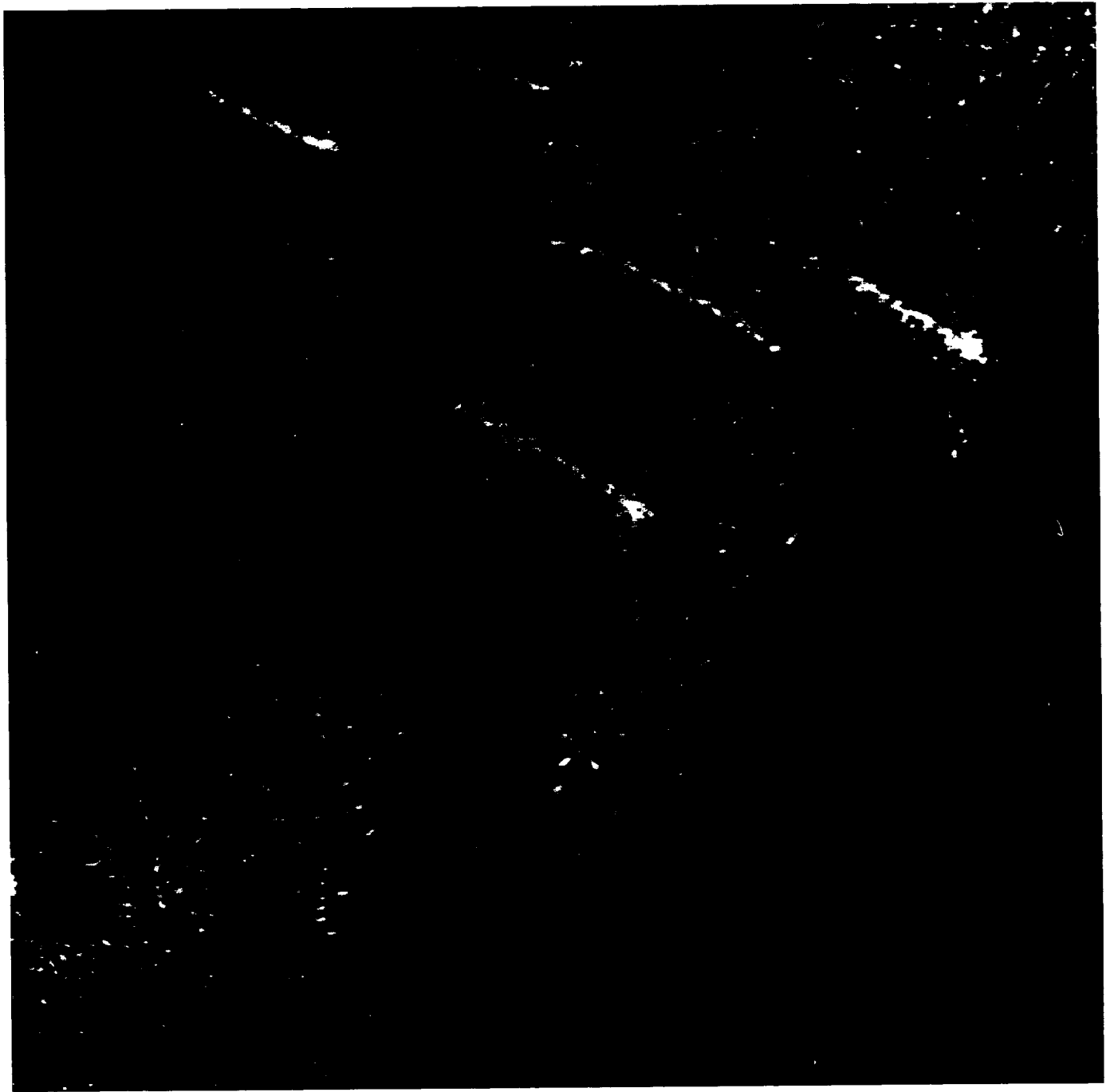
```
L_____L_____|
0                                  10 km
```

Figure 6-9. Enlargement of a center portion of Figure 6-8 showing dunes and radar-bright wind streaks. The streaks appear to originate from small volcanic domes in the dune field.

Figure 6-10. Cycle 2 right-looking image of the same area shown in Figure 6-8. There appears to have been no movement of the dunes or streaks between the two cycles. Radar illumination is from the right at an incidence angle of 25 deg.
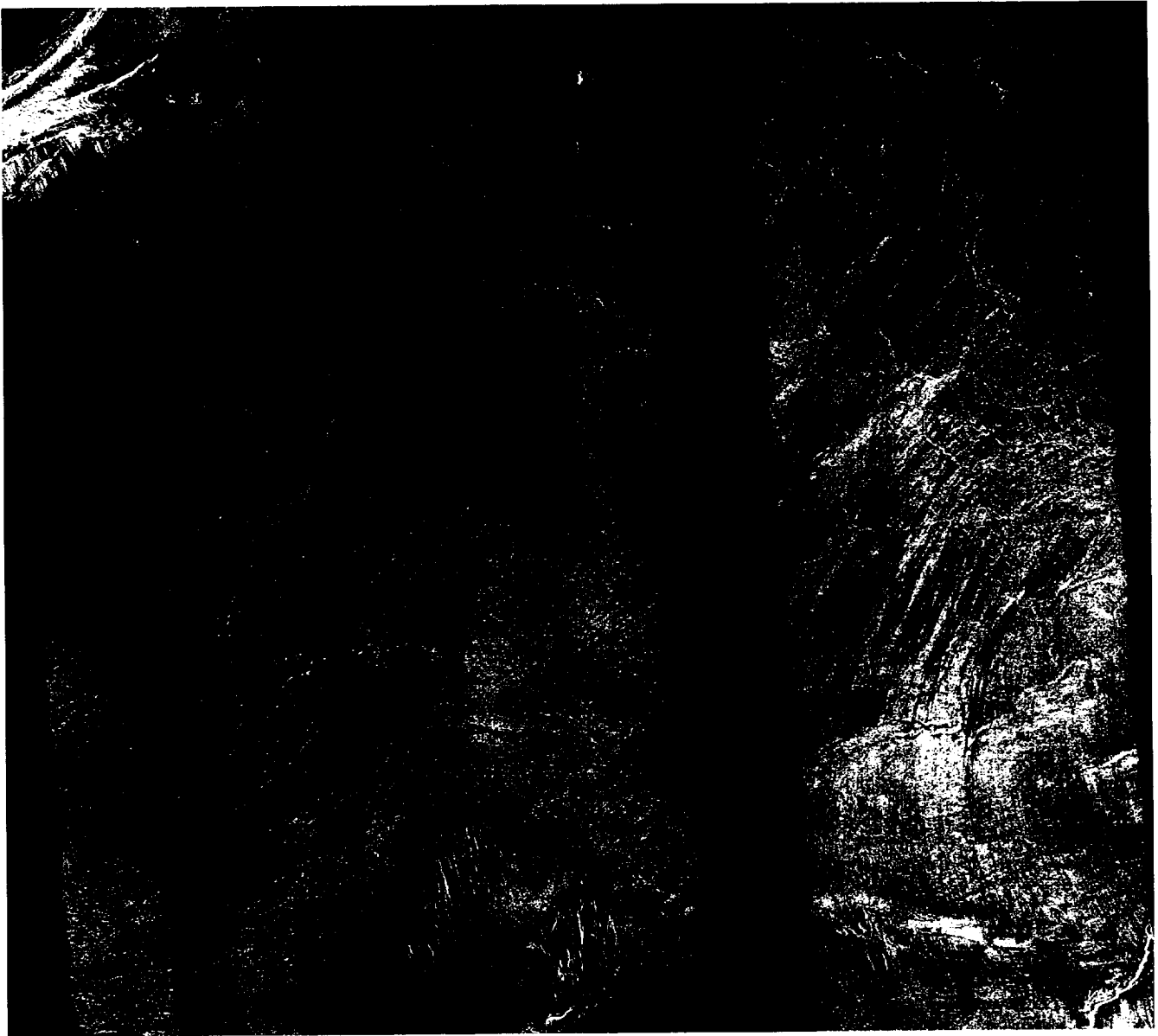
Figure 6-11. The radar-dark linear features in this figure may represent yardangs. The eroded portions of the yardangs are darker than the surrounding terrain possibly because they contain smoother deposits of debris. Radar illumination is from the left at an incidence angle of 46 deg.
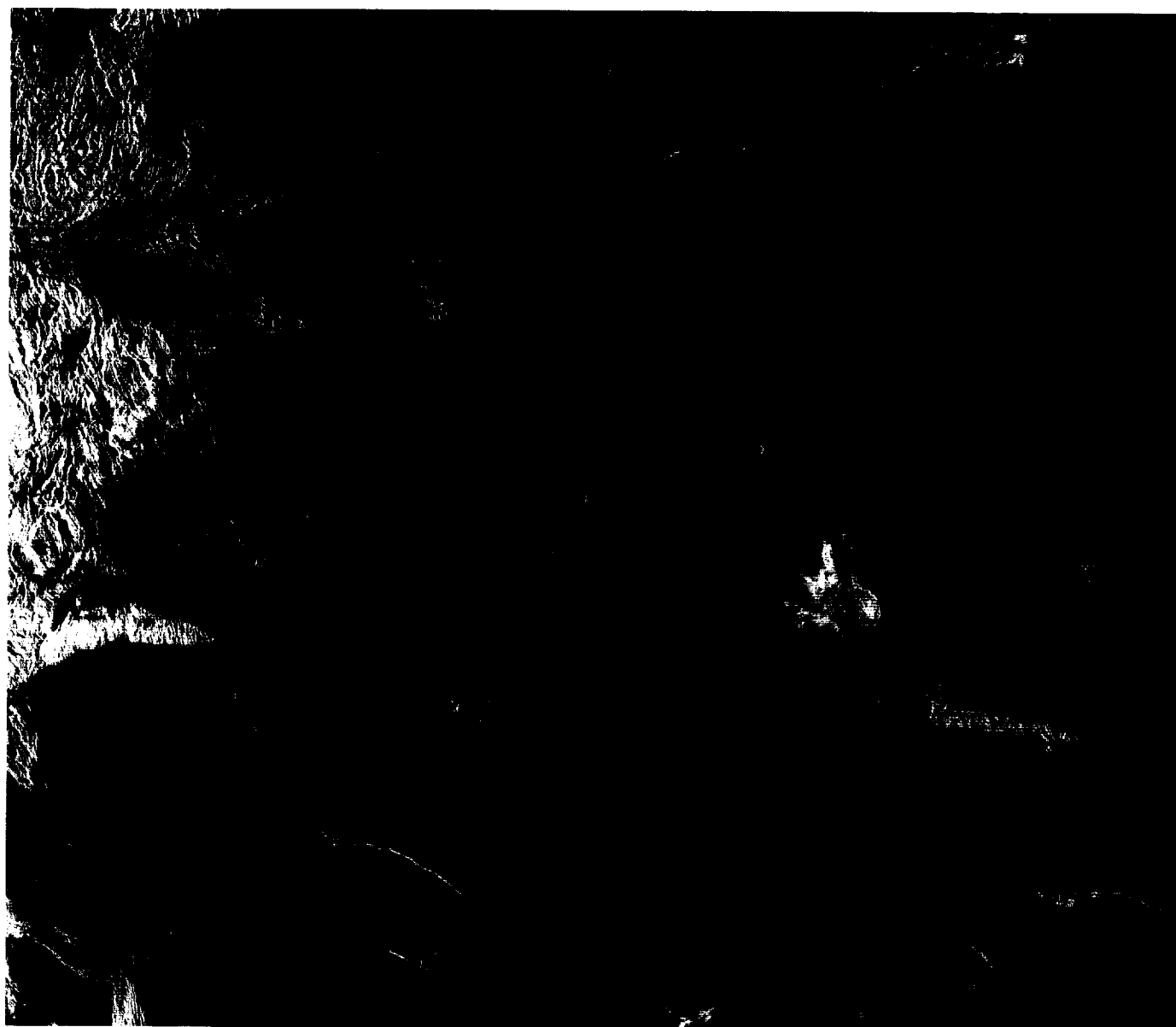
L_____L_____L
0   300 km

Figure 6-12. The crater Stuart (30.8°S, 20.5°E) has a radar-dark parabola associated with it. The crater has a radar-bright floor and low emissivity, as do many of the craters with parabolic features. The parabola extends over 1000 km to the west and it covers all the underlying terrain. Radar illumination is from the left at an incidence angle of 33 deg.
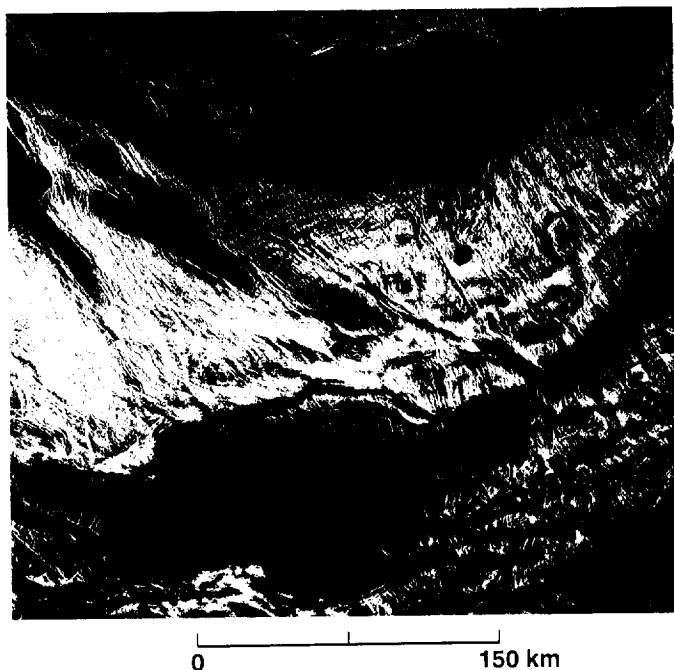
0   150 km

Figure 6-13. Chemical alteration at high elevations may cause the very high backscatter cross-sections seen in this image of Ovda Regio. The regions of high backscatter also have very high reflectivities and low emissivities. Radar illumination is from the left at an incidence angle of 45 deg.
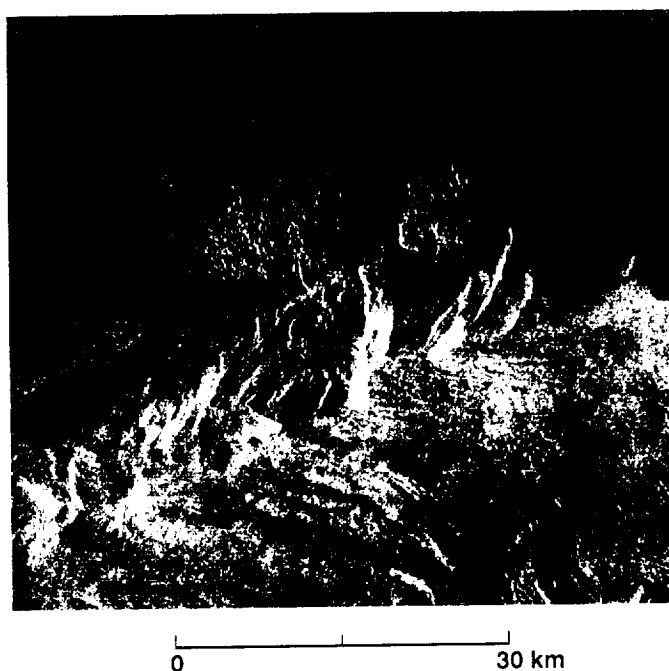

0   30 km

Figure 6-14. At least three landslides extending from a steep scarp can be identified in this figure. The lobate landslides are radar bright because they are composed of rough blocks that produce a hummocky surface and overlie the finer deposits that show a smoother, radar-dark surface. Radar illumination is from the left at an incidence angle of 41 deg.
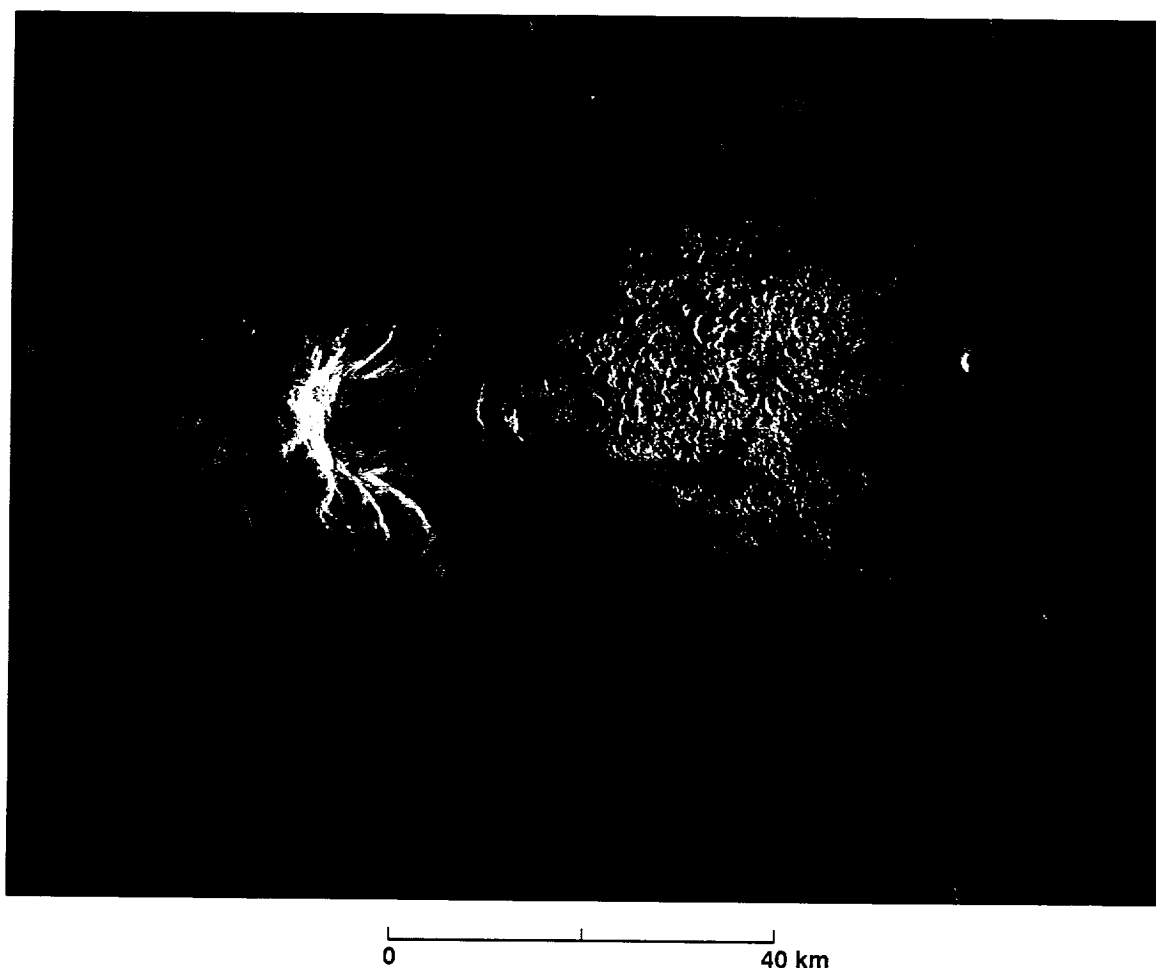
71

0   40 km

Figure 6-15. A debris apron has formed after the collapse of the eastern flank of a volcanic dome. The very rough, hummocky surface of the landslide is radar bright compared with the smoother plains surrounding it. Radar illumination is from the left at an incidence angle of 30 deg.

References

Arvidson, R. E., V. R. Baker, C. Elachi, R. S. Saunders, and J. A. Wood, 1991, "Magellan: Initial analysis of Venus surface modification," *Science*, v. 252, p. 270–276.

Arvidson, R. E., R. Greeley, M. C. Malin, R. S. Saunders, N. Izenberg, J. J. Plaut, E. R. Stofan, and M. K. Shepard, 1992, "Surface modification of Venus as inferred from Magellan observations of plains," *J. Geophys. Res.*, v. 97, p. 13,303–13,317.

Blom, R., and C. Elachi, 1981, "Spaceborne and airborne imaging radar observations of sand dunes," *J. Geophys. Res.*, v. 86, p. 3061–3073.

Blom, R., and C. Elachi, 1987, "Multifrequency and multipolarization radar scatterometry of sand dunes and comparison with spaceborne and airborne radar images," *J. Geophys. Res.*, v. 92, p. 7877–7889.

Breed, C. S., M. J. Grolier, and J. F. McCauley, 1979, "Morphology and distribution of common 'sand' dunes on Mars: Comparison with the Earth," *J. Geophys. Res.*, v. 84, p. 8183–8204.

Campbell, D. B., N. J. S. Stacy, W. I. Newman, R. E. Arvidson, E. M. Jones, G. S. Musser, A. Y. Roper, and C. Schaller, 1992, "Magellan observations of extended impact crater features on Venus," *J. Geophys. Res.*, v. 97, p. 16,249–16,277.

Cutts, J. A., and R. S. U. Smith, 1973, "Eolian deposits and dunes on Mars," *J. Geophys. Res.*, v. 78, p. 4139–4154.

Florensky, K. P., L. B. Ronca, A. T. Basilevsky, G. A. Burba, O. V. Nikolaeva, A. A. Pronin, A. M. Trakhtman, V. P. Volkov, and V. V. Zasetsky, 1977, "The surface of Venus as revealed by Venera 9 and 10," *Geol. Soc. Amer. Bull.*, v. 88, p. 1537–1545.

Garvin, J. B., J. W. Head, G. H. Pettengill, and S. H. Zisk, 1985, "Venus global radar reflectivity and correlations with elevation," *J. Geophys. Res.*, v. 90, p. 6859–6871.

Greeley, R., Y. Asmerom, and S. Barnett, 1983, "Radar signatures of wind streaks: Preliminary SIR-A analysis," *Lunar Planet. Sci. XIV*, p. 259–260.

Greeley, R., J. Iversen, R. Leach, J. Marshall, B. White, and S. Williams, 1984, "Windblown sand on Venus: Preliminary results of laboratory simulations," *Icarus*, v. 57, p. 112–124.

Greeley, R., P. Christensen, and R. Carrasco, 1989, "Shuttle radar images of wind streaks in Altiplano, Bolivia," *Geology*, v. 17, p. 665–668.

Greeley, R., R. E. Arvidson, C. Elachi, M. A. Geringer, J. J. Plaut, R. S. Saunders, G. Schubert, E. R. Stofan, E. J. P. Thouvenot, S. D. Wall, and C. M. Weitz, 1992, "Aeolian features on Venus: Preliminary Magellan results," *J. Geophys. Res.*, v. 97, p. 13,319–13,345.

Guest, J. E., M. H. Bulmer, J. Aubele, K. Beratan, R. Greeley, J. W. Head, G. Michaels, C. Weitz, and C. Wiles, 1992, "Small volcanic edifices and volcanism in the plains of Venus," *J. Geophys. Res.*, v. 97, p. 15,949–15,966.

Klose, K. B., J. A. Wood, and A. Hashimoto, 1992, "Mineral equilibria and high radar reflectivity of Venus mountain tops," *J. Geophys. Res.*, v. 97, p. 16,353–16,369.

Malin, M. C., 1992, "Mass movements on Venus: Preliminary results from Magellan cycle 1 observations," *J. Geophys. Res.*, v. 97, p. 16,337–16,352.

Pettengill, G. H., P. G. Ford, and B. D. Chapman, 1988, "Venus: Surface electrical properties," *J. Geophys. Res.*, v. 83, p. 14,881–14,892.

Plaut, J. J., and R. E. Arvidson, 1992, "Comparison of Goldstone and Magellan radar data in the Equatorial plains of Venus," *J. Geophys. Res.*, v. 97, p. 16,279–16,291.

Saunders, R. S., A. R. Dobrovolskis, R. Greeley, and S. D. Wall, 1990, "Large-scale patterns of eolian sediment transport on Venus: Predictions for Magellan," *Geophys. Res. Lett.*, v. 17, 1365–1368.

Schaber, G. G., R. G. Strom, H. J. Moore, L. A. Soderblom, R. L. Kirk, D. J. Chadwick, D. D. Dawson, L. R. Gaddis, J. M. Boyce, and Joel Russell, 1992, "Geology and distribution of impact craters on Venus: What are they telling us?" *J. Geophys. Res.*, v. 97, p. 13,257–13,301.

Schultz, P. H., 1992, "Atmospheric effects on ejecta emplacement and crater formation on Venus from Magellan," *J. Geophys. Res.*, v. 97, p. 16,183–16,248.

Weitz, C. M., C. Elachi, and R. Blom, 1992, "Two possible dune fields on Venus," *LPSC XXIII*, p. 1511–1512.

Chapter 7. Impact Craters

Catherine M. Weitz

Introduction

Impact craters are a common feature on most planetary bodies because projectiles (such as meteoroids, asteroids, and comets) have collided with planetary surfaces for billions of years. Projectiles able to penetrate a planet's atmosphere impact the surface at a velocity of tens of kilometers per second with enough energy to generate shock waves in the crustal rocks. These shock waves propagate to produce craters by the ejection of vapors, melted rocks, hot particles and fragments, sheared and fractured rocks, and large blocks [Melosh, 1989]. Stratigraphy reverses during this process, with the deepest target material exposed closest to the crater rim and the most shallow material deposited farthest from the rim. Generally, impact craters have a circular outline, a raised rim, and a depth that is shallow relative to the diameter. The crater is surrounded by ejecta deposits that decrease in thickness outward from the crater rim; correspondingly, the detailed morphologies and radar backscatter characteristics of these deposits change systematically with distance from the crater rim. Because of the dense Venusian atmosphere, some aspects of crater formation and morphology on Venus are different from those on other bodies. These differences are of interest in themselves, but they do not overshadow the basic characteristics of impact craters.

There is a general progression in morphology between large, intermediate, and small craters: large craters may have several rings and smooth floors; intermediate craters tend to have a central peak and smooth floors; small craters have a simple bowl floor that is rough. Impact craters exhibit a wide range of degradation on different planets, so they are useful indicators of resurfacing and modification of surfaces. On Earth, craters are rapidly degraded and destroyed by surficial weathering processes. In contrast, Venusian craters remain pristine because they are young, and there is very little weathering that affects them.

General Characteristics

Impact craters are found on both the plains and the highlands of Venus. Schaber et al. [1992] found the spatial distribution of craters to be highly uniform with a size–frequency distribution lower than those of the other terrestrial planets (except that of Earth), indicating a relatively young age of 0.5 Ga. The number of small craters is much smaller than that on other planets because of atmospheric filtering. One theory holds that the majority of Venusian craters appears pristine because the planet was resurfaced 0.5 Ga ago and there has been very little geologic activity and weathering since to degrade and destroy the craters [Schaber et al., 1992]. Phillips et al. [1992] found that the crater size–frequency distributions, locations, and preservation states implied a range of surface ages. Many craters display radar-bright or -dark halos, and a number of craters have extended deposits that are parabolically shaped and open to the west [Campbell et al., 1992]. A feature unique to Venusian craters is radar-bright outflow deposits that extend over great distances, following the local topography [Asimow and Wood, 1992; Schaber et al., 1992; Schultz, 1992].

Although radar images can be used to observe and discriminate the morphology, size, symmetry, slope, ejecta, crater-floor roughness, and other characteristics of impact craters, no single characteristic is a criterion for the impact origin of a crater; rather, an assemblage of criteria is required. The features that best determine an impact origin for a crater are (1) a circular rim crest outline, (2) flanks that gently rise

above the surrounding terrain, (3) floors with elevations lower than those of the surrounding terrain, (4) an ejecta blanket surrounding the crater, and (5) an inner basin that may be present in very large craters. Figure 7-1(a) shows the 48-km-diameter Venusian impact crater Danilova, which lies on the plains; Figure 7-1(b) is a geologic sketch map. The crater has a central peak, a crater wall, a crater floor, an ejecta blanket, and crater outflow deposits. Figure 7-2 represents a schematic cross section through a central-peak crater such as Danilova.

The ejecta blanket and the circular rim of a crater are very bright in the radar image because both are rough with many facets oriented perpendicular to the radar illumination; hence, a strong received echo results from the rim and the ejecta. Typically, the crater wall that slopes toward the radar appears compressed while the wall that slopes away from the radar appears expanded. Walls parallel to the illumination have intermediate brightness and widths.

The diameter of a crater on Magellan images should always be measured from the northern rim to the southern rim, as this is the direction normal to the illumination direction where radar distortion is minimal. The apparent symmetry of a crater on an image depends on both the radar geometry and the angle of impact of the projectile that formed the crater. The smaller the incidence angle of the radar, the more foreshortening of crater walls and slopes that face toward the radar illumination. Craters produced by an impact that is normal to the surface tend to be radially symmetric: Rim crests have roughly equal elevations everywhere and are concentric with the crater floor outline, while flanks appear the same in all radial directions. However, most impact craters are produced by projectiles with trajectories that are oblique to the surface. When the angle is very oblique, the crater has a bilateral symmetry about the plane of the trajectory, with rim crests highest on the down-trajectory side and lowest on the up-trajectory side, while crater flanks extend to distances greater on the down-trajectory sides than on the up-trajectory sides. The outline of the crater rim crests is offset in the down-trajectory direction with respect to the outline of the crater floor. The degree of development of this bilateral symmetry increases with a decrease in the impact angle of the projectile (measured from the surface).

Within and around impact craters, topographic undulations that are larger than the resolution of the image also modulate the backscatter echoes to reveal morphologic expressions of crater materials and their areal distributions. Venusian impact craters may have either a radar-bright or -dark crater floor, or both. The brightness of the crater floor in the Magellan images appears to depend on the incidence angle of the radar, the size of the crater, the terrain on which

the crater formed, and the amount of infilling by lava or impact melt. In this chapter, each of these general radar responses will be discussed using examples from Venusian craters.

Venera Results

In studies by Ivanov et al. [1986] and Basilevsky et al. [1987], Venera radar images revealed about 150 impact craters with diameters from 8 to 144 km, which are distributed over less than 20% of the Venusian surface. The craters were classified into three morphological types according to the extent of their degradation [Ivanov, 1992]. Fresh craters were found to have radar-bright halos with bilateral symmetry. Mature craters showed no apparent halo, perhaps because the halo was removed by modification of the surface; mature craters were further classified into those that appeared fresh and those that appeared degraded. Basilevsky et al. [1987] compared halo-bearing craters in Venera 15/16 imagery (10-deg incidence angle; 8-cm wavelength) to Arecibo Earth-based radar images (40- to 70-deg incidence angle; 13-cm wavelength) and found that while some kinds of craters always had halos, others had halos only in Arecibo images but not in Venera 15/16 images. They interpreted this to be a time-dependent degradation of the impact-generated surface roughness.

Figure 7-3 shows the crater Golubkina as seen by both Venera 15/16 and Magellan images. The 34-km-diameter crater is located at 60.5°N latitude and 287.2°E longitude. Magellan's resolution of the crater morphology is a tenfold improvement over that of the Venera image (120 m versus 1.5 km). The crater has a central peak surrounded by a smooth, radar-dark floor. The crater walls and ejecta are very bright due to great roughness and steep slopes that cause a large quasi-specular return. The crater appears to have a dark halo, perhaps from the shock wave associated with the impact or from the deposition of fine debris that subdued the roughness of the surrounding terrain.

Magellan Results

Schaber et al. [1992] have classified the Venusian impact craters seen in Magellan images into six morphologic types. (1) Multiringed craters are similar to the larger multiringed basins on Moon, Mercury, and Mars. They include all craters larger than 100 km in diameter. (2) Double-ring craters have an outer rim and an inner ring.

Figure 7-1. Danilova, a 48-km-diameter central peak crater: (a) Magellan image—illumination is from the left at a 35-deg incidence angle; (b) sketch map, showing geologic units typical for Venusian impact craters.
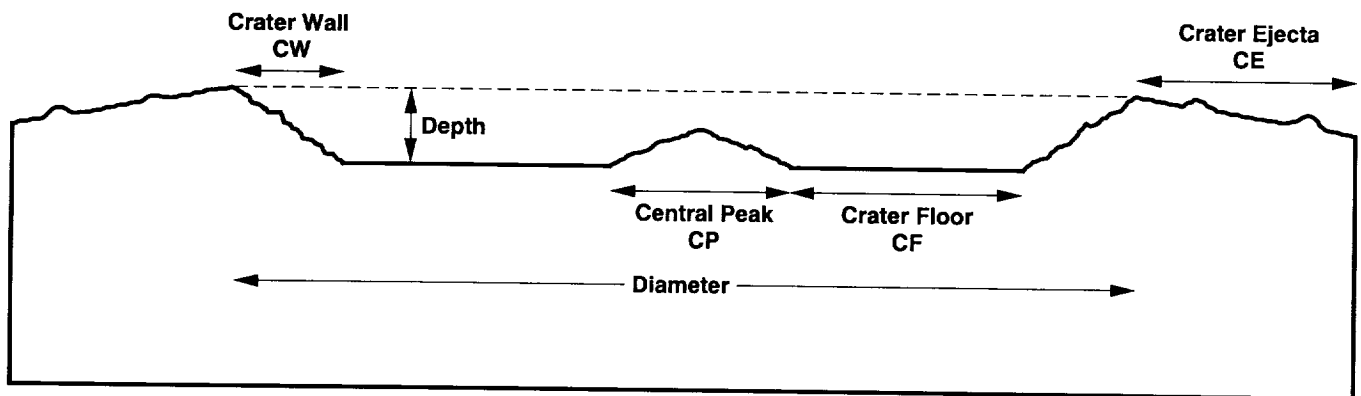
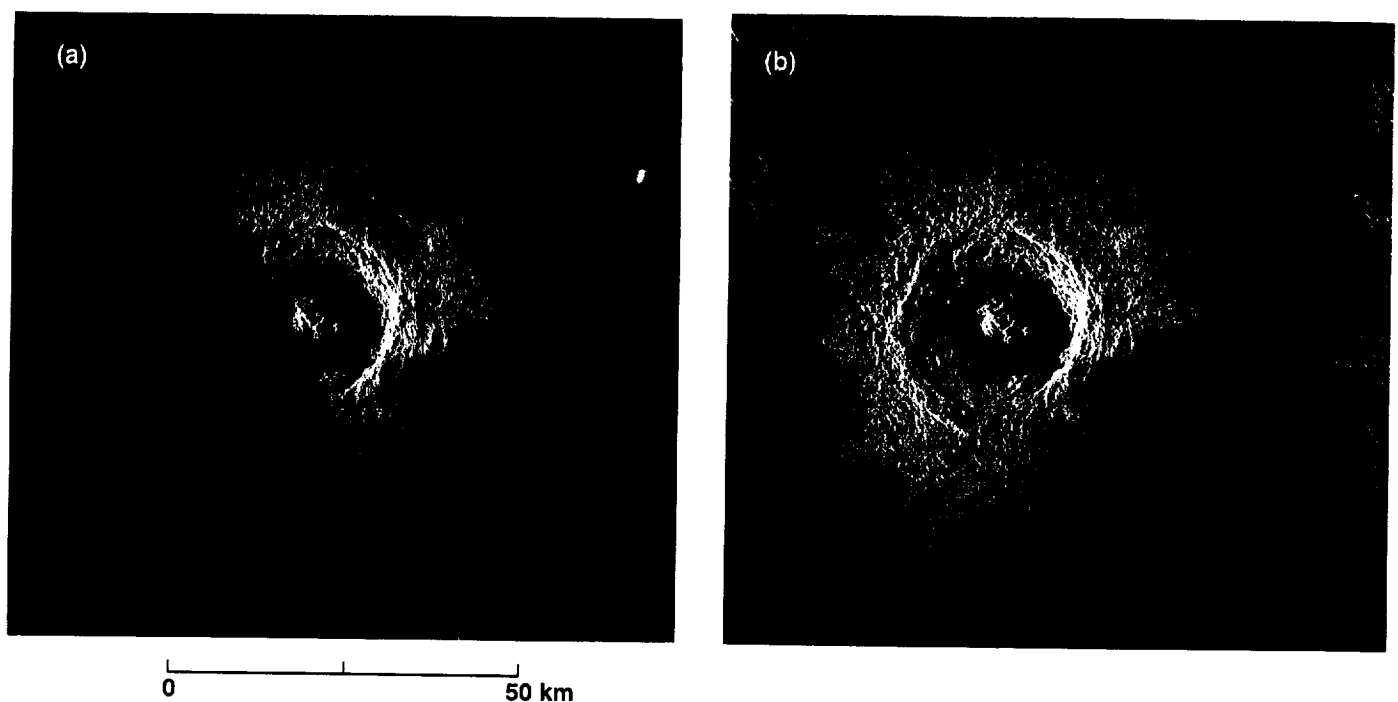**Figure 7-2.** Schematic cross section for a typical central peak crater, such as Danilova.

Figure 7-3. Golubkina crater as seen by (a) Venera 15/16 and Magellan combined and (b) Magellan only. The Magellan image was acquired at a 27-deg incidence angle and the Venera 15/16 image at a 10-deg incidence angle; because of the better resolution and larger incidence angle of the Magellan image, there are more variations in the Magellan imagery. Illumination is from the right for the Venera 15/16 image and from the left for the Magellan image.

The inner ring is radar bright because it is rough and has steep slopes due to the arrays of peaks and hills rising above the relatively flat floor. Most craters with diameters larger than 40 km are of this type. (3) Central peak craters account for approximately 37% of the craters on Venus; they have central mounds or a radar-bright jagged central peak. (4) Craters with structureless floors generally have terraced walls and flat floors. (5) Irregular craters represent the smallest craters (less than 16 km in diameter), and their floors are usually radar bright because they are rough and complex. (6) Multiple craters are characterized by two or more craters produced by projectiles that impacted very close to each other; in some cases the crater rims may overlap. Simple bowl-shaped craters, which are quite common small craters on the Moon and Mars, are scarce on Venus. Instead, small Venusian craters form tight clusters and they overlap.

Distinguishing Impact Craters from Volcanic Craters

The Venera 15/16 and Arecibo images of Venus reveal several circular features that resemble both impact craters and volcanic features. Cleopatra, 105 km in diameter and lying on Maxwell Montes, is one of these controversial features (Figure 7-4). Cleopatra was originally interpreted as a caldera on top of a giant volcanic construct [Masursky et al., 1980]. From the Venera 15/16 and Arecibo images, Basilevsky and Ivanov [1990] interpreted Cleopatra to be a peak-ring structure, which supported an impact origin for the crater. However, the lack of evidence for crater-rim deposits, the large depth of Cleopatra, and extensive plains deposits to the east that apparently emanated from the crater led Schaber et al. [1986] to suggest a possible volcanic origin.

Magellan has solved the mystery of Cleopatra crater because of its high-resolution images. These images show (1) an inner basin, (2) an outer basin, and (3) rough ejecta deposits. Although the crater rim resembles that of a volcanic caldera, the ejecta and the inner basin provide compelling evidence that the structure is an impact crater. The ejecta deposits surrounding Cleopatra appear to be incomplete and do not extend as far as they should for a crater of this size,

possibly because the crater was produced on the highlands rather than the plains. The ejecta can be identified as such because they are rougher and have more large-scale slopes than those of the surrounding terrain. The crater wall at the right, which faces the radar illumination, appears compressed while the opposite wall appears extended. This is why more of the crater wall is visible on the side closest to the direction of radar illumination. The direction of illumination and the angle of incidence lower the apparent circularity of the crater outline in plan view and impart a bilateral symmetry.

Flows of impact melt or lavas of impact-triggered volcanism breached the crater rim and filled the troughs in the upper-right corner of the image. These flows and the floor of the crater are radar-dark because they are smoother than the surrounding terrain, so more of the radar signal is reflected forward and away from the radar. A rougher terrain would be radar bright because more of the signal would be reflected back to the radar to produce a stronger echo.

The surrounding tesserae are rough and have large-scale slopes, which result in extremely bright returns. A chemical transition at high elevations that leads to a high dielectric constant in the rocks is thought to accentuate the high radar reflectivity [Pettengill et al., 1988; Klose et al., 1992].
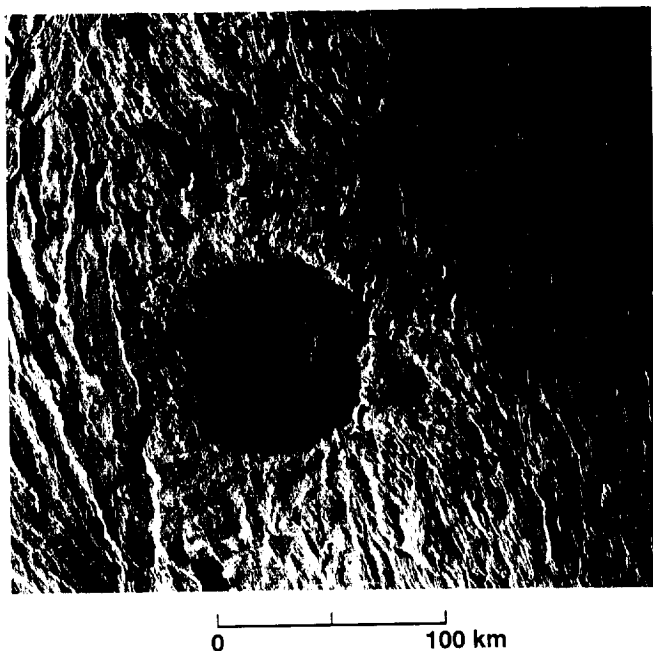


```
0                    100 km
```

Figure 7-4. Cleopatra crater. Once believed to be a volcanic caldera, this crater was shown by Magellan data to have an impact origin. A small ejecta blanket is visible surrounding the crater rim and an inner, radar-dark basin can be seen on the crater floor. Illumination is from the left at an incidence angle of 25 deg.
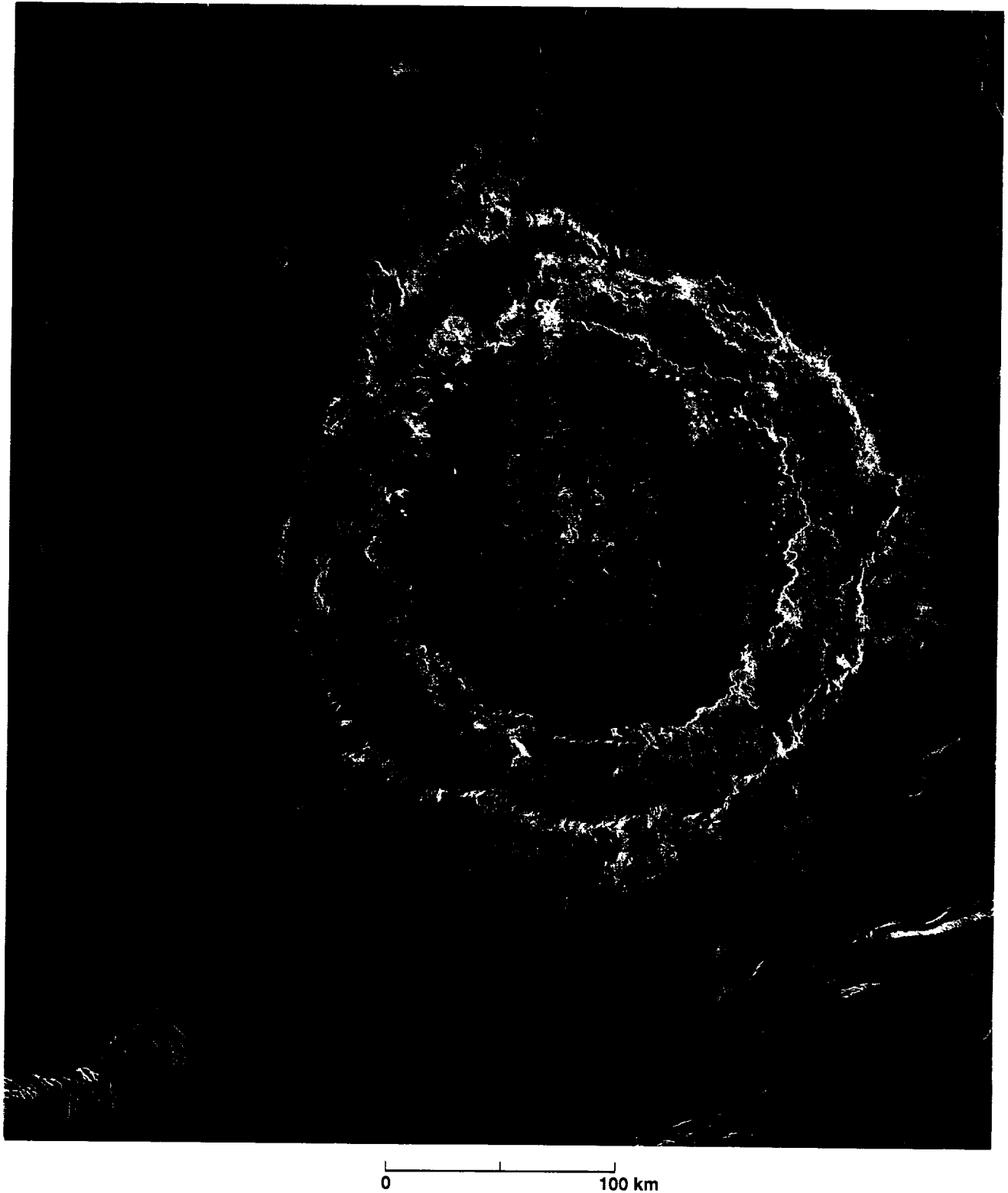
Radiophysical Properties

Mead crater, with a diameter of 280 km, is the largest impact crater on Venus (Figure 7-5). The inner ring is thought to represent the original rim of the crater cavity, while the outer scarp is thought to be the expression of a ring fault that has downdropped the flank terrace [Schaber et al., 1992]. The crater floor has a slightly higher backscatter than the surrounding plain. The surrounding plain is covered by fine debris that decreases the return to the radar, and hence it appears darker on the image. The floor of the crater has several large cracks that show as bright lines due to radar-facing slopes. Ejecta from the crater that appear as diffuse patches surrounding the crater rim are brighter than the surrounding plain because they are rougher and have more slopes facing the radar. At lower incidence angles, the difference in radar brightness between the ejecta and the surrounding terrain would be minimal because diffuse scattering dominates only at large incidence angles. However, at low incidence angles, quasi-specular scattering from radar-facing slopes of the ejecta will cause stronger backscatter than the flatter surrounding plain.

The topography, emissivity, reflectivity, and rms slope data sets from Magellan are very useful in determining the

Figure 7-5. Mead crater is the largest impact crater on Venus, with a diameter of 280 km. The crater has an inner and an outer ring and a small ejecta blanket surrounding the outer ring. The crater floor looks very similar in morphology to the surrounding plain. The dark vertical bands running through the image are artifacts associated with processing the SAR data. Illumination is from the left at an incidence angle of 45 deg.

depth and physical properties of Venusian impact craters. The altimetry for the crater Mead is shown in Figure 7-6(a). The 100-m-contour intervals indicate an altitude above a 6052-km planetary radius. The drop in elevation from the crater rim to the center of the crater is approximately 1.0 km. This is quite shallow for a crater the size of Mead; it may be that Mead has experienced relaxation of its floor, or a large amount of material has flooded the crater floor. The rms slopes on the crater floor are about twice as high as those on the surrounding plain (2.6 deg vs. 1.3 deg). This indicates that the floor of the crater is rougher than the surrounding plain at the meter scale.

Figure 7-6(b) shows the emissivity for Mead and the surrounding terrain, with a contour interval of 0.01. While the surrounding plain and western edge of Mead have values near 0.81, the eastern half of Mead has very low emissivities, with a low of 0.715. Because reflectivity is generally the complement of emissivity, the highest reflectivity values for Mead occur at the place of lowest emissivities, which is in the northeast of the crater floor. Furthermore, because the radar backscatter coefficient is partly a function of the dielectric constant, the low emissivity/high reflectivity may be due to a high dielectric constant on the eastern crater floor. This latter correlation is not seen in the SAR image of Mead, implying that some other scattering effect (e.g., volume scattering) may be causing the low emissivity on the eastern floor of Mead.

Estimating Slopes and Depths

The 63-km-diameter crater Yablochkina has one peak ring, seen on Figure 7-7 as an incomplete circle of bright hills surrounded by a darker, smoother floor. The peak ring is similar to the outer rim found on all craters, except that it is not as well developed. Both the peak ring and the outer rim are bright because they are rough and have radar-facing slopes. These slopes must therefore be oriented perpendicular to the radar illumination, which is from the left in this Cycle 1 image. The crater wall facing the radar (the right side of the crater) appears compressed compared to the wall on the opposite side—the same phenomenon that occurred on the image of Cleopatra, discussed earlier.

A good estimate of the slope and depth of a crater can be calculated using the diagram shown in Figure 7-8. It should be noted that these equations apply only to craters with no layover (i.e., the slope of the crater wall is less than the nominal incidence angle) and craters that are symmetric.

In the case of Yablochkina, the values of X and Y measured from the radar image are 4.35 and 7.5 km, respectively, and the incidence angle, θ, is 33 deg. Application of

the formulas in Figure 7-8 results in a depth (H) of 1.02 km and slope (α) of 9.8 deg. Altimetry for the crater shows a depth of 0.8 km. While the depth of the crater varies by only 0.22 km between the two measurements, caution must be used in calculating topographic data for smaller craters; the altimeter footprint for smaller craters may include both the crater floor and the surrounding rim and plains, which are at higher elevations. Hence, the depths measured by the altimeter for the smaller craters will generally be too shallow.

Halos, Outflow Deposits, and Splotches

The crater shown in Figure 7-7 has two other interesting features: a radar-dark halo and radar-bright outflow deposits. The crater and its ejecta are surrounded by a dark halo. These areas of low backscatter cross sections partially or wholly surround approximately half of the impact craters on Venus [Phillips et al., 1991]. The Venera 15/16 radar images show very few craters with dark margins. It is likely that the dark margins seen on the Magellan images, which were taken at higher incidence angles, represent smooth areas with little surface roughness at the scale of the radar wavelength. Atmospheric shock waves produced as the meteoroid passed through the thick atmosphere may have removed wavelength-size structures from the existing terrain and pulverized the surface materials to produce these dark margins. Alternatively, fine debris produced by the destruction of the target material or the meteoroid as it passed through the atmosphere and exploded at the surface may have been deposited before the crater formed. In addition to dark halos, many Venusian craters have bright halos, also thought to have formed from atmospheric shock waves.

Also surrounding the Yablochkina crater in many locations, but particularly to the northeast, are deposits or flows that are often brighter than the crater ejecta. These flows originate predominantly downrange from the point of the impact. Decreasing the impact angle (measured from the surface) appears to increase the runout flow mass [Schultz, 1992]. The great distances that these deposits travel and the fact that they follow the topography suggest that they consist of low viscosity material [Schaber et al, 1992; Asimow and Wood, 1992; Schultz, 1992]. The disruption of Yablochkina's ejecta to the east by the laminar-style runout flows and the radar brightening of the surface to the northeast led Schultz [1992] to suggest an impact direction from the west at an angle of at least 45 deg from the vertical. The high backscatter of the outflow deposits suggests either a very rough surface or wavelength-size facets facing the radar, or both. The similar emissivity and reflectivity values of these deposits
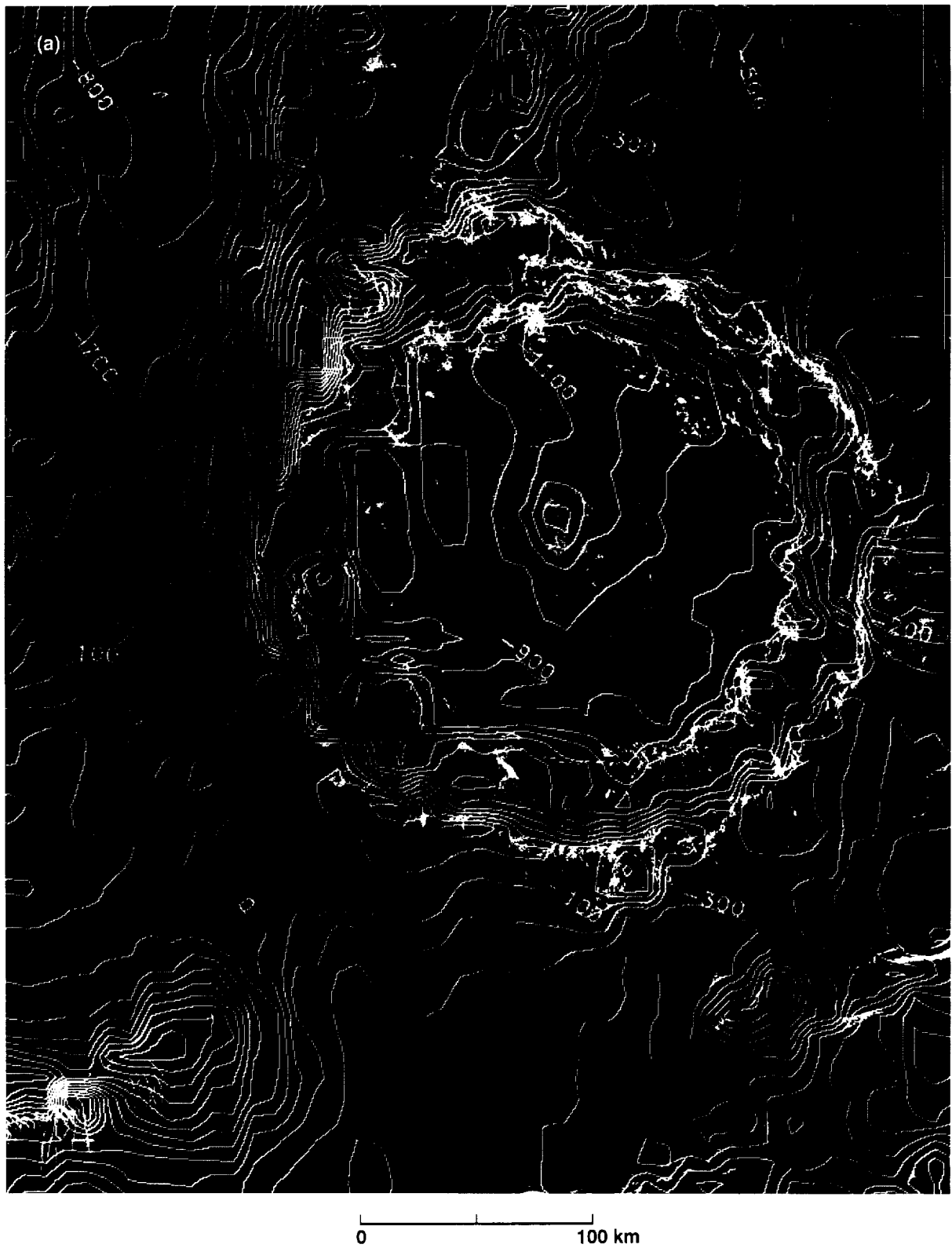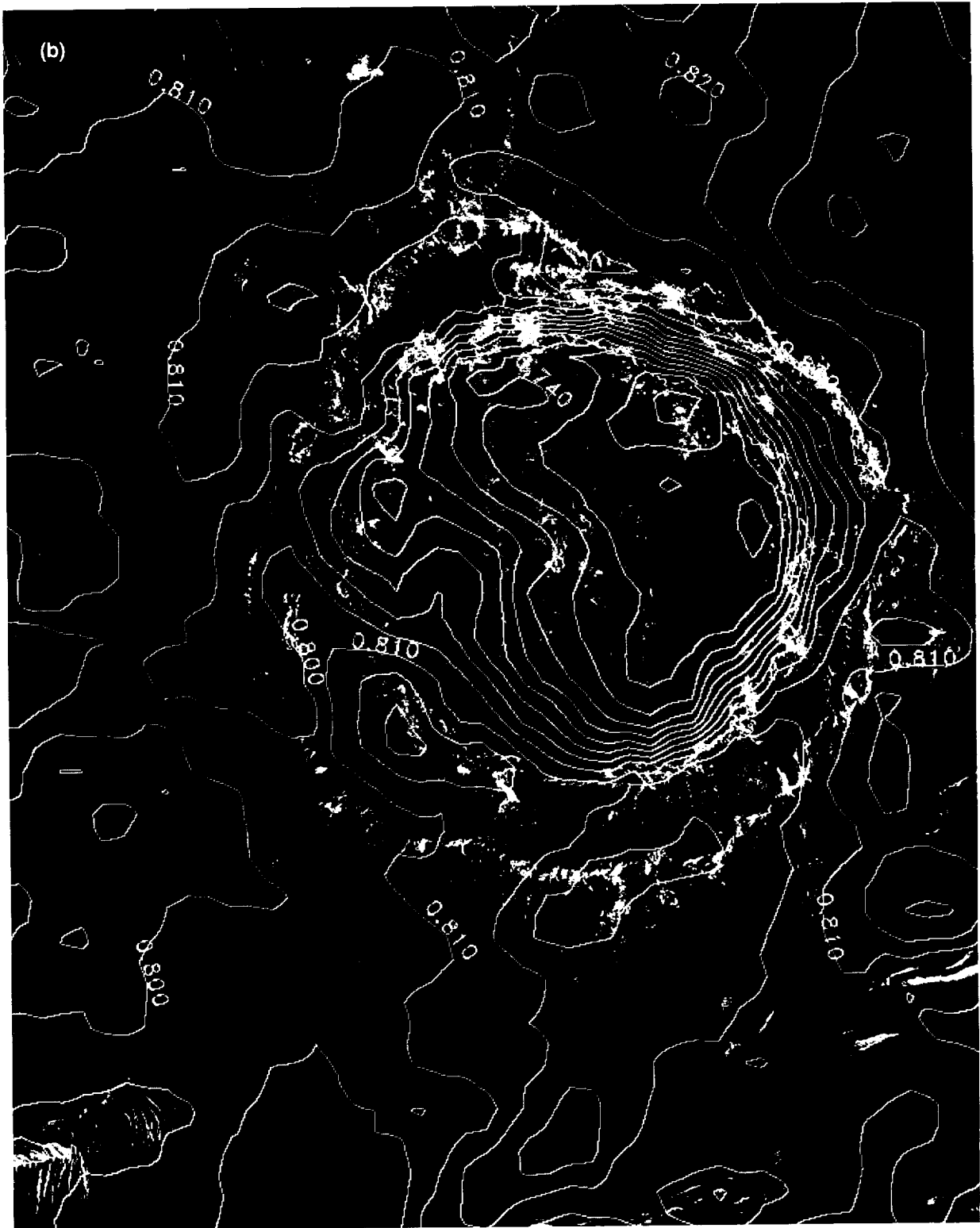
Figure 7-6. Radiophysical properties of Mead crater superimposed on the SAR image: (a) altimetry contours at 100-m intervals—the reference altitude is 6052-km planetary radius, and the drop in elevation from the crater rim to the cen-

ter of the crater is approximately 1.0 km; (b) emissivity contours at 0.01 intervals—the lowest emissivity is 0.715 on the eastern floor of the crater, while the western floor and the surrounding plain have higher emissivities.

(a)

0   50 km

(b)

Plain

CO

CE

CF

DM

CW

PR

CO

CE

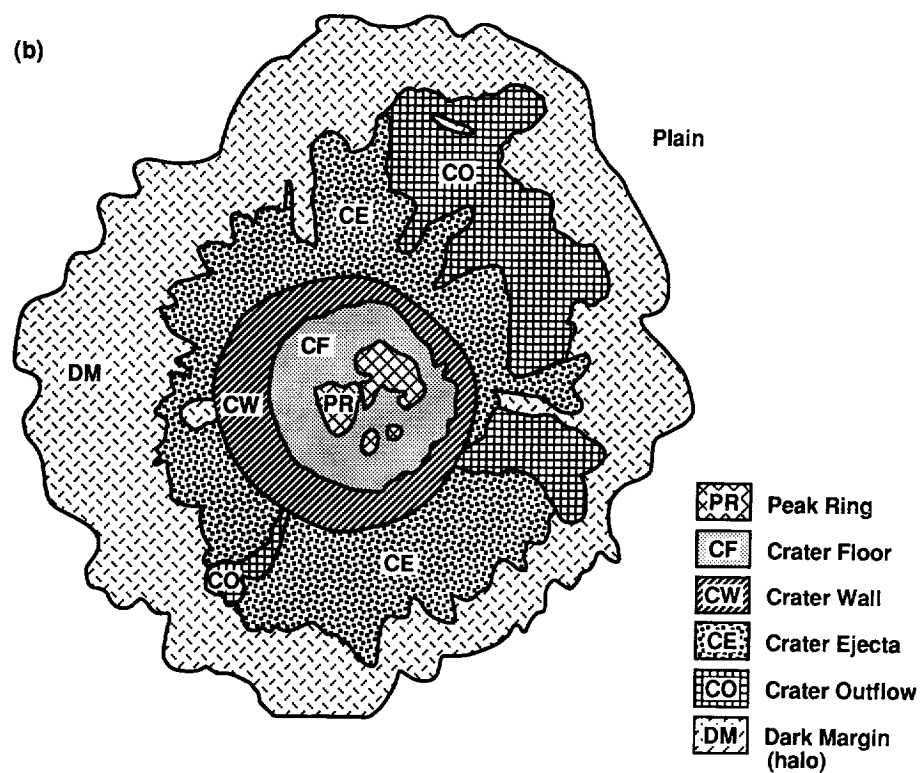|	
PR	Peak Ring
CF	Crater Floor
CW	Crater Wall
CE	Crater Ejecta
CO	Crater Outflow
DM	Dark Margin (halo)

Figure 7-7.   Yablochkina, a 63-km-diameter crater: (a) Magellan image—illumination is from the left at a 33-deg incidence angle;   (b) geologic sketch map.
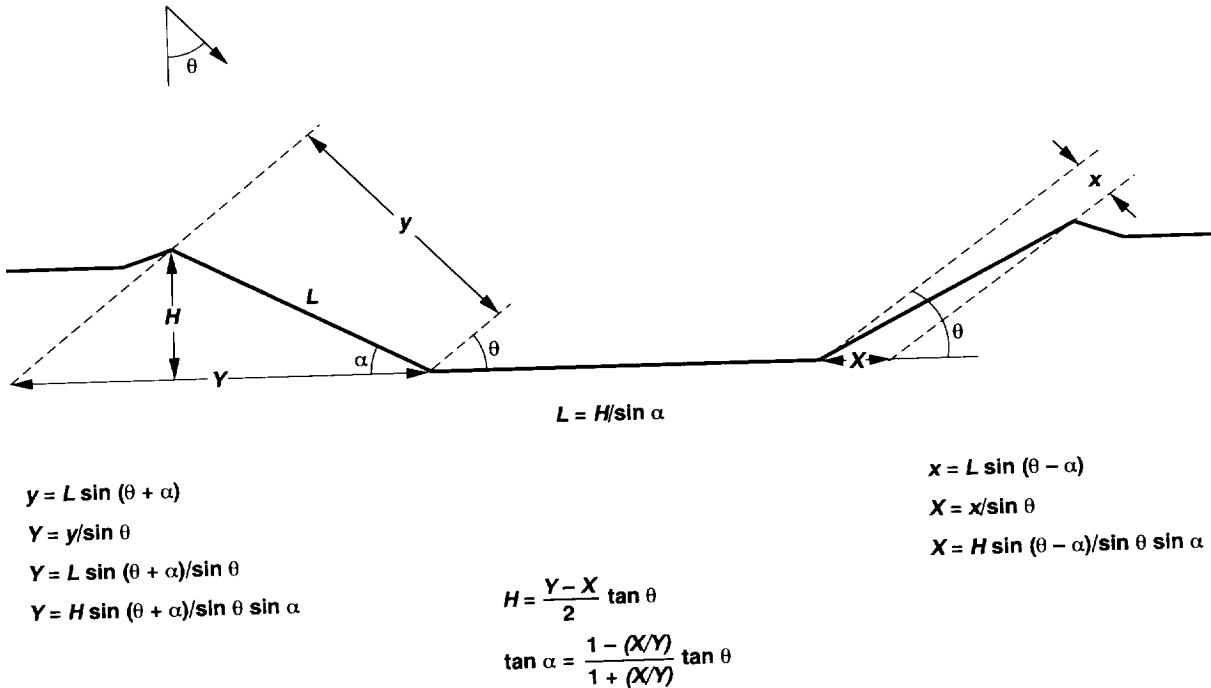
Figure 7-8. Profile outline and equations showing calculations for crater depth and slope. These equations are applicable only for craters where no radar layover has occurred.

$L = H/\sin \alpha$

$y = L \sin (\theta + \alpha)$

$Y = y/\sin \theta$

$Y = L \sin (\theta + \alpha)/\sin \theta$

$Y = H \sin (\theta + \alpha)/\sin \theta \sin \alpha$

$x = L \sin (\theta - \alpha)$

$X = x/\sin \theta$

$X = H \sin (\theta - \alpha)/\sin \theta \sin \alpha$

$$H = \frac{Y - X}{2} \tan \theta$$

$$\tan \alpha = \frac{1 - (X/Y)}{1 + (X/Y)} \tan \theta$$

and the surrounding plains do not support high dielectric constants as the cause of the high backscatter cross sections.

Smaller impactors may be broken up as they enter the Venusian atmosphere [Basilevsky et al., 1987; Ivanov et al., 1992; Schaber et al., 1992]. Except for the smallest members of some crater clusters, no craters smaller than 3 km in diameter have been observed [Phillips et al., 1991]. Figure 7-9 shows an irregular crater of approximately 14-km mean diameter. The crater is actually a cluster of four separate craters in rim contact. The noncircular rims and multiple, hummocky floors are probably the result of the breakup and dispersion of a meteoroid during its passage through the dense Venusian atmosphere; subsequently, the meteoroid fragments impacted simultaneously to create the cluster. Meteoroids that would form craters smaller than the observed cutoff diameter of 3 km either are not able to penetrate the atmospheric column or they decelerate to velocities insufficient to form impact craters [Phillips et al., 1991]. However, the shock or pressure wave created as such a meteoroid travels through the atmosphere may still have energy sufficient to deform the surface.

Figure 7-10 shows three dark splotches on the plains of Venus. The impact crater in the splotch at the right indicates that the meteoroid was not completely destroyed and reached the surface to produce a crater. Much of the meteoroid, however, was destroyed and its remnants and/or shock wave

produced the large dark margin that surrounds the crater. The other two splotches, at near center and the extreme left, have no associated impact crater, indicating that only a shock wave disturbed the surface. Evidence that these splotches represent a deposit of material is the change in brightness of the underlying lava flows from the center of the splotches outward. The dark margin to the left has associated wind streaks, suggesting that the splotch is composed of material fine enough to be moved by the wind.

Crater Modification

The majority of impact craters on Venus (62%) are pristine and unmodified [Schaber et al., 1992]. This indicates that impact craters have not been significantly altered by surficial processes. In only a few cases have craters been modified by lava flows or tectonism. Figure 7-11 shows the crater Somerville, a 37-km-diameter crater in Beta Regio, which has been cut by many fractures and faults. The crater was split in half during the formation of a rift that is up to 20 kmwide and apparently quite deep. A north–south profile through the center of this crater is visible as a result of the downdropping. Most of the central peak is visible as a bright spot in the middle of the crater. A radar-bright ejecta blanket is also visible through the fractures. A small portion of the
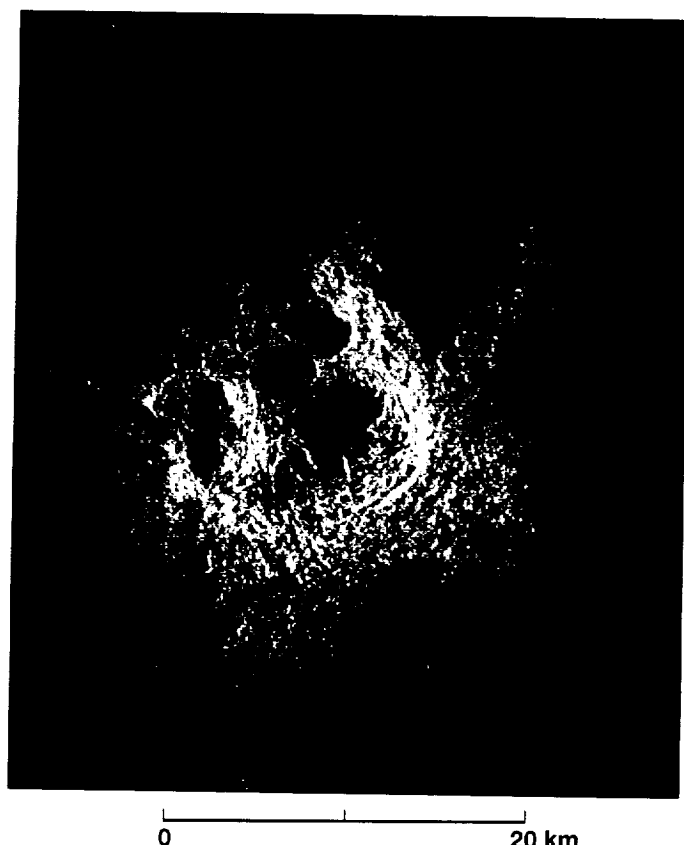
Figure 7-9. Cluster of four craters in rim contact. A small projectile broke up in the atmosphere to form four smaller impactors that struck nearly simultaneously to form this crater cluster. Illumination is from the left at an incidence angle of 38 deg.

eastern half of the crater can be seen on the far side of the rift. While the majority of large impact craters on Venus have floors that are radar-dark (probably due to flooding of the crater floor by lavas from below after the crater was produced), craters that have been modified by volcanism not associated with the impact process are rare on Venus.

One such rarity is Alcott, a 63-km-diameter crater extensively flooded by lava (Figure 7-12). A remnant of rough, radar-bright radial ejecta is preserved outside the crater's southeast rim. The large, trough-like depression to the southwest is a rille or channel through which lava once flowed; the very radar-bright eastern side and radar-dark western side indicate that this feature is a trough with steep slopes. The presence of partly lava-flooded craters like this one is important in understanding the rate of resurfacing on Venus by volcanism. The lack of flooded craters suggests that the surface may have been covered by lava flows about 0.5 Ga ago, burying all existing craters [Schaber et al., 1992]. According to this model, the craters now visible in the Magellan images represent impacts that occurred after this

resurfacing event, and there has been very little volcanic and other resurfacing since.

Illumination Geometry Effects

Left-Looking vs. Right-Looking Geometry

After Magellan completed one cycle of left-looking imaging, the radar geometry changed to obtain right-looking, constant, 25-deg incidence-angle coverage. Figures 7-13(a) and (b) are examples of a Cycle 1 (left-looking) and Cycle 2 (right-looking) image pair of the 26-km-diameter crater Guilbert. In the Cycle 1 image taken at a 20-deg incidence angle, the crater has a bright outer rim, a radar-bright central peak, and a radar-dark floor. The right side of the wall, which faces the radar, looks compressed compared to the left side of the wall, which appears extended. In contrast, the central peak is a topographic high so the radar-facing left side of the peak is compressed and the right side of the peak is extended. This geometric effect is similar to the radar geometry of the steep ridges in the highlands of Venus, where the ridges are geometrically distorted in the same manner (see Chapter 8).

The Cycle 2 image obtained 243 days later at roughly the same incidence angle (25 deg) has equal but opposite illumination geometric effects because it was taken from the opposite side. Here the left side of the crater is compressed and the right side of the crater wall is extended while the central peak is compressed on the right side and extended on the left. The distal (left) side of the Cycle 2 crater wall shows large blocks of the wall that have fallen onto the adjacent crater floor, and this is why the wall does not appear as compressed as the distal (right) wall in the Cycle 1 image, where no blocks of the wall are seen on the crater floor. The crater ejecta look very similar in both the Cycle 1 and 2 images because they contain many rough blocks with facets oriented in all directions. Thus, these facets produce strong echoes from both the left and right illuminations. Because the incidence angle differs by only 5 deg between each image, the diffuse component, which contributes a large amount to the received echo, is roughly equal in both images. However, in cases where the incidence angle difference is great, the ejecta brightness and shape can change considerably.

Stereo Images

During Cycle 3, Magellan was able to image parts of Venus with a different left-looking incidence angle than that used in Cycle 1; this viewing geometry allows stereo mapping. Figure 7-14(a) shows an area on Venus imaged at a 44-deg incidence angle in Cycle 1. Figure 7-14(b) shows the

Figure 7-10. Dark splotches on lava flows. The splotch at far right contains a crater while the others (at center and far left) do not. The diffuse boundaries of the splotches and the wind streaks from the splotch at the left indicate that the splotches are composed of fine debris. Radar illumination is from the left at an incidence angle of 30 deg.

same area imaged in Cycle 3 at a 24-deg incidence angle. The impact crater is De Lalande, 21 km in diameter and located on the distal flanks of the volcano Gula Mons. The crater has an outer rim but no central peak. The floor of the crater is both radar-bright and -dark; the dark floor represents a smooth, flat plain and the bright floor indicates a rougher surface. Surrounding the crater, but particularly to the north and east, are radar-bright outflow deposits. South of the crater, some of the preexisting radar-bright complex ridge terrain on which the projectile impacted is visible.

In general, the difference between the two images is not significant. The Cycle 3 image, however, has several vertical radar-dark bands and more speckle than the Cycle 1 image

due to a lower signal-to-noise ratio (SNR) in the Cycle 3 image; thus, some caution must be used when comparing the two. Another noticeable difference is the brighter crater wall in the Cycle 3 image, especially on the distal (right) wall. This greater brightness is most likely the result of the smaller incidence angle, which brings the radar wavefront closer to the normal of the wall and thus produces a strong return. At the larger incidence angle of the Cycle 1 image, the crater wall is oriented further from the perpendicular to the radar, and a smaller received echo results. The ejecta and the crater floor look very similar in both images. The crater ejecta have both a diffuse and a specular component and while the diffuse component decreases in the Cycle 3 image, the specular
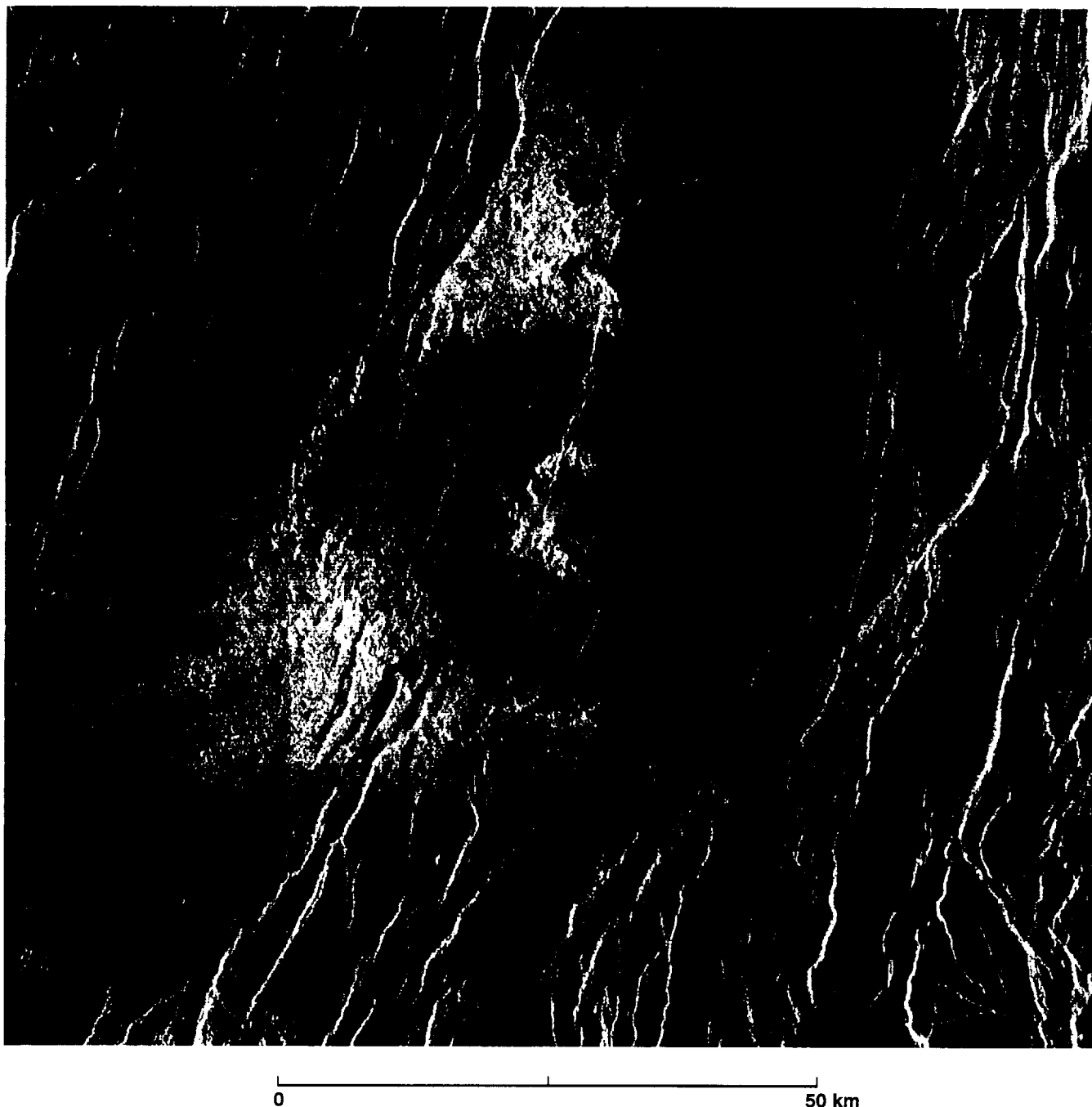
87

0	50 km

Figure 7-11. Somerville crater is split in half by a rift valley. A north–south profile through the crater is visible in the rift. The eastern half of the crater is visible on the opposite side of the rift. Illumination is from the left at an incidence angle of 42 deg.

component increases. The crater floor of the Cycle 3 image has a slightly higher backscatter than that of the Cycle 1 image because, at the smaller incidence angle, a stronger return results for relatively smooth surfaces. This is why the Venera 15 and 16 images, which were acquired at much smaller incidence angles (approximately 10 deg), appear much brighter than the corresponding Magellan images of the same areas. When both images of Figure 7-14 are viewed through a stereoscope, a three-dimensional image results. The height of the crater wall and the depth of the crater floor can be determined from these stereo images by measuring the parallax between the Cycle 1 and 3 images (see Chapter 4).

0   50 km

Figure 7-12. Alcott crater was extensively flooded by lava. A remnant of radar-bright ejecta is preserved outside the crater's southeast rim. Illumination is from the left at an incidence angle of 27 deg.
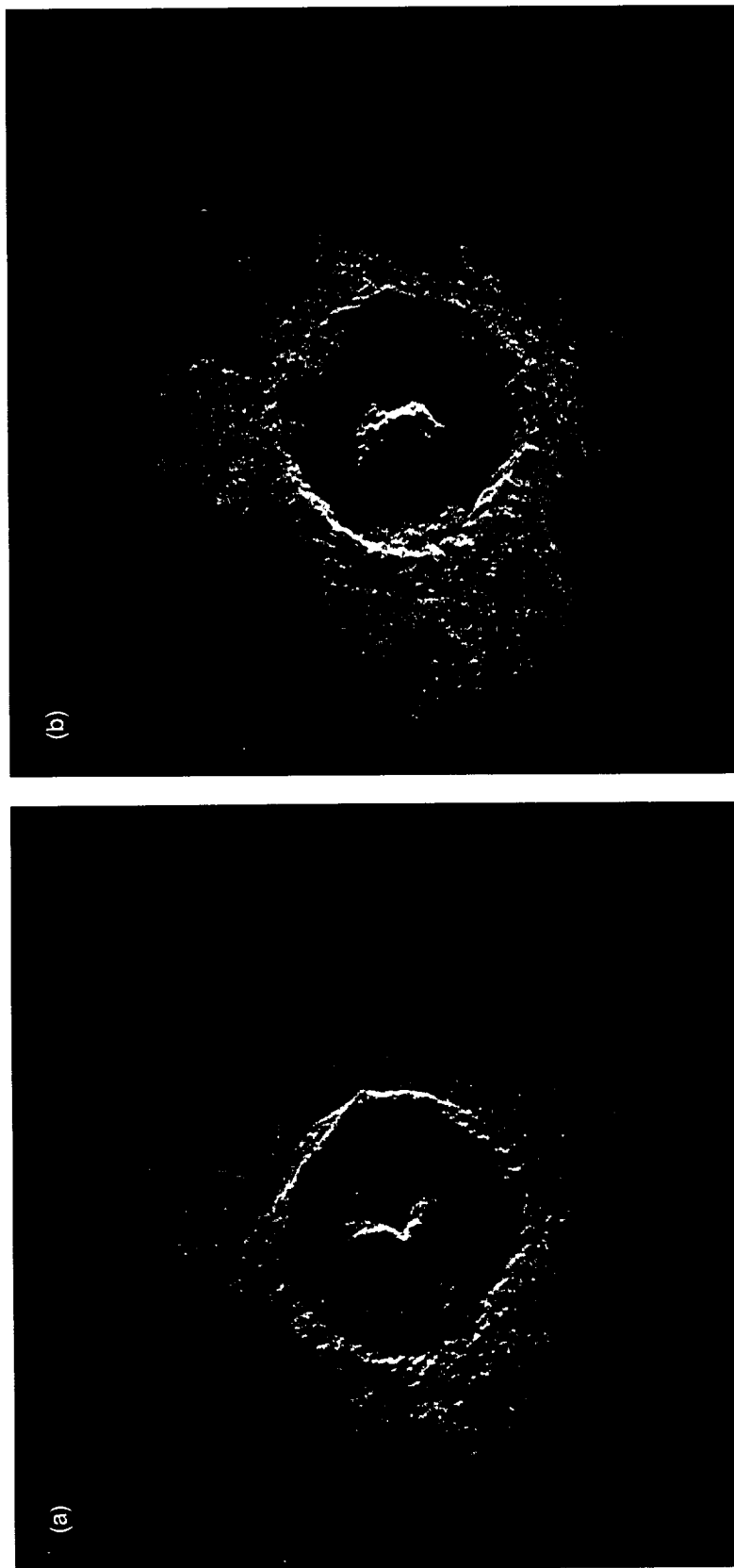
Figure 7-13. Guilbert crater: (a) Cycle 1 left-looking image at an incidence angle of 20 deg; (b) Cycle 2 right-looking image at an incidence angle of 25 deg. The images display opposite geometric effects in the crater rim and central peak, while the crater floor and ejecta are relatively unchanged.
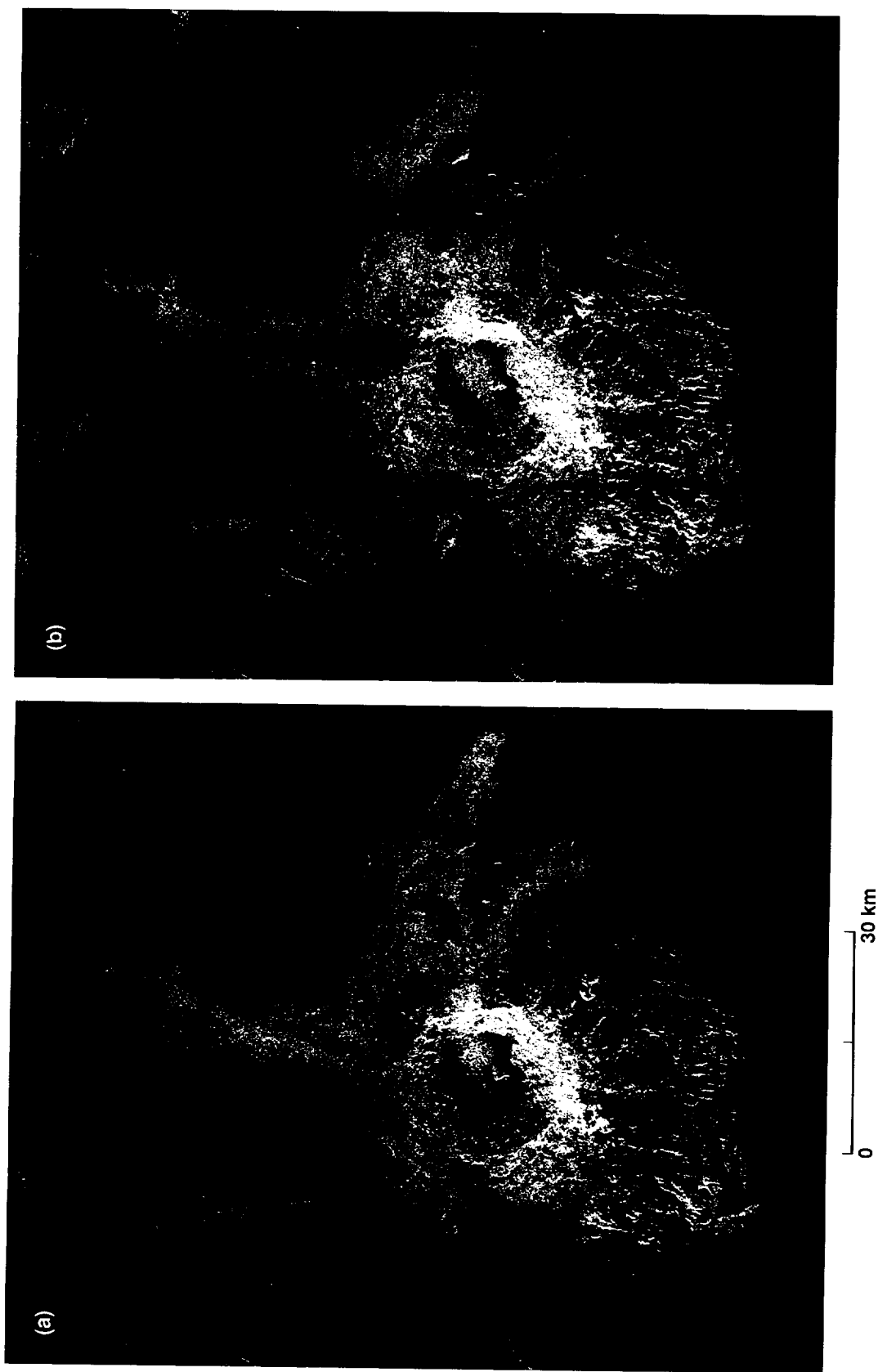
Figure 7-14. Left-looking stereo images of the crater De Lalande: (a) Cycle 1 image at a 44-deg incidence angle; (b) Cycle 3 image at a 24-deg incidence angle. The eastern crater wall is much brighter in the Cycle 3 image because the wall is closer to the normal of the radar wavefront than it is in the Cycle 1 image.

References

Asimow, P. D., and J. A. Wood, 1992, "Fluid outflows from Venus impact craters: Analysis from Magellan data," *J. Geophys. Res.*, v. 97, p. 13,643–13,665.

Basilevsky, A. T., B. A. Ivanov, G. A. Burba, I. M. Chernaya, V. P. Kryuchkov, O. V. Nikolaeva, D. B. Campbell, and L. B. Ronca, 1987, "Impact craters of Venus: A continuation of the analysis of data from the Venera 15 and 16 spacecraft," *J. Geophys. Res.*, v. 92, p. 12,869–12,901.

Basilevsky, A. T., and B. A. Ivanov, 1990, "Cleopatra crater on Venus: Venera 15/16 data and impact/volcanic origin controversy," *Geophys. Res. Letters*, v. 17, no. 2, p. 175–178.

Campbell, D. B., N. J. S. Stacy, W. I. Newman, R. E. Arvidson, E. M. Jones, G. S. Musser, A. Y. Roper, and C. Schaller, 1992, "Magellan observations of extended impact crater features on Venus," *J. Geophys. Res.*, v. 97, p. 16,249–16,277.

Ivanov, B. A., A. T. Basilevsky, V. P. Kryuchkov, and I. M. Chernaya, 1986, "Impact craters on Venus: Analysis of Venera 15 and 16 data," *J. Geophys. Res.*, v. 91, p. D414–D430.

Ivanov, B. A., 1992, "Impact Craters," in *Venus Geology, Geochemistry, and Geophysics*, Tucson, Arizona: University of Arizona Press, p. 113–128.

Ivanov, B. A., I. V. Nemchinov, V. A. Svetsov, A. A. Provalov, V. M. Khazins, and R. J. Phillips, 1992, "Impact cratering on Venus: Physical and mechanical models," *J. Geophys. Res.*, v. 97, p. 16,167–16,181.

Klose, K. B., J. A. Wood, and A. Hashimoto, 1992, "Mineral equilibria and high radar reflectivity of Venus mountain tops," *J. Geophys. Res.*, v. 97, p. 16,353–16,369.

Masursky, H., E. Eliason, P. G. Ford, G. E. McGill, G. H. Pettengill, G. G. Schaber, and G. Schubert, 1980, "Pioneer Venus radar results: Geology from images and altimetry," *J. Geophys. Res.*, v. 85, p. 8232–8260.

Melosh, H. J., 1989, *Impact Cratering—A Geologic Process*, Oxford Monog. Geol. Geophys., no. 11, New York: Oxford University Press, 245 pp.

Pettengill, G. H., P. G. Ford, and B. D. Chapman, 1988, "Venus: Surface electrical properties," *J. Geophys. Res.*, v. 83, p. 14,881–14,892.

Phillips, R. J., R. E. Arvidson, J. M. Boyce, D. B. Campbell, J. E. Guest, G. G. Schaber, and L. A. Soderblom, 1991, "Impact craters on Venus: Initial analysis from Magellan," *Science*, v. 252, p. 288–297.

Phillips, R. J., R. F. Raubertas, R. E. Arvidson, I. C. Sarkar, R. R. Herrick, N. Izenberg, and R. E. Grimm, 1992, "Impact craters and Venus resurfacing history," *J. Geophys. Res.*, v. 97, p. 15,923–15,948.

Schaber, G. G., R. C. Kozak, and H. Masursky, 1986, "Cleopatra crater on Venus: New evidence for a volcanic origin," *LPSCXVII*, p. 762–763.

Schaber, G. G., R. G. Strom, H. J. Moore, L. A. Soderblom, R. L. Kirk, D. J. Chadwick, D. D. Dawson, L. R. Gaddis, J. M. Boyce, and J. Russell, 1992, "Geology and distribution of impact craters on Venus: What are they telling us?" *J. Geophys. Res.*, v. 97, p. 13,257–13,301.

Schultz, P. H., 1992, "Atmospheric effects on ejecta emplacement and crater formation on Venus from Magellan," *J. Geophys. Res.*, v. 97, p. 16,183–16,248.

Chapter 8. Tectonic Features in Magellan Data

Ellen R. Stofan, David A. Senske, and Gregory Michaels

Introduction

The surface of Venus has been modified by a wide range of tectonic processes. This deformation has produced a complex surface characterized by fractured plains, ridge belts, rifts, fracture belts, complex ridge terrain (tesserae), and mountain belts [Masursky et al., 1980; Barsukov et al., 1986; Basilevsky et al., 1986; Solomon et al., 1991 and 1992]. Reliable identification and mapping of these tectonic features are critical to formulating and testing models for the evolution of Venus [Solomon and Head, 1982 and 1991]. Recognition of tectonic features in radar images is often difficult and strongly dependent on viewing geometry and incidence angle [MacDonald, 1980; Ford, 1980]. In this chapter, the techniques for identifying and interpreting tectonic features in radar images are discussed.

Features of Extensional Origin

Troughs and Graben

Troughs and valleys interpreted to be primarily extensional in origin are clearly identifiable in many regions of Venus. These features range from individual troughs within the plains to radial or circumferential graben associated with calderas and coronae, to major rift valleys (e.g., Devana Chasma) (Figures 8-1(a) through (c)). A discussion of trough morphology in general is useful for identifying the wide range of linear depressions seen in the Magellan data. The interpretation that troughs are extensional in origin must be used with caution. For example, numerous sinuous rilles and lava channels that are not formed by extension are abundant on Venus. The morphology of the troughs, the regional structure, the types of associated features, and an understanding of the geologic setting must all be taken into account to determine if troughs have resulted from crustal or lithospheric stretching and are therefore graben.

Troughs are identified in both Magellan synthetic-aperture radar (SAR) and altimetry data. As with illumination by natural sunlight, illumination by radar reveals the presence of positive or negative topography. Troughs or depressions are characterized by a dark band closer to the direction of illumination than the following bright band, as shown in Figure 8-2. The ability to identify troughs is constrained by the spatial resolution of the Magellan SAR. The 210-m average resolution of the image data makes it difficult to distinguish troughs with widths less than a kilometer. These narrow depressions are usually resolved as radar-bright lineaments that are often indistinguishable from small-scale ridges. In addition, troughs with small depth-to-width ratios may not have slopes sufficiently steep to cause noticeable brightness differences. In contrast, troughs in the range of 20 km to several hundred km in width can be easily identified in the Magellan altimetry data or radar stereo images. The 4- to 20-km altimeter footprint is useful in identifying the morphology of major rift zones whose widths are greater than 10 km.

The direction of radar illumination relative to a trough may either enhance or subdue the structure of a depression. Features aligned parallel to the radar look direction are often difficult to identify; a slight change in the look azimuth, in a direction away from an alignment parallel to a feature, can reveal the structure of a feature. Because of this dependence on look direction, multiple data sets (Magellan, Arecibo, and Venera 15/16) with various viewing geometries should be used for the positive identification of troughs and when attempting to compile rose diagrams to quantify the orientation of surface structures [Stofan et al., 1989].
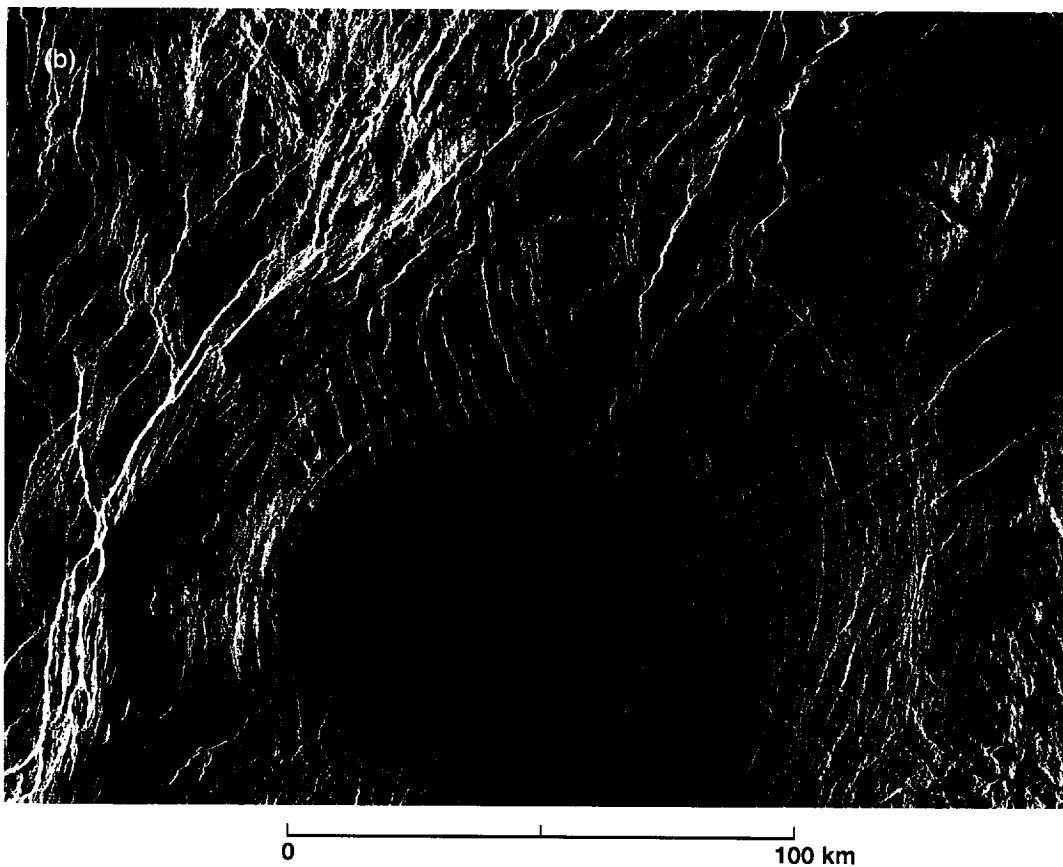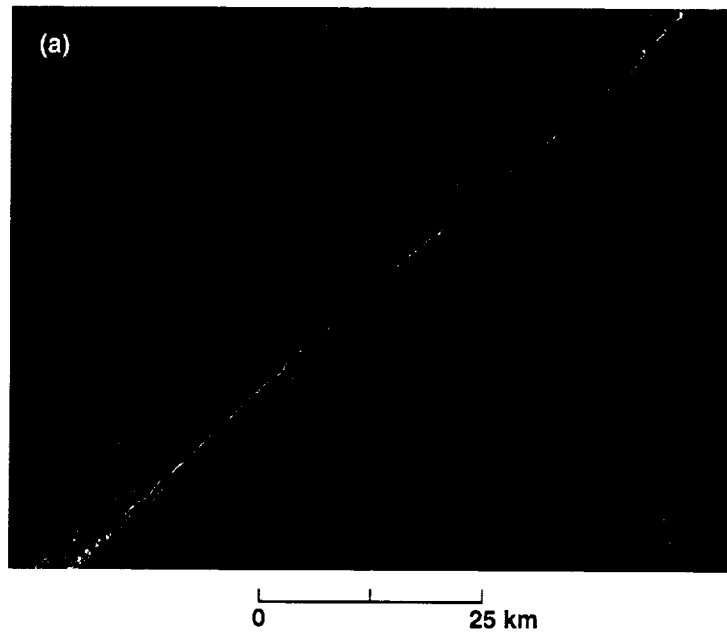
Figure 8-1. Extensional troughs and graben: (a) narrow trough 1.5 km wide in plains adjacent to Alpha Regio (30°S, 11.8°E); (b) radial graben in 49-km-diameter corona Sarpanitum (52.3°S, 14.6°E) —individual troughs are 1 to 2 km wide; (c) rift valley Devana Chasma, 1050 km long and 80 to 240 km wide, in Beta Regio (28°N, 283°E). Illumination is from the left in each image.
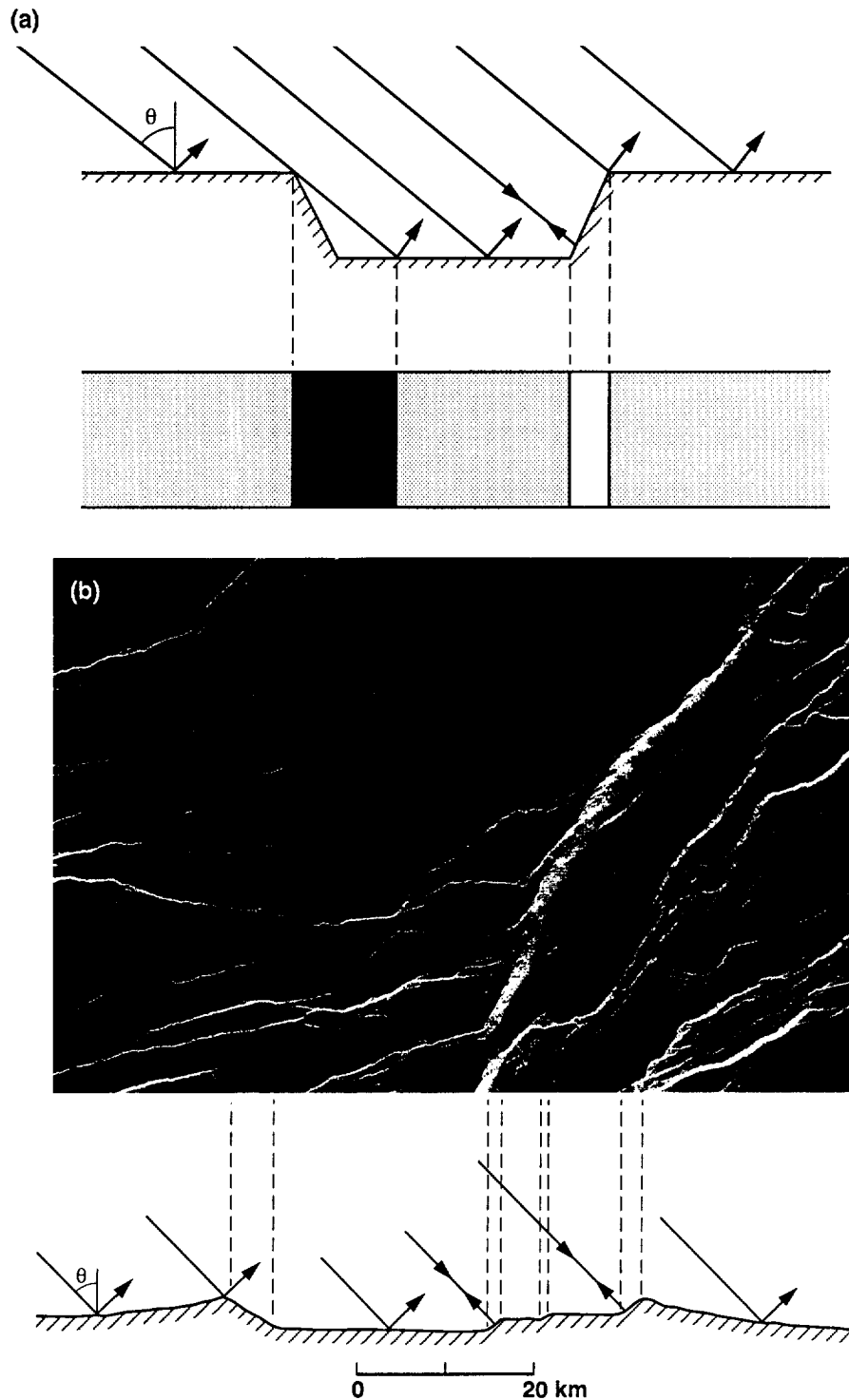
C-2

(c)

0   200 km

(a)

(b)

0   20 km

Figure 8-2. Schematic cross sections show radar responses of troughs. (a) The foreslope is bright because of strong returns caused by the combination of the slope and small-scale roughness of the surface. The backslope is concealed by radar shadow and the area appears black. Backslopes are not seen when the surface slope exceeds the nominal incidence angle θ. (b) Radar image and interpretative cross section of the rift valley, Guor Linea (18.8°N, 0.3°E). In areas such as this where the slope of the scarp is less than the incidence angle (45 deg), the radar can image the surfaces of backslopes.

96

Scarp and Normal Fault Morphology

A number of large-scale troughs on Venus (e.g., Devana Chasma and Ganis Chasma) are characterized by bright lineaments interpreted to be normal faults aligned parallel to the strike of the trough and that in some places cover a region broader than the trough itself (Figure 8-2(b)). These features are interpreted to be rifts produced by broad-scale lithospheric extension, similar to that which occurs at the East African rift on Earth [McGill et al., 1981; Stofan et al., 1989; Senske et al., 1991].

In contrast to the large rift valleys, some regions within the plains contain bright lineaments that have a low degree of sinuosity and are interpreted to be individual normal faults, fractures, or small graben produced by extension. In some places, intersecting sets of linear features (e.g., the "gridded plains" [Saunders et al., 1991]) are interpreted to be fractures produced by lithospheric extension [Banerdt and Sammis, 1992] (Figure 8-3).

There is an abundance of scarps within the plains and on the highlands that are interpreted to be the result of normal faulting. If scarps are not high (i.e., less than 200 m of vertical offset) or do not have a rough surface, they can be difficult to distinguish from other lineaments on radar images. Compared with the surrounding plains, they appear typically as bright, relatively straight, linear features if they face the radar illumination or dark lineaments if they face away. They also appear compressed when facing the illumination direction and extended when facing away. If scarps lie parallel to the direction of illumination, they may be visible only at points where they are faceted or deviate from the parallel.

Features of Compressional Origin

Mountain Belts

Three major mountain belts on Venus—Akna (Figure 8-4), Freyja, and Maxwell Montes, located within Ishtar Terra—are interpreted to have been formed by compression and crustal shortening, which produced folding and thrust faulting [Solomon and Head, 1984; Crumpler et al., 1986; Vorder Bruegge and Head, 1990; Solomon et al., 1992; Kaula et al., 1992]. Features interpreted to be folds are characterized by bright/dark lineament pairs, and have a high degree of sinuosity along strike (Figures 8-5(a) and (b)). Many features interpreted to be folds occur in chevron patterns (Figure 8-6). On Earth, most folded mountain belts are heavily eroded. In comparison, inferred low rates of erosion suggest that folds on Venus are likely to be primary features. Some asymmetric lineaments are interpreted to be thrust faults within the mountains [Barsukov et al., 1986]. In
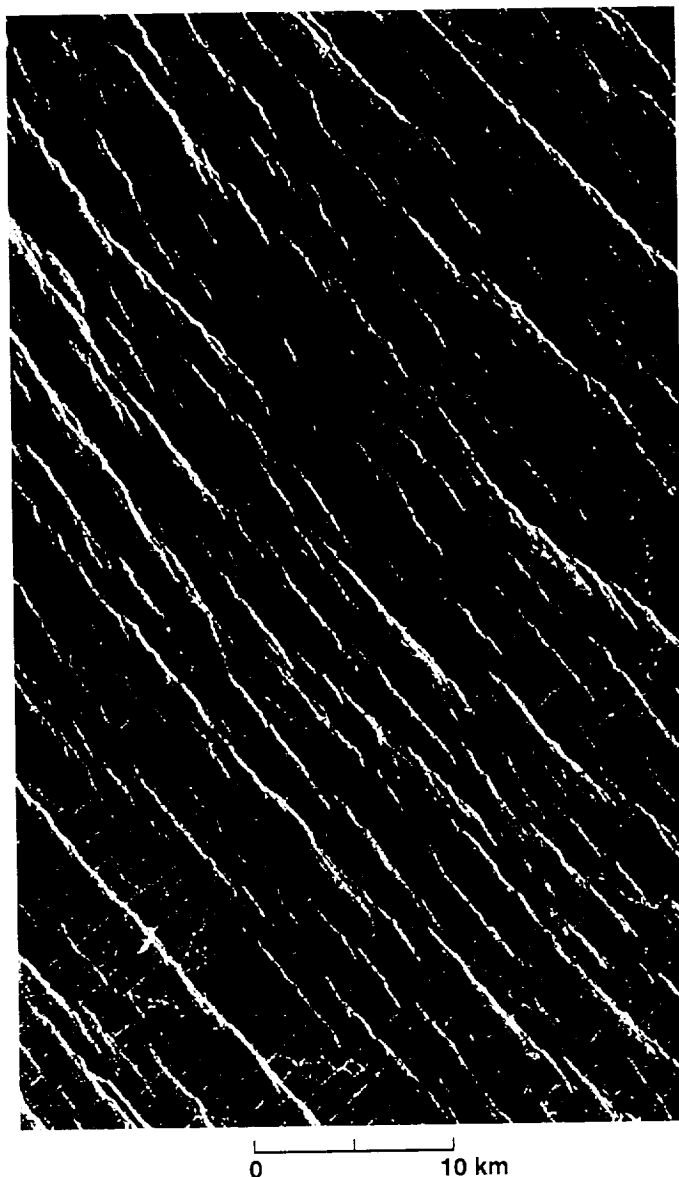

Figure 8-3. Bright parallel lineations on the "gridded plains" in Guinevere Planitia have been interpreted as fracture sets [Banerdt and Sammis, 1992]. Illumination is from the left at an incidence angle of 42 deg.

addition, evidence for strike-slip faulting can be identified by fractures or folds offset in a consistent sense along a linear zone that cuts across the strike of most mountain belts. Typically, cross-cutting relationships can be used to determine the sequence of events, with most mountain belts characterized by early folding and imbrication followed by late-stage extension (cross-cutting graben) indicative of gravitational relaxation [Smrekar and Phillips, 1988; Solomon et al., 1991 and 1992; Kaula, et al., 1992; Smrekar and Solomon, 1992]. Mountain belts on Venus are located at high
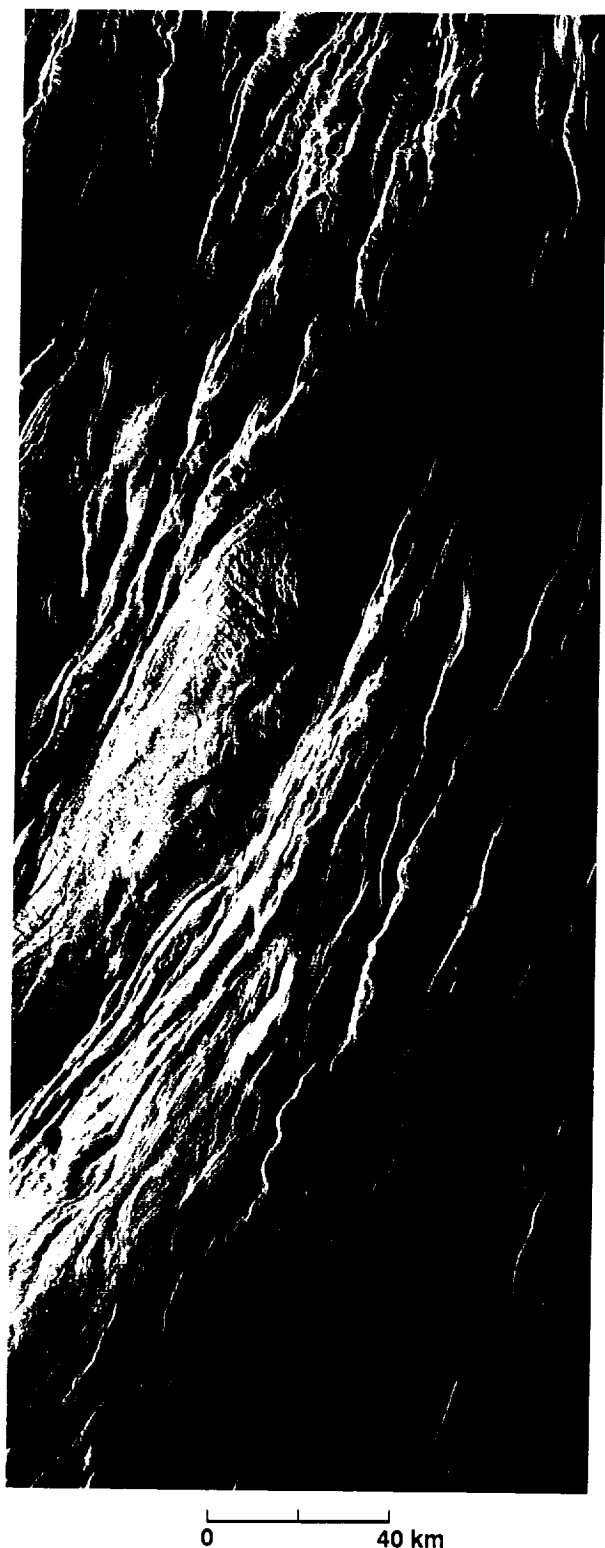
Figure 8-4. The mountain belt Akna Mons (69°N, 318.5°E) is interpreted as a fold belt associated with NW–SE-oriented compression. Illumination is from the left at an incidence angle of 24 deg.

latitudes where the incidence angle of the Magellan radar ranges from 20 to 25 deg. At these low incidence angles, roughness effects are less significant and layover is quite common (Figure 8-7); therefore asymmetric features in images of high latitude areas should be interpreted with caution.

Ridges

Features identified as ridges are characterized by elevated topography and a high degree of sinuosity; they fall into two groups: (1) widely spaced sinuous ridges and (2) collections of ridges that form belts. The widely spaced sinuous ridges tend to be only 2 to 5 km across and are found in almost all plains regions on Venus (Figure 8-8). Since they are found at most latitudes, care must be exercised when comparing features of similar appearance that have been imaged at different incidence angles. Plains ridges bear many similarities to wrinkle ridges found on other terrestrial planets [Watters, 1988 and 1992]. On the basis of their high degree of sinuosity and frequent asymmetry, these ridges are generally interpreted to be thrust faults [Solomon et al., 1992]. In some places, the radar signature is indicative of a more flat-topped, steep-sided feature consistent with a fault-bend fold or a horst [Suppe and Connors, 1992].

Ridge Belts

Ridge belts are found along the borders of major regions of complex ridge terrain (tesserae) and in two major groups located in Lavinia Planitia and in the Atalanta/Vinmara Planitae region (Figure 8-9). The belts are characterized by relatively elevated arch-shaped topography and sinuous ridges; occasionally, troughs lie along the summit and flanks of the elevated topography. Ridges and troughs within the belts tend to be spaced approximately 5 km apart. In some places, faults and folds that exhibit a consistent sense of offset suggest shear. On the basis of a high degree of sinuosity and the presence of arches indicative of folding and thrusting, ridge belts are interpreted to be compressional in origin [Frank and Head, 1990; Solomon et al., 1991 and 1992; Squyres et al., 1992a], although an extensional origin has also been suggested [Sukhanov and Pronin, 1988]. Belts containing extensional graben (Figure 8-9(b)) are also interpreted to be of compressional origin, with summit graben produced by bending stresses as the crust is warped by compressional forces [Squyres et al., 1992a].
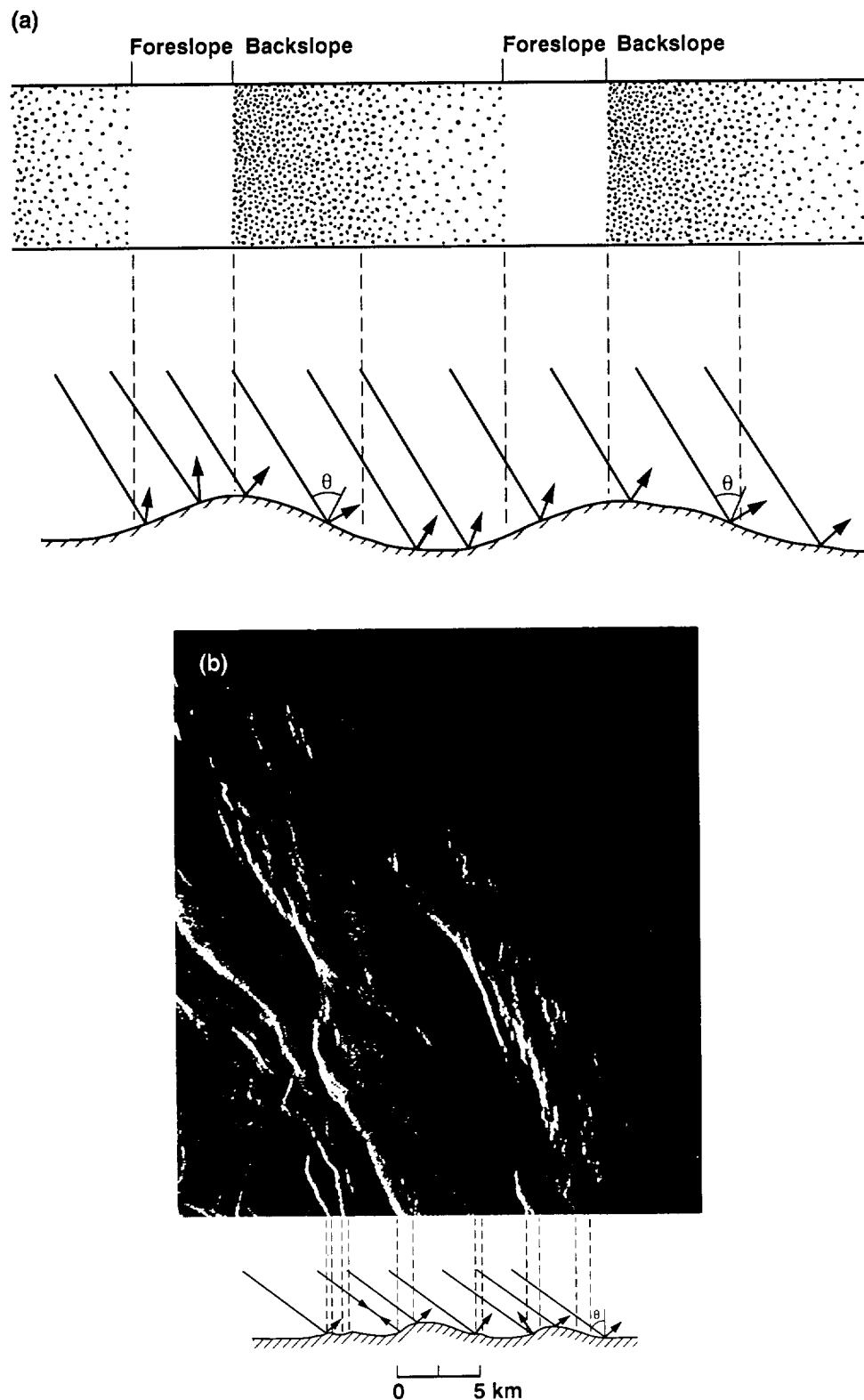
Figure 8-5. Schematic cross sections show radar responses of folds. (a) At a nominal incidence angle θ = 30 deg, symmetric folds appear asymmetric in the image. Foreslopes are compressed and backslopes are expanded. (b) Radar image and interpretive cross section of a series of folds in Lavinia Planitia located at 36.4°S, 337.9°E. Illumination is from the left at an incidence angle of 29 deg.

Figure 8-6. Part of Ovda Regio (Aphrodite Terra) centered at 35°S, 88°E. Chevron structure was produced by folding. Illumination is from the left at incidence angles of 44 to 44.5 deg.

Features of Complex or Indeterminate Origin

Complex Ridge Terrain (Tesserae)

All complexly deformed regions on Venus are categorized as complex ridge terrain (CRT), but they vary in style and sequence of deformation and may differ in origin. CRT, also called tesserae, was first identified in Venera 15/16 images of Venus [Barsukov et al., 1986]. It consists of raised, plateau-shaped regions characterized by at least three sets of intersecting lineaments (Figure 8-10). In a number of places, relatively small outliers of embayed highly deformed terrain are found within the plains and at locations distal to larger

areas of CRT. These relationships may indicate that laterally extensive regions of low-lying CRT have been flooded by later plains volcanism [Ivanov et al., 1992]. Theories for the origin of CRT include (1) deformation of a highly silicic basement [Nikolayeva et al., 1988]; (2) late-stage plume plateaus [Herrick and Phillips, 1990]; and (3) crustal shortening followed by gravitational relaxation over a mantle downwelling [Bindschadler and Parmentier, 1990; Bindschadler et al., 1992a]. Structural features within CRT include folds, thrust faults, graben, and strike-slip faults [Solomon et al., 1991 and 1992; Bindschadler et al., 1992a]. The sequence of events within some major regions of CRT indicate crustal shortening followed by extension [Bindschadler et al., 1992b]. However, detailed kinematic studies of most of these regions are presently lacking.

Coronae

Coronae are circular to elongate features that range from 75- to over 2000-km across and are primarily characterized by an annulus of troughs and/or ridges (Figure 8-11) [Barsukov et al., 1986; Pronin and Stofan, 1990]. The annuli around coronae are 10- to 150-km across and generally correspond to elevated topography. Topographically, coronae are domes, plateaus, plateaus with interior depressions, and rimmed depressions. The majority of the features are surrounded by a peripheral trough. Coronae are also characterized by an association of volcanic features, such as small volcanic domes, lava flows, and moderate-size edifices (see Chapter 9). A group of features with a morphology similar to coronae but lacking a distinct annulus is classified as corona-like features [Stofan et al., 1992].

Coronae are concentrated in a few clusters and along chains, such as those at Parga and Hecate Chasmata. Coronae are interpreted to be surface manifestations of mantle upwelling [Stofan and Head, 1990; Stofan et al., 1991 and 1992; Squyres et al., 1992b]. Within the complexly deformed rims of some large coronae, such as Quetzalpetlatl and Nightingale, layover and foreshortening are observed in images. Stereo imaging and/or analyses that combine radar with altimeter data are critical to interpreting the tectonic structures at coronae and the geologic sequence of events.

Arachnoids

Arachnoids are circular to elongate features that may be generically related to coronae. Arachnoids were first identified in Venera 15/16 data as "spider and cobweb structures" due to their complex appearance. Arachnoids are characterized by a central structure, either a dome or a central circular depression, surrounded by circumferential and radial linear features (Figure 8-12). The inner dome or depression tends to
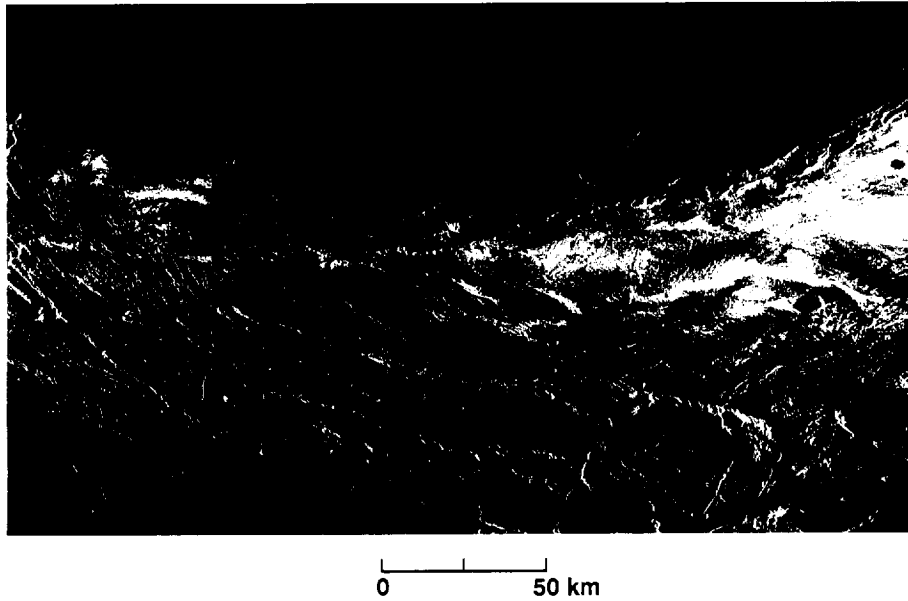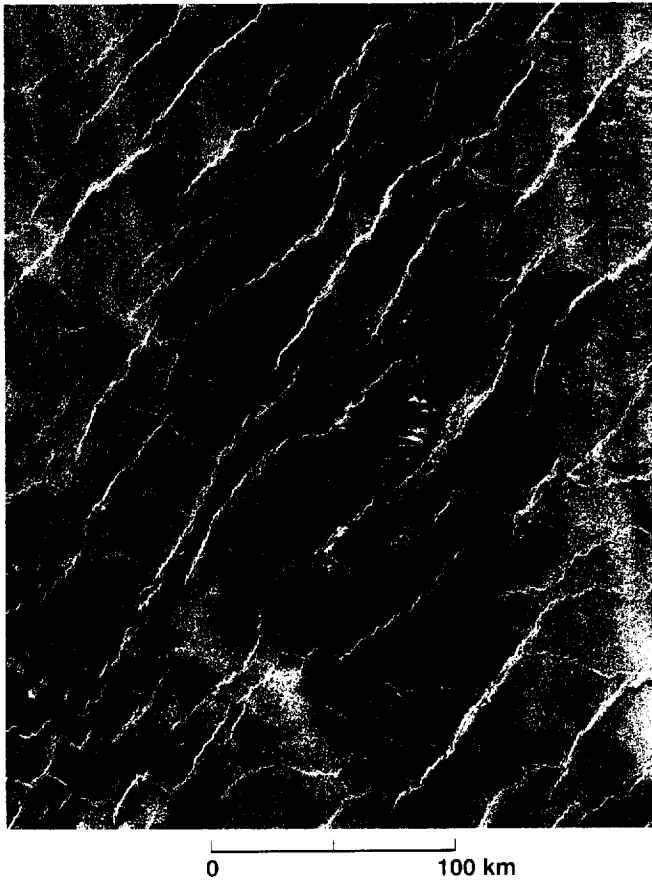
0   50 km

Figure 8-7. Part of Danu Montes at southern Lakshmi Planum (60°N, 333°E). Bright V-shaped pattern pointing in the direction of the radar was produced by layover. Illumination is from the left at an incidence angle of 28 deg.
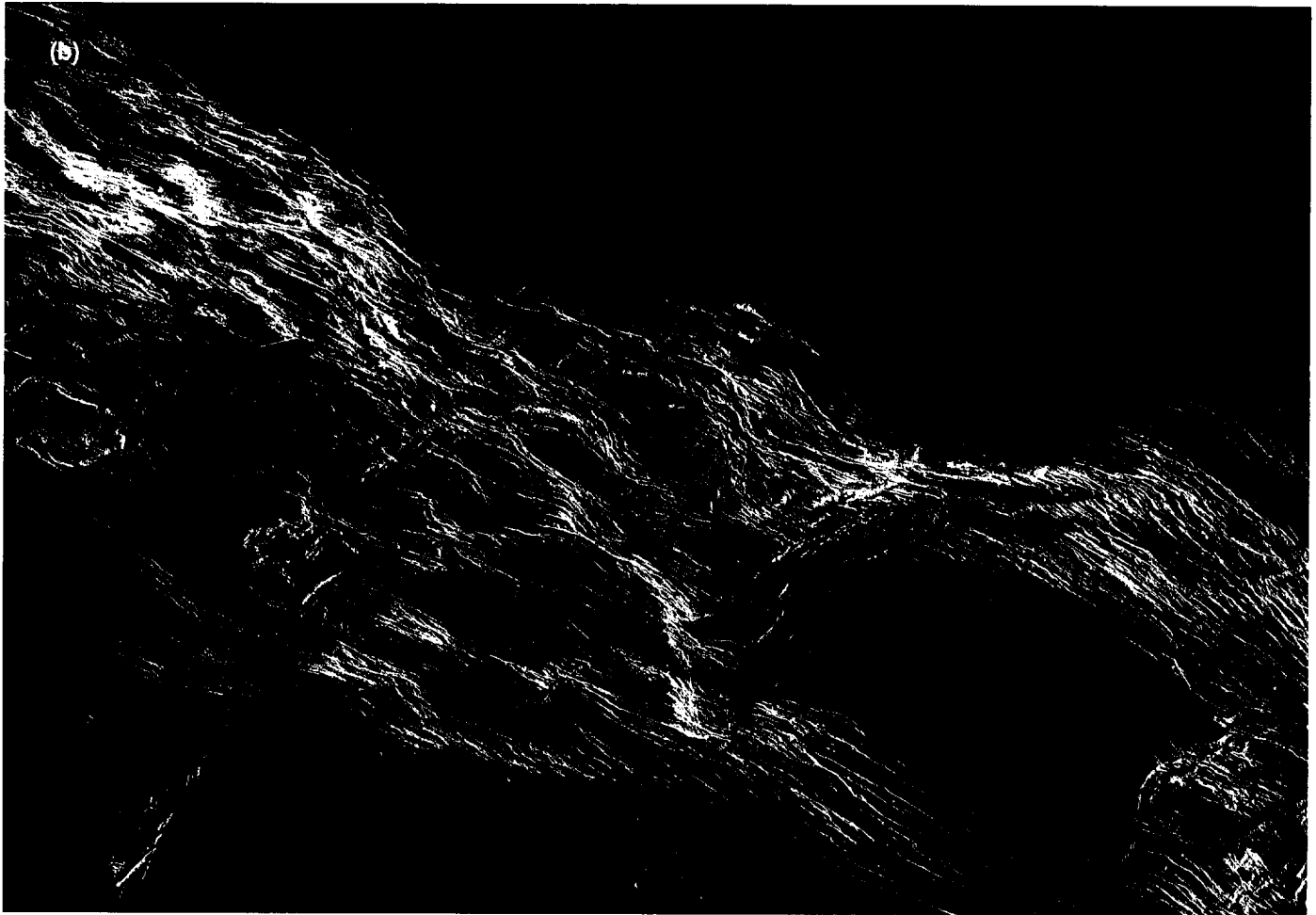

0   100 km

be 10 to 30 km across, with radiating fractures extending from 50 to over 150 km from the central feature. The fractures may have been produced when magma intruded near the surface, forming a small central edifice and producing a system of radiating dikes and fractures [McKenzie et al., 1992]. The emplacement of dikes has been used to understand regional stress patterns at the time of their emplacement [e.g., Muller and Pollard, 1977].

Figure 8-8. Sinuous ridges 2 to 5 km across centered at 34°S, 172°E in the plains are interpreted to be compressional in origin. Illumination is from the left at an incidence angle of 34 deg.

101

0   100 km

Figure 8-9. Ridge belts are characterized by sinuous ridges and arch-shaped topography. (a) Ridge belts centered at 60°N, 208.5°E in Atalanta Planitia show maximum compressive stress in an east–west direction. Illumination is from the left at an incidence angle that varies from 27 to 29.5 deg. (b) A major ridge belt (Hippolyta Linea) in Lavinia Planitia exhibits fractures along its crest, unlike the ridge belts in Atalanta Planitia. Illumination is from the left at an incidence angle of 27.5 deg.
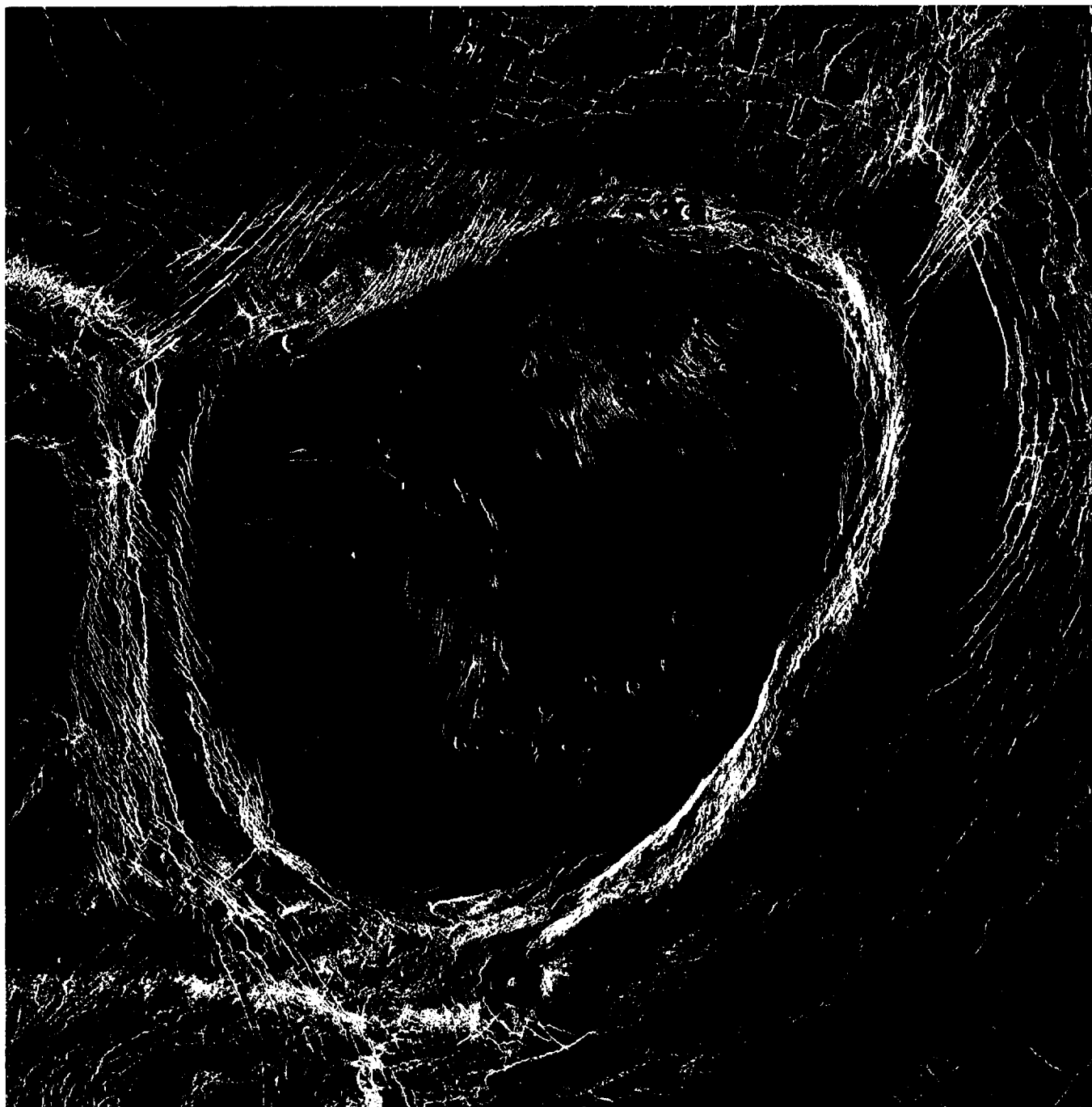
0   100 km

103
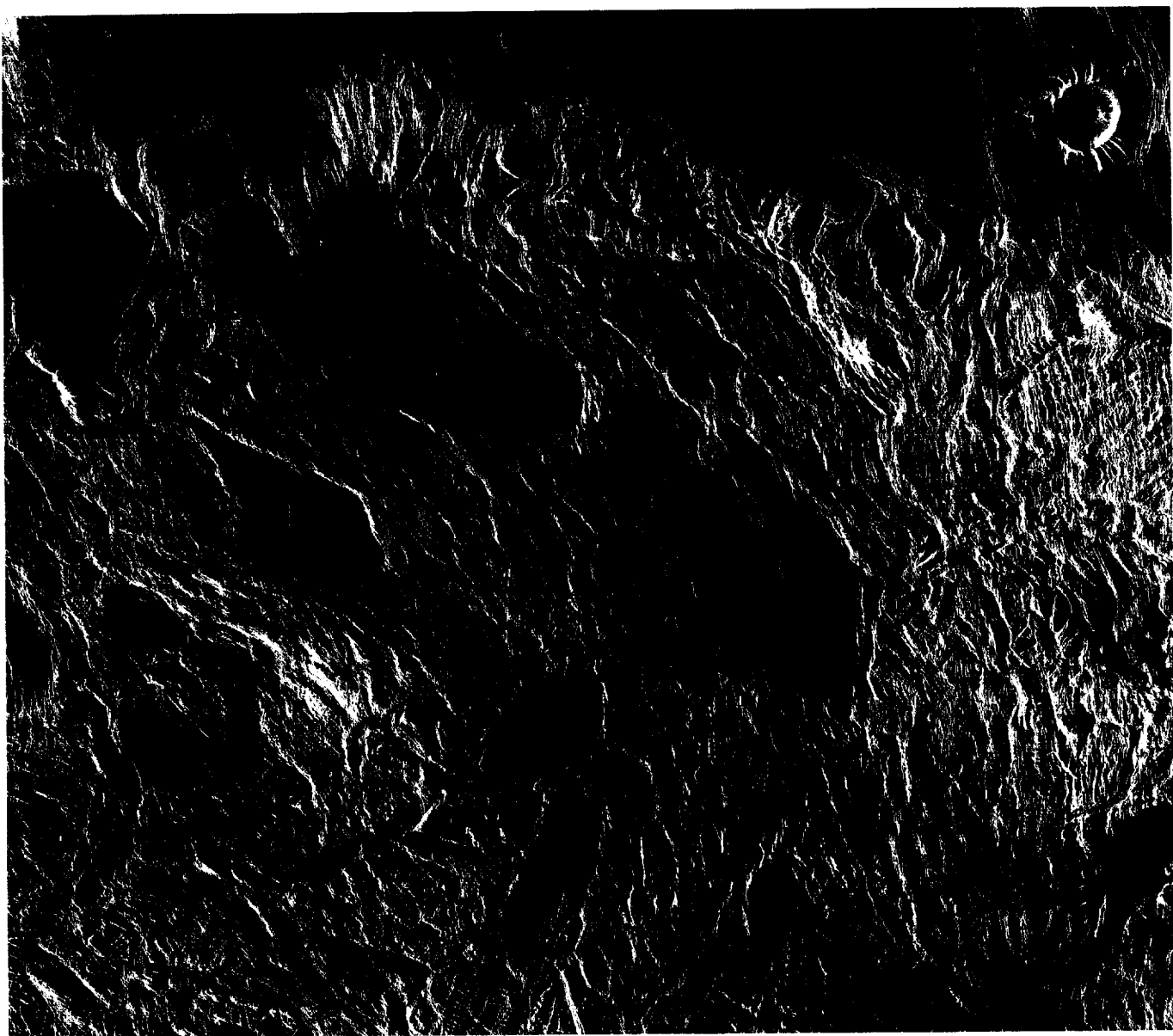
Figure 8-10. Complex ridge terrain (tesserae), centered at 21°S, 2.5°E in Alpha Regio, is characterized by three or more sets of intersecting lineaments. Illumination is from the left at an incidence angle of 37.5 deg.

Figure 8-11. The 225 × 210-km corona Neyterkob, centered at 49.5°N, 204°E, shows associated volcanic deposits within the annulus and around the outer edge of the corona. Illumination is from the left at an incidence angle of 33.6 deg.
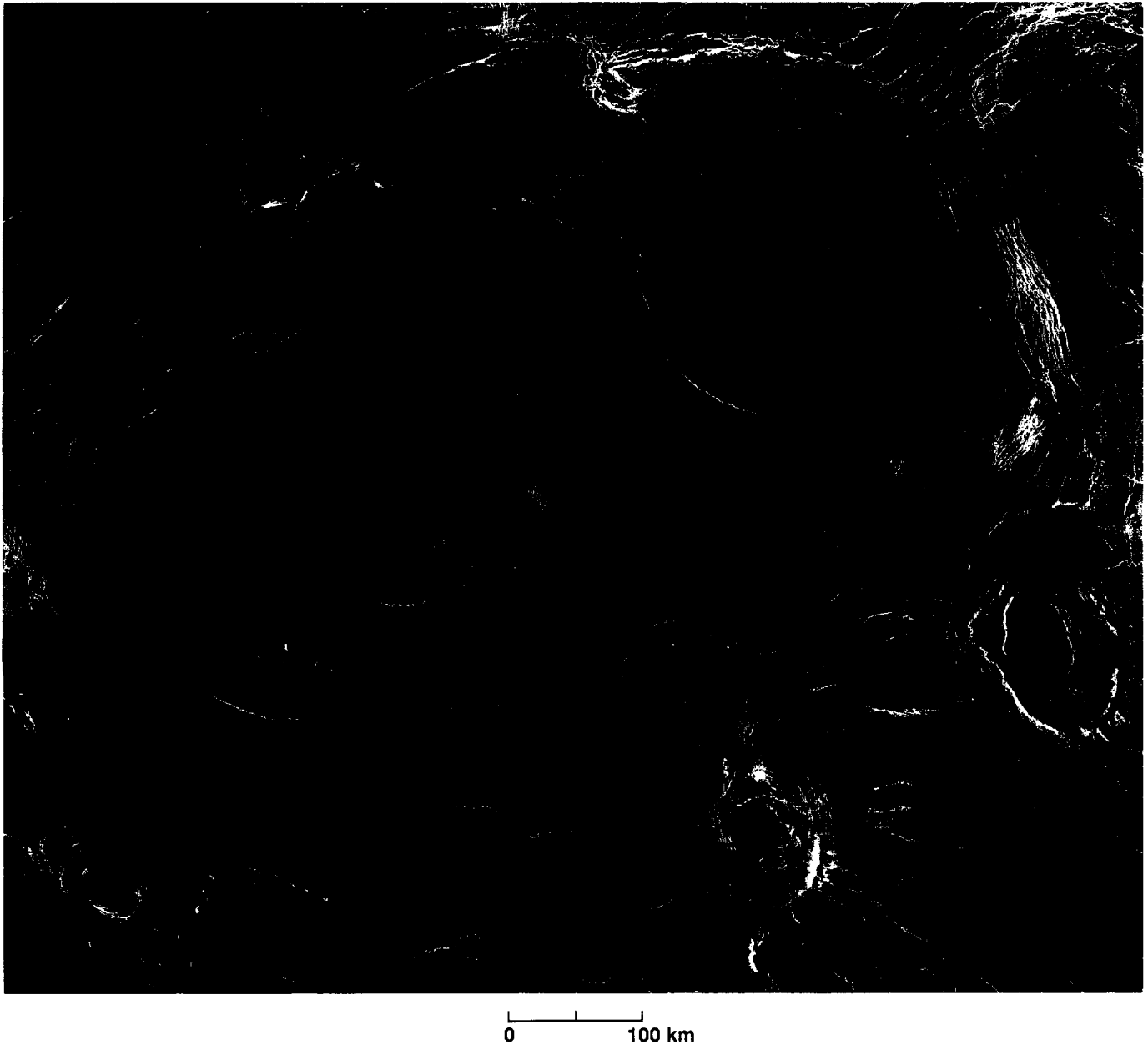
Figure 8-12. Arachnoids located in Sedna Planitia. Illumination is from the left at an incidence angle of 45 deg.

References

Banerdt, W. B., and C. G. Sammis, 1992, "Small-scale fracture patterns on the volcanic plains of Venus," *J. Geophys. Res.,* v. 97, p. 16149–16166.

Barsukov, V. L., et al., 1986, "The geology and geomorphology of the Venus surface as revealed by the radar images obtained by Veneras 15 and 16," *J. Geophys. Res.,* v. 91, p. D378–D398.

Basilevsky, A. T., A. A. Pronin, L. B. Ronca, V. P. Kryuchkov, A. L. Sukhanov, and M. S. Markov, 1986, "Styles of tectonic deformation on Venus: Analysis of Veneras 15 and 16 data," *J. Geophys. Res.,* v. 91, p. D399–D411.

Bindschadler, D. L., and E. M. Parmentier, 1990, "Mantle flow tectonics and a ductile lower crust: Implications for the formation of large-scale features on Venus," *J. Geophys. Res.,* v. 95, p. 21329–21344.

Bindschadler, D. L., G. Schubert, and W. M. Kaula, 1992a, "Cold-spots and hot-spots: Global tectonics and mantle dynamics of Venus," *J. Geophys. Res.*, v. 97, p. 13495–13532.

Bindschadler, D. L., A. deCharon, K. K. Beratan, S. E. Smrekar, and J. W. Head, 1992b, "Magellan observations of Alpha Regio: Implications for formation of complex ridged terrains on Venus," *J. Geophys. Res.*, v. 97, p. 13563–13577.

Crumpler, L. C., J. W. Head, and D. B. Campbell, 1986, "Orogenic belts on Venus," *Geology*, v. 14, p. 1031–1034.

Ford, J. P., 1980, "Seasat orbital radar imagery for geologic mapping: Tennessee–Kentucky–Virginia," *Amer. Assoc. of Petrol. Geol. Bull.*, v. 64, p. 2064–2094.

Frank, S. L., and J. W. Head, 1990, "Ridge belts on Venus: Morphology and origin," *Earth, Moon, and Planets*, v. 50/51, p. 421–470.

Herrick, R. R., and R. J. Phillips, 1990, "Blob tectonics: A prediction of Western Aphrodite Terra, Venus," *Geophys. Res. Lett.*, v. 17, p. 2129–2132.

Ivanov, M. A., T. Tormanen, and J. W. Head, 1992, "Global distribution of tesserae: Analysis of Magellan data" (abstract), *LPSC XXII*, p. 581–582.

Kaula, W. M., D. L. Bindschadler, R. E. Grimm, V. L. Hansen, K. M. Roberts, and S. E. Smrekar, 1992, "Styles of deformation in Ishtar Terra and their implications," *J. Geophys. Res.*, v. 97, p. 16085–16120.

MacDonald, H. C., 1980, "Techniques and Applications of Imaging Radar," in *Remote Sensing in Geology*, edited by B. S. Siegel and A. R. Gillespie, New York: John Wiley and Sons, Chapter 10.

Masursky, H., E. Eliason, P. G. Ford, G. E. McGill, G. H. Pettengill, G. G. Schaber, and G. Schubert, 1980, "Pioneer Venus radar results: Geology from images and altimetry," *J. Geophys. Res.*, v. 85, p. 8232–8260.

McGill, G. E., S. J. Steenstrup, C. Barton, and P. G. Ford, 1981, "Continental rifting and the origin of Beta Regio," *Geophys. Res. Lett.*, v. 8, p. 737–740.

McKenzie, D., J. M. McKenzie, and R. S. Saunders, 1992, "Dike emplacement on Venus and on Earth," *J. Geophys. Res.*, v. 97, p. 15977–15990.

Muller, O. H., and D. D. Pollard, 1977, "The state of stress near Spanish Peaks, Colorado, determined from a dike pattern," *Pure Appl. Geophys.*, v. 115, p. 69–86.

Nikolayeva, O. V., A. A. Pronin, A. T. Basilevsky, M. A. Ivanov, and M. A. Kreslavsky, 1988, "Are tesserae the outcrops of feldspathic crust on Venus?" (abstract), *LPSC XIX*, p. 864–865.

Pronin, A. A., and E. R. Stofan, 1990, "Coronae on Venus: Morphology and distribution," *Icarus*, v. 87, p. 452–474.

Saunders, R. S., R. E. Arvidson, J. W. Head, G. G. Schaber, E. R. Stofan, and S. C. Solomon, 1991, "An overview of Venus geology," *Science*, v. 252, p. 249–252.

Senske, D. A., J. W. Head, E. R. Stofan, and D. B. Campbell, 1991, "Geology and structure of Beta Regio, Venus: Results from Arecibo radar imaging," *Geophys. Res. Lett.*, v. 18, p. 1159–1162.

Smrekar, S. E., and R. J. Phillips, 1988, "Gravity-driven deformation of the crust of Venus," *Geophys. Res. Lett.*, v. 15, p. 693–696.

Smrekar, S. E., and S. C. Solomon, 1992, "Gravitational spreading of high terrain in Ishtar Terra, Venus," *J. Geophys. Res.*, v. 97, p. 16121–16148.

Solomon, S. C., and J. W. Head, 1982, "Mechanisms of lithospheric heat transfer on Venus: Implications for tectonic style and volcanism," *J. Geophys. Res.*, v. 87, p. 7763–7771.

Solomon, S. C., and J. W. Head, 1984, "Venus banded terrain: Tectonic models for band formation and their relationship to lithospheric thermal structure," *J. Geophys. Res.*, v. 89, p. 6885–6897.

Solomon, S. C., and J. W. Head, 1991, "Fundamental issues in the geology and geophysics of Venus," *Science*, v. 252, p. 252–260.

Solomon, S. C., J. W. Head, W. M. Kaula, D. McKenzie, B. Parsons, R. J. Phillips, G. Schubert, M. Talwani, 1991, "Venus tectonics: Initial analysis from Magellan," *Science*, v. 252, p. 297–312.

Solomon, S. C., S. E. Smrekar, D. L. Bindschadler, R. E. Grimm, W. M. Kaula, G. E. McGill, R. J. Phillips, R. S. Saunders, G. Schubert, S. W. Squyres, and E. R. Stofan, 1992, "Venus tectonics: An overview of Magellan observations," *J. Geophys. Res.*, v. 97, p. 13199–13255.

Squyres, S. W., D. G. Jankowski, M. Simons, S. C. Solomon, B. H. Hagar, G. E. McGill, 1992a, "Plains tectonism on Venus," *J. Geophys. Res.*, v. 97, p. 13579–13599.

Squyres, S. W., D. M. Janes, G. Baer, D. L. Bindschadler, G. Schubert, V. L. Sharpton, and E. R. Stofan, 1992b, "The morphology and evolution of coronae on Venus," *J. Geophys. Res.*, v. 97, p. 13611–13634.

Stofan, E. R., J. W. Head, D. B. Campbell, S. H. Zisk, A. F. Bogomolov, O. N. Rzhiga, A. T. Basilevsky, and N. Armand, 1989, "Geology of a rift zone on Venus: Beta Regio and Devana Chasma," *GSA Bull.*, v. 101, p. 143–156.

Stofan, E. R., and J. W. Head, 1990, "Coronae of Mnemosyne Regio, Venus: Morphology and origin," *Icarus,* v. 83, p. 216–243.

Stofan, E. R., D. L. Bindschadler, J. W. Head, and E. M. Parmentier, 1991, "Coronae on Venus: Models of origin," *J. Geophys. Res.,* v. 96, p. 20933–20946.

Stofan, E. R., V. L. Sharpton, G. Schubert, G. Baer, D. L. Bindschadler, D. M. Janes, and S. W. Squyres, 1992, "Global distribution and characteristics of coronae and related features on Venus: Implications for origin and relation to mantle processes," *J. Geophys. Res.,* v. 97, p. 13347–13378.

Sukhanov, A. L., and A. A. Pronin, 1988, "Spreading features on Venus" (abstract), *LPSC XIX,* p. 1147–1148.

Suppe, J., and C. Connors, 1992, "Critical taper wedge mechanics of fold-and-thrust belts on Venus: Initial results from Magellan," *J. Geophys. Res.,* v. 97, p. 13545–13561.

Vorder Bruegge, R. W., and J. W. Head, 1990, "Tectonic evolution of eastern Ishtar Terra," *Venus, Earth, Moon, and Planets,* v. 50/51, p. 251–304.

Watters, T. R., 1988, "Wrinkle ridge assemblages on the terrestrial planets," *J. Geophys. Res.,* v. 93, p. 10236–10254.

Watters, T. R., 1992, "System of tectonic features common to Earth, Mars, and Venus," *Geology,* v. 20, p. 609–612.

Chapter 9. Volcanic Features

John P. Ford, Jeffrey J. Plaut, and Timothy J. Parker

Introduction

Magellan SAR images show that volcanic features are abundant and widely distributed on Venus. Notable features include widespread, mostly lowland lava plains, extensive flows, lava channels, small shields, cones, domes, intermediate to large shields, and caldera-like structures not associated with shield volcanoes. Other large features such as coronae and arachnoids (considered to be volcanotectonic in origin [Stofan et al., 1992]) are discussed in Chapter 8. Outflow features associated with impact craters are covered in Chapter 7.

Observations from Magellan images supported by Magellan altimetry and radiometry data have provided quantitative information about the morphology (size, shape, and relief), radar backscatter, reflectivity, and emissivity of these volcanic features, as well as their frequency distribution, geologic associations, and general correlations with elevation. Such observations have been used to infer the physical properties of the planetary surface—for example, centimeter-scale roughness, decameter-scale slope, lithologic composition, and dielectric properties.

The majority of volcanic materials on Venus (e.g., plains and shields) are thought to be basaltic in composition, partly because of their geomorphic expression. This view is supported to some extent by compositional information returned from Soviet Vega and Venera space probes [Barsukov et al., 1982 and 1986].

Volcanic Plains

Volcanic plains cover large, mostly lowland areas separated by mountains or ridge belts; they extend over 85%

of the planetary surface (Figure 9-1). The plains range in elevation from about 1.5 km below to 2 km above the mean planetary radius of 6051.84 km [Guest et al., 1992]. They consist of extensive sheets of flood lavas hundreds of kilometers in width and mostly 100 to 700 km in length, and they show a range of radar backscatter characteristics. Wide sheets of flood lavas with uniform radar responses may represent complexes composed of multiple flow units. In the absence of defining radar characteristics, however, it may not be possible to discriminate individual flow units in the image data.

Lava Flows

Lava flows form important radar mapping units in Magellan images. The outlines and large-scale dimensions of lava flows together with such small-scale features as the smoothness or blockiness of the surfaces, the presence or absence of channels, levees, and pressure ridges, and the characteristics of the flow margins, provide important information about the mechanisms of flow emplacement. Preferred flow directions may reveal topographic and/or structural control. The age relations of adjacent flows can be determined where superposition is evident, particularly where older lavas are transected by fractures that do not disrupt younger, overlying lavas.

Variations in image brightness between flows or in different portions of a single flow are commonly thought to denote changes in surface roughness at the scale of the radar wavelength (12.6 cm). Flood lavas may be strongly contrasted, or they may show mottling over large areas. A radar mosaic of plains in the Navka Planitia region (Figure 9-2) shows bright and dark patches that represent
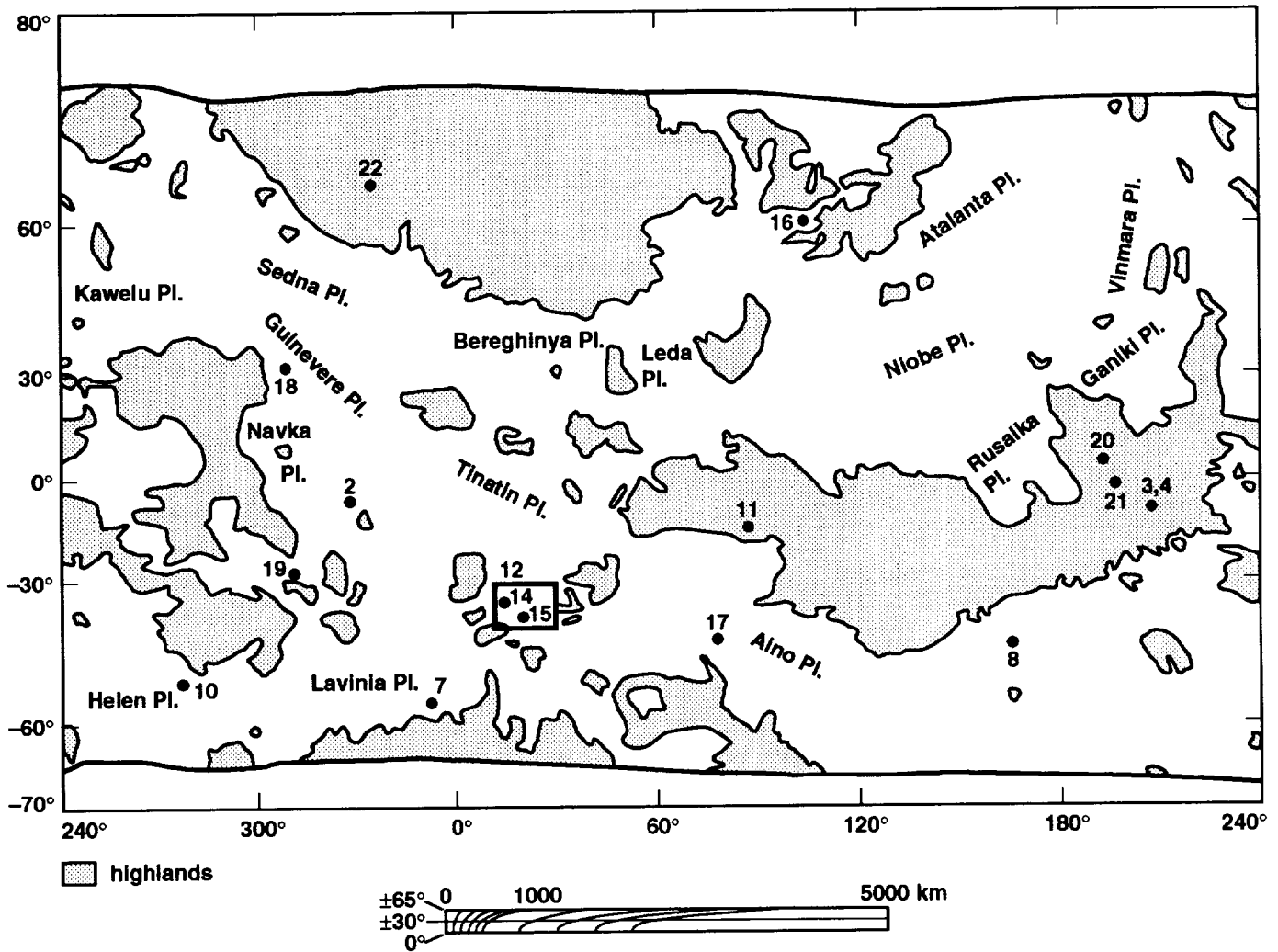
Figure 9-1. Global distribution of volcanic plains (Pl. = Planitia) on Venus [modified from Guest et al., 1992]. Locality numbers (e.g., 2, 3, ...) correspond to figure numbers (e.g., 9-2, 9-3, ...).

overlapping flows. However, the sources of the flood lavas are not generally perceptible. The significance of the brightness changes may relate to such variables as the rheology of the flows at the time of emplacement or to differences in preservation states caused by postdepositional surface processes (see Chapter 6) [Arvidson et al., 1992]. Many flows contain small volcanic shields and cones.

Other physical parameters, such as dielectric properties or the radar viewing geometry, may also affect the radar brightness of flow surfaces. At different incidence angles, the sensitivity of backscatter to variations in roughness and dielectric constant may differ [Plaut and Arvidson, 1992]. Corresponding images of lava flows taken in successive imaging cycles at different incidence angles indicate that

some brightness variations are caused by such intrinsic reflectivity differences. A flow field south of Ozza Mons in Atla Regio (Figure 9-3) consists of numerous adjacent and overlapping flows that show varying backscatter strengths. A simple interpretation of this image, which was taken at 43.7 deg incidence (Cycle 1), would relate image brightness directly to wavelength-scale surface roughness. However, the image taken at 24.9 deg incidence (Cycle 2, Figure 9-4) provides different contrast relations. In particular, one of a number of bright flows in the Cycle 1 image appears in the Cycle 2 image as the brightest flow in the field. A plot of backscatter values as a function of incidence angle (Figure 9-5) shows that this bright flow and a more typical flow to the east differ greatly in backscatter at smaller angles, but converge to nearly identical values at larger angles.
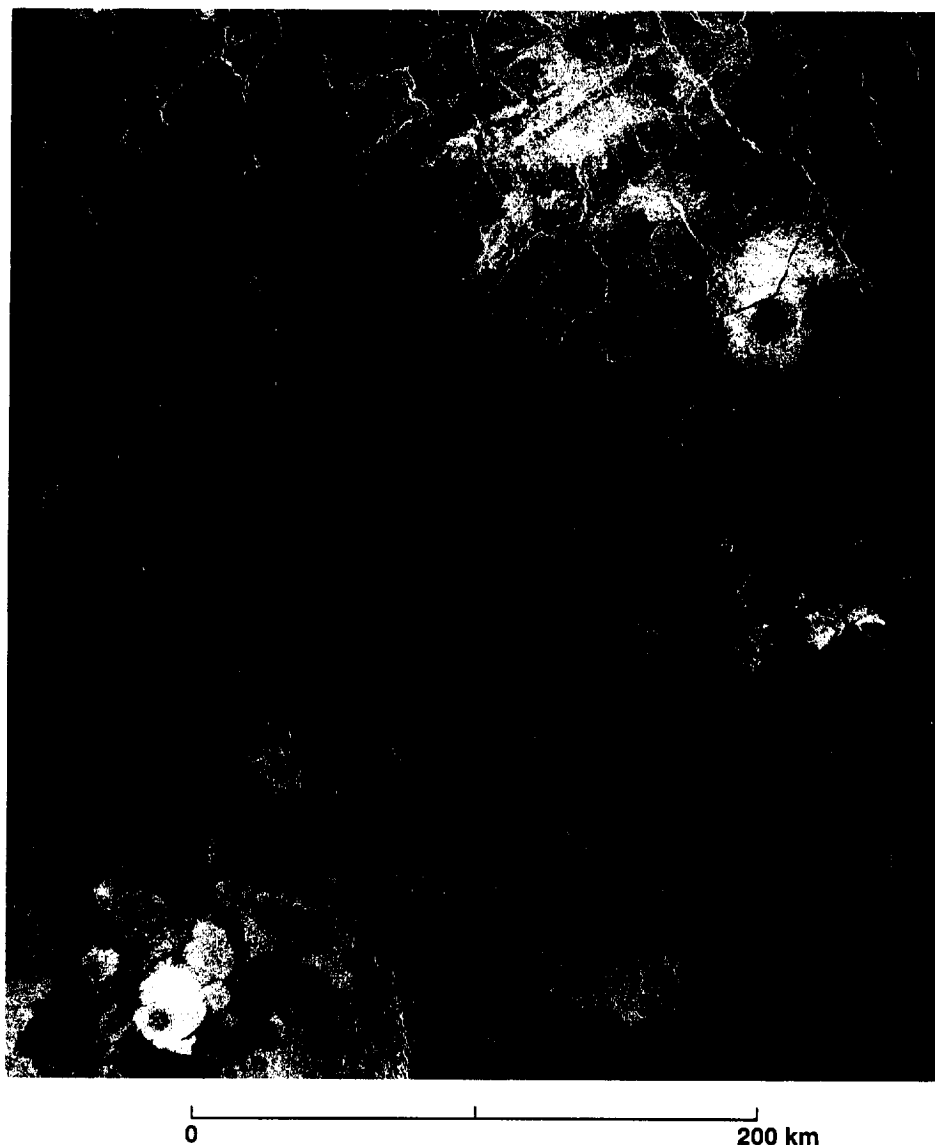
Figure 9-2. Radar mosaic of broad plains in the region of Navka Planitia shows bright and dark flows with many small shields and cones. Vertical striping in the mosaic is an artifact of processing. Illumination is from the left at an incidence angle of 44 deg.

The scattering function of the flow to the east is not strongly dependent on incidence angle, a condition consistent with a very rough surface. The bright flow, however, shows a strong dependence on incidence angle, with a scattering function slope similar to that of a plains surface to the south and to the average Venus scattering function itself. The bright flow may have a relatively smooth upper surface that, because of a high dielectric constant, appears bright at both incidence angles. This interpretation is supported by measurements (Figure 9-6) that show the bright flow has lower emissivity, and thus higher dielectric constants, than any of the other

flows that appear bright in the Cycle 1 image. The higher dielectric constants of the bright flow may be the result of a greater bulk density, unusual chemical composition, or a combination of both.

Mylitta Fluctus is a complex of six flow fields in the southern hemisphere of Venus [Roberts et al., 1992]. The area is similar in size to the Columbia River flood basalt province on Earth. Each flow field is composed of numerous individual flow episodes identified by continuities in flow boundaries and central channels and by similarities in radar backscatter and surface texture. Many of the flows are long
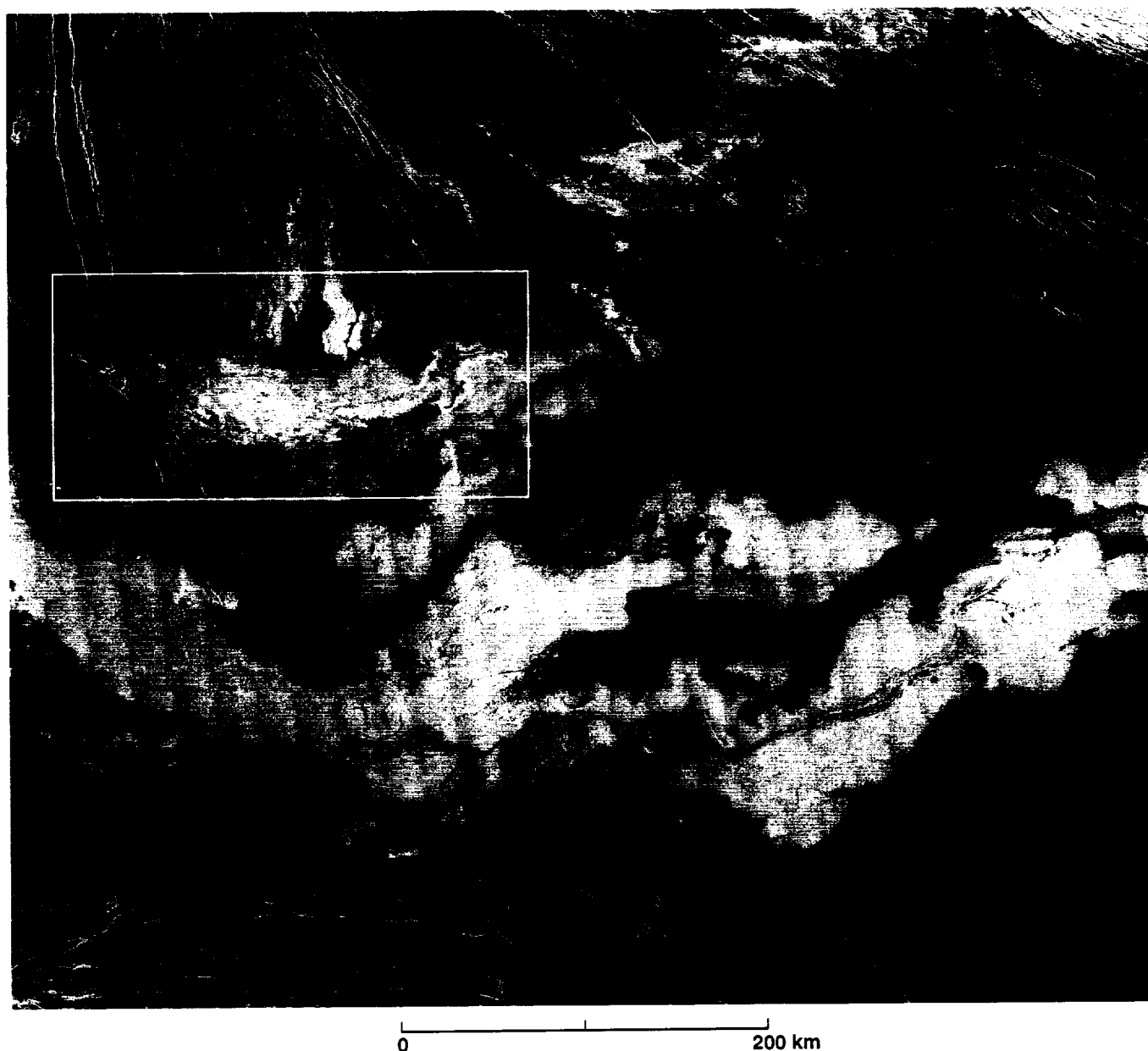
111

Figure 9-3. Lava flow field south of Ozza Mons. The image was obtained at about a 44-deg incidence angle in Cycle 1 (F-MIDR 05S205). Box denotes the area of detail shown in Figure 9-4.

(hundreds of kilometers), comparatively narrow (tens of kilometers), and have uniform radar textures that show no pronounced transverse ridges (Figure 9-7). Combined with measurements of relief, radar backscatter, and dielectric constant, these landform and surface characteristics are thought to indicate a generally basaltic composition [Campbell and Campbell, 1992].

A volcano on the plains between Artemis Chasma and Imdr Regio displays a sheet of thick radar-bright flows and

broad flow lobes. The lobes and flows show prominent transverse ridges that have an average spacing of about 750 m. The flow features are associated with a complex domical structure about 100 km across and 1 km in relief (Figure 9-8). They are surrounded at a lower elevation by plains surfaces that expose radar-bright volcanic deposits [Moore et al., 1992]. These materials extend some 360 to 400 km from the volcano. They appear to overlie the radar-dark, lowland plains that dominate this region of the surface.
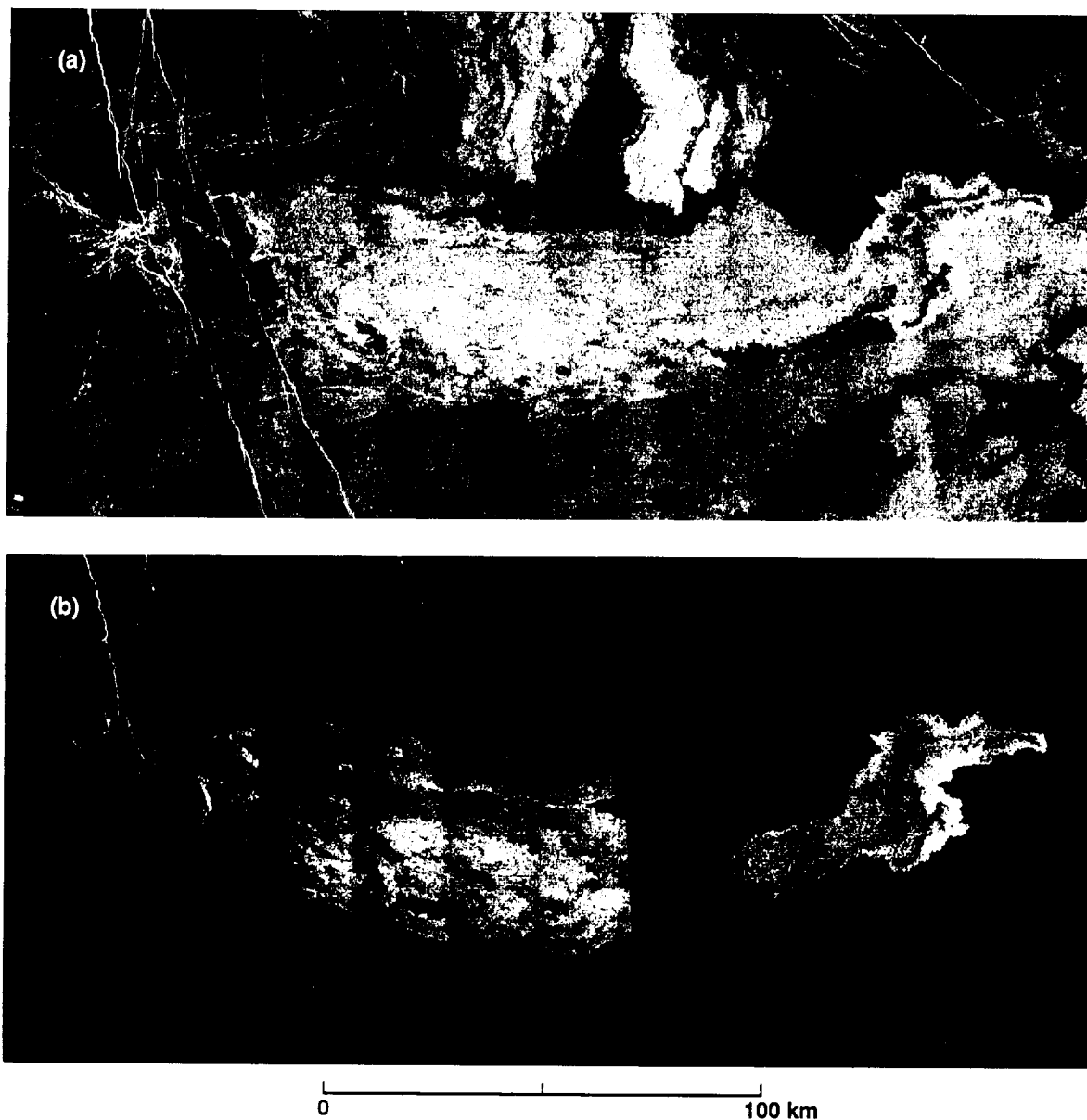
Figure 9-4. Enlargement of area in the box of Figure 9-3: (a) at a 43.7-deg incidence angle from Cycle 1; (b) at a 24.9-deg incidence angle from Cycle 2. Note that the flow with strong backscatter relative to surrounding flows in (b) shows very little contrast with the surrounding flows in (a).

This volcano and the surrounding radar-dark plains were imaged from the left at about 27.5 deg incidence (Cycle 1) and 15.6 deg incidence (Cycle 3), and from the right at about 25.3 deg incidence (Cycle 2). Contrasts in backscatter intensities combined with stereo observations of fine-scale topography in the image data provided the basis for discriminating eight radar mapping units (Figure 9-9). Stratigraphic ages determined from contact relations indicate that the plains units are older than the mesa units and that

backscatter increases systematically with decrease in relative age of the units.

Local relief of the scarps and lobes in the mesa units was computed from geometric distortions (parallax) of corresponding features observed in the left- and right-side viewing images. Where appropriate, the measurements were compared with calculations based on an assumed symmetry of features parallel to the illumination vector (details of these methods are given in Chapters 4 and 7). The measurements
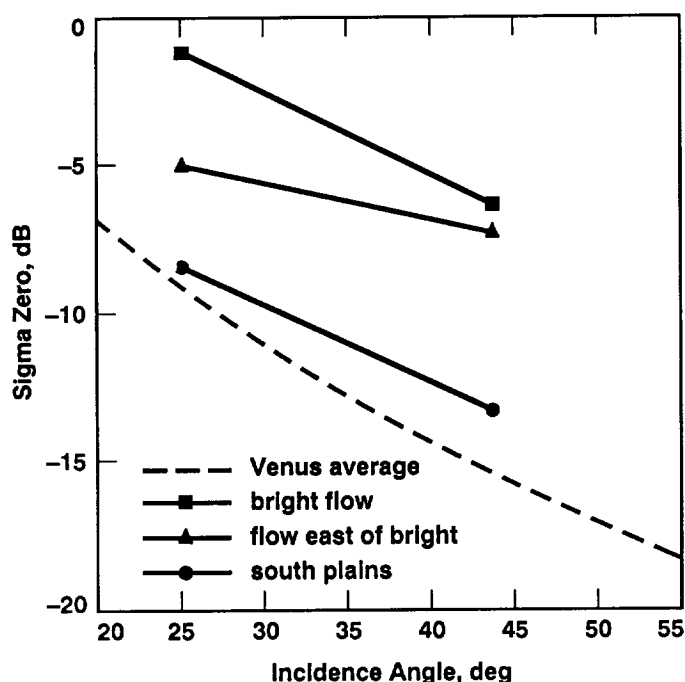
113

Figure 9-5. Backscatter plotted as a function of incidence angle for several surfaces in the area covered by F-MIDR 05S205. Small incidence angle data are from Cycle 2; large incidence angle data from Cycle 1. The bright flow has a steep scattering function compared to the surrounding flows. This suggests that higher dielectric constants, rather than greater roughness, are responsible for the prominent brightness in the Cycle 2 image.

indicate that in the ridged mesas the scarps have relief up to 205 m; in the lobate mesas, the relief is from 133 to 723 m.

The contrasted distribution, form, and thickness of the sheet flows and lobes with the deposits on the adjacent radar-bright plains are thought to have resulted from the differentiation of a primary magma source [Moore et al., 1992]. By analogy with volcanism on Earth, it is postulated that an initial, low-viscosity, mafic eruptive phase could have produced the extensive, thin, bright-plains deposits. A more viscous, silicic secondary phase resulted in the emplacement of the much thicker, more areally restricted sheet flows and broad flow lobes.

Lava Channels

Lava channels hundreds to thousands of kilometers in length are conspicuous on the volcanic plains of Venus. Simple channels typically show little or no branching. They include long sinuous forms, termed "canali," and sinuous rilles. However, Venusian channels are not as tightly sinuous as terrestrial rivers. Complex channels show anastomosing or braided patterns. Integrated valleys that may have formed by sapping processes have also been observed in Magellan images [Baker et al., 1992].

Canali are best preserved in regions of subdued relief. They have a high width-to-depth ratio and maintain a remarkably constant width over very long distances. Images reveal the presence of meanders, point bars, cut banks, and abandoned channel segments. Canali that are transverse to the radar illumination may show bright radar response from the far-range banks of some meander segments (Figure 9-10). This may indicate localized steepening of the cross channel slope due to bank cutting.

Both the source and the distal ends of many canali are buried or extensively subdued by lava flows younger than those that formed the channels. Measurements have shown considerable relief in longitudinal channel profiles, implying significant tectonic deformation of the plains since the channels formed [Parker et al., 1992]. Wrinkle ridges and ridge belts commonly transect canali. Vertical displacements of hundreds of meters over horizontal distances of a few kilometers are common at ridge crossings.

Sinuous rilles emanate from roughly circular to elongate depressions and become progressively narrower and more shallow in the downstream direction (Figure 9-11). They are typically 1 to 2 km wide and tens to hundreds of kilometers in length. Channel walls form a distinct boundary between the channel floor and the surrounding terrain. Channel material is similar to that of the surrounding terrain and may be either radar dark or radar bright.

An example of complex flow channels occurs in the proximal region of Mylitta Fluctus (Figure 9-7, area 6). Channels in the medial and distal regions are wider, broadly sinuous, relatively constant in width, and generally radar dark. A radar-dark channel that extends for about 100 km in the medial region of Mylitta Fluctus (Figure 9-7 north of area 4) shows infilling of one segment by a younger lava flow.

A channel over 1200 km long that displays both simple and complex reaches is located in the northern Lada Terra region (Figures 9-12 and 9-13). The channel originates in a collapse structure on the southwest flank of the volcano Ammavaru. The main channel (about 5.5 km wide) flows south-southeast in a linear trough for about 300 km. This channel is too narrow to be resolved in Magellan altimetry data.

Profiles from stereo measurements indicate relief up to 600 m across the collapsed source area [Parker et al., 1992]. Because the linear trough is oriented transverse to the illumination, the distal wall appears very bright and the proximal wall is dark in the images (Figures 9-12 and 9-14).
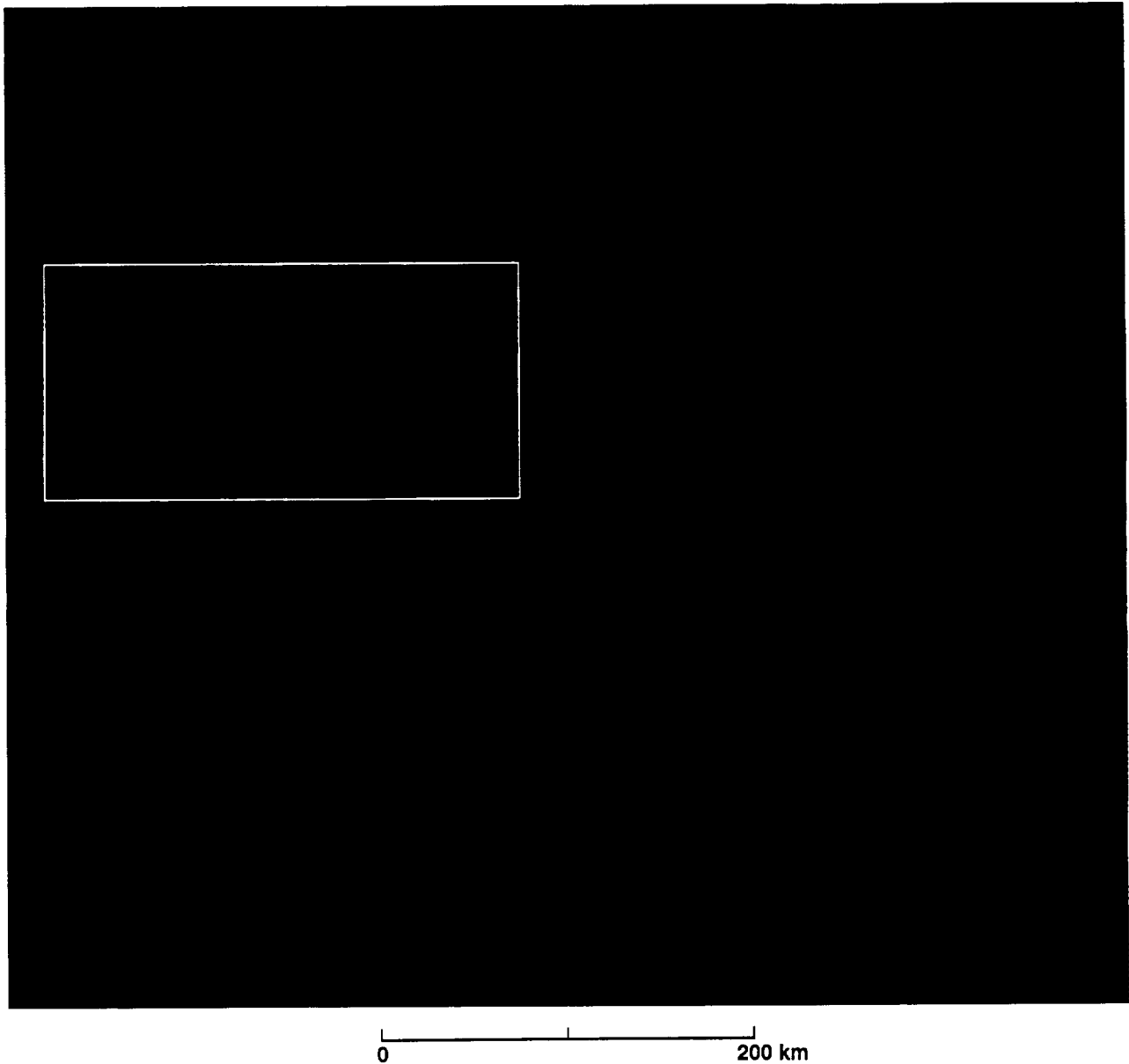
Figure 9-6. F-MIDRP.05S205, Cycle 1, with emissivity overlay in color, encoded from 0.65 (purple) to 0.92 (red). Note that the bright flow in Figure 9-4 is the only bright flow that also shows low emissivity. This supports the interpretation that higher dielectric constants are responsible for the stronger backscatter.

The southern, topographically lower end of the trough was flooded with lavas that appear radar-dark in the image (Figure 9-12). At 51.5°S, 25.5°E (Figure 9-13), the flood spreads into a broad anastomosing reach (Figure 9-15). East of the highlands at this locality the channel branches into a distributary reach for about 130 km. Three radar-dark distributaries change to radar-bright with dark margins about midway along this reach (Figure 9-12). Bright flow deposits

with lobate morphology are extensively distributed here. The deposits are ponded on the west side of a north-trending ridge belt for over 300 km. The main distributary channel extends through these deposits and terminates eastward at an extensive radar-bright plain east of a breach in the ridge belt. The radar-bright deposits from the outflow channel cover an area of about 100,000 km^2; they show broad lobate margins typical of lava flows.

115

0   200 km

Figure 9-7. Flow fields of Mylitta Fluctus in Lavinia Planitia. Numbered rectangles show (1) a bright flow across the flank of the shield volcano with dark channels and bright levees (south) and mottled marginal channels and levees (north); (2 and 7) flows blocked by arcuate lineaments (scarps or troughs); (3) dark, relatively uniform textured flows; (4) mottled texture (which may represent short overlapping flows); (5) subparallel elongate flows with reasonably uniform texture, widths of 20 to 30 km, and perimeters bounded by areas of lower backscatter; (6) a branching and braided channel with some well-defined, radar-bright levees. The black band is data dropout. Illumination is from the left at an incidence angle of 22 deg.

Small Volcanoes

Volcanic constructs and edifices on Venus have been classified and subdivided on the basis of their size and morphology [Slyuta and Kreslavsky, 1990; Head et al., 1992]. Centers with a diameter less than 20 km are considered small. Small features occur typically on the plains but they are found also on the flanks of large volcanoes and in association with coronae and arachnoids; they consist mostly of small shields and cones. Some domes are included in this size category.

Small Shields

Small shields have outlines that range from circular to elongate. Generally they display very shallow slopes and are not associated with flow deposits. In cases where the slope angle is low (less than about 5 deg), it is not possible to determine the height or slope of the features from single images. Nevertheless, the height of such features can be measured by stereo techniques provided corresponding coverage is available at different incidence angles (see Chapter 4). Many small shields have been discriminated by their smooth circular outlines and image tones that are darker than the surrounding plains. The outlines may also be diffuse. However, in cases where there is no clear backscatter contrast, the shields may be distinguished by the presence of a centrally located, circular summit pit about 1 km or less in diameter. With respect to the radar illumination vector, the distal wall of the pit is bright and the proximal wall is dark.

Clusters of small shields (~10 km in diameter) are widely distributed in association with linear fracture belts on the plains, mostly at intermediate elevations (Figure 9-2). Though many shields in a cluster show circular outlines, some are elongate with the long axis parallel to the strike of the associated fractures. In this type of setting, individual flows may be perceptible in association with the small shields. Possible terrestrial analogues include plains volcanism in the Snake River Plain of southern Idaho [Greeley, 1982] and clusters of central vent edifices that have been identified on the Mid-Atlantic Ridge [Smith and Cann, 1990].

Cones

Cones are circular features with steep slopes and a centrally located summit pit. Slopes from 12 to 23 deg and heights from 200 to 1700 m have been measured [Guest et al., 1992]. Because of their steepness, foreslopes appear compressed and bright in images; correspondingly, backslopes are elongated and dark (Figure 9-16). Individual flows are mostly not visible. Cones tend to occur in clusters on the plains. A temporal relation between cones or shields in a cluster and fractures on the plains is evident in cases where

some of the cones or shields are cut by fractures and therefore are older, while other cones or shields in the cluster are superposed on the fractures and thus are younger.

Small Domes

Comparison of image pairs obtained at significantly different incidence angles demonstrates that the discrimination of small, low-relief features on the volcanic plains may be strongly governed by the radar incidence angle. In the Aino Planitia region, a group of small domes with diameters of 6 km or less and relief up to 140 m was imaged from approximately the same illumination direction at incidence angles of 28.5 deg in Cycle 1 and 15.6 deg in Cycle 2 (Figure 9-17).

At the smaller incidence angle (Cycle-2 image), the radar backscatter from the steep slopes that face toward the illumination is dominantly specular. Small changes in slope give large changes in backscatter. This provides bright radar responses that enhance the perception of the domes in the image. At the larger incidence angle (Cycle-1 image), backscatter is much less sensitive to topographic variations. Thus, the ability to discriminate these comparatively small-scale features on the surrounding plains is much reduced.

The perception of small-scale roughness differences on the plains also varies with the incidence angle. At the higher incidence angle (Cycle-1 image), the radar scattering is dominantly diffuse for rough surfaces and dominantly specular (forward scattering) for smooth surfaces. This results in strongly contrasted levels of radar brightness that enable the discrimination of rough (bright) and smooth (dark) surfaces in the images. At the lower incidence angle (Cycle-2 image), the backscatter from the plains surfaces is controlled primarily by topographic variations. As a consequence, the contrasts in radar image brightness that provide surface roughness discrimination in the Cycle-1 image are mostly not perceptible in the Cycle-2 image.

Intermediate Volcanoes

Intermediate volcanoes are defined as centers between 20 to 100 km in diameter. Typically they consist of relatively symmetrical shields characterized by radial lava flows and fracture patterns. Domes are prominent features in this size class.

Domes

The majority of Venusian domes range in diameter from less than 10 km to about 100 km with a mean of about 24 km and in height from 70 to 2000 m with a mean of about 700 m

0   100 km

Figure 9-8. Volcano on plains between Artemis Chasma and Imdr Regio. This image shows lobate mesas with pronounced transverse ridges on many of the flows. Plains are transected by ridges (northeast) and fractures (northwest). The black band is data dropout. Illumination is from the right at an incidence angle of 25 deg.
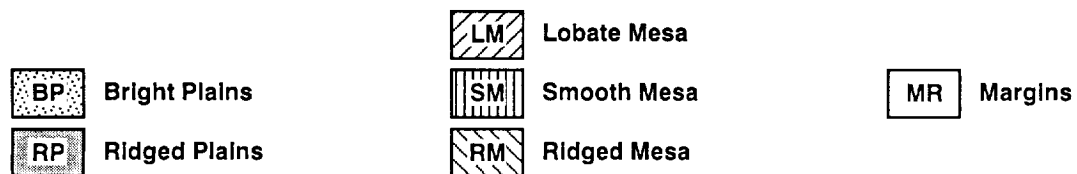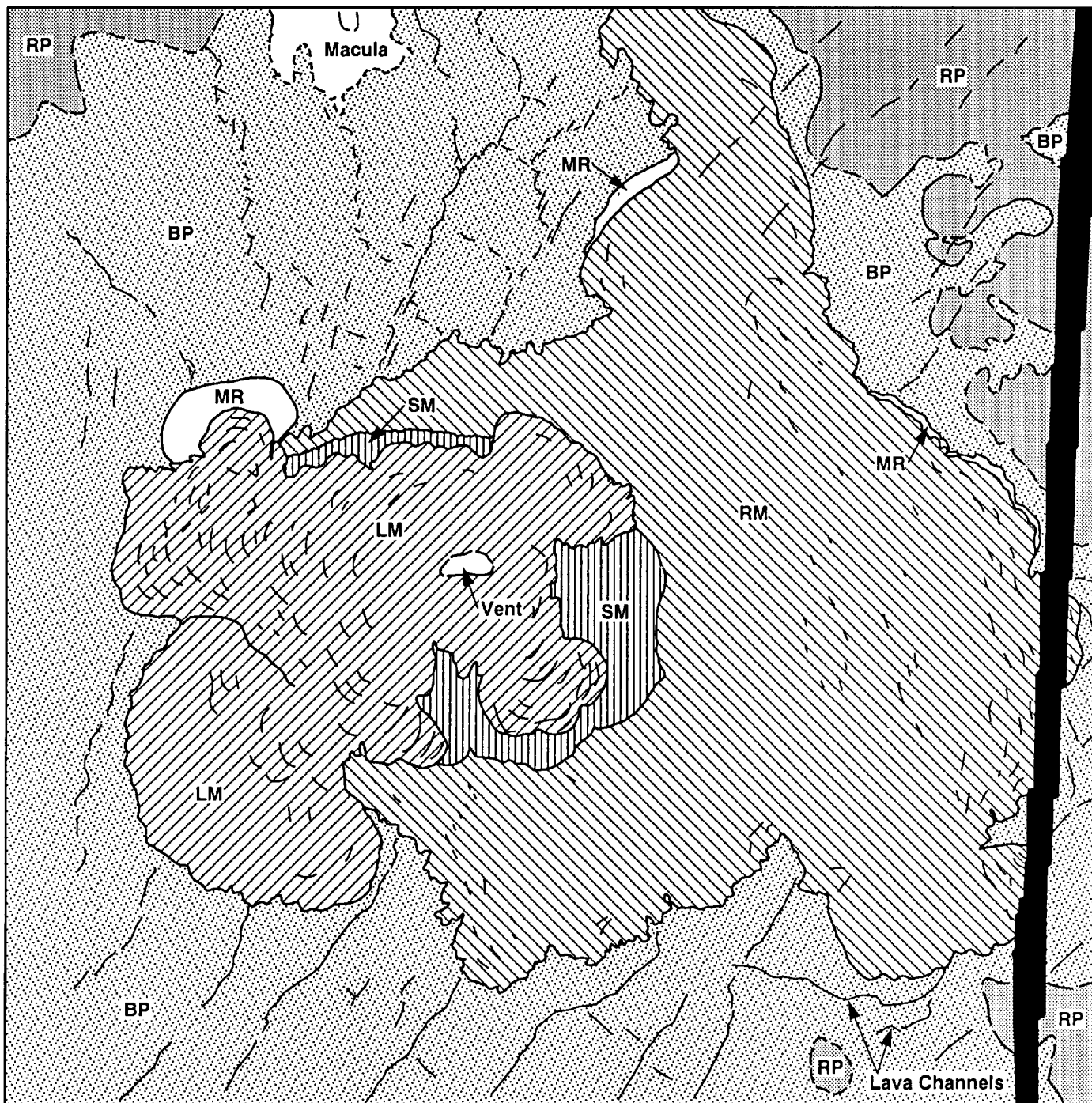
Figure 9-9. Radar map units of volcano in Figure 9-8 [modified from Moore et al., 1992].
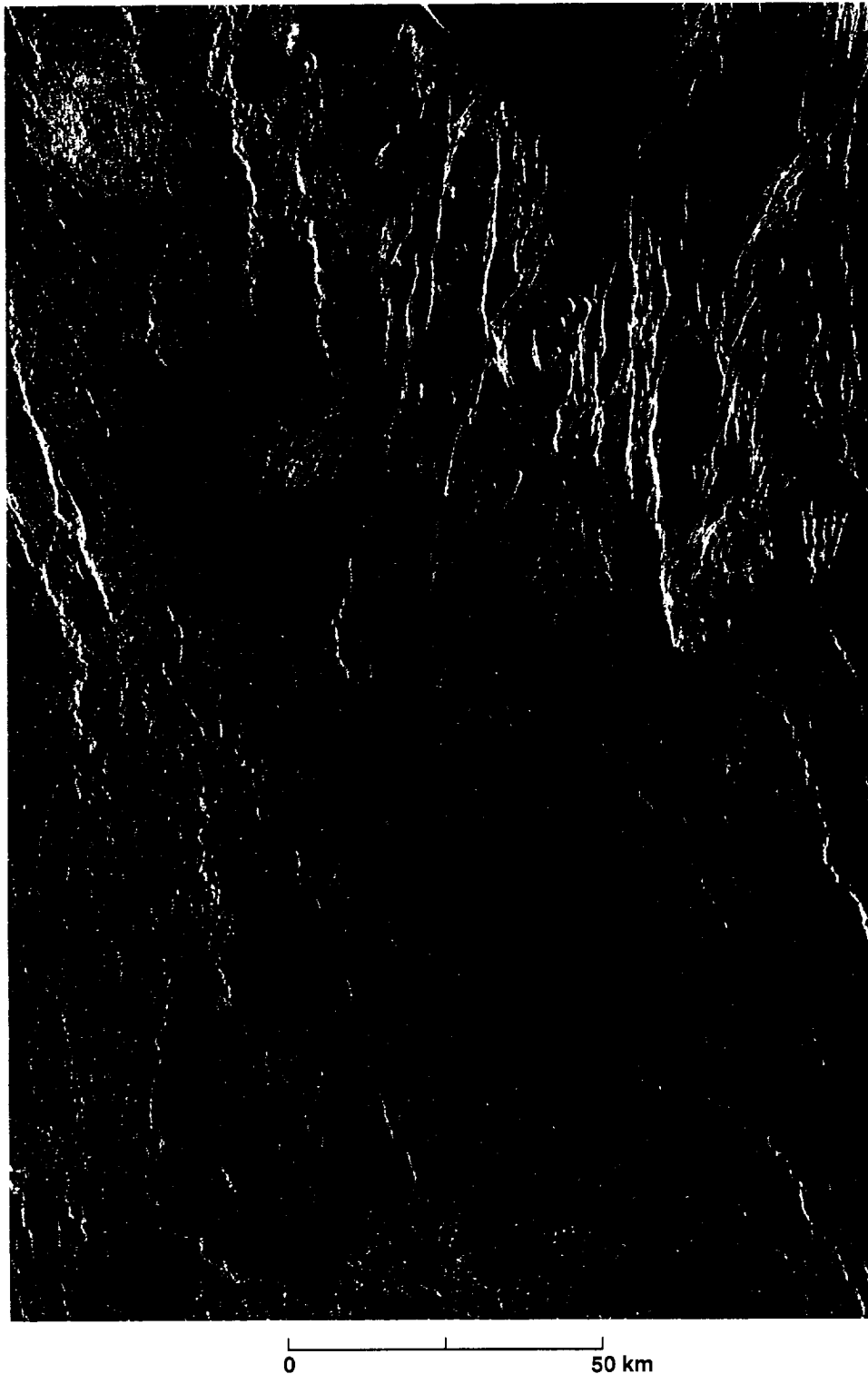
119

0   50 km

Figure 9-10. Sinuous segment of simple radar-dark channel about 200 km long and 2 km wide. Channel outline at both ends is indistinct, probably because of infilling by younger lavas. Thin bright returns from channel walls denote steep slopes that face toward the illumination vector. A transecting relict channel of approximately similar width is denoted by parallel bright margins (levees) that cross the lava plains in a northwest direction on each side of the radar-dark channel. Illumination is from the left at an incidence angle of 23 deg.

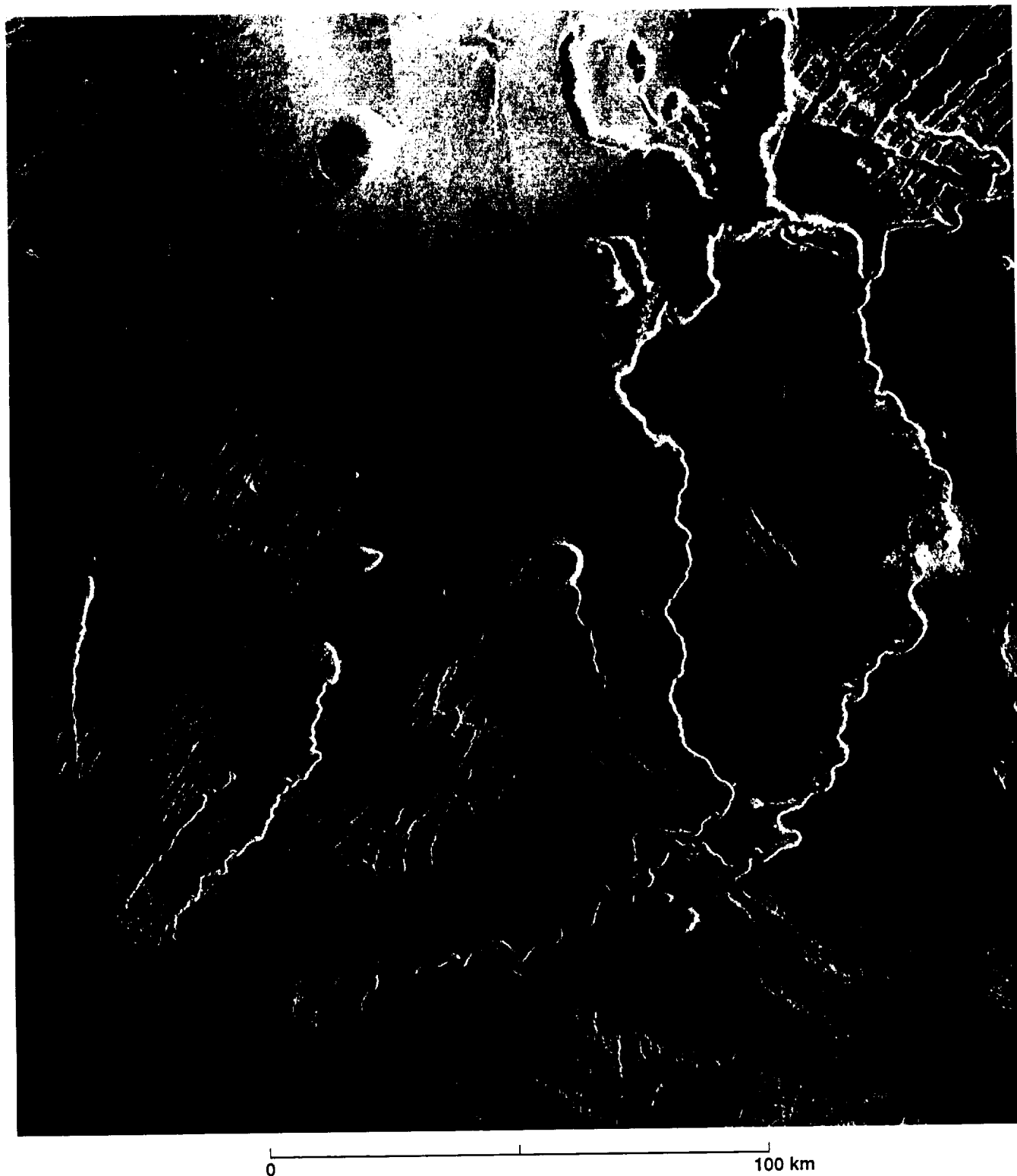0   100 km

Figure 9-11. Sinuous rilles emanate from depressions and enlarged fractures south of Ovda Regio. Segments of the channels trend parallel to the structural strike (some northeast; others northwest). Note radar-bright responses of steep channel walls that face toward the illumination. An impact crater about 12 km in diameter has disrupted the eastern channel at center right. Illumination is from the left at an incidence angle of 41 deg.

```
L_____I_____J
0                                             400 km
```
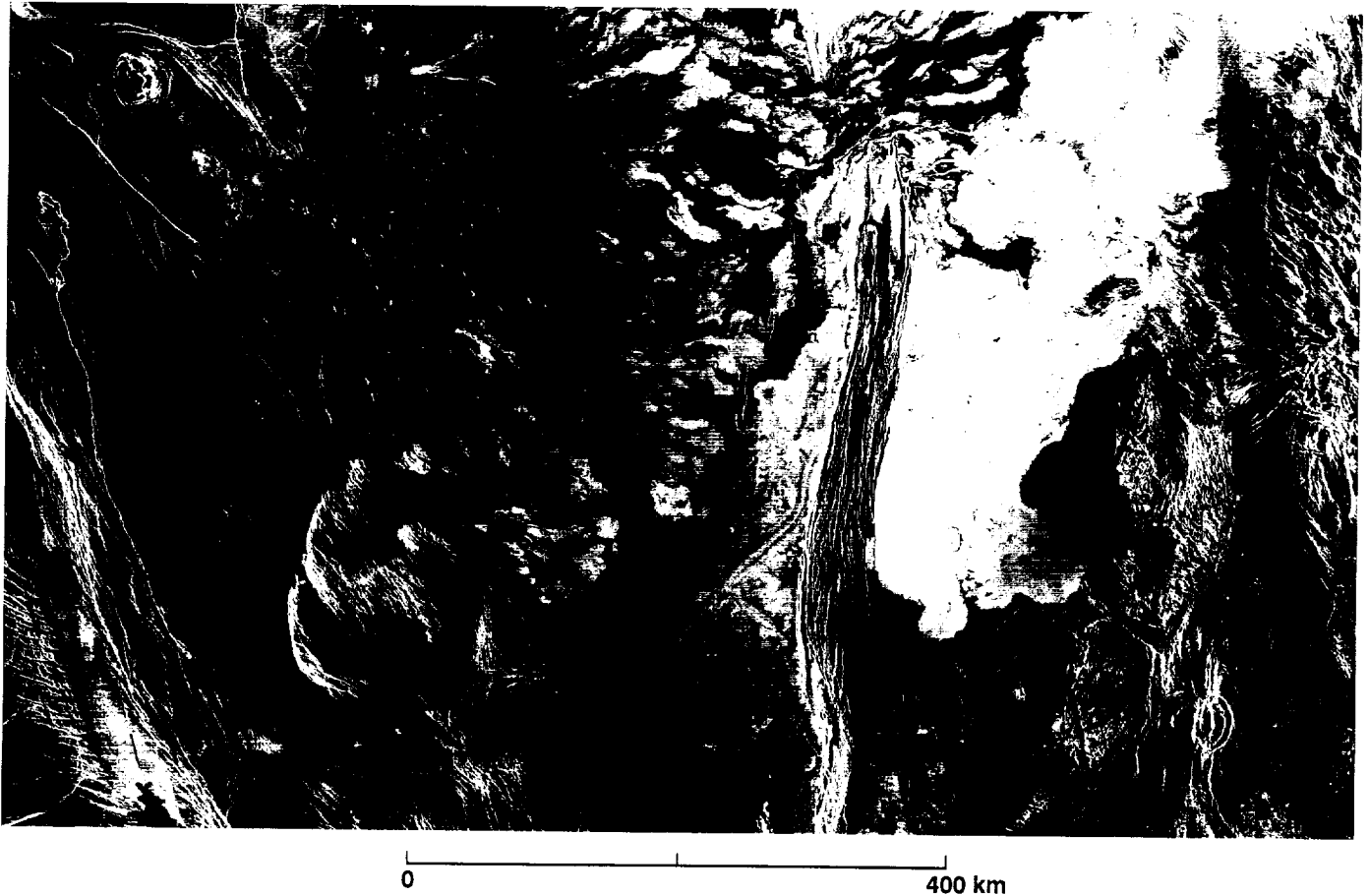
Figure 9-12. Radar mosaic of Ammavaru volcanic complex and associated outflow channel in the Lada Terra region. The channel displays a broadly U-shaped outline across the image that extends from a collapse source on the southwest flank of Ammavaru (upper left), through reaches that are anastomosing (lower left center) and distributary (lower center), to terminal flow deposits east of a breach in the north-trending ridge (upper right). Illumination is from the left at an incidence angle that ranges from 25 deg (north) to 23 deg (south).

above the surrounding terrain. Mostly, they are surrounded by a steep perimeter and have a relatively flat top. Images reveal that these features are remarkably circular in outline. Measurements indicate that the surfaces are slightly rough and have a slightly lower reflectivity and correspondingly higher emissivity than the surrounding terrain. The combination of radial symmetry, a steeply sloping perimeter, and strong relief exhibited by many domes suggests that they may have formed from viscous lava that erupted uniformly from a central vent [Pavri et al., 1992].

Small craters are a common feature of the surfaces of all domes; they may or may not be central. Breakouts occur on the flanks of some domes and radial fractures extend down the slopes into the surrounding plains. Numerous domes show evidence of postemplacement alteration by processes that include gravitational collapse, slumping, tectonism, impact, and lava flooding.

Domes occur singly, in pairs, groups, or overlapping clusters. Many domes are associated with coronae (see Chapter 8), but the eruptive mechanism is not clearly understood. They are preferentially concentrated at elevations near or just below the mean planetary radius (~6052 km).

A cluster of four overlapping domes is shown in Figure 9-18. The large dome with a diameter of about 50 km in the upper center shows strongly contrasted radar brightness around the perimeter. Very bright returns in a narrow band around the northwest quadrant denote steep foreslopes in this sector. Dark tones from segments around the northeast quadrant denote weak backscatter from steep backslopes there. The outline of the standing walls shows that the perimeter of the dome has collapsed in this quadrant. Outflow toward the northwest is indicated by the nature of the surface in the collapsed area between the existing periphery of the dome and isolated remnants of its formerly circular perimeter walls.
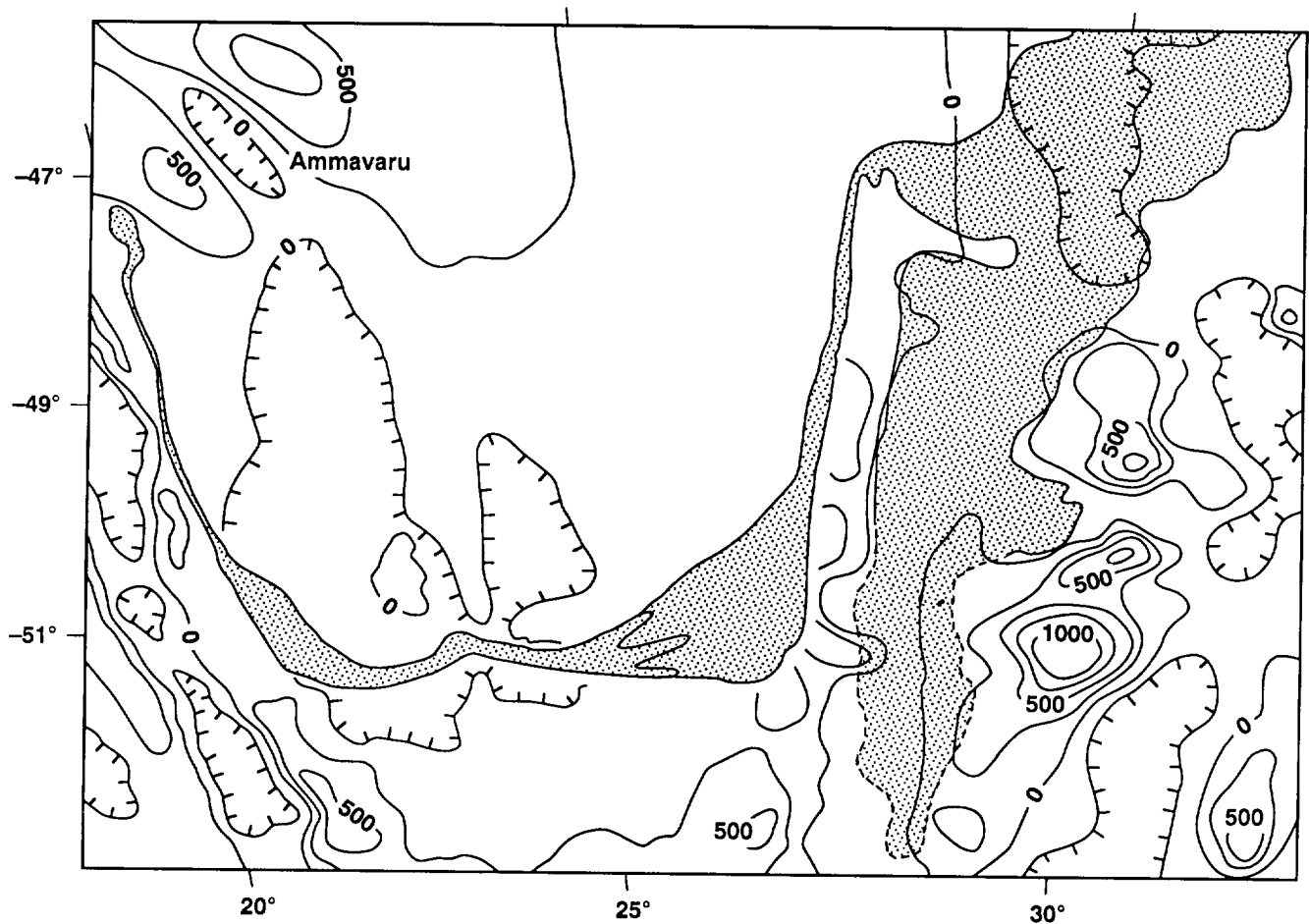
Figure 9-13. Topographic map of area covered in Figure 9-12. Outflow channel and associated flow deposits are stippled. Topography is derived from altimetry data. Datum is planetary radius (~6052 km). Contour interval is 250 m [modified from Baker et al., 1992].

In the southern half, the perimeter is topographically less pronounced and it intersects the equally less pronounced perimeters of two nearly equidimensional domes to the south. The absence of brightness from the foreslopes of these perimeter segments indicates subdued topography compared to the northwest quadrant of the central dome.

Collapse Features

Some volcanic domes have steep scalloped margins. The outline of the scallops and the presence of debris aprons in places around the margins suggests that the scallops were formed by slope failure (see Chapter 6). In addition, scalloped-margin domes are often surrounded by concentric fractures. The dome in Figure 9-19 shows collapsed margins and associated landslide deposits in both the northwest and the northeast quadrants. Two pronounced slump scarps in the northwest provide very bright linear to curvilinear image

responses. The landslide deposits show hummocky surfaces that extend up to 10 km away from the dome. In general, the scale of lava domes and collapse features on Venus is orders of magnitude larger than that on Earth.

Large Volcanoes

Large volcanoes have diameters mostly in the 100- to 600-km range. Such edifices are characterized by a dominance of radial lava flows in association with positive topography. They occur mostly at higher elevations in broad rises and at tectonic junctions. They do not occur in the linear concentration that characterizes subduction-related plate tectonic boundaries on Earth.

Sapas Mons is a large volcano approximately 400 km in diameter and 1.5 km high located on a topographic rise in Atla

123
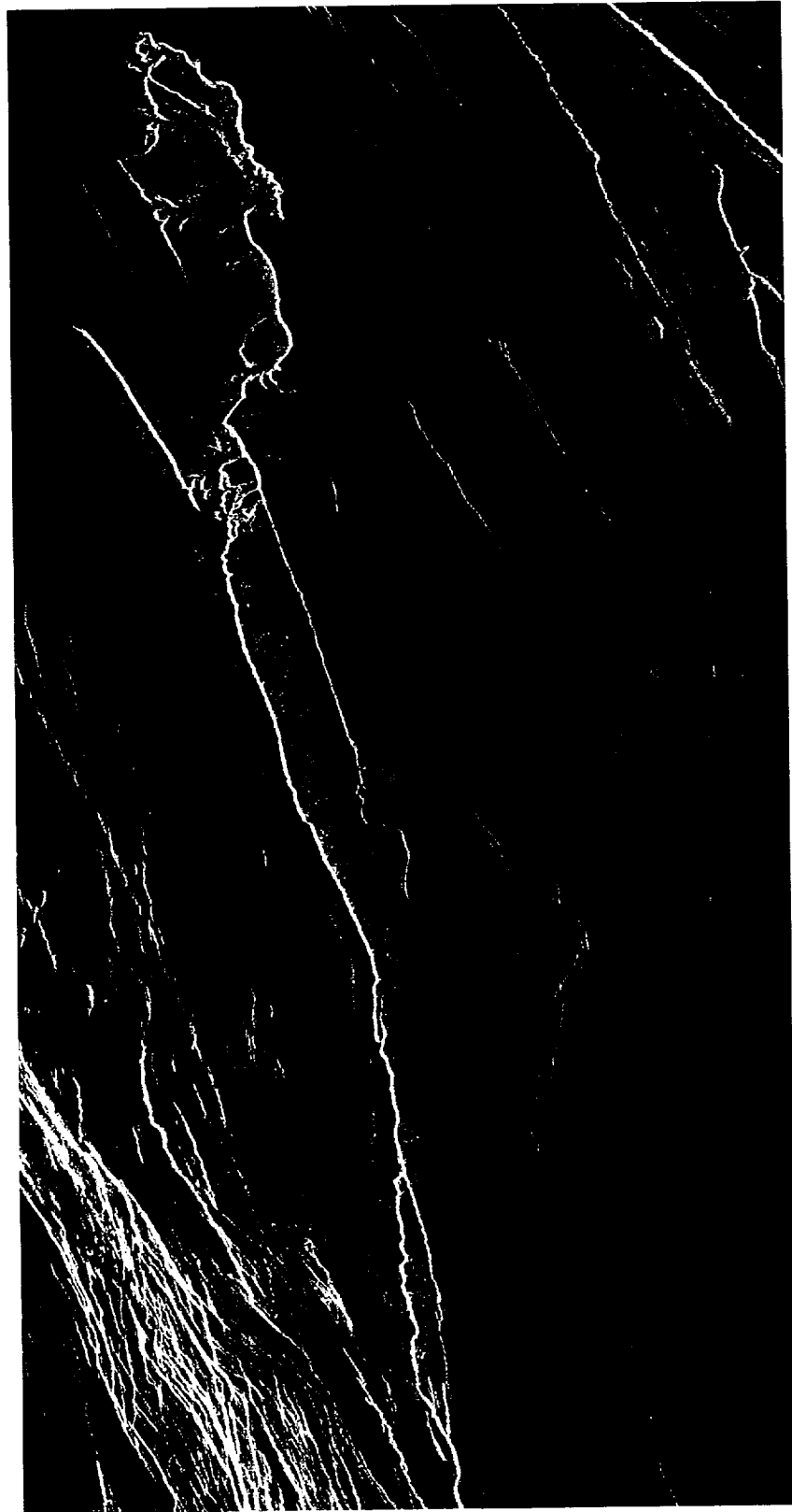
0   100 km

Regio. The summit consists of two mesas with flat to slightly convex tops and smooth surfaces that appear radar-dark in the image (Figure 9-20). Surrounding radar-bright collapsed areas provide the mesas with plan view outlines that resemble those of some scalloped-margin domes (see Domes, above). The foreslopes of both mesas appear very bright and strongly compressed.

A discrepancy occurred between the positive topography of the summit mesas observed in the image and the negative topography indicated for the same area in best-fitting model echo templates derived from altimetry measurements (ARCDR data) [Plaut, 1992]. Discrepancies of this type have demonstrated that, under certain circumstances, derived altimetry data may contain spurious values. The details are outlined in Chapter 3.

The sides of the volcano show numerous bright overlapping flows that provide the edifice with a roughly radial outline. Many of the flows appear to be flank eruptions. Radial fractures clearly transect the flows to the east and south. Darker flows in the southeast quadrant are probably smoother than the bright flows closer to the eruptive center.

An impact crater with a diameter of 20 km located in the northeast quadrant is partially buried by lava flows. A medium-to-light gray flow appears to be ponded to the west by the crater. This flow has been diverted south and east where it has buried a portion of the hummocky ejecta on the southeast side of the crater.

Maat Mons is a large elliptical volcano (195 × 125 km) that rises 9.2 km in Atla Regio. A three-dimensional perspective obtained by combining radar altimetry data with the two-dimensional image data (Figure 9-21) shows lava flows that extend north for hundreds of kilometers across fractured plains in the foreground.

Calderas

Calderas on Venus have been defined as circular to elongate depressions not associated with well-defined edifices. Characteristically they show the concentric patterns of surrounding fractures [Head et al., 1992]. They may lie in a broad region of elevated topography. They are distinct from impact craters in lacking a hummocky raised rim and an associated ejecta pattern.

Sacajawea Patera is an elliptical caldera (260 × 175 km) that forms a depression about 2 km deep (Figure 9-22). The depression is enclosed by a zone of concentric troughs that show radar-bright outlines extending from 60 to 130 km outward from the caldera floor. The floor is covered with smooth mottled plains. The brightest deposits occur around the periphery and near the center of the caldera floor where there is a ponded leveed flow. Linear to sinuous scarps show bright outlines that extend southeast from the eastern margin of the caldera. A small shield (12 km in diameter) is transected by one of these features.

Figure 9-14. Collapse source and upper reach of outflow channel on southwest flank of volcano Ammavaru. Main channel, about 5.5 km wide, is contained within a linear trough that extends south-southeast for about 300 km. A subsidiary channel about 1 km wide divides at the south limit of a linear scarp and reunites farther downstream. Radar-bright responses from banks on both sides of the channel south of the scarp probably denote levees in a plains environment. Illumination is from the left at an incidence angle of 24 deg.

Figure 9-15. Anastomosing reach of outflow channel shows streamlined islands that point eastward in the flow direction of the lava deposits. Radar-dark embayments in highland areas denote lava ponding and flooding that occurred prior to eastward channel cutting and formation of the distributary reach east of the highlands (right center). Illumination is from the left at an incidence angle of 23 deg.

0   60 km

Figure 9-16. Cluster of cones about 2 km in diameter, 200 m
high, with steep slopes (12 deg) overlying a fracture network in
Niobe Planitia. Some cones are cut by younger, more widely
spaced, north-striking fractures with curvilinear outlines.
Illumination is from the left at an incidence angle of 26 deg.
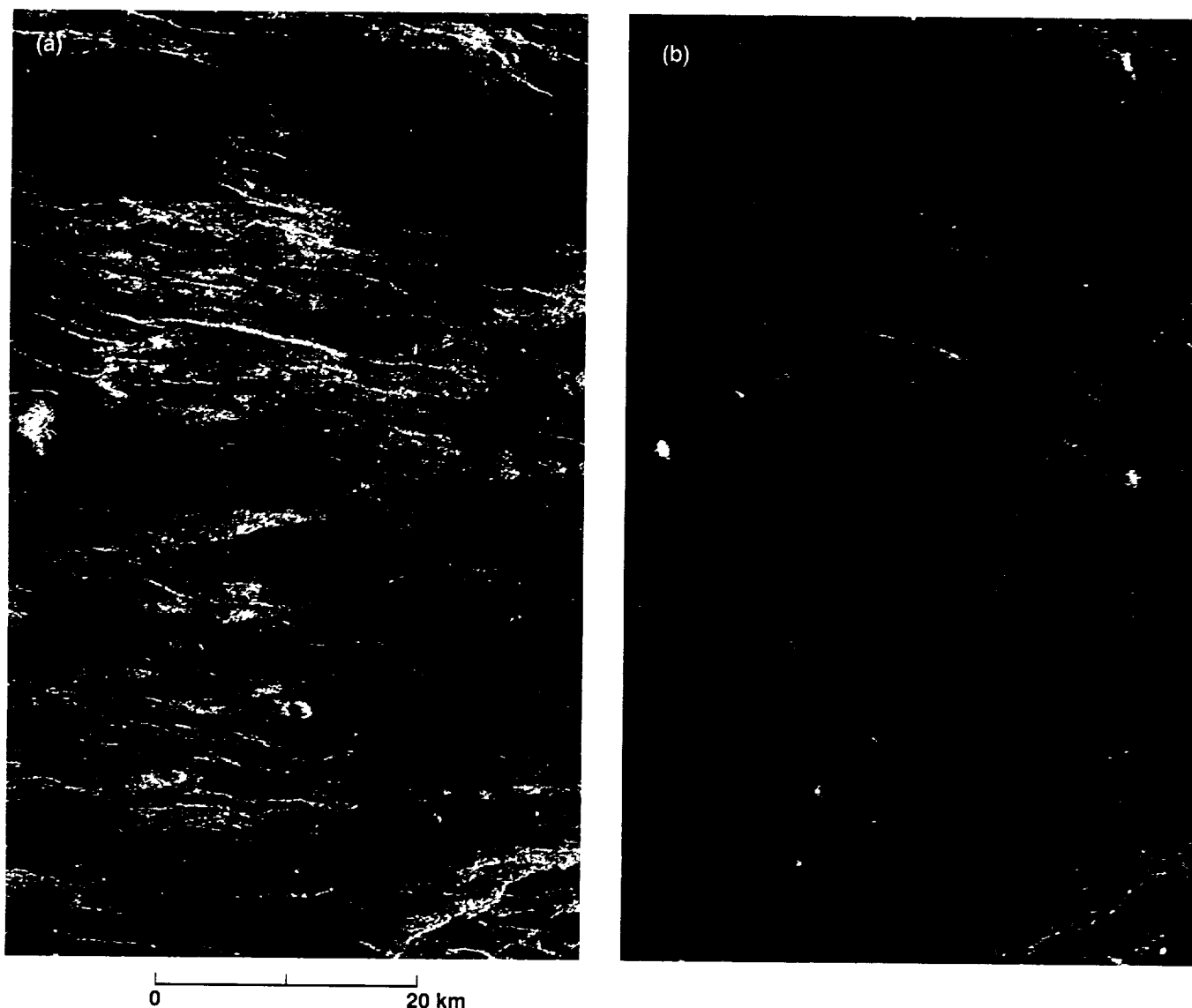
0 |——————————|——————————| 20 km

Figure 9-17. About 30 small, low-relief domes located on the plains of Aino Planitia. Image (a), obtained at a 28.5-deg incidence angle (Cycle 1), discriminates brighter rough surfaces from darker smooth surfaces on the plains but does not provide sufficient topographic contrast to discriminate most of the domes. Corresponding image (b), obtained at a 15.6-deg incidence angle (Cycle 2), shows pronounced contrast between the domes and the plains but fails to reveal a significant contrast between the smooth and rough surfaces. Illumination is from the left.
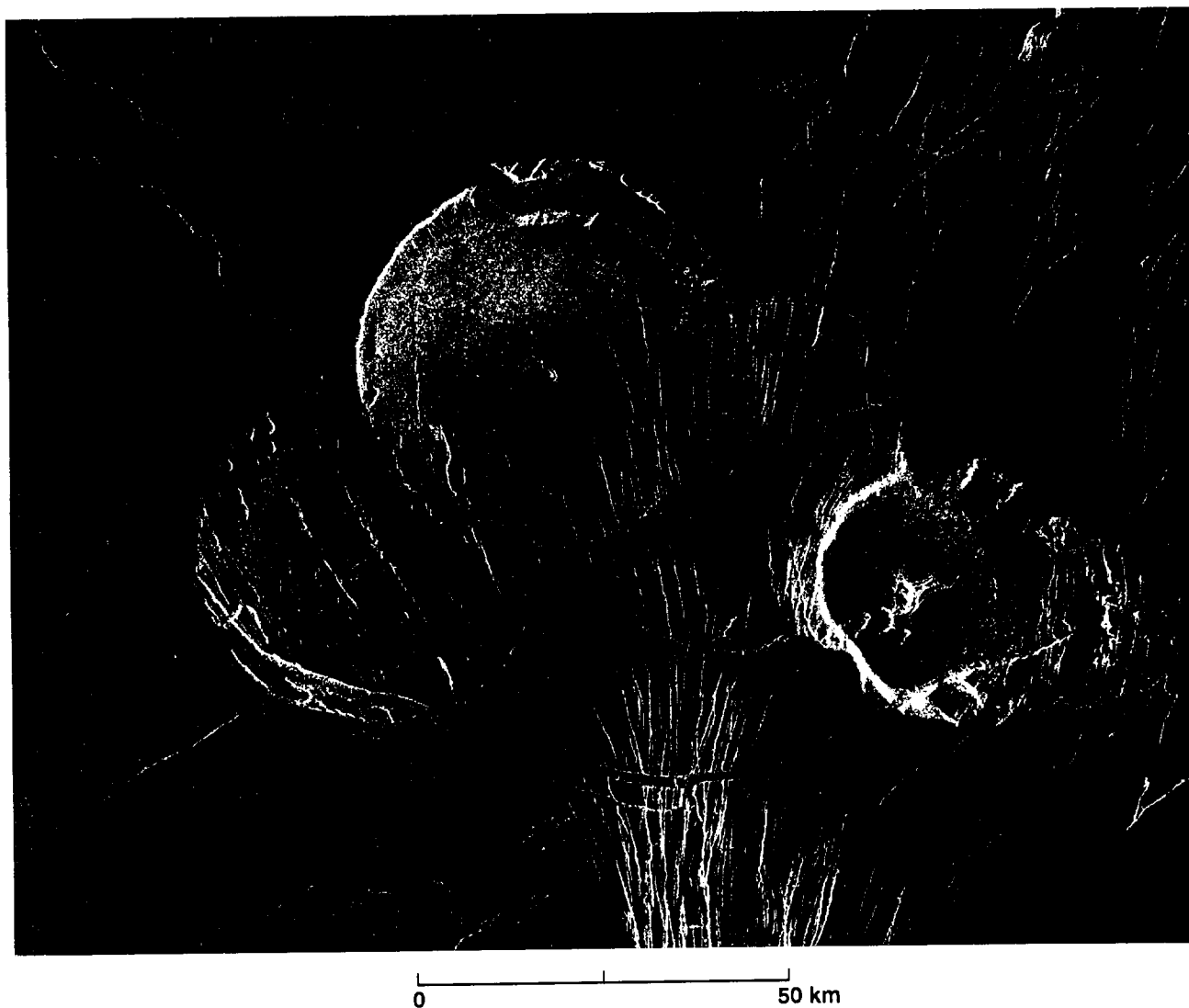
0   50 km

Figure 9-18. Cluster of domes in Guinevere Planitia shows collapsed margins and disruption by curvilinear fractures that emanate from the south. The planimetric form of the overriding central dome is not significantly modified by relief of the two underlying domes. Illumination is from the left at an incidence angle of 39 deg.
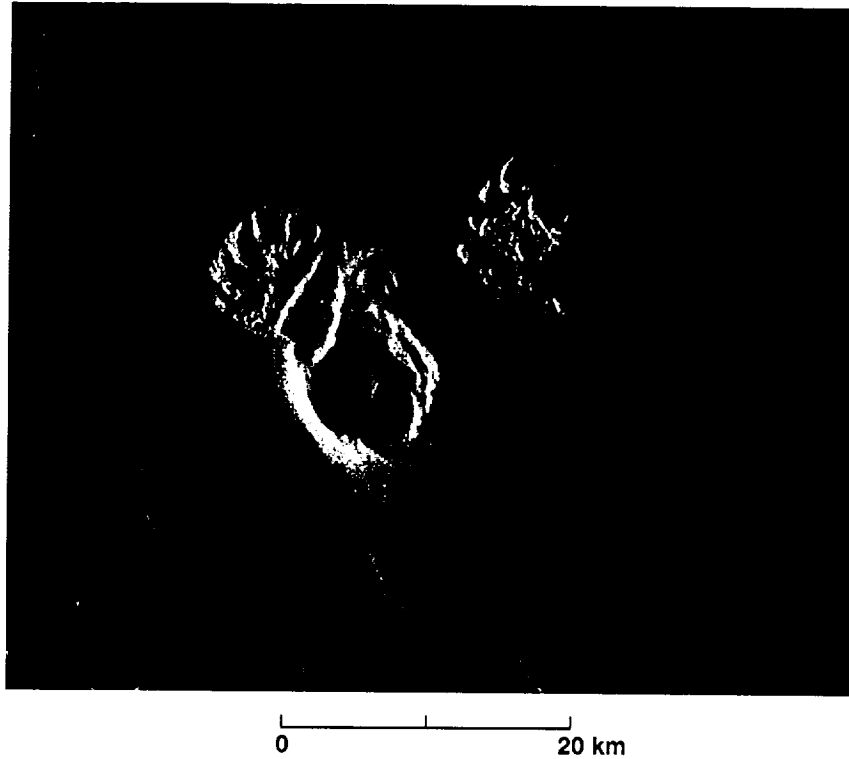
0   20 km

Figure 9-19. Small dome (17.4 km in diameter) in Navka Planitia shows collapsed margins in northwest and northeast quadrants. Landslides have deposited hummocky debris up to 10 km out on the plains. Dome is about 1.86 km high and has a slope of about 23 deg. Because of illumination geometry, the foreslope appears strongly compressed and bright; the backslope is correspondingly stretched and dark. Illumination is from the left at an incidence angle of 43 deg.
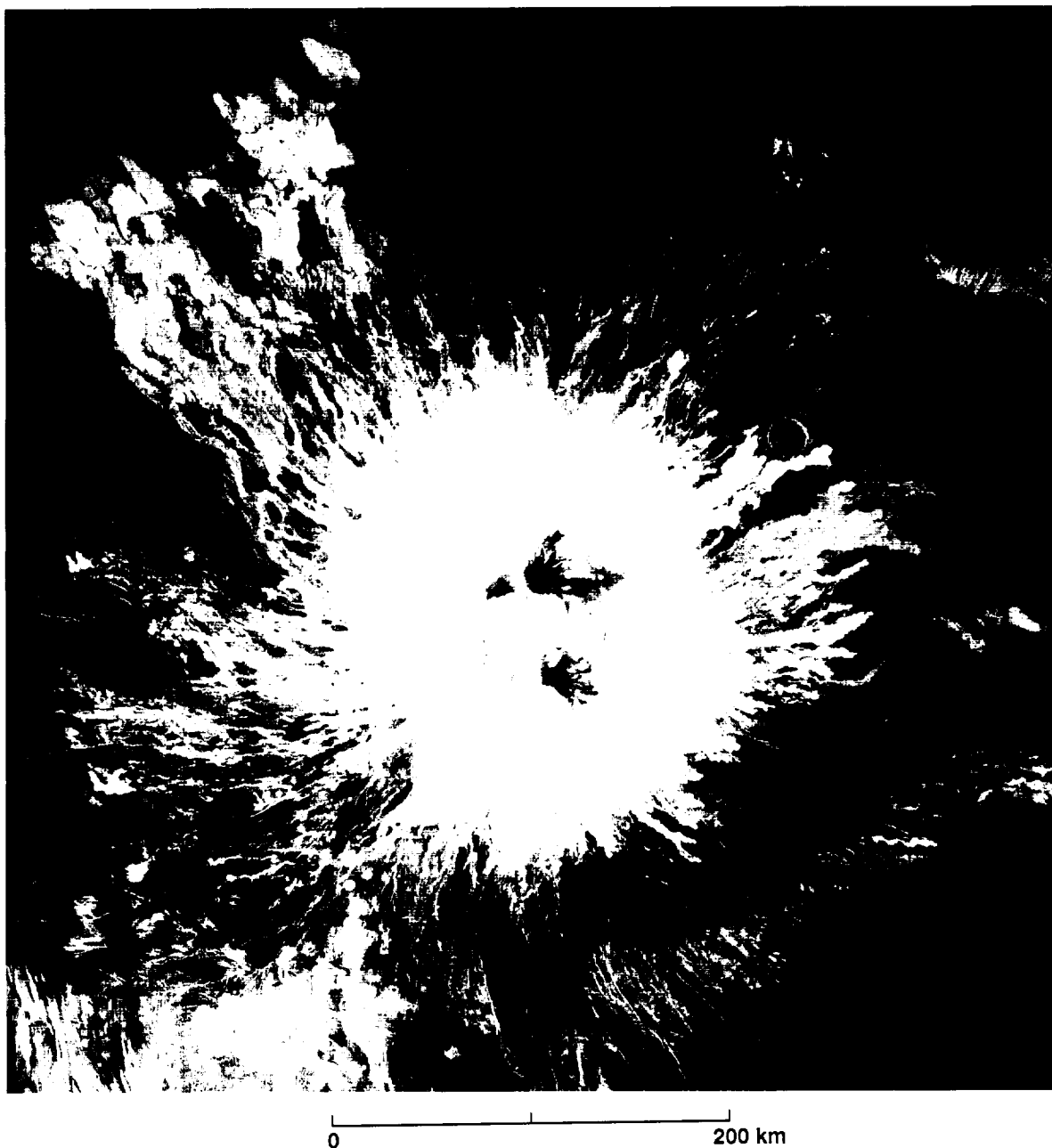
Figure 9-20. Sapas Mons is located on a topographic rise in Atla Regio. The summit area consists of two mesas with smooth tops that appear radar dark; surrounding collapsed areas are radar bright. The sides of the volcano show numerous bright overlapping flows that provide the edifice with a roughly radial outline. Note radial fractures to the east and south. Darker flows in the southeast quadrant are probably smoother than the bright flows closer to the eruptive center. An impact crater located in the northeast quadrant (20 km in diameter) is partially buried by lava flows. Illumination is from the left at an incidence angle of 46 deg.
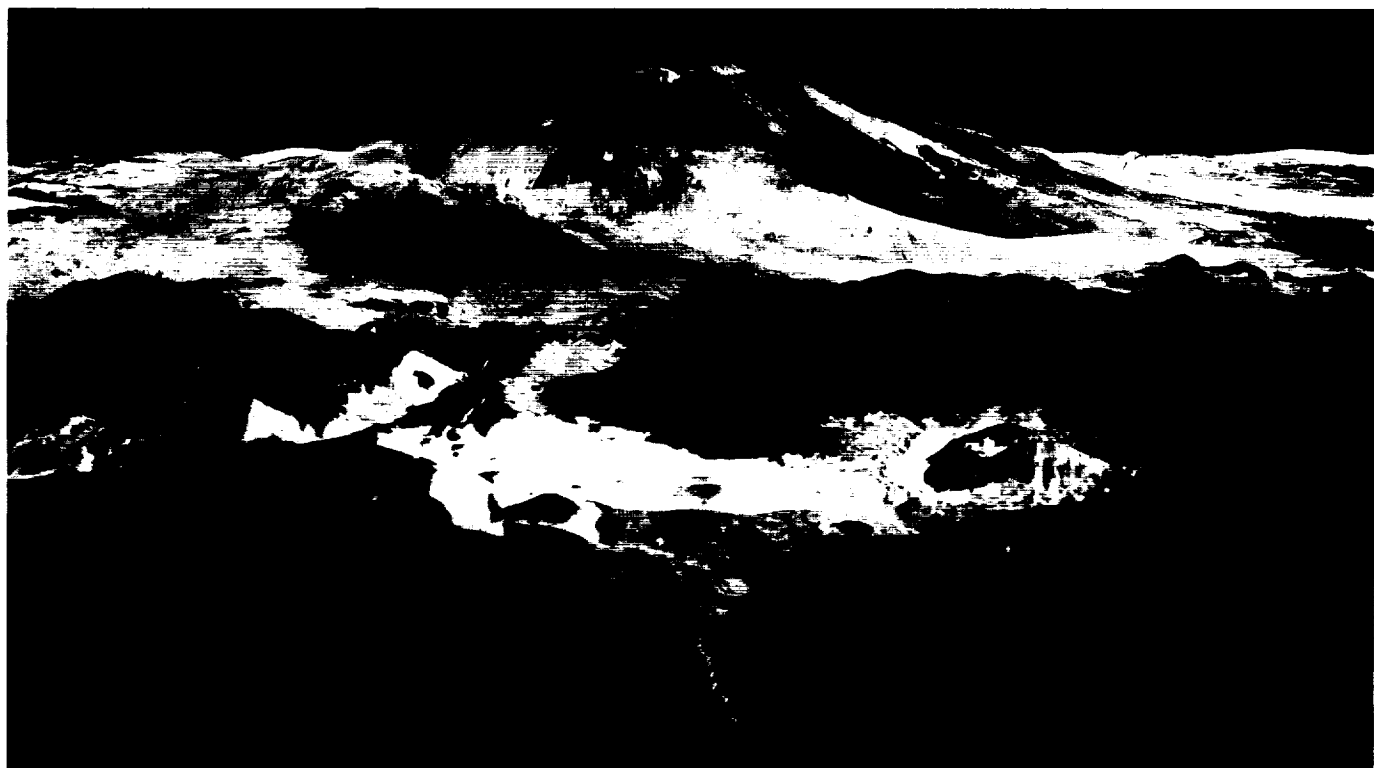
Figure 9-21. Three-dimensional perspective obtained by combining SAR and altimetry data shows lava flows that extend north from Maat Mons for hundreds of kilometers across fractured plains in the foreground. Vertical exaggeration is about 10:1.
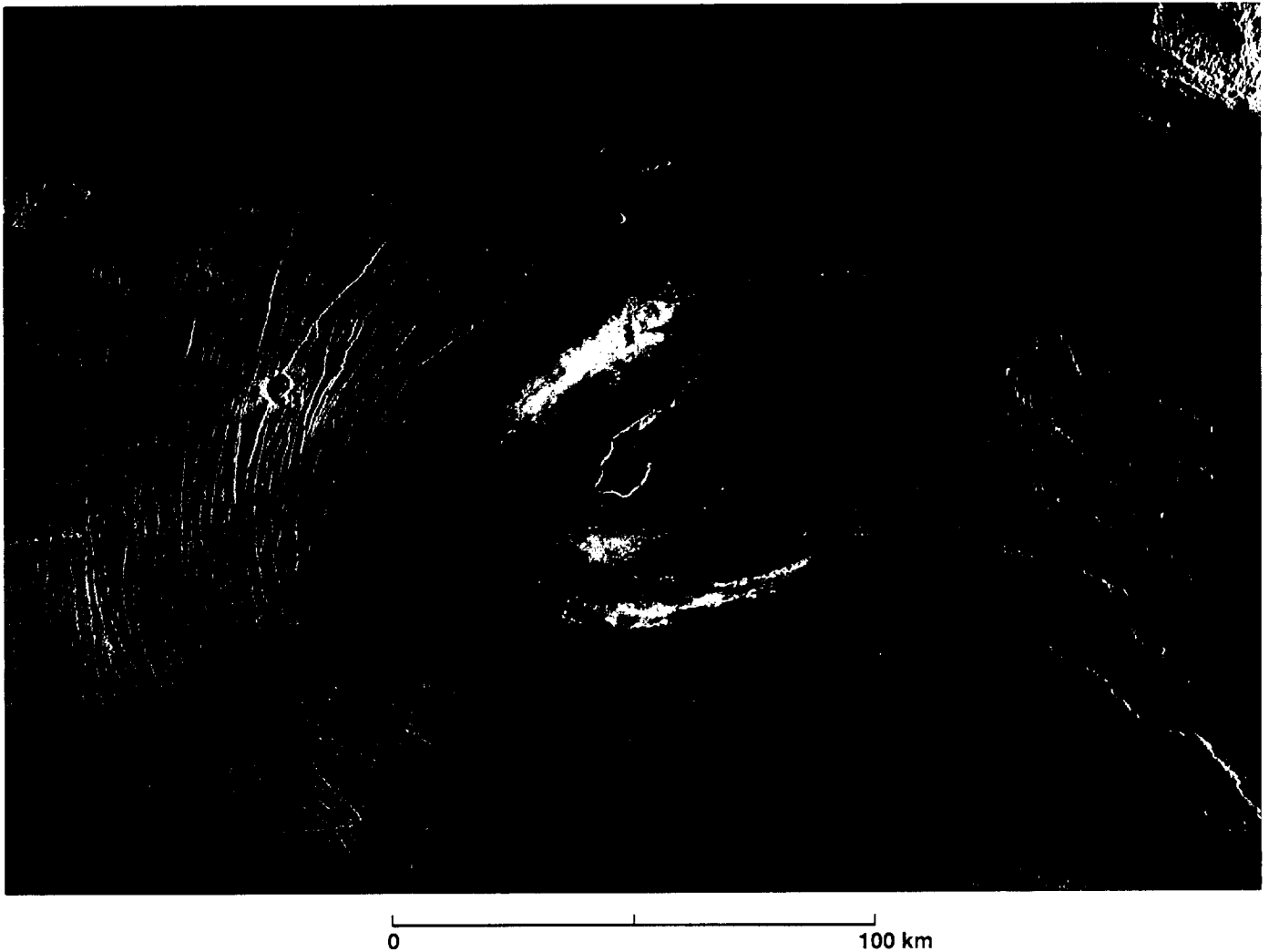
L_____L_____J
0   100 km

Figure 9-22. Sacajawea Patera is an elliptical caldera on Lakshmi Planum in western Ishtar Terra. The depression is enclosed by a zone of concentric troughs that show radar-bright outlines. The floor is covered with smooth mottled plains and has bright deposits near the center and around the periphery. Linear to sinuous scarps have bright outlines that extend southeast from the eastern margin of the caldera. A small shield with a pronounced central pit is transected by one of these features. Illumination is from the left at an incidence angle of 27 deg.

References

Arvidson, R. E., R. Greeley, M. C. Malin, R. S. Saunders, N. Izenberg, J. J. Plaut, E. R. Stofan, and M. K. Shepard, 1992, "Surface modification of Venus as inferred from Magellan observation of plains," *J. Geophys. Res.*, v. 97, no. E8, p. 13,303–13,317.

Baker, V. R., G. Komatsu, T. J. Parker, V. C. Gulick, J. S. Kargel, and J. S. Lewis, 1992, "Channels and valleys on Venus: Preliminary analysis of Magellan data," *J. Geophys. Res.*, v. 97, no. E8, p. 13,421–13,444.

Barsukov, V. L., V. P. Volkov, and I. L. Khodakovsky, 1982, "The crust of Venus: Theoretical models of chemical and mineral composition," *Proc. Lunar Planet. Sci. Conf. 13th, J. Geophys. Res.*, v. 87, p. A3-A9.

Barsukov, V. L., Yu. A. Surkov, L. Dimitriev, and I. L. Khodakovsky, 1986, "Geochemical study of Venus by landers of Vega-1 and Vega-2 probes," *Geokhimiya*, p. 275–289 (in Russian).

Campbell, B. A., and D. B. Campbell, 1992, "Analysis of volcanic surface morphology on Venus from comparison of Arecibo, Magellan, and terrestrial airborne radar data," *J. Geophys. Res.*, v. 97, no. E10, p. 16,293–16,314.

Greeley, R., 1982, "The Snake River Plain, Idaho: Representative of a new category of volcanism," *J. Geophys. Res.*, v. 87, p. 2705–2712.

133

Guest, J. E., M. H. Bulmer, J. Aubele, K. Beratan, R. Greeley, J. W. Head, G. Michaels, C. Weitz, and C. Wiles, 1992, "Small volcanic edifices and volcanism in the plains of Venus," *J. Geophys. Res.*, v. 97, no. E10, p. 15,949–15,966.

Head, J. W., L. S. Crumpler, J. C. Aubele, J. E. Guest, and R. S. Saunders, 1992, "Venus volcanism: Classification of volcanic features and structures, associations, and global distribution from Magellan data," *J. Geophys. Res.*, v. 97, no. E8, p. 13,153–13,197.

Moore, H. J., J. J. Plaut, P. M. Schenk, and J. W. Head, 1992, "An unusual volcano on Venus," *J. Geophys. Res.*, v. 97, no. E8, p. 13,479–13,493.

Parker, T. J., G. Komatsu, and V. R. Baker, 1992, "Longitudinal topographic profiles of very long channels in Venusian plains regions," *Lunar and Planet. Sci. Conf. 23rd*, Lunar and Planet. Inst., Houston, Texas, p. 1035–1036.

Pavri, B., J. W. Head III, K. B. Klose, and L. Wilson, 1992, "Steep-sided domes on Venus: Characteristics, geologic setting, and eruption conditions from Magellan data," *J. Geophys. Res.*, v. 97, no. E8, p. 13,445–13,478.

Plaut, J. J., 1992, "'Problem' footprints in Magellan altimetry data," Lunar and Planet. Inst., Contribution 789, Houston, Texas, p. 90–92.

Plaut, J. J., and R. E. Arvidson, 1992, "Comparison of Goldstone and Magellan radar data in the equatorial plains of Venus," *J. Geophys. Res.*, v. 97, no. E10, p. 16,279–16,291.

Roberts, K. M., J. E. Guest, J. W. Head, and M. G. Lancaster, 1992, "Mylitta Fluctus, Venus: Rift-related, centralized volcanism and the emplacement of large-volume flow units," *J. Geophys. Res.*, v. 97, no. E10, p. 15,991–16,015.

Slyuta, E. N., and M. A. Kreslavsky, 1990, "Intermediate-sized (20–100 km diameter) volcanic edifices on Venus," *Proc. Lunar and Planet. Sci. Conf. 21st*, Lunar and Planet. Inst., Houston, Texas, p. 1174–1175.

Smith, D. K., and J. R. Cann, 1990, "Hundreds of small volcanoes on the floor of the Mid-Atlantic Ridge at 24-30°N," *Nature*, v. 348, p. 152–155.

Stofan, E. R., V. L. Sharpton, G. Schubert, G. Baer, D. L. Bindschadler, D. M. Janes, and S. W. Squyres, 1992, "Global distribution and characteristics of coronae and related features on Venus: Implications for origin and relation to mantle processes," *J. Geophys. Res.*, v. 97, no. E8, p. 13,347–13,377.

Chapter 10. Geologic Mapping on Venus

David A. Senske and Ellen R. Stofan

Introduction

The purpose of geologic mapping of a planet's surface is to characterize and classify areas and materials and to organize information for ready analysis in terms of geologic processes and history. In common with terrestrial geologic mapping, stratigraphic procedures are used to define the distribution and geometry of planetary rock bodies. Rock units are delineated on the basis of their composition and related lithic characteristics without regard to the mode of origin. Boundaries between units are placed at positions of change in physical properties [North American Commission on Stratigraphic Nomenclature, 1983]. The relative age of rock units is determined primarily from contact relations with adjacent units. Stratified rock units that commonly occur in tabular form are younger in the order of their superposition—younger units lie above older units. Nonstratified units that are commonly massive are generally younger than the host rocks they transect or deform.

In mapping the Moon, Wilhelms [1970 and 1972] and others used surface albedo, morphology, topography, and color to define units. The units can be thought of as "morphostratigraphic material units," with lithology inferred from other physical characteristics. Lunar geologic units were mapped to reflect consistency in processes of formation and were subdivided into discreet time intervals [Wilhelms, 1972]. A variety of observational criteria define and characterize a unit, including texture (e.g., the presence of ridges, the presence of domical hills, and the degree of radar roughness), albedo, and topographic information. For the Magellan data, emissivity and radar reflectivity are also used to characterize geologic units. Standard symbols are used to show morphologic features such as ridges and troughs [Compton, 1962].

Previous mapping of Venus using Arecibo and Venera 15/16 data has produced geomorphologic/geologic maps of Venus with the definition of units based mainly on morphology and topography [Sukhanov et al., 1989; Campbell and Campbell, 1990; Senske et al., 1991a and 1991b]. Analyses of Magellan radar images indicate that geologic terrains defined previously in Venera and Arecibo radar images have complex and variable characteristics. Magellan data can be used to compile maps based on geomorphology, as was done with the Venera 15/16 data [Sukhanov et al., 1989].

Geomorphologic maps do not necessarily represent stratigraphic rock units, but they are extremely useful in determining the regional- and global-scale distribution of features such as ridge belts and coronae. Other maps that concentrate on a particular type or particular types of features, such as structural maps, can be produced.

True geologic maps, that include the identification of rock-stratigraphic units, are difficult to construct and require the use of Magellan image, altimetry, emissivity, reflectivity, roughness, and, where possible, lander geochemical data.

This guide includes an example of a map compiled for Gula Mons in western Eistla Regio. The map combines both geologic and geomorphologic units. The area is centered at 22°N, 358°E, at a highland that rises over 2 km above the surrounding plains (Figure 10-1). Eistla Regio is composed of an east–west trending group of uplands that cover a distance of over 6000 km and link up with Aphrodite Terra to the east. Western Eistla Regio is dominated by two large volcanic constructs, Sif Mons and Gula Mons. These volcanoes are cut by extensional faults and graben and are surrounded by extensive radar-bright and -dark lava flows [Campbell and Campbell, 1990 and 1992; Senske et al., 1991b and 1992].
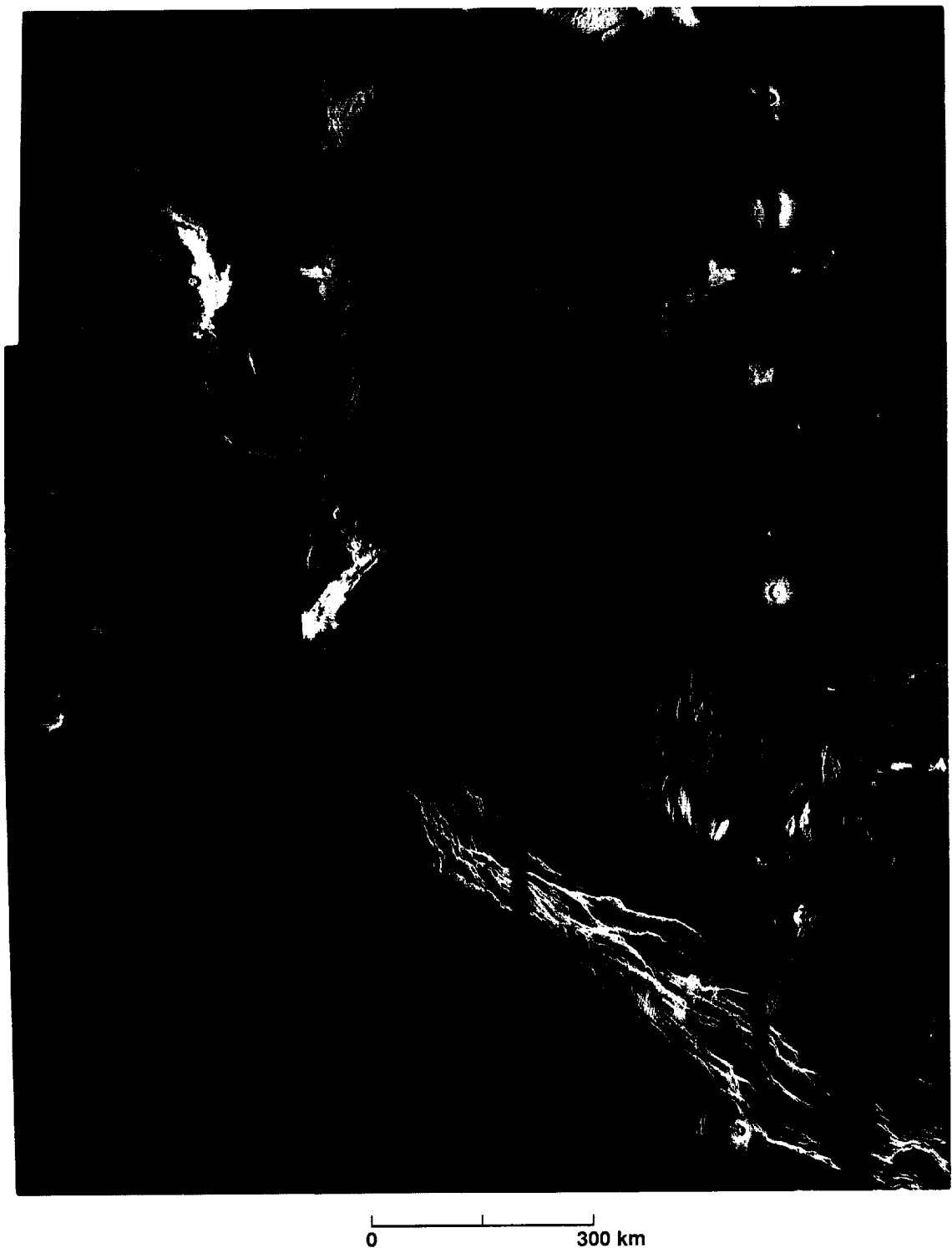
0   300 km

Figure 10-1. Magellan radar image of Gula Mons. The image covers an area of 1500 km × 1700 km and was imaged at an angle of 42 to 45.5 deg with illumination from the left.

Geologic Map of Gula Mons

A geologic map of Gula Mons and its surrounding area is shown in Figure 10-2. Thirteen units are identified on the basis of variations in surface texture, patterns of tectonic features, and an assessment of the degree of radar backscatter (ranging from bright to dark). The region was mapped at the Compressed Once Mosaicked Image Data Record (C1-MIDR) scale and includes seven plains units (including units mapped on Gula Mons and surrounding low lying areas), two tectonic terrain units, one volcanic/tectonic unit, and three surficial materials units (crater materials and bright and dark diffuse deposits). In addition, structural features including depressions, faults, fractures, and small domes are identified.

Unit Characteristics

Plains. Plains make up a large part of the lowland area surrounding Gula Mons; three classes are identified: (1) reticulate plains (Pr); (2) mottled plains (Pm); and (3) lobate plains (Pl) (Figure 10-2). Areally extensive reticulate plains are typically radar-dark and contain few identifiable volcanic centers, i.e., small shields (diameters of 2 to 10 km). Pervasive within this unit are the low, narrow, sinuous ridges responsible for its reticulate character. Mottled plains, located on the distal part of the highland in the northwest part of the area, contain abundant small volcanoes that often lie in clusters forming shield fields. The mottled texture is due to the presence of numerous lava flows that range from rough (bright) to smooth (dark) at radar wavelengths. The edge of this unit is embayed by reticulate plains, indicating that the mottled plains predate the reticulate plains. Localized areas of radar-bright lobate plains are made up of linear, long and narrow (500 km long and 10 to 20 km wide) lava flows. Source areas for these lava flows are associated with a corona or vents within the reticulate plains.

Lava Flows. Although numerous lava flows are observed at Gula Mons, the units at this volcano are simplified to show the major flow complexes. Three assemblages of lava flow units are identified: (1) mottled dark plains (Pmd); (2) bright/dark digitate plains (Pd); and (3) bright plains (Pb) [Senske et al., 1992]. Laterally extensive mottled dark plains radiate for distances of 300 to 600 km from the summit of the peak and are superposed on the surrounding regional plains units. This unit is composed of narrow (5 to 10 km) 150- to 200-km-long lava flows that are relatively smooth at radar wavelengths and is interpreted to represent an episode of large-scale lava emplacement early in the history of the volcano. The central part of the construct (bright/dark digitate plains) is made up of narrow, radar-bright lava flows 100 to 300 km long and interpreted to be associated with

constructional volcanism at the central part of the volcano. The summit of Gula (bright plains) is cut by a northeast/southwest trending radar-bright linear zone of faulting (150 km long and 30 km wide). Other deposits, located in the western part of the mapped area, are associated with volcanic construction at Sif Mons and are collectively identified as a Sif Mons Unit (S).
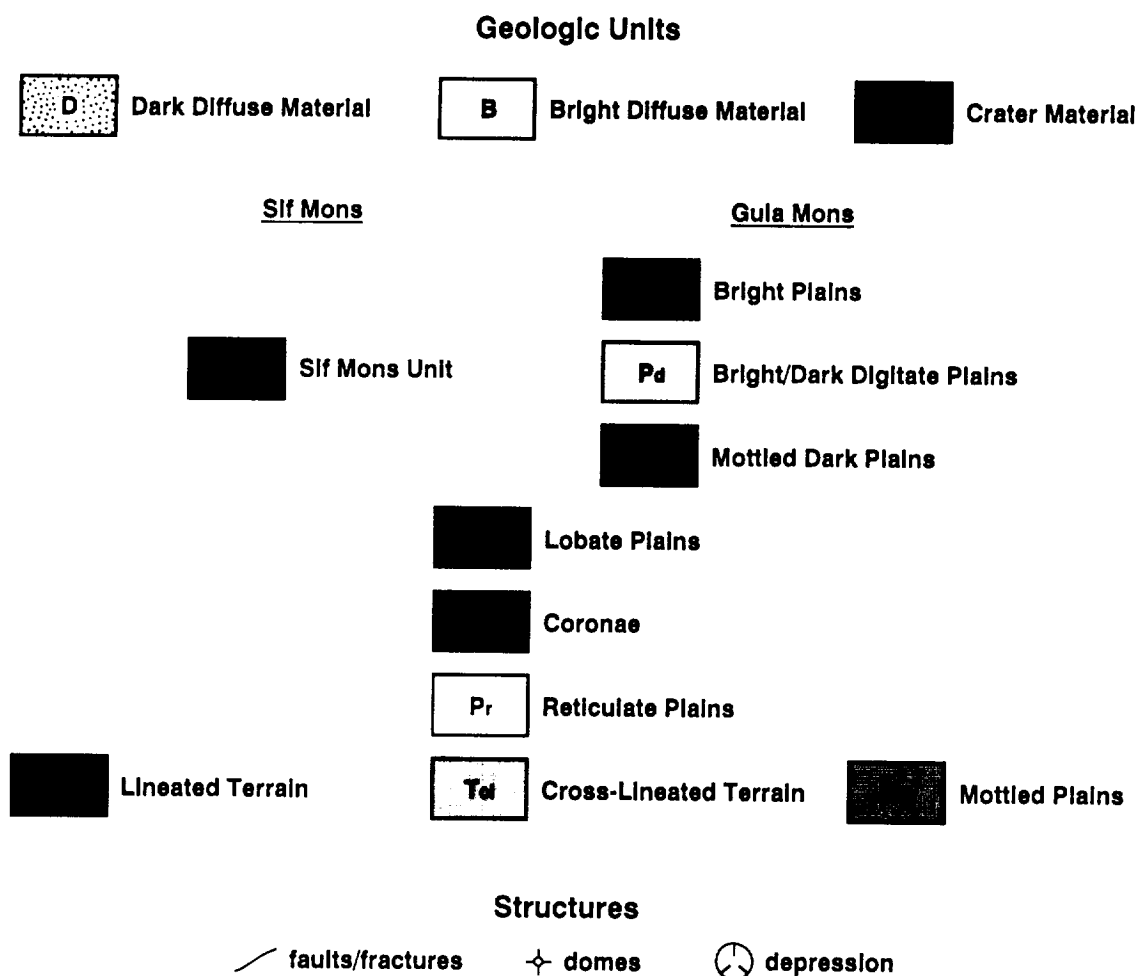
Coronae. Adjacent to the northern part of Gula are two coronae (Co). These volcanic/tectonic features are circular to elliptical in plan view and are characterized by an annulus of concentric ridges or fractures/faults. The interiors of coronae are complex and contain lava flows, domes, and ridges and fractures that are arrayed radially or concentrically to the feature [Pronin and Stofan, 1990]. The first corona, Idem-Kuva (25°N, 358°E), is a nearly circular, 225-km-diameter structure 600 m high. This feature is surrounded by graben that are arrayed in a concentric pattern and lie within flanking U-shaped troughs. The troughs are source regions for lobate plains. A second, elliptical (300 km × 200 km), 360-m-high corona (Nissaba) is located to the west of Idem-Kuva. Lava flows radiate from a low, circular region, in the southeast part of this structure, suggesting the presence of a shallow caldera.

Tectonic Units. In addition to the volcanic features, two tectonic units are identified. To the north of Gula are several isolated regions of cross-lineated terrain (Tcl). This unit, characterized by locally elevated topography and multiple directions of deformation, is extensively embayed by surrounding reticulate plains. Areas of lineated terrain (Tl), made up of narrowly spaced (less than 1 km to 2.5 km) north–south trending ridges, are identified on the southeast part of Gula Mons. Like the cross-lineated terrain, this unit is embayed by reticulate plains along with volcanic deposits that originate from a source on the east flank of Gula. An isolated occurrence of lineated terrain is located within Guor Linea where it is embayed by plains and crosscut by faulting. On the basis of these crosscutting and superposition relationships, this unit and the cross-lineated terrain are interpreted to be the oldest features on this part of the planet.

Impact Craters. Six impact craters (C), varying from 5 to 48.5 km in diameter, are mapped in the vicinity of Gula Mons. All of these craters are associated with a diffuse radar-dark halo [see Phillips et al., 1991, and Arvidson et al., 1991, for detailed discussions of radar-dark deposits surrounding impact craters]. Two of the dark deposits (D) extend for over 300 km, and both extend from west to east. The dark material and the craters superpose all other units, including plains, tectonic units, and deposits from Gula Mons, making them stratigraphically the most recent features in the region. A dark unit northwest of the summit of Gula Mons is very

Figure 10-2. Geologic map of Gula Mons. The units are shown in stratigraphic order.

138

Geologic Units

| ▒ D ▒ Dark Diffuse Material | | B | Bright Diffuse Material | ███ Crater Material |

Sif Mons

███ **Sif Mons Unit**

Gula Mons

███ **Bright Plains**

| Pd | **Bright/Dark Digitate Plains**

███ **Mottled Dark Plains**

███ **Lobate Plains**

███ **Coronae**

| Pr | **Reticulate Plains**

███ **Lineated Terrain** | Tel | **Cross-Lineated Terrain**   ▓▓▓ **Mottled Plains**

Structures

╱ **faults/fractures**   ✛ **domes**   ⊕ **depression**

linear and narrow, less than 40 km across. In comparison, a dark unit on the eastern part of Gula has a parabolic shape and is far more extensive, having a width of over 450 km. One diffuse radar-bright unit (B) is also mapped. The center may be an impact crater, but it is obscured by a data gap.

Geologic History

Superposition, crosscutting relationships, and the areal distributions of units lead to the following sequence of tectonic and volcanic events: (1) deformation forming the cross-lineated terrain and the lineated terrain, and emplacement of the mottled plains; (2) volcanism forming the reticulate plains that embay the three earliest units; and (3) emplacement of coronae, lobate plains, and volcanic construction forming Gula Mons. Gula Mons appears to have had a complex evolution, undergoing multiple episodes of lava emplacement.

Geologic mapping shows that much of the early volcanic history of the area surrounding Gula Mons was characterized by the emplacement of mottled plains. These plains were subsequently subjected to lava flooding

(formation of the reticulate plains) and uplifted to form the western Eistla Regio highland.

The tendency of many lava flows to change in brightness along their length often makes their mapping difficult. It is also difficult to establish temporal relationships between flows that are separated geographically. The age relationship between Gula Mons and Sif Mons to the west is not clear [Senske et al., 1992]. Superposition relationships between deposits are often ambiguous, indicating that the two constructs may have formed concurrently. Along with the construction of volcanic complexes, a great deal of extensional deformation is evident along a summit rift zone of Gula and at Guor Linea (Figure 10-2). Flows from Gula generally overlie Guor Linea, a rift valley formed in association with the uplift of western Eistla.

Lava flows from Gula appear to be deflected around both Idem-Kuva and Nissaba, indicating that at least some volcanism associated with Gula postdates formation of these coronae. Dark diffuse material associated with impact craters is superposed on a number of units (units both at Gula Mons

and Nissaba). This indicates that some of the most recent events in this part of western Eistla Regio are associated with impact cratering.

Detailed geologic mapping of this region and the rest of Venus using Magellan data is ongoing. The results presented here indicate that multiple episodes of tectonic and volcanic activity have occurred, with impact cratering and eolian processes also modifying the surface. Unraveling the complex interconnected history of these processes through detailed mapping is critical to understanding the evolution of Venus.

References

Arvidson, R. E., V. R. Baker, C. Elachi, R. S. Saunders, J. A. Wood, 1991, "Magellan: Initial analysis of Venus surface modification," *Science*, v. 252, p. 270–275.

Campbell, B. A., and D. B. Campbell, 1990, "Western Eistla Regio: radar properties of volcanic deposits," *Geophys. Res. Lett.*, v. 17, p. 1353–1356.

Campbell, B. A., and D. B. Campbell, 1992, "Analysis of volcanic surface morphology on Venus from comparison of Arecibo, Magellan, and terrestrial airborne radar data," *J. Geophys. Res.*, v. 97, p. 16293–16314.

Compton, R. R., *Manual of Field Geology*, 1962, John Wiley and Sons, Inc., New York, 378 p.

North American Commission on Stratigraphic Nomenclature, 1983, "North American Stratigraphic Code," *Amer. Assoc. Petrol. Geol.* Bull., v. 67, p. 841–875.

Phillips, R. J., R. E. Arvidson, J. M. Boyce, D. B. Campbell, J. E. Guest, G. G. Schaber, and L. A. Soderblom, 1991, "Impact craters on Venus: Initial analysis from Magellan," *Science*, v. 252, p. 288–297.

Pronin, A. A., and E. R. Stofan, 1990, "Coronae on Venus: Morphology and distribution," *Icarus*, v. 87, p. 452–474.

Senske, D. A., D. B. Campbell, J. Head, P. Fisher, A. Hine, A. deCharon, S. Frank, S. Keddie, K. Roberts, E. Stofan, J. Aubele, L. Crumpler, and N. Stacy, 1991a, "Geology and tectonics of the Themis Regio–Lavinia Planitia–Alpha Regio–Lada Terra area, Venus: results from Arecibo image data," *Earth, Moon, and Planets*, v. 55, p. 97–161.

Senske, D. A., D. B. Campbell, E. R. Stofan, P. C. Fisher, J. W. Head, N. Stacy, J. C. Aubele, A. A. Hine, and J. K. Harmon, 1991b, "Geology and tectonics of Beta Regio, Guinevere Planitia, Sedna Planitia, and Western Eistla Regio, Venus: Results from Arecibo image data," *Earth, Moon, and Planets*, v. 55, p. 163–214.

Senske, D. A., G. G. Schaber, and E. R. Stofan, 1992, "Regional topographic rises on Venus: Geology of western Eistla Regio and comparison to Beta Regio and Atla Regio," *J. Geophys. Res.*, v. 97, p. 13395–13420.

Sukhanov, A. L., A. A. Pronin, G. A. Burba, A. M. Nikishin, V. P. Kryuchkov, A. T. Basilevsky, M. S. Markov, R. O. Kuzmin, N. N. Bobina, V. P. Shashkina, E. N. Slyuta, and I. M. Chernaya, 1989, *Geomorphic/Geologic Map of Part of the Northern Hemisphere of Venus*, United States Geological Survey Miscellaneous Investigators Series Map I-2059.

Wilhelms, D. E., 1970, "Summary of lunar stratigraphy—telescopic observations," *U.S.G.S. Prof. Paper 599-F*, p. F1- F47.

Wilhelms, D. E., 1972, *Geologic Mapping of the Second Planet*, U.S.G.S. Interagency Report: Astrogeology 55, 36 p.

Appendix

Availability of Magellan Data Products[1]

Researchers interested in additional information about the Magellan mission, access to imagery or data collected, or detailed catalog information will find the following sources most useful:

National Space Science Data Center
Goddard Space Flight Center
Coordinated Request and User Support Office
Mail Code 933.4
Greenbelt, Maryland 20771
(301) 286-6695, Facsimile: (301) 286-4952
On-line Catalog: NSSDC::
or   nssdc.gsfc.nasa.gov
                  (128.183.36.25)
                  Username: nssdc
E-mail: NSSDC::REQUEST
or   request@nssdc.gsfc.nasa.gov

The National Space Science Data Center (NSSDC) at NASA's Goddard Space Flight Center is the principal archive and distribution center for all NASA missions. It has all of Magellan's standard mosaic image products that have been released by the Project in both photographic and digital form on CD-ROMs. It also has press-released images, videotapes, software with which to display the CD-ROM digital images, planning maps of Venus, a fact sheet, and documentation.

NSSDC's principal charter is to support data distribution to researchers. Requests from NASA centers, Federal, State, and local governments, and NASA-funded researchers are supplied without charge. Other requests are supplied at a nominal charge. NSSDC will consider waiving these charges for educational requests for a limited quantity of material if the requester explains the need for such treatment.

NSSDC has the equipment necessary to supply special requests, such as large photographic enlargements. It has a limited staff able to assist with questions about the products or the identification of products showing a specific feature. It is not, however, able to support requests for extensive assistance either by researchers, the public, or teachers.

A general catalog showing the classes of materials available through NSSDC is available for on-line computer access. Requests for materials can be made through the on-line catalog, by electronic mail, or by telephone.

Regional Planetary Image Facilities

NASA's Planetary Geology and Geophysics program supports a group of Regional Planetary Image Facilities (RPIFs) around the United States, as well as overseas.

The RPIF at NASA's Jet Propulsion Laboratory may have the broadest collection of Magellan materials available most quickly. In practice, it is open by appointment on Monday, Wednesday, and Friday to both researchers and members of the public. The RPIF houses a complete image library of NASA's lunar and planetary missions, including Magellan. Visitors can browse through Magellan materials, including the CD-ROM digital imagery collection and videotapes.

---

[1] From Okerson, D., 1992, *Magellan Resources: Access to Magellan Project Information and Science Data*, JPL D-9934 (internal document), Jet Propulsion Laboratory, Pasadena, California, 28 p.

Jet Propulsion Laboratory
Regional Planetary Image Facility
Mail Stop 202-101
4800 Oak Grove Drive
Pasadena, California 91109
(818) 354-3343
Facsimile: (818) 354-3437

Planetary Data System
Jet Propulsion Laboratory
4800 Oak Grove Drive
Mail Stop 525-3610
Pasadena, California 91109
(818) 306-6130, Facsimile: (818) 306-6929
E-mail: JPLPDS::PDS_OPERATOR or
    pds_operator@jplpds.jpl.nasa.gov
                    (137.79.104.100)

Researchers funded by NASA's Solar System
Exploration Division can obtain Magellan materials through
the Planetary Data System (PDS). PDS consists of a central
on-line catalog at the Jet Propulsion Laboratory and a number
of "nodes" located at research facilities with particular
expertise in specific planetary research areas. The
Geosciences Node at Washington University is particularly
responsible for cataloging and supporting Magellan data.

PDS provides an on-line central catalog showing the
general classes of Magellan material available and allowing
the user to identify specific digital and photographic products.
Requests for materials can be made through this central
catalog. The requests are typically fulfilled by forwarding the
request to NSSDC. Contact PDS to request an account.

The Geosciences Node provides a much more detailed
catalog of the Magellan materials. This node can be reached
through the central PDS catalog or directly. The Geophysics
Node also supports visiting researchers and provides image
processing capabilities to use the digital imagery. Contact

Planetary Data System, Geosciences Node
Earth and Planetary Remote Sensing Laboratory
Washington University, Campus Box 1169
One Brookings Drive
St. Louis, Missouri 63130-4899
(314) 935-5493, Facsimile: (314) 935-7361
E-mail: WURST::MGNSO or
    mgnso@wurst.wustl.edu
                    (128.252.135.4)

The Washington University PDS Node provides a direct
and knowledgeable source of assistance in using Magellan
data through a Magellan Data Products Support Office. The
purpose of the Support Office is to provide users with
information about and assistance in getting Magellan data.
Standard and special data products are supported, including
digital products, photographs, slides, videotapes, and NASA
Public Information Office (PIO) products. The Support Office
serves NASA-sponsored scientists, other researchers and
educators, and the general public.

U.S. Geological Survey

The U. S. Geological Survey (USGS) has a program to
produce maps of the planets based on the best available data
from NASA and foreign missions, including Soviet missions.
The Venus maps currently available from USGS are based on
data from NASA's Pioneer Venus Orbiter and the Soviet
Venera 15/16 missions. New maps will be produced and made
available based on the Magellan data over the next several
years. NASA-funded researchers can obtain maps directly by
contacting

Ms. Jody Swann
Planetary Data Facility
U.S. Geological Survey
2255 North Gemini Drive
Flagstaff, Arizona 86001-1698
(602) 556-7262, Facsimile: (602) 556-7090

All interested persons can obtain a listing of planetary
maps from the same address. Those not funded by NASA can
order maps by writing

U.S. Geological Survey
Mail Stop 306
Branch of Distribution
Denver Federal Center
P.O. Box 25286
Denver, Colorado 80225

For more information, contact

Earth Science Information Center
U.S. Geological Survey
507 National Center
Reston, Virginia 22092
(703) 860-6045

On-Line Computer Access

In addition to the on-line computer catalogs provided by NSSDC and PDS described above, Magellan information and digital imagery can be obtained through several computer networks.

SPACELINK is an electronic information system for educators (a computer bulletin board) particularly oriented toward teachers interested in using NASA materials in their classes. It is operated by NASA's Marshall Space Flight Center in Alabama. SPACELINK can be reached by a telephone modem or through the Internet network. It contains a wide variety of information, as well as software and digital image files in the GIF format, which is suitable for classroom computer display. Contact

> telnet: spacelink.msfc.nasa.gov (192.149.89.61)
> modem: (205) 895-0028

NASA's Ames Research Center in California allows public access through the Internet network to a large collection of information on NASA's missions, as well as image display software, digital image files in a variety of formats, and captions for all the released (press) images. Magellan imagery is available in GIF and VICAR formats. In addition, the Magellan CD-ROMs are available in rotation with other NASA image CD-ROMs as a pair of publicly accessible directories. Contact

> ftp: ames.arc.nasa.gov (128.102.18.3)
> user: anonymous
> cd: pub/SPACE/MAGELLAN, VICAR, GIF,
>   CDROM, CDROM2, SOFTWARE

The PDS Geosciences Node at Washington University (described earlier) permits access through the Internet network to selected Magellan data and documentation. Contact

> ftp: wuarchive.wustl.edu (128.252.135.4)
> user: anonymous
> cd: graphics/magellan

Index[1]

A

altimeter/radiometer composite data record   7, 20
altimetry   19–20, 27, 109
anaglyph   36, *40*
arachnoids   100, *106*
ARCDR (see altimeter/radiometer composite data record)
autocorrelation   53

B

backscatter
    approximation   10
    coefficient   9–10, 81
    Venus average (Muhleman)   9
basic image data record   7, 9
BIDR (see basic image data record)
Bragg model   54

C

caldera   125, *133*
canali   114, *120*
collapse features   63, 114, *122*, 123, *125*
color overlay   27, *115*
combined SAR/non-SAR data   27–29, *115*
complex ridge terrain   100, *104*
compressional features
    mountain belts   97–98
    ridge belts   98, *102*
    ridges   98
cones   *111*, 117, *127*

coronae   100, *105*
correlation length   53
crater extended deposits   60–61
craters
    distinction of   79
    impact   75
    volcanic   122
cycles of coverage   7, 11–*17*

D

data
    altimetry   19
    availability   141–143
    collection modes   2–3, *4*
    non-SAR   19
    radiometry   25–26
    reflectivity, rms slope   20, 25
    SAR image   7
    stereo   34–35
    storage formats   9
DEM (see digital elevation model)
depression angle   45
dielectric constant   26, 28, 55, 110–112, *114*
digital elevation model   36–37
domes   *41, 67, 72*, 117, 122–123, *129*
dunes   58, 60, *65–68*

E

echo profile (template)   20, 125
ejecta   61, 75, 81

---

[1] Citations to figures are noted in italics.

emissivity   25–26, 28, *30, 83*
eolian features   57
    crater extended deposits   60–61
    dunes   58, 60, *65–68*
    wind streaks   57–58
    yardangs   60
extensional features
    graben/troughs   93, *94–95*
    rift (valley)   97
    scarps/normal faults   *96–97*

F

facet model   54
footprint
    altimeter   2, 19–20, 25
    radiometer   20, 26
Fresnel reflectivity   20, 25, 55

G

global data records   20, *21–24*
graben   93, *94–95*
gravity observations   13
GxDR (see global data records)

H

Hagfors model   54
Hagfors scattering function   25
halos   58, 75–76, 81

I

image
    brightness   11, 27, 109–111
    data records   7–9
    distortion   33, 45
    swath dimensions   7
imaging geometry   45–48, 86
    left-looking   11–13, *14, 16–17*
    right-looking   11, *15*
impact craters
    distinction of origin   79
    extended deposits   60–61

general characteristics   75
    halos   75–76, 81
    Magellan results   76–78
    modification   85–86
    morphological types   76–78
    outflow deposits   65, 81
    parabolic features   26, 60–61, *70, 75*
    radiophysical properties   79, *82–83*
    slope/depth measurements   81
    splotches   81, 85, *87*
    Venera results   76
incidence angle   45–*46*
    surface roughness relations   48–51
    variation with latitude   36–*37*

L

lava channels   114–115, *116*
    canali   114, *120*
    rille   114, *121*
lava flows   *61*, 109–115, *116, 118–119*
layover   33, 47, *49*
look angle   45–48
look direction (azimuth)   48, *51–52*
looks, number of   9

M

Magellan
    extended mission   1, 33
    mapping orbit profile   3, *5*
    mission requirements   1
    modes of data collection   2–3, *4*
    radar sensor   2–3
    scientific objectives   1
    stereo data   34–35
    system and orbit characteristics   3
mapping
    cycles   1, 7, 11, 13
    geologic   76–*77, 84,* 135–*139*
    orbit profile   3, 5
    radar units   113, *119,* 137–*139*
    stereo   86
    topographic   37
mass movements   63
MIDR (see mosaicked image data record)

V

volcanic features   109
    caldera   125, *133*
    canali   114, *120*
    collapse   63, 114, *122*, 123, *125*
    crater distinction   79
    lava channels   114–115, *116*
    lava flows   61, 109–115, *116, 118–119*
    plains   109
    rille   114, *121*
volcanoes
    cones   *111*, 117, *127*
    domes   *41, 67, 72*, 117, 122–123, *129*

intermediate   117
large   123–125
small domes   117
small shields   117

W

wind streaks   57–58

Y

yardangs   60